THE ELECTROREDUCTION OF L-CYSTINE HYDROCHLORIDE TO L-CYSTEINE HYDROCHLORIDE

by

Thomas R. Ralph

Thesis submitted to the University of Strathclyde in accordance with the regulations governing the award of the Degree of Doctor of Philosophy

Department of Pure and Applied Chemistry
University of Strathclyde
Glasgow G1 1XL

August 1991

ORIGINAL COPY TIGHTLY BOUND

PAGE NUMBERING AS ORIGINAL

PAGE NUMBERS ARE CLOSE TO THE EDGE OF THE PAGE.

SOME ARE CUT OFF

To my wife Susan

CONTENTS

CONTENTS

CHAPTER 2 EXPERIMENTAL FOR KINETIC STUDIES

CHAPTER 5 EXPERIMENTAL FOR BATCH REACTOR STUDIES

ABSTRACT

The electrosynthesis of L–cysteine hydrochloride is examined at a range of cathodes. Kinetic studies are possible only at mercury and lead. Both voltammetry and coulometry studies are reported. Based essentially upon electrochemical reaction orders of +1 for L–cystine hydrochloride and protons, and high Tafel slopes of ca. 180 mV/decade, attributed to disulphide adsorption, the mechanism of reduction is, as far as can be ascertained, equivalent at the metals. The RDS is transfer of the first electron to the disulphide molecule. For high disulphide concentrations k_f^o is ca. 7×10^{-10} m s^{-1} at mercury and ca. 2.5×10^{-11} m s^{-1} at lead. Several techniques yielded values for the diffusion coefficient of L–cystine hydrochloride, the relative merits of which are discussed.

Constant current electrolysis is performed in a parallel plate reactor operating in the batch recycle mode and the reactant concentration monitored with time. At mercury plated copper and lead cathodes the reactant depletion is predicted by mathematical models describing a reaction which is initially under charge transfer control followed by an instantaneous change to pure mass transport control. The models do not predict the reactant depletion at the other cathodes, because of an extensive mixed charge transfer–mass transport controlled region. To evaluate the models the average mass transport coefficient in the reactor is determined using the diffusion limited current technique. Additionally, using this technique, the enhancement in mass transport produced by various turbulence promoters is correlated with a specific geometrical characteristic of the promoters.

Parametric studies of current density and catholyte flowrate identified the optimum electrosynthesis conditions. High catholyte flowrates and the use of turbulence promoters are particularly important to the process economics. At 500

A m^{-2} mercury plated copper and lead are the most efficient cathodes but at 2,000 A m^{-2} titanium compares favourably with these metals. The durability of all three cathodes is, however, inadequate for an industrial process.

ACKNOWLEDGEMENTS

I would like to thank my supervisors Professor M. L. Hitchman and Dr. F. C. Walsh for their continued guidance, enthusiasm and interest shown over the number of years it has taken me to complete this study. I am indebted to my indusrial supervisor Professor P. J. Millington for his support and the provision of several months excellent industrial training at the Electricity Research and Development Centre (ERDC).

There are a number of people at the ERDC whom I must thank. My special gratitude to Mr. T. Crosby and Mr. T. Thorpe who devised and performed a large portion of the difficult HPLC analysis. Thanks are due to Mr. D. Campbell and Mrs. S. Northcote for assistance with the electrosyntheses experiments and finally to Mr. E. H. Kelly for the XRD analysis.

I must also thank Dr. P. Ash at Johnson Matthey Technology Centre for the ICP-MS analysis. My special thanks to Mrs. M. Lynch for the many painstaking hours of work involved in typing the thesis. Finally I wish to thank the SERC and ERDC for the award of a CASE studentship.

SYMBOLS

		Typical Units
A	Electrode area	m^2
c	Concentration	mol m^{-3}
c_b	Bulk reactant concentration	mol m^{-3}
c_o	Initial bulk reactant concentration	mol m^{-3}
c_t	Bulk reactant concentration at time t	mol m^{-3}
$c_{y,t}$	Bulk reactant concentration at distance y along the electrode at time t	mol m^{-3}
$c_{i,o}$	Initial reactant concentration at reactor inlet	mol m^{-3}
$c_{i,t}$	Reactant concentration at the reactor inlet at time t	mol m^{-3}
$c_{o,t}$	Reactant concentration at the reactor outlet at time t	mol m^{-3}
c^o	Reactant concentration at the electrode surface	mol m^{-3}
d_e	Equivalent diameter of a channel	m
D	Diffusion coefficient	m^2 s^{-1}
E	Electrode potential	V
E_e^C	Equilibrium cathode potential	V
E_e^A	Equilibrium anode potential	V
E^C	Cathode potential	V
E^A	Anode potential	V
E_{CELL}	Cell voltage(E^C-E^A)	V
E_s	Specific energy consumption	kWh Kg^{-1}
$E^{o'}$	Formal standard electrode potential	V
$E_{\frac{1}{2}}$	Half-wave potential	V
E_p	Peak potential in voltammetry	V

		Typical Units
F	Faraday constant	$A\ s\ mol^{-1}$
f	Force per unit volume excerted by gravity	$N\ m^{-3}$
ΔG	Gibbs free energy change	$J\ mol^{-1}$
I	Current	A
$I_{y,t}$	Current at distance y along the electrode at time t	A
I_L	Limiting current	A
$I_{L,t}$	Limiting current at time t	A
i	Current density	$A\ m^{-2}$
i_L	Limiting current density	$A\ m^{-2}$
i_p	Peak current density in voltammetry	$A\ m^{-2}$
k_f	Heterogeneous rate constant for electron transfer for a forward (cathodic) process	$m\ s^{-1}$
k_f^o	Heterogeneous rate constant for electron transfer for a forward (cathodic) process at E = 0 V vs. the reference electrode	$m\ s^{-1}$
k^o	Standard rate constant for an electrode process	$m\ s^{-1}$
$*K_L$	Average mass transport coefficient *(In engineering literature the lower case is used)	$m\ s^{-1}$
K_y	Local mass transport coefficient a distance y along the electrode surface	$m\ s^{-1}$
l	Length of electrode channel perpendicular to direction of electrolyte flow	m
L	Width of electrode channel perpendicular to direction of electrolyte flow	m
M	Molar mass	$kg\ mol^{-1}$
m	Electrochemical reaction order	dimensionless
m_{Hg}	Mass flow rate of mercury in polarography	$mg\ s^{-1}$
m_p	Moles of product	mol

		Typical Units
m_o	Initial moles of reactant	mol
m_t	Moles of reactant at time t	mol
n	Number of electrons	dimensionless
P	Pressure	$N\ m^{-2}$
q	Electrical charge	A s
Q	Volumetric flow rate	$m^3\ s^{-1}$
r	Electrode radius	m
R	Universal gas constant	$J\ K^{-1}\ mol^{-1}$
R	Electrical resistance	Ω
S	Overall selectivity	dimensionless
t	Time	s
T	Temperature	K
$\bar{v}$	Average linear electrolyte velocity	$m\ s^{-1}$
v	Potential sweep rate	$V\ s^{-1}$
V	Electrolyte volume	m^3
V_R	Volume of reactor	m^3
V_T	Volume of reservoir	m^3
y	Length of electrode channel parallel to direction of electrolyte flow	m
X	Fractional conversion	dimensionless
$X_{1,t}$	Fractional conversion per pass over the reactor	dimensionless
$X_{2,t}$	Fractional conversion in the reservoir	dimensionless
α_c	Cathodic transfer coefficient	dimensionless
β	Symmetry factor for electron transfer	dimensionless
β'	Adsorption coefficient	dimensionless

		Typical Units
γ	Effectiveness factor for mass transport control	dimensionless
γ	Aspect ratio of a channel	dimensionless
γ_c	Number of electrons preceeding the RDS in a multistep electrode process	dimensionless
η	Overpotential ($E-E_e$)	V
η^C	Overpotential at cathode	V
η^A	Overpotential at anode	V
θ	Surface coverage	dimensionless
θ_p	Material yield	dimensionless
κ	Electrolyte conductivity	Ω^{-1} m^{-1}
Λ	Molar conductivity of electrolyte	Ω^{-1} m^2 mol^{-1}
μ	Dynamic viscosity	kg m^{-1} s^{-1}
ν	Kinematic viscosity, (μ/ρ)	m^2 s^{-1}
ν	Stoichiometric coefficient	dimensionless
ρ	Density	kg m^{-3}
ρ_{ST}	Space-time yield	kg m^{-3} h^{-1}
τ_T	Residence time in the reservoir	s
τ	Surface excess	mol m^{-2}
τ_M	Maximum surface excess	mol m^{-2}
Φ	Current efficiency	dimensionless
ω	Rotation rate	s^{-1}
Sh	Sherwood number	dimensionless
Re	Reynolds number	dimensionless
Sc	Schmidt number	dimensionless
Le	Dimensionless length group	dimensionless

CHAPTER 1

INTRODUCTION

1.1 CHEMICAL BACKGROUND

Cystine and cysteine are sulphur containing α-amino acids and members of a group of only about 20 amino acids to be found commonly in natural proteins, all exclusively as the L-isomer. Two other stereoisomers are possible for cystine and one for cysteine as shown in Figure 1.1. The common abbreviations of RSSR for L-cystine and RSH for L-cysteine are used throughout the thesis.

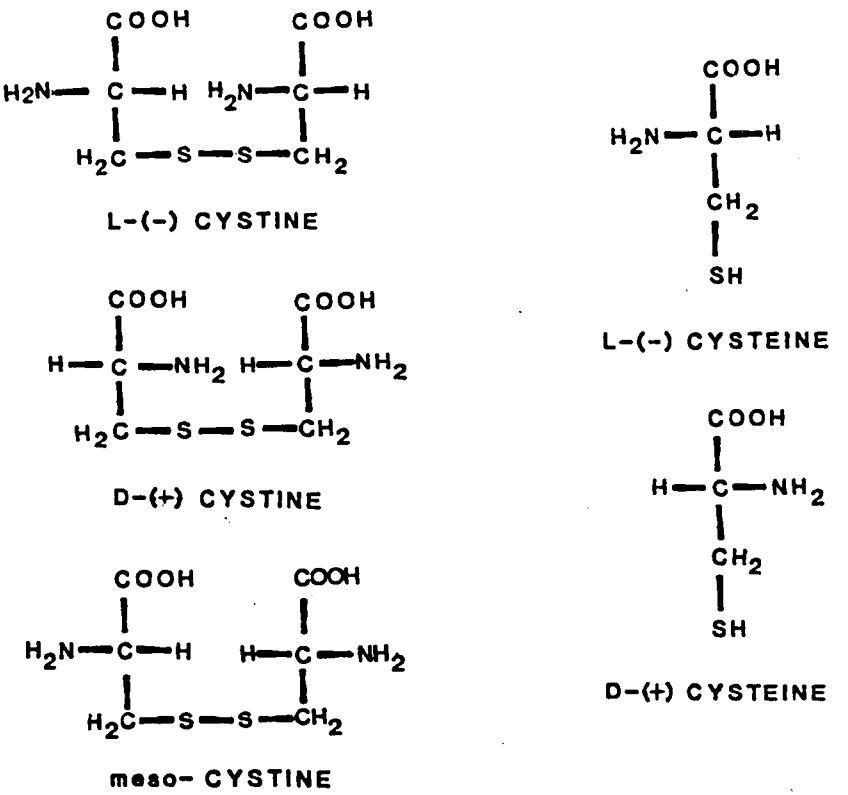

FIGURE 1.1 Stereoisomers of cystine and cysteine

In aqueous solution, ionisation of the amino acids depends upon pH as shown in Figure 1.2. At the isoelectric pH of the compounds [1], the molecules possess no net charge and are considered to have a zwitterion structure. Below or above this pH, the molecules are predominately cationic or anionic respectively. Seven acidic dissociation constants have been identified from pH titration data [2], four for cystine and three for cysteine. In the case of cysteine, identification of pK_2 with the thiol group and pK_3 with the charged amino group is an oversimplification since the two groups are acids of comparable strength with the thiol group slightly stronger [3].

Cystine is anomalous among the common amino acids showing a low solubility in all but strongly acidic or alkaline aqueous media (i.e. 0.46 mol m^{-3} in water at 25°C [2] compared with 770 mol m^{-3} in aqueous 2.0 mol dm^{-3} hydrochloric acid as determined experimentally). Cysteine has a solubility of 2300 mol m^{-3} in water at 25°C [2]. Electrosynthesis of L-cysteine from L-cystine is consequently restricted to strongly acidic or alkaline media. In alkaline solutions, however, both amino acids are decomposed [3] to a variety of products and cysteine is rapidly oxidised [3] to cystine by air or oxygen, especially in the presence of a small amount of catalyst, such as ferric chloride.

1.2 USES FOR L-CYSTEINE

L-Cystine and L-cysteine are both high value chemicals. Recent costs quoted are £82.80 per kg and £133.00 per kg [4], respectively. The combined world market is around 700 tonnes per annum [5], with the demand for L-cysteine approximately double that for L-cystine. In common with almost all amino acids there is no demand for the D-isomer or the racemic mixture due to their lack of function in biological systems. The major areas of application [5,6] are in the

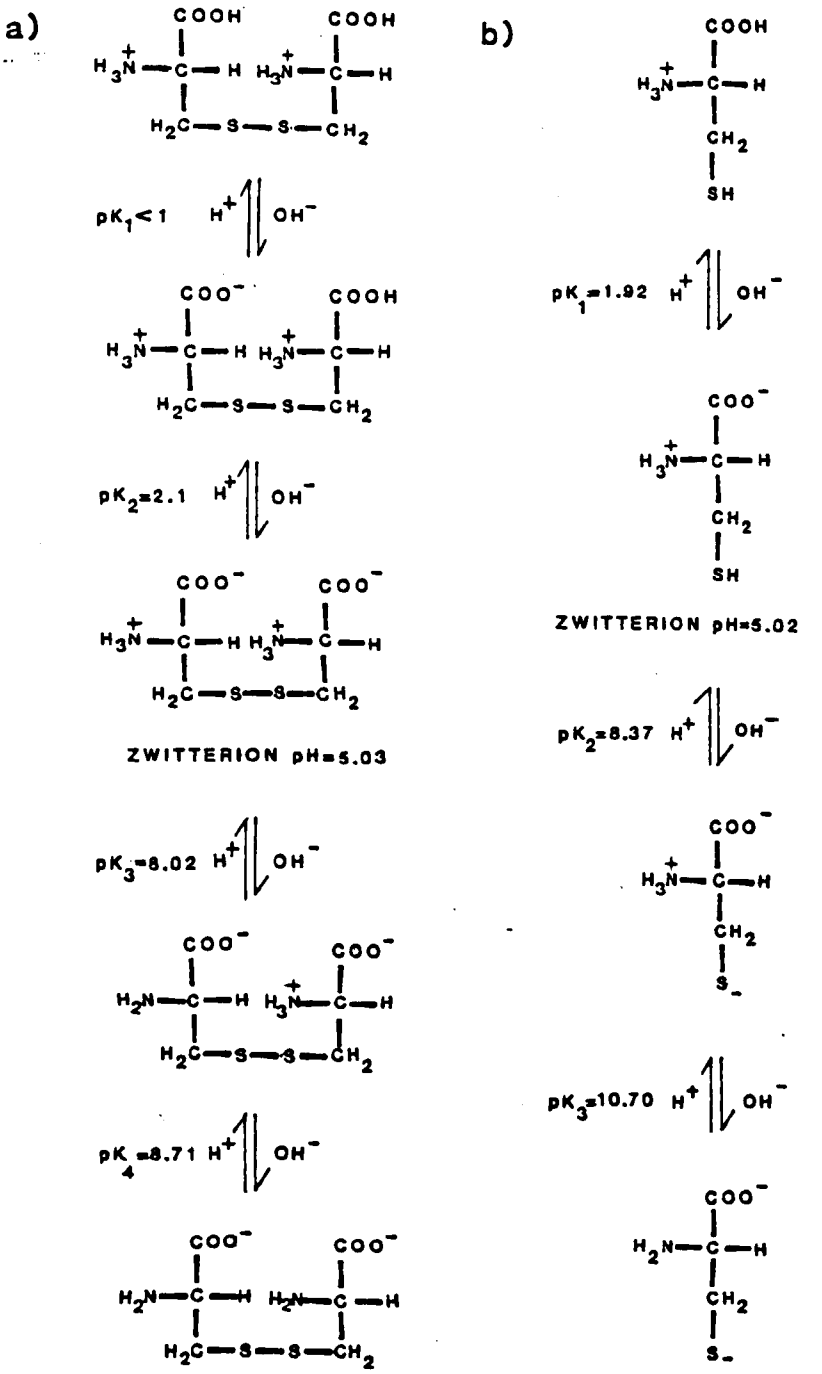

FIGURE 1.2 The ionisation of a) L-cystine and b) L-cysteine in aqueous solutions of different pH. The pK values quoted are at a temperature of 35°C [2].

foodstuffs, cosmetics and pharmaceutical industries. All applications of L-cysteine require either the free base or the hydrochloride salt, with L-cysteine hydrochloride preferred for many applications because of its greater resistance to oxidation. Indeed the free base should be converted to the hydrochloride salt for storage.

L-Cysteine is added to wheat flour by the baking and pasta industry to improve dough flexibility which improves the baked product and reduces baking time. It is the major component of the recipe for the meaty flavouring used in savoury snacks and pet foods and it is effective as an antioxidant in natural fruit juices and other foodstuffs.

L-Cysteine, and numerous derivatives, exhibit a normalising effect on skin metabolism and have a significant effect on hair. For example they are used in preparations to treat excess skin lipid production (seborrhea), acne, in anti-dandruff shampoos and, especially in Japan, as a substitute for thioglycolic acid for cold wave preparations that are less damaging to hair.

The pharmaceutical industry requires L-cysteine to produce N-acetyl-L-cysteine, S-carboxymethyl-L-cysteine and L-cysteine methylester which are used as muccolytic agents in the treatment of bronchitis and nasal catarrh. Many other derivatives are employed in the treatment of hepatitis, respiratory disorders, dermatitis and radiation damage. L-Cysteine is itself required as an antidote to snake venom.

1.3 SYNTHESIS OF L-CYSTEINE

1.3.1 Industrial Route

Several hundred tonnes per annum of L-cysteine, as the hydrochloride or less frequently the sulphate salt, is produced by the electrochemical reduction of L-cystine in the corresponding mineral acid catholyte. The free base is produced

by electrodialysis of the sulphate salt (or the hydrochloride salt if this is desired) in an additional step. The free base is not usually produced directly because of the poor stability of the amino acids in strongly alkaline media (see e.g. [3]). The major manufacturers are Degussa, Diamalt, Ajinomoto, Tanabe, Takeda, Nippon Chemical and Drug and Isochem. The available literature is reviewed in Section 1.4.4.

The reactant, L-cystine, is obtained by extraction from acid hydrolysates of keratins of hair, feathers, hooves, horn and wool, based upon the low solubility of the disulphide at neutral pH. This technology suffers from a high energy requirement, objectionable odours and intractable wastes.

1.3.2 Alternative Routes

(a) Microbial Production

A fermentation method for L-cysteine has not been established but enzymatic methods have recently been developed in the laboratory [7]. These procedures are still some years away from evaluation as industrial processes but are of interest because they produce the L-isomer in a one step reaction.

(b) Chemical Synthesis

With the exception of the chemical reduction of L-cystine chemical syntheses [8,9,10] are expensive, multi-step processes which produce a racemic mixture which must be optically resolved to give the desired L-isomer. In industry, the D-isomer would be racemised and recycled. The additional processes represent a significant economic disincentive.

Chemical reduction of L-cystine is normally performed by catalytic hydrogenation (reaction 1.01), usually with tin in hydrochloric acid [11]. The process compares favourably with electrochemical reduction for laboratory preparations but is inferior for industrial production. Toxic waste must be

disposed of and the metal recycled.

$$RSSR + 2M\text{-}H_{(ads)} \longrightarrow 2RSH + 2M \qquad (1.01)$$

1.4 THE ELECTROCHEMISTRY OF L-CYSTINE AND L-CYSTEINE

1.4.1 Thermodynamic Studies

A reliable standard electrode potential for the L-cystine/L-cysteine redox couple (reaction 1.02) is not available in the literature, although many workers [12-19] have attempted to determine the value. Table 1.1 lists reported $E^{o'}$ (i.e. formal standard electrode potential) values, with those quoted for pH values outside the range of the measurements, obtained by extrapolation from a linear plot of $E^{o'}$ versus pH, assumed to have a slope of 0.0591 V^{-1} over the entire pH range.

$$RSSR + 2H^+ + 2e^- \rightleftharpoons 2RSH \qquad (1.02)$$

Borsook, Ellis and Huffman [12] used thermal data to calculate the standard free energy of reaction (1.02) and, by incorporating values for ionisation constants, they evaluated $E^{o'}$ at intervals of one pH unit from pH 0 to 12. The calculations involved differences between large numbers, each uncertain to some degree, and a choice of slightly discordant ionisation constants which the authors estimated could have produced an error of up to 43 mV in $E^{o'}$.

Kinetic studies at a mercury electrode (Section 1.4.2(a)) have indicated that $E^{o'}$ values measured by Ghosh et al [13] and Green [14] are erroneous. L-cysteine reacts with the mercury electrode to form mercury cysteinate (reactions 1.11 and 1.13).

TABLE 1.1 Formal standard electrode potential of the L-cystine/L-cysteine redox couple at 25°C.

Method	$E^{o'}$ (V versus NHE) pH 7	pH 0	pH Range of the Measurements	Reference
Calculated from thermal data.	- 0.39	+ 0.02	Not applicable	[12]
Potentiometric at a mercury electrode	- 0.333 - 0.336	+ 0.080 + 0.077	7.5 to 8.6 8.5 to 9.2	[13] [14]
From the equilibrium constant for the reaction between the L-cystine/L-cysteine couple and various dye redox couples	- 0.222	+ 0.191	7.1 to 9.2	[18]
From the equilibrium constant for the reaction below $RSSR+2H^{+}+2Fe^{2+} \rightleftharpoons 2RSH+2Fe^{3+}$	- 0.33	+ 0.08	10.03 to 10.12	[19]

Potential measurements at platinum or gold electrodes [15-17] are slow to equilibriate and do not give $E^{o'}$ for the couple. $E^{o'}$ does not respond to changes in L-cystine concentration. There is evidence (Section 1.4.2(c)) of strong adsorption of both amino acids at the electrodes.

A method free from the objections of the action of the amino acids on electrodes involves determination of an equilibrium constant for reaction between the L-cystine/L-cysteine redox couple and another couple of known standard electrode potential. Fruton and Clarke [18] equilibriated the amino acids with various dyes of known redox potential and measured the dye concentrations spectrophotometrically. Tanaka, Kolthoff and Stricks [19] claim to have established the equilibrium constant for reaction with the ferric/ferrous couple.

1.4.2 Kinetic Studies

(a) Mercury

Both L-cystine reduction and L-cysteine oxidation have been studied. The electrochemistry is complicated by the formation of mercury cysteinate complexes.

Kolthoff and Barnum [20] suggested mercurous cysteinate (RSHg) as the product of L-cysteine oxidation (reaction 1.03).

$$RSH + Hg \rightleftharpoons RSHg_{(ads)} + H^+ + e^- \qquad (1.03)$$

The mercurous ion was postulated to be Hg^+ rather than Hg_2^{++} at the low concentrations (typically 1×10^{-20} mol dm^{-3}) of mercury ions present. Polarograms showed a diffusion controlled wave with an $E_{\frac{1}{2}}$ (i.e. half-wave potential) of -0.04 V (vs. SCE) in aqueous 0.1 mol dm^{-3} hydrochloric acid and -0.5 V (vs. SCE) in aqueous 0.1 mol dm^{-3} sodium hydroxide. The change of 48 mV per pH unit is low for electrode reaction (1.03). In buffer solutions of pH

2.0 to 9.0, at L-cystine concentrations above 0.2 mol m^{-3}, rather than the diffusion controlled wave a small limiting current was obtained which was almost independent of the amino acid concentration. This was attributed to mercurous cysteinate film formation. At more positive potentials a series of poorly reproducible anodic waves, with several breaks in the current typical of adsorption, were ascribed to further diffusion controlled oxidation of L-cysteine, either after film breakdown or by reactant diffusing through the film [21-24]. Evidence for the film has been obtained by Kolthoff, Stricks and Tanaka [25] who found that a cathodic sweep from high positive potentials produced a small reduction current immediately cathodic of the oxidation waves. This reduction current they postulated was due to reduction of the film. From the charge passed, the film thickness was estimated to correspond to a monolayer of mercurous cysteinate.

Kolthoff and Barnum [26] also tried to elucidate the mechanism of L-cystine reduction. They found a single, diffusion controlled, irreversible wave on polarographic reduction in acid or alkali solutions with an additional small prewave in buffer solutions of pH 3.0 to 7.0. The main wave was attributed to the reduction of L-cystine to L-cysteine (reaction 1.04).

$$RSSR + 2H^+ + 2e^- \longrightarrow 2RSH \qquad (1.04)$$

Reduction commenced at -0.1 V (vs. SCE) in aqueous 0.1 mol dm^{-3} hydrochloric acid and at -0.6 V (vs. SCE) in aqueous 0.1 mol dm^{-3} sodium hydroxide (electrocapillary maxima make it difficult to quote precise $E_{\frac{1}{2}}$ values). The shift of 45 mV per pH unit is low for electrode reaction (1.04). Kolthoff, Stricks and Tanaka [27] examined the prewave in detail. They concluded reaction of L-cystine with the electrode produced mercuric cysteinate ($(RS)_2Hg$) in the rate

determining step (reaction 1.05), which was reversibly reduced (reaction 1.06) at the prewave.

$$RSSR + Hg \longrightarrow (RS)_2Hg \qquad (1.05)$$

$$(RS)_2Hg + 2H^+ + 2e^- \longrightarrow 2RSH + Hg \qquad (1.06)$$

This was based upon the near independence of the limiting current on mercury head height, which indicated the prewave was kinetically controlled, and upon its proportionality to L-cystine concentration. From $E^{o'}$ of the L-cystine/L-cysteine (+0.08 V vs. NHE) and mercuric cysteinate/L-cysteine (+0.175 V vs. NHE) redox couples, using the relationship between the couples shown in equation (1.07), reaction (1.05) was estimated to produce a ratio of mercuric cysteinate to L-cystine of 6×10^{-4}.

$$E^{o'}_{RSSR/RSH} - E^{o'}_{(RS)_2Hg/RSH} = \frac{RT}{2F} \ln \frac{[(RS)_2Hg]}{[RSSR]} \qquad (1.07)$$

A number of workers [21-24,28-30] essentially confirmed the findings of Kolthoff et al [21,26-28]. The stoichiometry of the mercury cysteinate complex was uncertain. RSHg, $(RS)_2Hg_2$ and $(RS)_2Hg$ were all proposed.

Miller and Teva [31] used cyclic voltammetry to investigate L-cystine reduction in nitric acid solutions, at a hanging mercury drop electrode (HMDE) (Figure 1.3). Two reduction peaks were found. A small apparently reversible peak at about -0.25 V (vs. SCE), corresponding to the prewave found in polarography, was postulated to be due to reactions (1.08 to 1.11).

$$RSSR + Hg \longrightarrow (RS)_2Hg_{(ads)} \qquad (1.08)$$

$$(RS)_2Hg_{(ads)} + Hg \longrightarrow 2RSHg_{(ads)} \qquad (1.09)$$

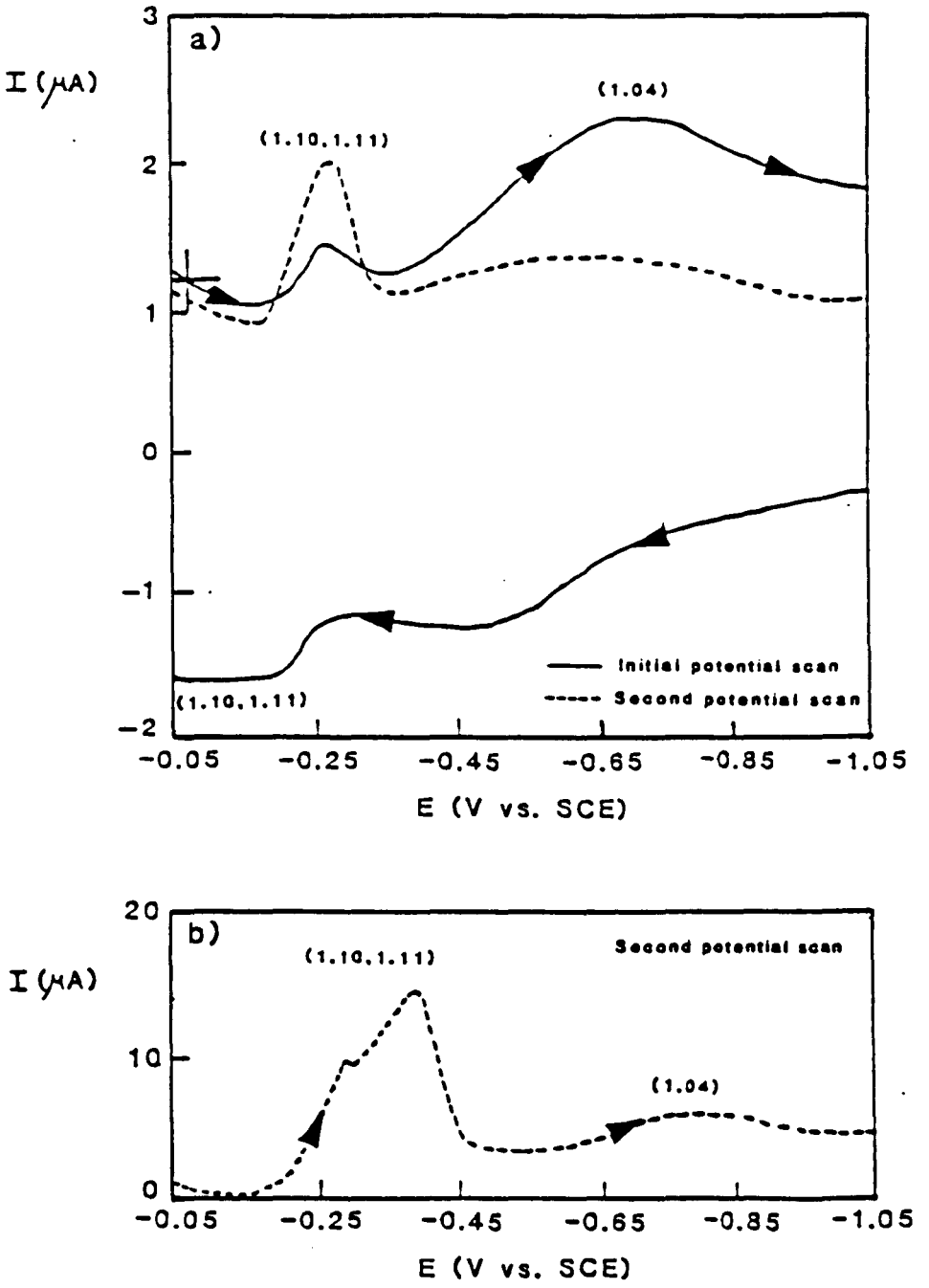

FIGURE 1.3 Cyclic voltammetry of a) 0.025 mol m^{-3} and b) 0.5 mol m^{-3} L-cystine in aqueous 0.01 mol dm^{-3} HNO_3 and 0.09 mol dm^{-3} $NaNO_3$ at a HMDE. Potential sweep rate 2 V s^{-1} [31].

$$(RS)_2Hg_{(ads)} + 2H^+ + 2e^- \rightleftharpoons 2RSH + Hg \qquad (1.10)$$

$$RSHg_{(ads)} + H^+ + e^- \rightleftharpoons RSH + Hg \qquad (1.11)$$

Evidence was proposed for a slow, rate determining surface reaction between L–cystine and the electrode (reactions 1.08 and 1.09), preceding the electrode reactions (reactions 1.10 and 1.11). A second peak at ca. –0.7 V (vs. SCE) was ascribed to the irreversible, diffusion controlled reduction of L–cystine to L–cysteine (reaction 1.04). The apparent oxidation peak at ca. –0.5 V (vs. SCE) (Figure 1.3a) was not eluded to.

After the initial potential scan, at the highest L–cystine concentration used, twin peaks were obtained for the reversible wave (Figure 1.3b). This was attributed to the presence of both mercurous and mercuric cysteinate on the electrode surface.

Bard and Stankovick [32] clarified the electrochemistry of both amino acids principally in a buffer solution of pH 7.4. Cyclic voltammograms for solutions of L–cystine (Figure 1.4) essentially agreed with those reported by Miller and Teva [31]. For the reduction peak at ca. –0.5 V (vs. SCE), however, reduction of adsorbed L–cystine to L–cysteine (reaction 1.12) was proposed rather than the reversible reduction of mercury cysteinate (reactions 1.10 and 1.11), suggested by Miller and Teva.

$$RSSR_{(ads)} + 2H^+ + 2e^- \longrightarrow 2RSH \qquad (1.12)$$

Strong evidence for reaction (1.12) was provided by a constant peak area in voltammograms at L–cystine concentrations above 0.01 mol m^{-3}, attributed to monolayer coverage of the electrode by L–cystine rather than mercury cysteinate.

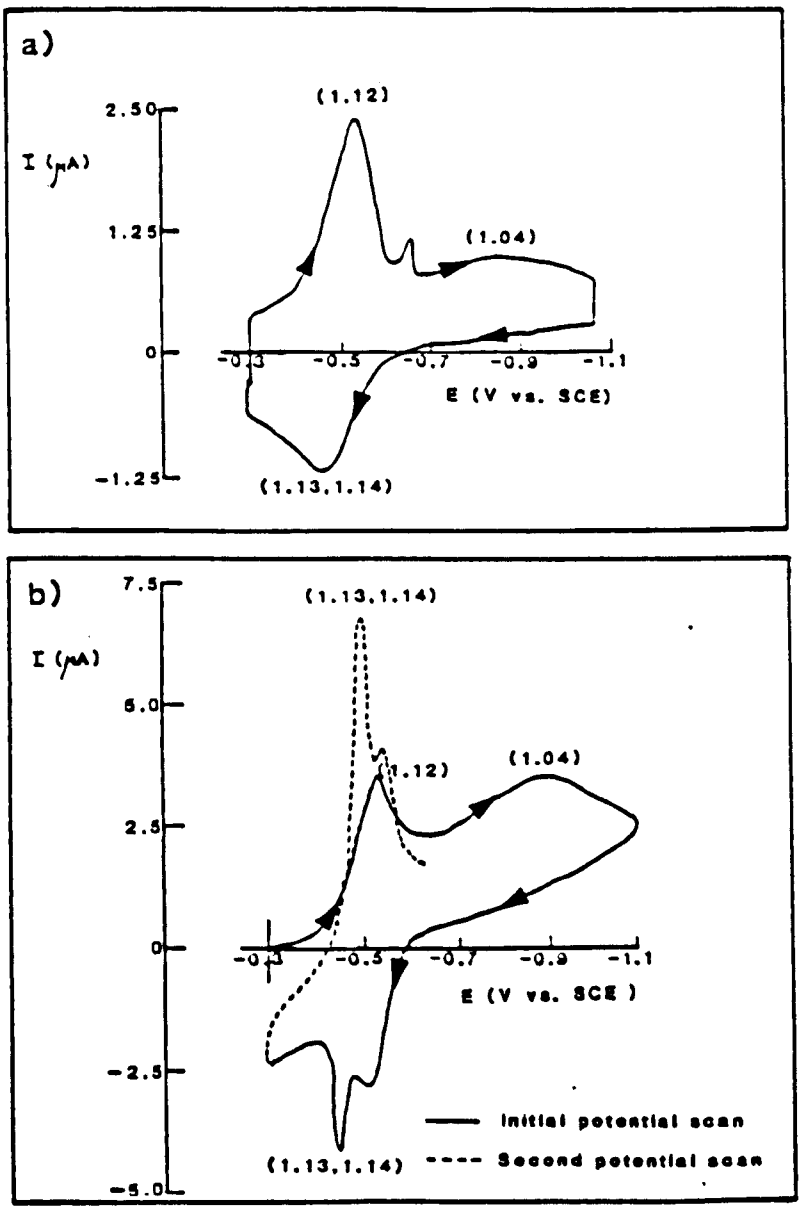

FIGURE 1.4 Cyclic voltammetry of a) 0.5 mol m^{-3} and b) 0.46 mol m^{-3} L-cystine in an aqueous buffer solution of pH 7.4 at a HMDE. Potential sweep rate 200 mV s^{-1} [32].

By the method of Kolthoff et al [27] only 5 x 10^{-5} mol m^{-3} of mercury cysteinate was calculated to form from the spontaneous reaction between L-cystine and the electrode, a concentration too small to give monolayer coverage. Conversely construction of a model of L-cystine and determination of the area occupied with the disulphide bond orientated on the electrode surface suggested the charge passed corresponded to monolayer coverage by the disulphide.

Mercurious ($(RS)_2Hg_2$) and mercuric cysteinate were suggested to be almost exclusively formed by reaction between L-cysteine and the electrode (reactions 1.13 and 1.14).

$$(RS)_2Hg_{2(ads)} + 2H^+ + 2e^- \longleftrightarrow 2RSH + 2Hg \qquad (1.13)$$

$$(RS)_2Hg_{(ads)} + 2H^+ + 2e^- \longleftrightarrow 2RSH + Hg \qquad (1.14)$$

Cyclic voltammograms of solutions of L-cysteine (Figure 1.5) showed a reversible wave attributed to electrode reactions (1.13 and 1.14). Above 0.3 mol m^{-3} L-cysteine current spikes appeared on the wave (Figure 1.5b) which were assigned to the formation of a tight film of mercury cysteinate after monolayer coverage, by lateral interaction between adsorbed molecules. The spiked response was also evident in cyclic voltammograms of solutions containing above 0.4 mol m^{-3} L-cystine (Figure 1.4b). This clearly differentiated the cathodic peak current for reaction (1.12) from that for reactions (1.13 and 1.14), confused in the earlier literature because of the nearly equivalent potentials (peak potentials are within 10 mV) for the reactions.

Bard and Stankovich proposed an order of increasing strength of adsorption on mercury of weakly adsorbed L-cysteine, L-cystine and mercury cysteinate. This was based upon cyclic voltammetry of a mixture of L-cystine and mercury

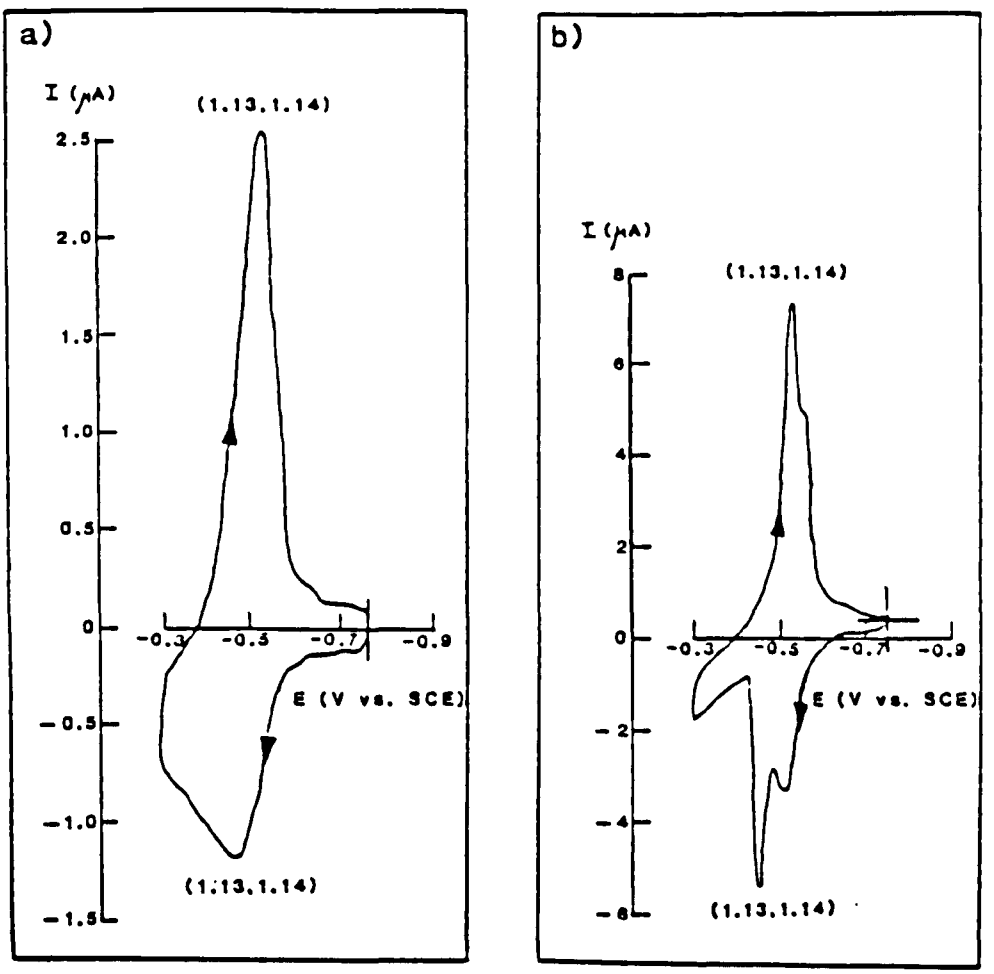

FIGURE 1.5 Cyclic voltammetry of a) 0.095 mol m^{-3} and b) 0.3 mol m^{-3} L-cystine in an aqueous buffer solution of pH 7.4 at a HMDE. Potential sweep rate 200 mV s^{-1} [32].

cysteinate, with L-cystine in large excess, which showed the spiked behaviour of mercury cysteinate reduction on the initial potential scan.

(b) Transition Metal Macrocycles

Zagal et al [33-36] investigated L-cystine reduction and L-cysteine oxidation, in a variety of electrolytes, at various transition metal tetrasulfophthalocyanines (Co-TSP, Fe-TSP, Mn-TSP, Cr-TSP, Ni-TSP, Cu-TSP and Zn-TSP) adsorbed onto ordinary pyrolytic graphite (OPG). Cyclic voltammetry (Figure 1.6) indicated L-cystine reduced to L-cysteine in the cathodic potential scan was regenerated by L-cysteine oxidation in the reverse anodic scan. The large peak potential separation for the two reactions (ca. 1.0 V) showed the L-cystine/L-cysteine redox couple (reaction 1.02) was electrochemically irreversible at these electrodes. Both reactions were diffusion controlled.

From the range of transition metal TSP's, only at a Co-TSP/OPG rotating disc electrode (RDE) was a diffusion controlled limiting current obtained for L-cysteine oxidation (Figure 1.7). Electrochemical reaction orders of + 1 for L-cysteine and for protons, - 1 below pH 8.5, and 0 above this pH were measured. The authors noted pH 8.5 is close to the pK_2 of L-cysteine (i.e. 8.37 [2]). Mechanism (1.15) was proposed.

$$\begin{aligned} RSH &\longleftrightarrow RS^- + H^+ \\ RS^- &\xrightarrow{RDS} RS^{\bullet} + e^- \\ 2RS^{\bullet} &\longrightarrow RSSR \end{aligned} \qquad (1.15)$$

Tafel slopes of 140 mV/decade in alkali and 120 mV/decade in acid suggested the first electron transfer either preceded or occurred at the rate determining step (RDS). Constant potential electrolysis with paper chromatographic analysis of the

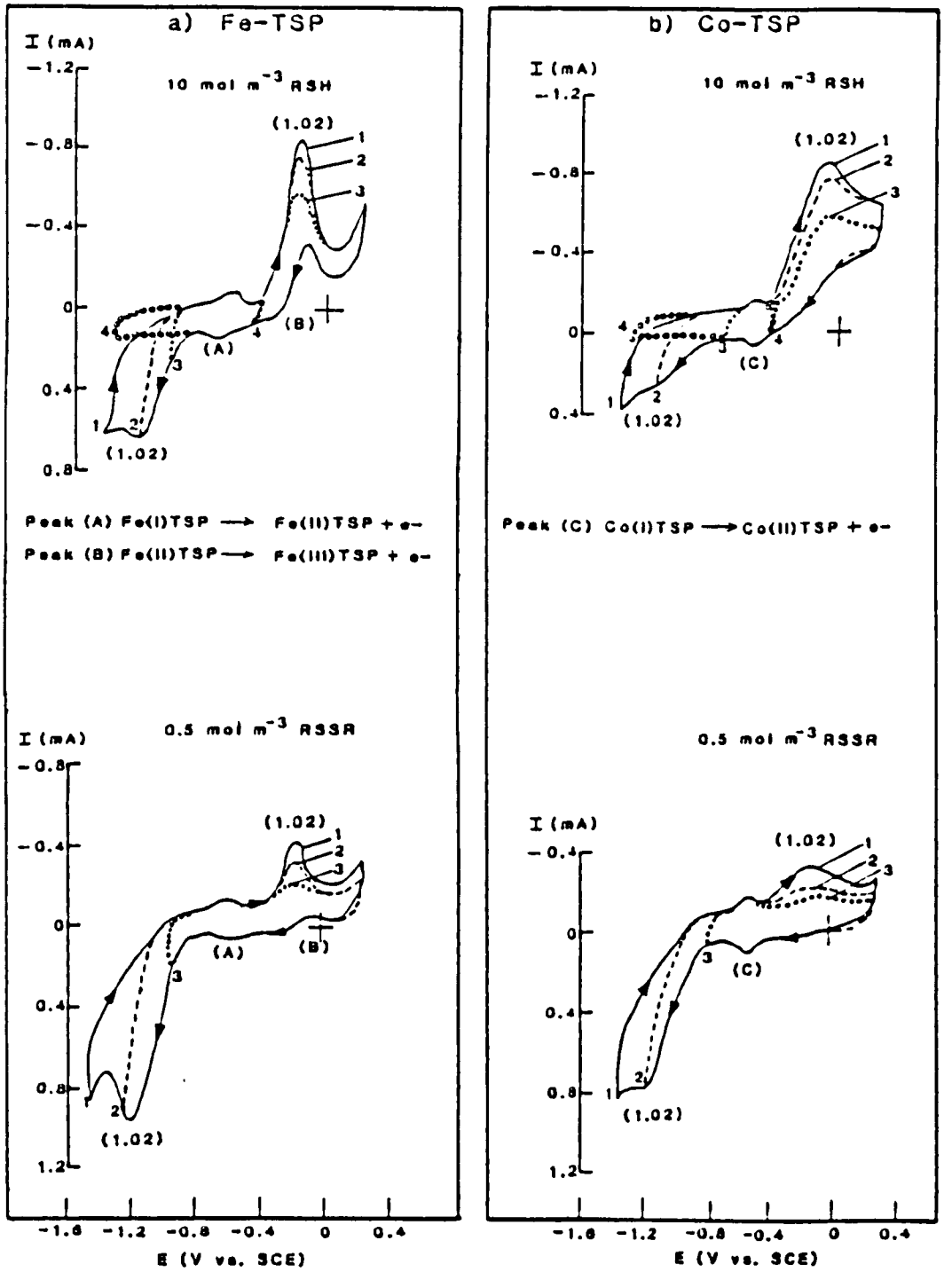

FIGURE 1.6 Cyclic voltammetry of the L-cystine/L-cysteine redox couple at Fe-TSP/OPG and Co-TSP/OPG electrodes. Potential sweep rate 200 mV s^{-1}. Background electrolyte 0.2 mol dm^{-3} NaOH [34,35].

electrolyte confirmed L-cystine as the major oxidation product in acidic media, with trace quantities of cysteic the only other product identified. In alkaline solutions many unknown products were obtained.

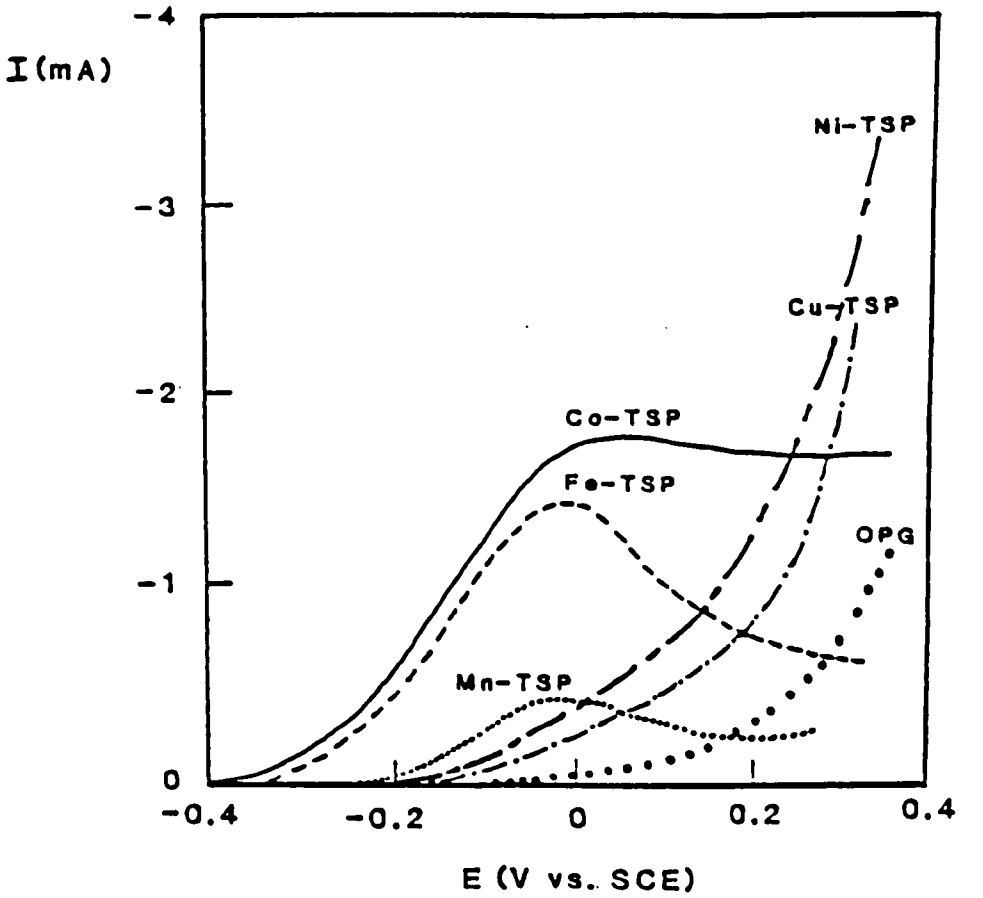

FIGURE 1.7 Voltammograms of 10 mol m^{-3} L-cysteine chlorhydrate in aqueous 0.2 mol dm^{-3} Na_2CO_3 and 0.6 mol dm^{-3} Na_2SO_4 at transition metal TSP/OPG RDE's. Electrode rotation rate 33 Hz. Potential sweep rate 2 mV s^{-1}. Temperature 25°C [34,35].

For L-cystine reduction a sloping plateau at Co-TSP/OPG was the only response which resembled a limiting current from the range of rotating disc

electrodes (Figure 1.8). Even at Co-TSP/OPG kinetic parameters for the reaction were not quoted, probably because of interference from hydrogen evolution which could account for the plateau inclination. During constant potential electrolyses the catalysts were gradually removed from the OPG by copious hydrogen evolution.

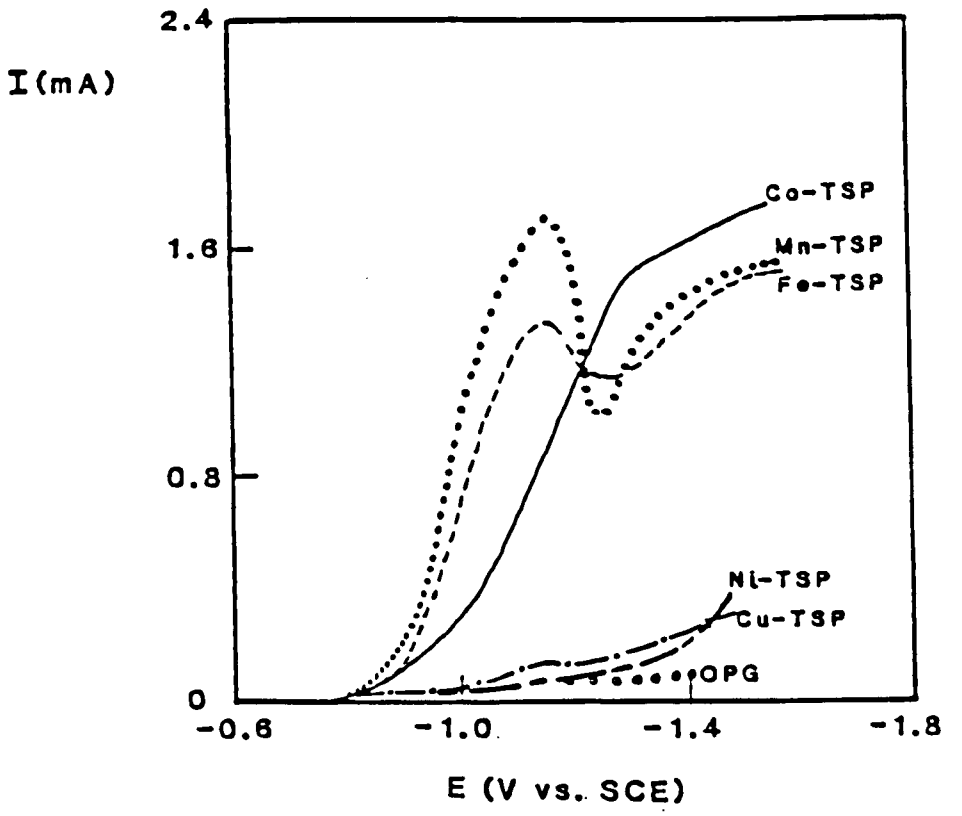

FIGURE 1.8 Voltammograms of 0.5 mol m^{-3} L-cystine in aqueous 0.2 mol dm^{-3} Na_2CO_3 at transition metal TSP/OPG RDE's. Electrode rotation rate 33 Hz. Potential sweep rate 1 mV s^{-1}. Temperature 25°C [34,35].

Zagal et al concluded that both L-cystine reduction and L-cysteine oxidation only proceeded at reasonable rates if the reactant molecules were adsorbed at the electrode surface. Adsorption at transition metal TSP was believed to be closely

linked to the ability of the central metal ion to bind extra-planar ligands. Preliminary studies with non-sulphur containing amino acids indicated that they were much less reactive. This suggested adsorption occured between the metal centre and the sulphur atoms of L-cystine and L-cysteine. For L-cystine, adsorption through only a single sulphur atom was proposed. The authors argued if the macrocylic complexes were adsorbed with the ring parallel to the OPG surface, although it was not conclusive this was the case [37], the metal centres in the TSP would be too far apart to adsorb L-cystine via both sulphur atoms.

In the absence of reliable heats of adsorption for the amino acids on transition metal TSP's the number of d electrons on the metal was used to correlate with the electrocatalytic activity for the reactions. Calculations indicated that the energy of the highest, occupied molecular orbital of the transition metal TSP's decreased almost linearly as the number of d electrons increased. Volcano plots resulted for both reactions using the most likely metal oxidation state(s) from the scant literature, at the electrode potentials selected for the electrocatlytic activity (i.e. current) measurements (Figure 1.9).

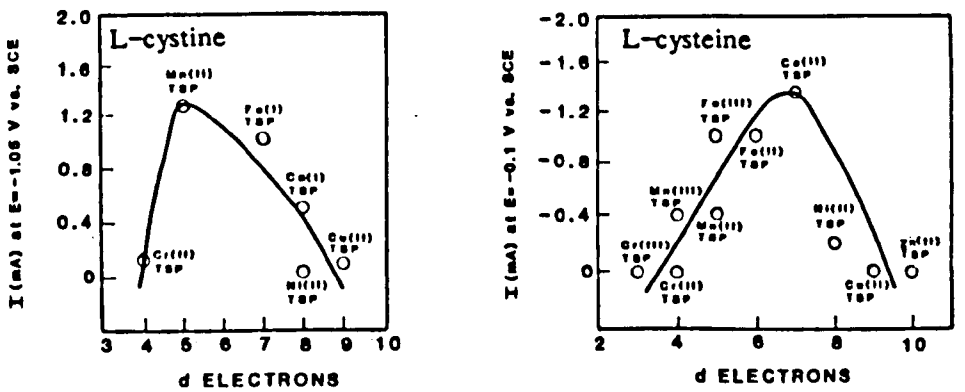

FIGURE 1.9 Volcano plots for the reduction of L-cystine and the oxidation of L-cysteine [36].

No attempt was made to account for the different number of d electrons required to produce the maximum rate of L–cystine reduction (i.e. 5 d electrons ; Mn(II) TSP) and L–cysteine oxidation (i.e. 7 d electrons; Co(II) TSP). The coulombic interaction between the sulphur atoms in the amino acids and the metal in the TSP, perhaps helps to explain the effect. For L–cysteine oxidation occurring by mechanism (1.15), the volcano plot suggests $RS^{\bullet}$, rather than RS^{-}, is the adsorbed species. If RS^{-} was adsorbed, on a coulombic basis, the metal–sulphur bond strength would have decreased with increasing number of d electrons, and a volcano plot would not have resulted. With $RS^{\bullet}$, however, the metal–sulphur bond strength increases with increased d electrons. An optimum bond strength was obtained with 7 d electrons, with the bond weaker below this value and above it too strong. For L–cystine reduction it is unlikely the disulphide bond dissociated before adsorption. Since the bond has 8 delocalised electrons, on a coulombic basis it might be expected, as observed, that the optimum metal–sulphur bond strength would be obtained with fewer d electrons than for $RS^{\bullet}$ adsorption. Above the optimum of 5 d electrons the metal–sulphur bond strength is weaker due to coulombic forces. Of course this explanation ignores the possible influence of steric effects.

Wang et al [38–40] examined heat–treated cobalt(II) tetramethoxyphenyl–porphyrin (Co–TMPP) adsorbed onto graphite. As in the case of transition metal TSP's, cyclic voltammetry indicated that the L–cystine/L–cysteine redox couple (reaction 1.02) was electrochemically irreversible, with the oxidation and reduction reactions diffusion controlled. Both electrode reactions, at a given pH, occurred at similar potentials on Co–TMPP and transition metal TSP. Adsorption of the amino acids at the cobalt(II) metal centre was advanced.

In support of disulphide adsorption at the metal centre Wang and Pang [41]

noted a similar electrocatalytic effect for L-cystine reduction at a glassy carbon electrode using cobalt(II) tetrakis(4-trimethylammoniumphenyl)porphyrin (Co-TTAPP) or cobalt(II) tetrakis(4-sulphophenyl)porphyrin (Co-TSPP) dissolved in aqueous sulphuric acid electrolyte. No such homogeneous effect was observed, however, with H_2TTAPP. Cobalt(II) complexing L-cystine in the N_4 internal ring of the porphyrin was proposed. The similar performance of Co-TTAPP and Co-TSPP was highlighted as indicative of the insignificant electrocatlytic effect of substituents on the porphyrin ring.

At a Co-TMPP/graphite rotating disc electrode, mechanism (1.15) was proposed for L-cysteine oxidation [40]. Tafel slopes and electrochemical reaction orders were identical to those reported for the oxidation at Co-TSP/OPG [33-36]. Constant potential electrolysis in acidic media produced L-cystine with current efficiencies in excess of 90%.

At a Co-TMPP/graphite rotating disc electrode a well defined, diffusion controlled, limiting current was not obtained for L-cystine reduction in electrolytes below pH 12 [38,39] (e.g. Figure 1.10), Sloping plateaus, attributed to simultaneous hydrogen evolution, were recorded. Despite this, Tafel slopes of 120 mV/decade were measured in all media and electrochemical reaction orders of + 1 for L-cystine and for protons, + 1 below pH 4 and 0 above pH 9, were recorded. Mechanisms (1.16) and (1.17) were proposed.

<u>pH < 4</u>

$$\begin{aligned} &RSSR + H^+ + e^- \xrightarrow{RDS} RSH + RS^\bullet \\ &RS^\bullet + H^+ + e^- \longrightarrow RSH \end{aligned} \qquad (1.16)$$

<u>pH > 9</u>

$$\begin{aligned} &RSSR + e^- \xrightarrow{RDS} RS^- + RS^\bullet \\ &RS^\bullet + e^- \longrightarrow RS^- \end{aligned} \qquad (1.17)$$

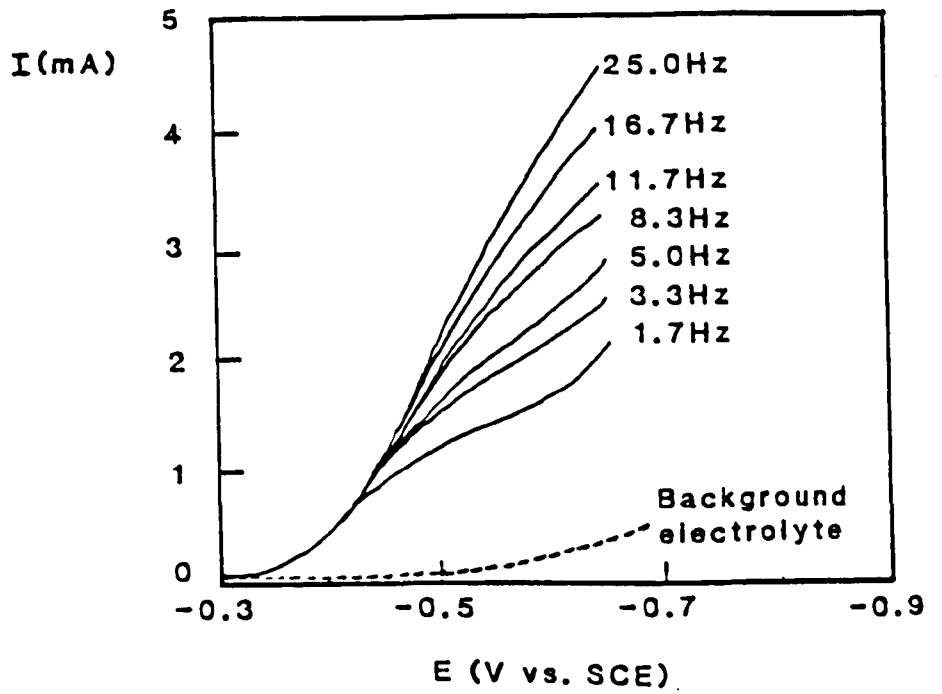

FIGURE 1.10 Voltammograms of 8.3 mol m^{-3} L-cystine in aqueous 2.0 mol dm^{-3} HCl at various electrode rotation rates of a Co-TMPP/graphite RDE. Potential sweep rate 5 mV s^{-1}. Temperature 25°C [38].

At a large Co-TMPP/graphite electrode constant current electrolysis of L-cystine in aqueous 2.0 mol dm^{-3} hydrochloric acid, at 200 A m^{-2}, yielded exclusively L-cysteine. The current efficiency was 60% with current losses ascribed solely to hydrogen evolution.

(c) Silver

Watanabe and Maeda [42] reported quasi-reversible reduction of L-cystine to L-cysteine (reaction 1.18 and Figure 1.11) on the surface of a silver electrode with the disulphide adsorbed from aqueous 2.0 mol dm^{-3} hydrochloric acid. The reaction was detected by surface-enhanced Raman spectroscopy (SERS).

$$RSSR_{(ads)} + 2e^- \longrightarrow 2RS^-_{(ads)} \qquad (1.18)$$

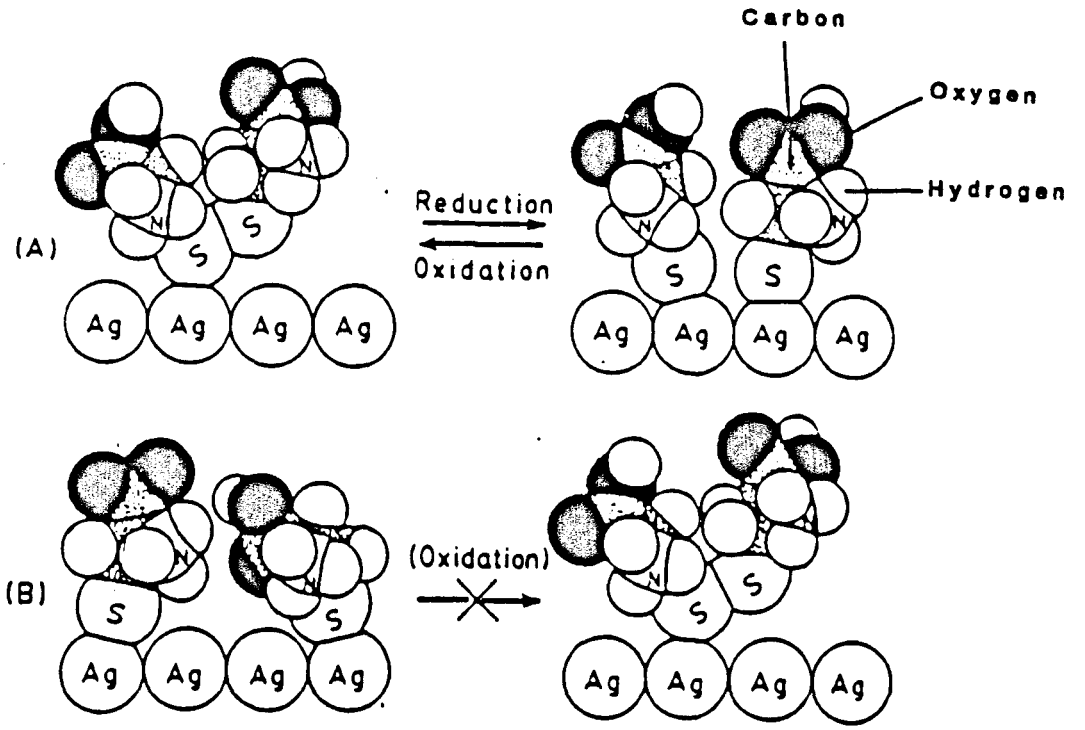

FIGURE 1.11 Surface adsorption of L-cystine and L-cysteine at silver. The atoms are scaled referring to the Ag-Ag distance (2.88 Å) for the silver (III) plane [42].

The redox reaction occurred in the potential range between -0.35 V and +0.25 V (vs. SCE). Lack of an S-H stretching peak (2565 cm^{-1}) suggested L-cysteine was adsorbed as RS^-. The redox reaction was monitored by observing the change in the intensity of the S-S stretching peak (502 cm^{-1}), as the electrode potential was

swept.

When L-cysteine was adsorbed on the silver electrode reaction (1.18) did not occur. This was rationalised in terms of the model for the adsorbed layer illustrated in Figure 1.11.

In view of a fairly intense S-S stretching peak obtained, it was believed the disulphide bond was tilted to some extent against the surface (Figure 1.11, (A)). Upon electrochemical reduction it was converted to two L-cysteine molecules, which because of strong Ag-S bonding, were trapped on neighbouring silver atoms, in spite of some steric hindrance between the amino acid molecules. Electro-oxidation readily formed the disulphide bond between the closely sitting sulphur atoms. Conversely, for a silver electrode in contact with an L-cysteine solution the steric hindrance was believed to operate first, at the time of adsorption, and the adjacent sitting of two L-cysteine molecules was unfavourable (Figure 1.11, (B)). The strong Ag-S bonding prevented surface diffusion, and L-cystine formation by electrooxidation was strongly hampered. Some indirect evidence for the model was provided by the quasi-reversible redox reaction of the ethane thiol/diethy disulphide couple, which was detected by SERS with either member of the couple adsorbed on the electrode. It was argued there was little steric hindrance from the samll ethyl group attached to the sulphur atom.

Voltammetry was not presented by Watanabe and Maeda [42]. Probably the redox reaction could not be separated from hydrogen evolution in the aqueous 2.0 mol dm^{-3} hydrochloric acid background electrolyte.

(d) Platinum and Gold

There appears to be no published work on L-cystine reduction at these electrodes, but there are a number of papers [43-50] on the electrochemical oxidation of both amino acids.

Davis and Bianco [43] reported a peak shaped voltammogram for L-cysteine oxidation in aqueous 1 mol dm^{-3} sulphuric acid at a platinum rotating disc electrode (Figure 1.12). At high anodic potentials, the oxidation was inhibited due to formation of a platinum oxide film (reaction 1.19).

$$Pt + H_2O \longrightarrow PtO + 2H^+ + 2e^- \qquad (1.19)$$

($E^{o'}$ = +0.88 V vs. NHE at pH 0)

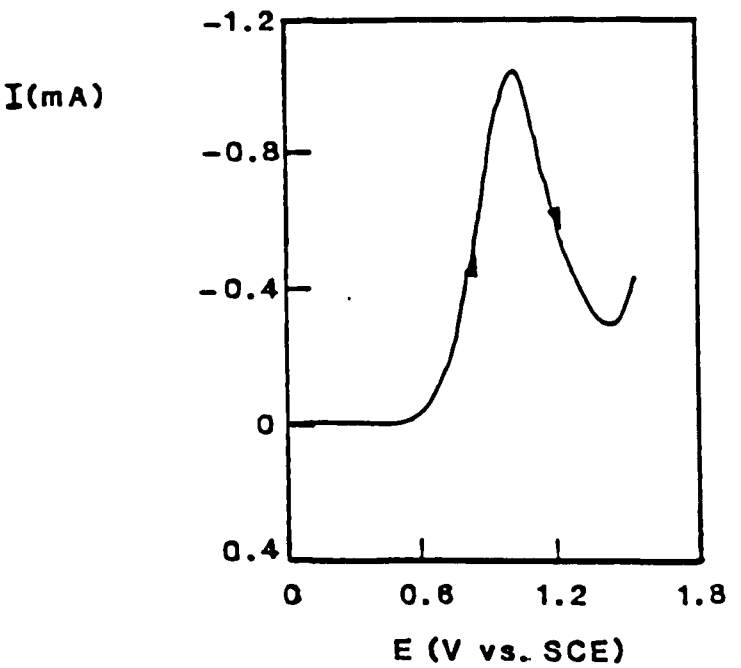

FIGURE 1.12 Voltammetry of 1 mol m^{-3} L-cysteine in aqueous 1.0 mol dm^{-3} H_2SO_4 at a platinum RDE. Potential sweep rate 2 mV s^{-1}. Temperature 25°C [43].

Constant potential electrolysis, at +0.9 V (vs. SCE), with infra-red spectroscopic analysis of the electrolyte, identified L-cystine (reaction 1.20) as the major oxidation product. During electrolysis, the current rapidly fell to about 3% of the initial value due to formation of the oxide film.

$$RSH \longrightarrow RS^{\bullet} + H^{+} + e^{-}$$
$$2RS^{\bullet} \longrightarrow RSSR \qquad (1.20)$$

Koryta and Pradac [44,45] presented cyclic voltammograms for solutions of L–cystine (Figure 1.13) and L–cysteine (Figure 1.14) in aqueous 1 mol dm^{-3} sulphuric acid, at platinum and gold electrodes. L–cystine completely suppressed the hydrogen adsorption peak(s) at both metals. This suggested the disulphide was adsorbed on the electrode surface. Radiometric analysis, with ^{35}S, confirmed strong adsorption (reaction 1.21), with a smaller quantitiy of the amino acid adsorbed at gold.

$$RSSR_{(ads)} \rightleftharpoons 2RS^{\bullet}_{(ads)} \qquad (1.21)$$

At platinum electrodes (Figure 1.13a), L–cystine oxidation to cysteic acid (RSO_3H) (reaction 1.22) and an adsorbed $R\dot{S}O_2$ radical (reaction 1.23) was proposed, together with surface oxide formation, between +0.45 V and −1.20 V (vs. SCE). A cathodic current, between +0.35 V and −0.25 V (vs. SCE) was attributed to reduction of the adsorbed $R\dot{S}O_2$ radical.

$$RS^{\bullet}_{(ads)} + 3H_2O \longrightarrow RSO_3^{-} + 6H^{+} + 5e^{-} \qquad (1.22)$$
$$RS^{\bullet}_{(ads)} + 2H_2O \longrightarrow R\dot{S}O_2 + 4H^{+} + 4e^{-} \qquad (1.23)$$

At gold electrodes (Figure 1.13b), L–cystine oxidation to cysteic acid (reaction 1.22), and simultaneous surface oxide formtion, occurred between +0.60 V and +1.35 V (vs. SCE). There was no evidence for production of the adsorbed $R\dot{S}O_2$ radical.

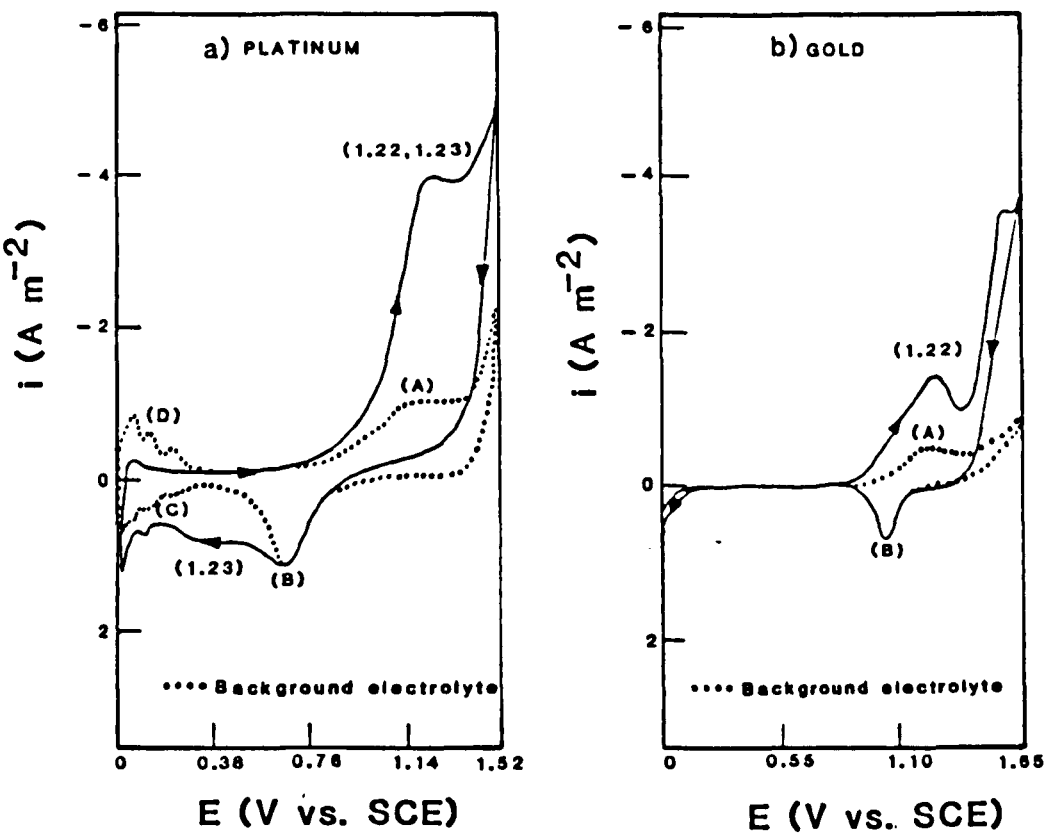

(A) Surface oxide formation
(B) Surface oxide reduction
(C) Hydrogen adsorption peak(s)
(D) Oxidation of adsorbed hydrogen

FIGURE 1.13 Cyclic voltammetry of 5.0 mol m^{-3} L-cystine in aqueous 1.0 mol dm^{-3} H_2SO_4 at a) platinum and b) gold electrodes [44,45].

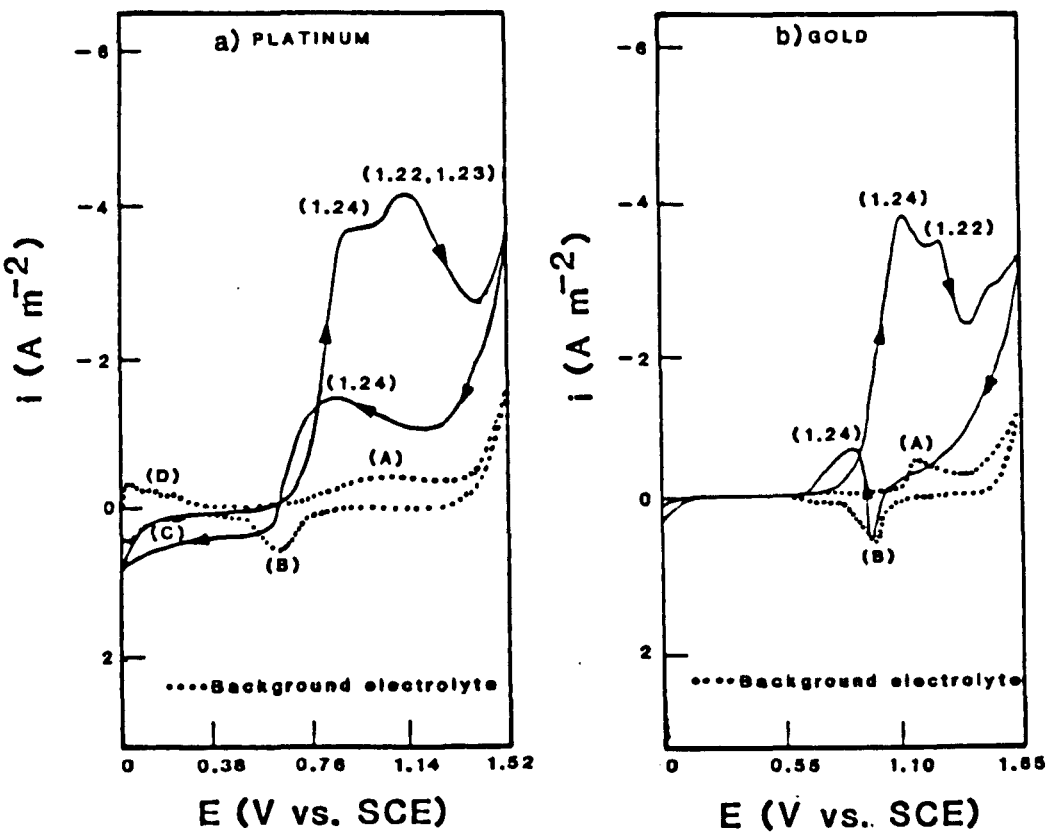

FIGURE 1.14 Cyclic voltammetry of 0.5 mol m^{-3} L-cysteine in aqueous 1.0 mol dm^{-3} H_2SO_4 at a) platinum and b) gold electrodes [44,45].

L-cysteine was oxidised to L-cystine at both platinum and gold electrodes. At platinum electrodes (Figure 1.14a), oxidation occurred at a peak potential of +0.8 V (vs. SCE) (reaction 1.24).

$$\begin{aligned} RSH &\longleftrightarrow RSH_{(ads)} \longrightarrow RS^{\bullet}_{(ads)} + H^{+} + e^{-} \\ 2RS^{\bullet}_{(ads)} &\longleftrightarrow RSSR \end{aligned} \qquad (1.24)$$

The L-cystine produced was oxidised (reactions 1.21 to 1.23) at a peak potential of +1.1 V (vs. SCE). At gold electrodes (Figure 1.14b), oxidation of L-cysteine (reaction 1.24) occurred at a peak potential of +1.0 V (vs. SCE), with the L-cystine produced oxidised (reactions 1.21 and 1.22) at a peak potential of +1.25 V (vs. SCE).

At both noble metals, Koryta and Pradac reported currents due to L-cystine oxidation were independent of electrolyte stirring, whereas those for L-cysteine oxidation were enhanced by faster stirring rates. This suggested the L-cystine surface reactions (1.21 to 1.23) were kinetically controlled, whilst, the thiol surface reaction (1.24) was under mixed kinetic-diffusion control. It was concluded that much less than a monolayer of L-cysteine was adsorbed on the electrodes.

As shown in Figures 1.13 an 1.14 surface oxide formation complicated the study at the nobel metals. Koryta and Pradac proposed possible involvement of the oxide in the mechanism of L-cystine oxidation at both metals. They cited the lack of separation of the two processes, even though oxidation commenced at electrode potentials some 0.15 V more positive on gold (Figure 1.13). In contrast, oxidation of L-cysteine was inhibited by surface oxide formation at the electrodes. During the reverse cathodic potential scan, oxidation continued as the surface oxide was reduced (Figure 1.14).

From measurements at a platinum rotating disc electrode Reddy and Krishnan [46,47] supported mechanism (1.24) for L-cysteine oxidation. Tafel slopes of 120 mV/decade and an electrochemical reaction order of -1 for protons were recorded.

At gold electrodes Safranov et al [48,49] reported that mechanism (1.24) for L-cysteine oxidation was applicable in neutral solution. From pH 3 to 12, Tafel slopes were 120 mV/decade and $(\delta E/\delta pH)$, at constant current, was 60 mV. Fractional electrochemical reaction orders, for L-cysteine and protons, were ascribed to a change in the amino acid adsorption with coverage.

From studies at a gold rotating disc electrode, with ex-situ X-ray photoelectron spectroscopic (XPS) analysis of the electrode surface, Raynaud et al [50] proposed a complex reaction pathway (1.25) for the oxidation of L-cystine and L-cysteine in a buffer solution of pH 1.7.

Adsorption of L-cystine and L-cysteine was confirmed by a.c. voltammetry. Steady state voltammograms were consistent with the cyclic voltammograms (Figures 1.13 and 1.14) reported by Koryta and Pradac [44,45]. Constant potential electrolysis of L-cystine solutions cathodic of +1.20 V (vs. SCE), followed by XPS analysis, identified $RSSO_3^-$ and RCOOH as adsorbed products. At potentials more positive than +1.40 V (vs. SCE), sulphur intermediates were not detected on the electrode surface. Dissolved RSO_3^- was proposed as the oxidation product. Adsorbed $RSSO_3^-$ and RCOOH were also detected after constant potential electrolysis of L-cysteine solutions, cathodic of +1.30 V (vs. SCE). Reynaud et al concluded the first step in the oxidation of L-cysteine was to L-cystine.

(e) Carbon

L-cystine reduction did not occur within the working potential range of vitreous carbon [50,51] or wax impregnated spectroscopic graphite (WISGE) [52] electrodes. Both L-cystine and L-cysteine were, however, oxidised.

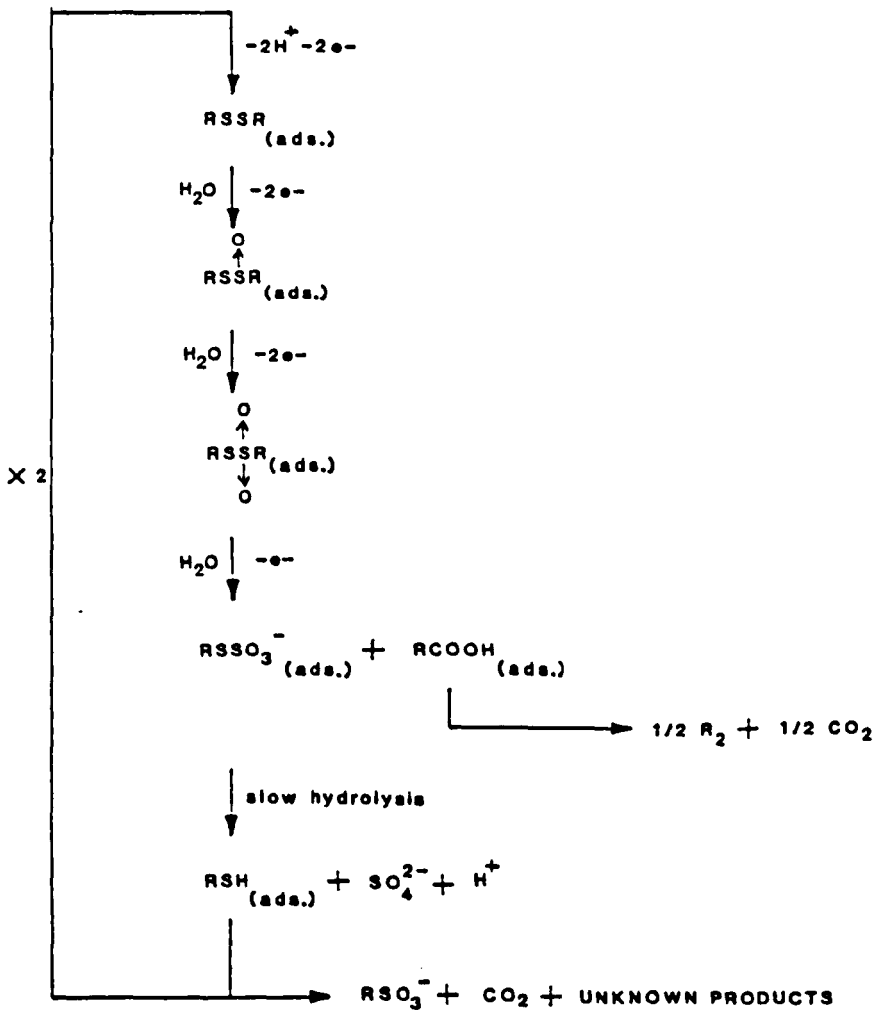
-2H+ -2e-
RSSR (ads.)
H2O -2e-
O
RSSR (ads.)
H2O -2e-
O
RSSR (ads.)
O
X 2
H2O -e-
RSSO3- (ads.) + RCOOH (ads.)
1/2 R2 + 1/2 CO2
slow hydrolysis
RSH (ads.) + SO4 2- + H+
RSO3- + CO2 + UNKNOWN PRODUCTS

(1.25)

At a vitreous carbon rotating disc electrode, L-cystine oxidation was electrochemically irreversible and diffusion controlled. Comparison of the limiting current with that obtained for ferrocyanide oxidation indicated 5 electrons were transferred. Oxidation to cysteic acid (reaction 1.26) was proposed.

$$RSSR + 3H_2O \longrightarrow RSO_3H + 5H^+ + 5e^- \qquad (1.26)$$

From Tafel slopes of 120 mV/decade the authors concluded the first electron transfer was the rate determining step. Since the $E_{\frac{1}{2}}$ (ca. +1.4 V vs. SCE) was constant from pH 1.7 to 6.2 proton involvement, either at, or preceding the rate determining step was precluded. The oxidation of L-cysteine produced an ill-defined current from +0.2 V (vs. SCE). From a.c. voltammetry it was deduced that a little L-cysteine was adsorbed on the electrode. L-cystine was not adsorbed.

In cyclic voltammograms at a WISGE, L-cystine and L-cysteine, were oxidised at peak potentials of about +1.4 V and +1.5 V (vs. SCE) respectively in pH 4.0 buffer solution. Both oxidations were electrochemically irreversible and diffusion controlled.

1.4.3 Conclusions from Thermodynamic and Kinetic Studies

The voltammetry indicates the reduction of dissolved L-cystine to L-cysteine is electrochemically irreversible. At lower overpotentials the kinetics of electron transfer are sluggish and the reduction is kinetically controlled. At higher overpotentials the electrochemcial kinetics are significantly enhanced (i.e. the relationship between the heterogeneous rate constant for electron transfer and overpotential is exponential) and the rate of mass transport of L-cystine now determines the rate of reduction. At intermediate overpotentials the reduction is

under mixed kinetic-mass transport contol.

Further evidence of the electrochemical irreversibility of the reduction is perhaps provided by lack of a reliable $E^{0'}$, from potentiometric studies, for the L-cystine/L-cysteine redox couple. For electrochemically irreversible reactions the electrode potential at zero current can wander between the two irreversible waves corresponding to the oxidation and reduction reactions of the couple. The slower the electrochemical kinetics the wider the potential gap. Consequently only a small error in the measured potential of zero current, due to, for example, impurities in the electrolyte, will lead to a large error in $E^{0'}$. The situation is further complicated for the L-cystine/L-cysteine couple, however, by interaction of the amino acids with the few electrodes used (see Section 1.4.1).

L-cystine and L-cysteine is reportedly adsorbed at all the electrode metals apart from carbon, with only a small amount of L-cysteine adsorbed at vitreous carbon. Significantly L-cystine is not reduced at vitreous carbon at electrode potentials positive of hydrogen evolution (i.e. ca. -1.2 V vs. SCE) in buffer solution of pH 1.7), whereas at mercury and transition metal macrocyles rates of L-cystine reduction are high at much less negative electrode potentials at a similarly low pH (e.g. Figures 1.3a and 1.10 respectively). This perhaps suggests adsorption of L-cystine promotes the sluggish electrochemical kinetics of L-cystine reduction. Adsorption of L-cystine does not, however, gaurantee efficient electrosynthesis of L-cysteine. For example at platinum, gold and silver although a significant amount of the disulphide is adsorbed at the electrode surface, reduction of the amino acid is masked by hydrogen evolution at these low hydrogen overpotential metals. Clearly it is required that the overpotential for disulphide reduction should be lower than that for hydrogen evolution and low hydrogen overpotential metals are not favoured.

At all of the electrodes L-cysteine is readily oxidised. In addition at platinum, gold and carbon electrodes L-cystine is only slightly more difficult to oxidise than L-cysteine. Consequently the electrosynthesis must be performed in a divided cell.

1.4.4 Electrosynthesis of L-Cysteine from L-Cystine

Little information is available in the literature relevant to the industrial electrosynthesis (reaction 1.04).

$$RSSR + 2H^+ + 2e^- \longrightarrow 2RSH \qquad (1.04)$$

Table 1.2 summarises the published work. As required a divided cell was used by all workers. Hydrochloric acid has been the preferred catholyte, yielding the favoured hydrochloride salt upon evaporation. Sulphuric acid has also been used but the sulphate salt has to be converted into the free base for all applications. A recent publication [62] has claimed efficient electrosynthesis of the free base directly using an aqueous ammonium hydroxide catholyte.

As early as 1955, Rambacher [53] patented the electrochemical reduction of L-cystine to L-cysteine in almost quantitative yield at tin and copper cathodes.

Suzuki and Karube [54] investigated the reduction at a series of cathodes at all of which L-cystine was readily reduced to L-cysteine. Zinc gave a quantitative chemical yield and the highest current efficiency (100%). The cathode corroded in the acidic catholyte, however, contaminating the product with zinc(II) ions. There was a suggestion that adsorbed, atomic hydrogen, produced during the corrosion process, aided the reduction. Corrosion of lead, silver and copper cathodes was not reported during the short duration (typically 6 hours) experiments. Current losses were attributed exclusively to hydrogen evolution, higher current efficiencies

TABLE 1.2 Synthetic studies of the electrochemical reduction of L-cystine to L-cysteine.

Cell Design	Cathode	Anode	Separator	Catholyte	Anolyte	Flow Rates		Current Density ($A\ m^{-2}$)	[a]Chemical Yield (%)	[b]Current Efficiency (%)	Reference
						Catholyte ($10^{-6} m^3 s^{-1}$)	Anolyte ($10^{-6} m^3 s^{-1}$)				
Tank cell	Sn, Cu	Graphite	Diaphragm	0.1M RSSR 1M HCl	1M HCl	N/A	N/A	300 to 600	Quantitative		[53]
Beaker cell 300 cm^3	Zn Pb Ag Cu	Pt	Anionic membrane	0.5M RSSR 2.7M HCl	1.4M HCl	N/A	N/A	500	100 100 70 65	100 50 19 14	[54]
Parallel plate tank cell 500 cm^3	S/S	S/S	Anionic membrane	0.25M RSSR 1.5M HCl	1.5M HCl	N/A	N/A	600 to 900 (cell voltage 5 V)	92	-	[55]
Parallel plate batch recycle	Pb	Pb	Cationic membrane	0.24M RSSR 1M HCl	1M H_2SO_4	150 50 40 20 10	30	700 (cell voltage 2.5 V to 3.5 V)	95.6 95.0 90.4 84.0 78.4	93.5 92.4 87.8 81.5 76.1	[56,57]
Parallel plate batch recycle	Pb	Pt	Cationic membrane	0.7M RSSR 2.7M HCl	2.7M HCl	40	40	200 to 700	98.2	61	[58-61]
Electrocell AB Parallel plate batch recycle	High area carbon felt	DSA	Cationic membrane	0.42M RSSR 8.6M NH_4OH	3M H_2SO_4	N/A	N/A	600 1500 2500	97 97 97	97 97 95	[62]

[a]Chemical yield $= \left[\frac{\text{Moles of L-cysteine formed}}{\text{Moles of L-cystine consumed}} \times 100\right]\%$

[b]Current efficiency $= \left[\frac{\text{Moles of L-cystine reduced}}{\text{Theoretical moles of L-cystine reduced}} \times 100\right]\%$

N/A Not applicable

- Not available

S/S Stainless steel

being obtained at high hydrogen overpotential cathodes such as lead. During electrolysis, L-cystine reduction and hydrogen evolution consumed protons. The resultant decrease in the acid concentration of the catholyte was promoted by the use of an anionic ion-exchange membrane, which prevented protons being transferred from the anolyte to catholyte. It was claimed this lowered the time required for product work up. Suzuki and Karube examined alkaline electrolytes but there was a considerable loss of both amino acids, due not only to oxidation and decomposition reactions (see Section 1.1) but from migration and diffusion of the negatively charged amino acid molecules into the anolyte compartment.

A series of Japanese patents [56,57] for Showa Denko K.K. dealt with the manufacture of L-cysteine hydrochloride in a parallel plate electrochemical reactor operated in the batch recycle mode. Lead was the preferred cathode giving at best a chemical yield of 95.6% and a current efficiency of 93.5%. From liquid chromatography, the product purity was better than 99%. The importance of catholyte flowrate on both the chemical yield and current efficiency was stressed. A high flow rate minimised side reactions. At lead electrodes, the cathode potential was monitored during electrolysis and a sharp rise from about -0.6 V (vs. SCE) to more cathodic potentials was associated with increased hydrogen evolution. Monitoring of the cathode potential was proposed as a method of determining the moment to terminate electrolysis. Excessive electrolysis times also reduced chemical yields and under these conditions, the pungent smell of hydrogen sulphide was noted.

Several papers [58-61] in the Chinese literature consider essentially the system patented by Showa Denko K.K.. No improvement on lead as a cathode was reported. At lead electrodes, increasing the electrolyte flowrate and the current density reduced electrolysis times.

The Electrosynthesis Company [62] have investigated electrosynthesis of L-cysteine free base in aqueous ammonium hydroxide catholyte at a proprietary high surface area carbon felt cathode. They claim a chemical yield of 97% and a current efficiency of 95% at a very high current density of 2,500 A m^{-2}. There must, however, be concern over the stability of the amino acids in the concentrated ammonium hydroxide catholyte. Additionally the conductivity of the catholyte is such that cell voltages as high as 9.5 V were measured towards the end of electrolyses, giving rise to correspondingly high specific energy consumption values. Presumably ammonium hydroxide was selected to facilitate efficient catholyte evaporation to yield the product.

1.4.5 Conclusions from Electrosynthesis Studies

In acidic catholytes L-cystine reduction occurs with a near quantitative chemical yield and high current efficiency in the most favourable cases (see Table 1.2). High hydrogen overpotential cathodes give the highest current efficiencies, as current losses are due principally to hydrogen evolution, and selection of an appropriate cathode material is clearly paramount for an efficient electrosynthesis. Evidence that L-cystine reduction is mass transport controlled under appropriate conditions (i.e. high overpotentials) in electrochemical reactors operated in the batch recycle mode is provided by the reported increased rates of reduction with increased catholyte flowrates.

1.5 AIMS OF AND APPROACH ADOPTED IN THE PRESENT STUDY

The principal objective is to determine the most efficient conditions for the electrosynthesis of L-cysteine hydrochloride from L-cystine hyrochloride. Since selection of an appropriate cathode material is the key to electrosynthesis the study focuses on a detailed examination of the reaction at a wide selection of candidate

cathode materials (i.e. mercury, lead, cadmium, zinc, titanium, tin, carbon, stainless steel, copper, nickel and molybdenum). Electrode selection was based upon the hydrogen overpotential of the metals and upon their ready availability in rod and planar sheet form. The metals span the range from materials which exhibit among the lowest reported rates of hydrogen evolution (e.g. mercury, lead) to those which are fairly electrocatalytic (e.g. nickel, molybdenum). Examining such a range of cathodes in a single study may confirm not only the importance of a high hydrogen overpotential, but may highlight adsorption of the amino acids at the cathode, as significant at some of the metals in terms of promoting a more efficient electrosynthesis. Two different but complementary types of study are lacking at all cathodes.

Polarography, cyclic voltammetry and rotating disc electrode studies should establish and provide information on those cathodes at which L-cystine reduction is separated from hydrogen evolution in aqueous hydrochloric acid, which should be the most efficient for the electrosynthesis. At these cathodes voltammograms should confirm the electrochemical irreversibility of the reduction, suggested by the literature, and a detailed kinetic study might allow the mechanism of reduction to be proposed and the electrochemical activity of the metals to be compared. This strictly requires, however, the mechanism to be identical at all metals. Tafel slopes, transfer coefficients, heterogeneous rate constants and reaction orders are not available in aqueous hydrochloric acid media at any of the chosen cathodes. The voltammetric techniques may also yield valuable information on the extent of amino acid adsorption at these cathodes and the effect upon L-cystine reduction (e.g. see the mercury studies in Section 1.4.2(a)).

Coulometry at the more efficient cathodes should reinforce the voltammetry by confirming any voltammetric waves obtained are due to L-cystine reduction with

close to 100% current efficiency. This is required for calculation of kinetic and other parameters from voltammograms (i.e. any current not due to L-cystine reduction must be subtracted and if large the accuracy of the calculated parameters will be low).

The second area in which information is lacking is electrosynthesis studies in a suitable electrochemical reactor. Although the voltammetry may grade the activity of the metals for the reduction because of significant differences between the two types of experiment the majority of cathodes will be examined. Particularly important is the much longer time scale of electrosynthesis experiments during which electrode surfaces and therefore synthesis performance can be modified. This is a common concern in electroorganic syntheses. In addition electrosynthesis in a large reactor is performed at constant current rather than with a controlled electrode potential which can lead to the formation of by-products, and generally much higher concentrations of reactant and product are present in a reactor.

The electrosynthesis will be studied in a parallel plate cell design operating in the batch recycle mode, which is the most common system used by industry. System selection was based upon a number of factors. The parallel plate design offers a number of advantages over all alternatives. The potential and current distribution should be most uniform in this design. Also, the electrode materials are readily available in a suitable form as are a wide selection of electrolyte separators. The reduction is restricted to batch operation because of the difficulty in separating the reactant and product allied to the requirement for a product purity of at least 98.5% w/w and the presence in the product of not greater than 1% w/w of other amino acids. A typical product specification is given in Table 1.3. Batch recycle operation was chosen over a simple batch reactor principally because mass transport is easily varied in the reactor and the scant literature

suggests mass transport of L-cystine to the cathode is important.

TABLE 1.3 Product specification for L-cysteine hydrochloride [63, 64].

Minimum assay	98.5% w/w
Specific Rotation $[\alpha]_D^{25^oC}$(20 g dm^{-3} in 5 mol dm^{-3} HCl)	+ 5.5° to + 6.5°
Other amino acids	< 1% w/w
Loss on drying	< 0.5% w/w
Residue on ignition (as sulphate)	< 0.1% w/w
Heavy metals	< 10 ppm

The aim is to monitor the reactor performance as constant current electrolysis proceeds, by analysing the catholyte for the reactant and product concentrations at measured time intervals. A parametric study of the important process variables (i.e. current density and catholyte flowrate) should allow determination of the optimum electrosynthesis conditions at each cathode. Important figures of merit will be used to analyse the reactor performance, an approach sadly lacking in the literature [65]. At the most promising cathodes extended durability tests will be performed. This is particularly important in light of the earlier comments regarding the often observed problems with changes in electrode surface state during prolonged electrolysis.

1.6 CONTENTS OF THE PRESENT STUDY

First the small scale kinetic studies are disclosed in Chapters 2 to 4. The experimental details are first given in Chapter 2, followed by the detailed studies of mercury in Chapter 3. Results of the other electrode metals (essentially lead) are presented in Chapter 4. The latter chapters cover the experiments performed in the electrochemical reactor. Chapter 5 shows the construction of the reactor system and gives the necessary detail to perform all experiments. A study of the mass transport performance of the reactor using the diffusion limited current technique is given in Chapter 6. The electrosynthesis studies at mercury and lead (Chapter 7) are separated from those at the other cathodes (Chapter 8). Finally Chapter 9 presents some general observations and suggestions for further work.

REFERENCES

1. Jakubke H.D. & Jeschkeit H. "Amino Acids, Peptides and Proteins An Introduction". Akademie-Verlag, Berlin (1977). Page 25.

2. Dawson R.M.C., Elliott D.C., Elliott W.H. & Jones K.M. "Data for Biochemical Research". Clarendon Press, Oxford (1986). Pages 12 and 13.

3. Liu Teh-Yung in "The Proteins". Eds. Neurath H., Hill R.L. & Boeder C-L.,Academic Press, New York (1977). Volume 3, Chapter 3.

4. Sigma Chemical Catalogue page 301 (1991).

5. Kleemann A., Leuthtenberger W., Hoppe B. & Tanner H. in "Ullmann's Encyclopedia of Industrial Chemistry". 5th Edition, VCH Verlagsgesellschaft mbh, Weinheim (FRG) (1985). Volume A2, pages 57-97.

6. Itoh T. in "Synthetic Production and Utilisation of Amino Acids". Eds. Kaneko T., Izumi Y., Chibata I. & Itoh T., Halsted Press, New York (1974). Chapter 6.

7. Nagasawa T. & Yamada H. in "Progress in Industrial Microbiology. Vol. 24 Biotechnology of Amino Acid Production". Eds. Aida K., Chibata I., Nakayama K., Takinami K. & Yamada H., Elsevier, Amsterdam (1986). Chapter 19.

8. Greenstein J.P. & Winitz M. "Chemistry of the Amino Acids". John Wiley & Sons, New York (1961). Volume 3, Chapter 24.

9. Izumi Y. in "Synthetic Production and Utilisation of Amino Acids". Eds. Kaneko T., Izumi Y., Chibata I. & Itoh T., Halsted Press, New York (1974). Chapter 4.

10. Martens J., Offermanns H. & Scherberich P.; *Angew. Chem. Int. Ed.* 20, 668, (1981).

11. Baumann E. & Preusse C.; *Z. Physiol Chem.* 5, 309, (1881).

12. Borsook H., Ellis E.L. & Huffman H.M.; *J. Biol. Chem.* 117, 281, (1937).

13. Ghosh J.C., Raychaudhurri S.N. & Ganguli S.C.; *J. Indian Chem. Soc.* 9, 43, 53, (1932).

14. Green D.E.; *Biochem. J.* 27, 678, (1933).

15. Dixon M. & Quastel H.H.; *J. Chem. Soc.* 123, 2943, (1923).

16. Williams J.W. & Drissen E.M.; *J. Biol. Chem.* 87, 441, (1930).

17. Ryklan L.K. & Schmidt C.L.A.; *Univ. Calif. Publ. Physiology* 8, 257, (1944).

18. Fruton G.S. & Clarke H.T.; *J. Biol. Chem.* 106, 667, (1934).

19. Tanaka N., Kolthoff I.M. & Stricks W.; *J. Am. Chem. Soc.* 77, 2004, (1955).

20. Kolthoff I.M. & Barnum C.; *J. Am. Chem. Soc.* 62, 3061, (1940).

21. Nygard B.; *Acta Chem. Scand.* 15, 1039, (1961).

22. Nygard B.; *Arkiv. Kemi* 27, 341, 405, 425, (1967); 28, 75, 89, (1967).

23. Nygard B.; *Acta Unversitatis Upsaliensis* Uppsala 104, (1967).

24. Nygard B., Olefsson J. & Bergson G.; *Arkiv. Kemi* 28, 41, (1967).

25. Kolthoff I.M., Stricks W. & Tanaka N.; *J. Am. Chem. Soc.* 77, 5211, (1955).

26. Kolthoff I.M. & Barnum C.; *J. Am. Chem. Soc.* 63, 520, (1941).

27. Kolthoff I.M., Stricks W. & Tanaka N.; *J. Am. Chem. Soc.* 77, 4739, (1955)

28. Issa I.M., Samahy A. El., Issa R.M. & Temerik Y.M.; *Electrochim. Acta* 17, 1615, (1972).

29. Ducarmois-Mairesse C.A., Patriarche G.J. & Vandenbalck J.L.; *J. Pharm. Belg.* 28, 300, (1973).

30. Ducarmois-Mairesse C.A., Patriarche G.J. & Vandenbalck J.L.; *Anal. Chim. Acta* 71, 165, (1974).

31. Miller I.R. & Teva J.; *J. Electroanal. Chem.* 36, 157, (1972).

32. Stankovich M.T. & Bard A.J.; *J. Electroanal. Chem.* 75, 487, (1977).

33. Zagal J., Fierro C. & Rozas R.; *J. Electroanal. Chem.* 119, 403, (1981).

34. Zagal J., Herrera P., Brinck K. & Zanartu-Ureta S.; *Proc. Electrochem. Soc.* 84-12, 602, (1984).

35. Zagal J. & Herrera P.; *Electrochim. Acta* 30, 449, (1985).

36. Zagal J., Paez C. & Barbato S.; *Proc. Electrochem. Soc.* 87-12, 211, (1987).

37. Nikolic B.Z., Adzic R.R. & Yeager E.B.; *J. Electroanal. Chem.* 103, 281, (1979).

38. Wang Z., Li C., Deng Z. & Zha Q.; *Huaxue Xuebao* 44, 863, (1986). Chem. Abs. 105, 199030z, (1986).

39. Wang Z., Li C., Deng Z. & Zha Q.; *Huaxue Xuebao* 45, 931, (1987). Chem. Abs. 108, 64491s, (1988).

40. Wang Z., Li C., Deng Z. & Zha Q.; *Gaodeng Xuexiao Huaxue Xuebao* 8, 453, (1987).
Chem. Abs. 108, 12940t, (1988).

41. Wang Z. & Pang D.; *J. Electroanal. Chem.* 283, 349, (1990).

42. Watanabe T. & Maeda H.; *J. Phys. Chem.* 93, 3258, (1989).

43. Davis D.G. & Bianco E.; *J. Electroanal. Chem.* 12, 254, (1966).

44. Pradac J. & Koryta J.; *J. Electroanal. Chem.* 17, 167, 177, 185, (1968).

45. Pradac J., Ossendorfova N. & Koryta J.; *Croat. Chem. Acta* 45, 97, (1973).

46. Reddy S.J. & Krishnan V.R.; *Anal. Chem. Symp. Ser.* 2 155, (1980).

47. Reddy S.J. & Krishnan V.R.; *Trans. SAEST* 15, 99, (1980).

48. Safranov A. Yu., Tarasevich M., Bogdanovskaya V.A. & Chernyak A.S.; *Sov. Electrochem.* 19, 378, (1983).

49. Safranov A. Yu., Tarasevich M., Bogdanovskaya V.A. & Cernyak A.S.; *J. Electroanal. Chem.* 202, 147, (1986).

50. Reynaud J.A., Malfoy B. & Canessan P.; *J. Electroanal. Chem.* 114, 195, (1986).

51. Eggli R. & Asper R.; *Anal. Chim. Acta* 101, 253, (1978).

52. Brabec V. & Mornstein V.; *Biophysical Chem.* 12, 159, (1980).

53. Rambacher P.; German Patent 1024518 (1955).

54. Suzuki S. & Karube I.; *Recent Dev. Sep. Sci.* 3, 355, (1977).

55. Wong Chi-H. & Wang Kung-T.; *J. Chin. Chem. Soc.* 25, 149, (1978)

56. Nakayasu K., Furuya O., Inoue N. & Moriguchi S.; Jap. Patent 140966 (1981).

57. Takahashi N. & Nakayasu K.; Jap. Patents 98684 (1982); 98685 (1982).

58. Chen M.; *Huaxue Shiji* 5, 173, (1983).
Chem. Abs. 99, 140338k, (1983).

59. Yang R. & Wu B.; *Shengwu Huaxue Yu Shengwu Wuli Jinzhan* 56, 67, (1984).
Chem. Abs. 101, 131064a, (1984).

60. Zhu W.; *Nanjing Daxue Xuebao Ziran Kexue* 22, 566, (1986).
Chem. Abs. 107, 154725e, (1986).

61. Zhu C. & Song X.; *Huazhong Shifan Daxue Xuebao Ziran Kexueban* 20, 307, (1986).
Chem. Abs. 107, 78219a, (1987).

62. Genders J.D., Weinberg N.L. & Zawodzinski C. Extended Abstracts Volume 90-1 The Electrochem. Soc. Spring Meeting, Montreal 6-11th May, (1990).

63. Itoh T. in "Synthetic Production and Utilisation of Amino Acids". Eds. Kaneko T., Izumi Y., Chibata I. & Itoh T., Halsted Press, New York (1974). Chapter 5.

64. Millington P.J. Personal Communication.

65. Pletcher D. & Walsh F.C. "Industrial Electrochemistry". Chapman and Hall, London (1990).

CHAPTER 2

EXPERIMENTAL FOR KINETIC STUDIES

2.1 WORKING ELECTRODES

2.1.1 Electrode Materials

The specification of the metals employed are listed in Table 2.1.

2.1.2 Rotating Disc Electrodes

The electrode construction (Figure 2.1) consisted of a brass shaft in an epoxy resin shell with a detachable bottom section containing the metal disc, which was machined to give a tight press fit into a PTFE sheath. A brass spring provided electrical contact between the disc and shaft. The sheath diameter was close to 2.5 times larger than that of the disc. Consequently, the fluid flow to the disc can essentially be considered as flow to a planar surface of infinite diameter as required by rotating disc electrode theory [1]. The electrodes were, in overall size, approximately 9 cm long and 2 cm in diameter with a geometrical electrode area of 0.50 cm^2.

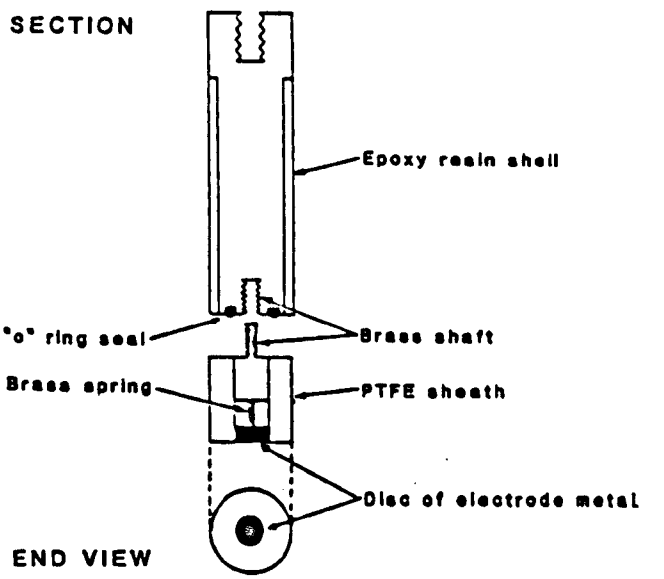

FIGURE 2.1 Section through a rotating disc electrode and end view.

Table 2.1 Specification of the electrode materials employed in the voltammetry and coulometry experiments.

Metal	Source	Specification
Mercury	Belgrave Mercury Ltd.	Polarographic Grade BM3. Triply distilled.
Copper	Goodfellow	99.99 + % w/w Copper Ag 70 ppm, (Fe,Pb,Ni,Si) 2 ppm, (Al,Bi,Ca,Mg,Sn) 1 ppm, (Cr,Mn,Na) < 1 ppm.
Lead	Goodfellow	99.99 + % w/w Lead (Fe,Ag) 1 ppm, (Cu,Cd) < 1 ppm.
Titanium	Goodfellow	99.6 + % w/w Titanium O_2 2000 ppm, (Al,Cr,Mn,Ni,V) 500 ppm, Fe 300 ppm (Cu,Si,Sn,C) 200 ppm, N_2 80 ppm, H_2 30 ppm, Mg 20 ppm, Ta 10 ppm, Co 2 ppm.
Tin	Goodfellow	98.8 + % w/w Tin Sb 1.1 % w/w, Pb 600 ppm, Cu 100 ppm, As 20 ppm, (Ag,Bi,Cd,Fe,Ni,Zn) 10 ppm.
Nickel	Goodfellow	99.98 + % w/w Nickel C 70 ppm, (Cu,Fe,Mg,Mn,Ti,S) 10 ppm, (Co,Cr,Si) 8 ppm.
Molybdenum	Goodfellow	99.9 + % w/w Molybdenum (Si,Fe,Cr) < 50 ppm, C 40 ppm, (Pb,Ti) < 30 ppm, O_2 30 ppm, (Al,Ca,Cu,Mg) < 20 ppm, (W,N_2) 10 ppm, H_2 5 ppm, K < 2 ppm.
Cadmium	Goodfellow	99.999 + % w/w Cadmium Pb 10 ppm, (Cu,Fe,Ag) < 1 ppm
Zinc	Goodfellow	99.99 + % w/w Zinc B 2 ppm, Cd 1 ppm, (Fe,Si,Ag) < 1 ppm.
Stainless Steel	Imperial Metal Industries	Cr 17-20 % w/w, Ni 7-10 % w/w, Mn < 2 % w/w, C 1500 ppm, Ti 4xC ppm, Fe balance.
Vitreous Carbon	Electricity Council Research Centre	Not available.
Platinum	Johnson Matthey	20 ppm maximum total metal impurities.

2.1.3 Mercury Plated Copper Rotating Disc Electrode

A method due to Daly et al [2] was used. A copper electrode was wet polished to a mirror finish, initially on fine silicon carbide paper followed by 1 μm, 0.5 μm and 0.05 μm alumina, in turn, on polishing cloths. After rinsing with absolute alcohol and doubly distilled water, the electrode was ultrasonicated to remove any remaining alumina particles. Electroplating was performed from aqueous 0.15 mol dm^{-3} mercuric nitrate and 0.12 mol dm^{-3} potassium cyanide (250 cm^3) previously deoxygenated with nitrogen for an hour. The copper electrode was rotated at 30 Hz and a constant current of 25 mA passed for 5 minutes using a platinum foil anode, whilst nitrogen blanketed the cell to prevent air ingress. The mercury surface was rinsed with doubly distilled water then wiped with a tissue to obtain a mirror finish.

The plating solution was prepared from BDH Analar grade chemicals and doubly distilled water. The cell (Figure 2.4a) and platinum anode (Figure 2.3) are described in Sections 2.3.1 and 2.2 respectively. The constant current was supplied by an E. G. & G. PARC Model 371 potentiostat/galvanostat and the electrode rotated with an Oxford Electrodes assembly. The rotor was capable of providing rotation rates of between 0 and 50 Hz to ± 0.1 Hz. Calibration of the rotor was performed using a tachometer.

2.1.4 Stationary Mercury Disc Electrode

The design (Figure 2.2), was based on a syringe altered to give a cup at one end with a piece of platinum placed around the rim to provide an approximately planar surface. Electrical contact to the mercury was made via a platinum wire protruding into the cup and sealed within the syringe. The cup diameter of 1.01 cm gave a geometrical electrode area of 0.80 cm^2.

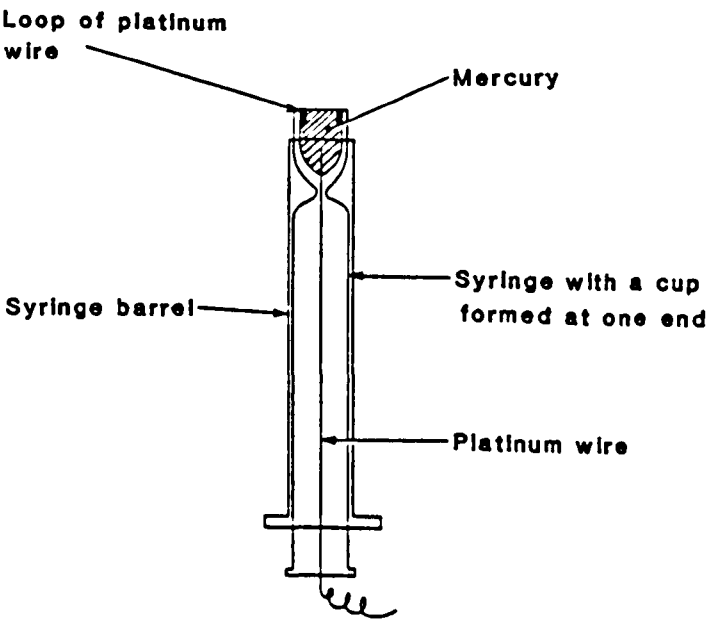

FIGURE 2.2 Stationary mercury disc electrode.

2.1.5 Static Mercury Drop and Hanging Mercury Drop Electrode

An E. G. & G. PARC Model 303A static mercury drop electrode fitted with a Model G0199 glass capillary was used. The capillary bore was siliconised with E. G. & G. PARC G0092 solution to minimise penetration by electrolyte. Two capillaries were used which gave mercury drops of geometrical area 0.021 cm^2 and 0.014 cm^2. The areas were determined by weighing a measured number of drops.

2.2 REFERENCE AND AUXILIARY ELECTRODES

Commercially available reference electrodes were employed. A silver/silver chloride (Ag/AgCl) reference electrode was supplied with the E. G. & G. PARC

Model 303A static mercury drop electrode. For other experiments, an Ingold double junction SCE was used. The internal electrolytes were changed weekly to preclude potential drift. Aqueous 3.8 mol dm^{-3} potassium chloride, saturated with silver chloride, was used as the filling solution for the Ag/AgCl electrode, whilst aqueous 3.8 mol dm^{-3} potassium chloride, with an outer junction solution of aqueous 1.0 ml dm^{-3} potassium nitrate, was preferred for the SCE.

A platinum foil auxiliary electrode was constructed as shown in Figure 2.3. A length of copper wire was soldered onto a small section of platinum wire using a high temperature solder, to facilitate sealing into the glass. A platinum foil of geometrical area 4.7 cm^2 was spot welded onto the protruding platinum wire.

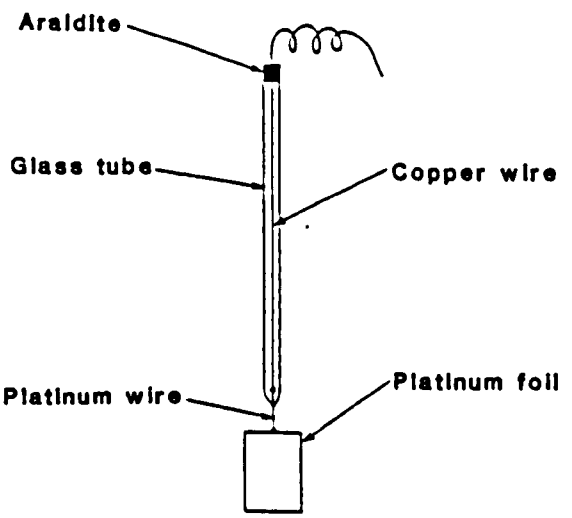

FIGURE 2.3 Platinum foil auxiliary electrode.

2.3 ELECTROCHEMICAL CELLS

All cells employed typical three electrode systems consisting of the working electrode, a reference electrode and an auxiliary electrode. In the process of cell design, three points were observed:

1) The auxiliary electrode was much larger than the working electrode to prevent possible rate control from the counter electrode reaction.

2) A Luggin capillary was used to communicate the reference electrode close to the working electrode to minimise the effect of electrolyte resistance.

3) The cell was divided to prevent oxidation of L-cystine hydrochloride and L-cysteine hydrochloride at the anode and possible interference from oxidation products at the cathode.

2.3.1 Rotating Disc Electrode Cell

The glass cell is shown in Figure 2.4a. The Luggin capillary, manufactured from a syringe, communicated the SCE to within less than 1 mm of the rotating disc surface. Nafion 324 cationic ion-exchange membrane divided the cell. The catholyte compartment accommodated a 250 cm^3 volume of electrolyte and allowed experiments to be thermostated via a water jacket. The large volume ensured the cell walls did not modify the catholyte flow pattern at the disc. A Perspex top sealed the compartment mainly to prevent the dissolution of oxygen into purged catholytes, although it aided centralisation of the disc and facilitated attachment of a thermometer and purging line. The rotating disc and platinum auxiliary electrodes were not parallel to each other but the large distance between them should have promoted a reasonably uniform potential and current distribution.

2.3.2 Stationary Mercury Disc Electrode Cell

As shown in Figure 2.4b the cell was similar to the rotating disc electrode cell. In this case, however, a two-piece luggin capillary was used to allow easy removal of the capillary from the cell.

2.3.3 Static Mercury Drop and Hanging Mercury Drop Electrode Cell

The E. G. & G. PARC Model 303A static mercury drop electrode and cell (Figure 2.5) consisted of a metal stand into which a mercury reservoir was built

a)

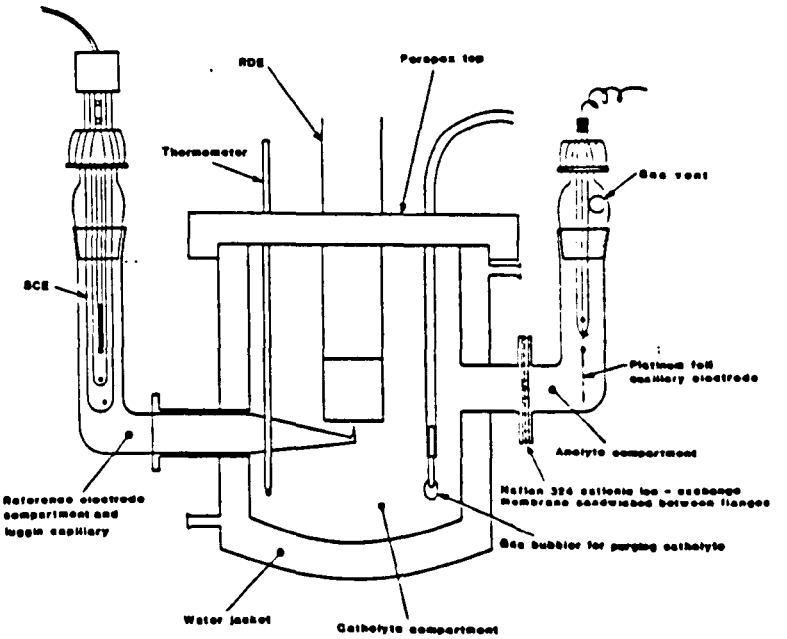

b)

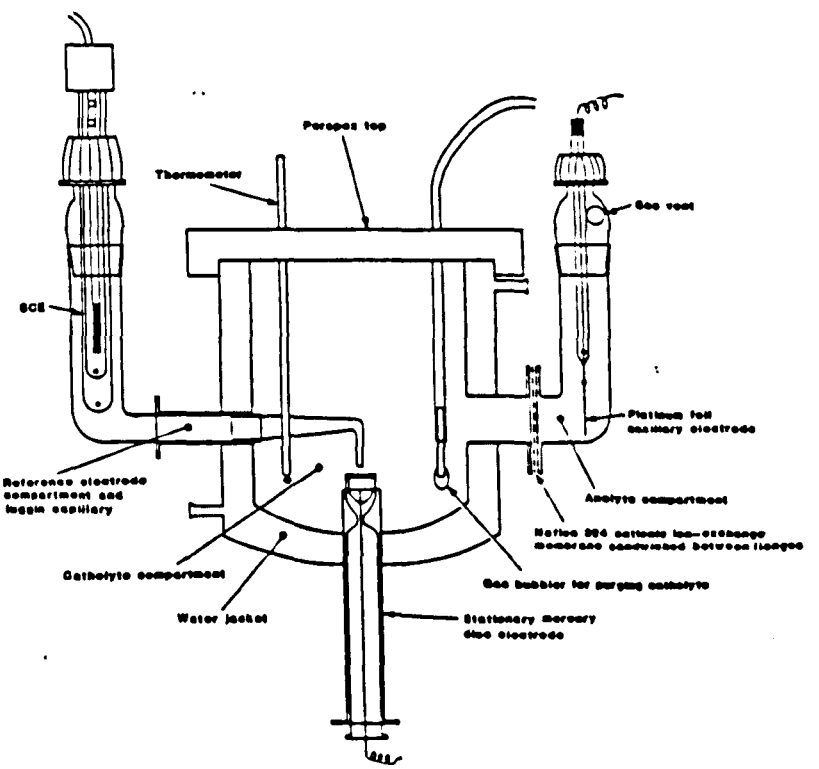

FIGURE 2.4 a) Rotating disc and b) stationary mercury disc electrode cells.

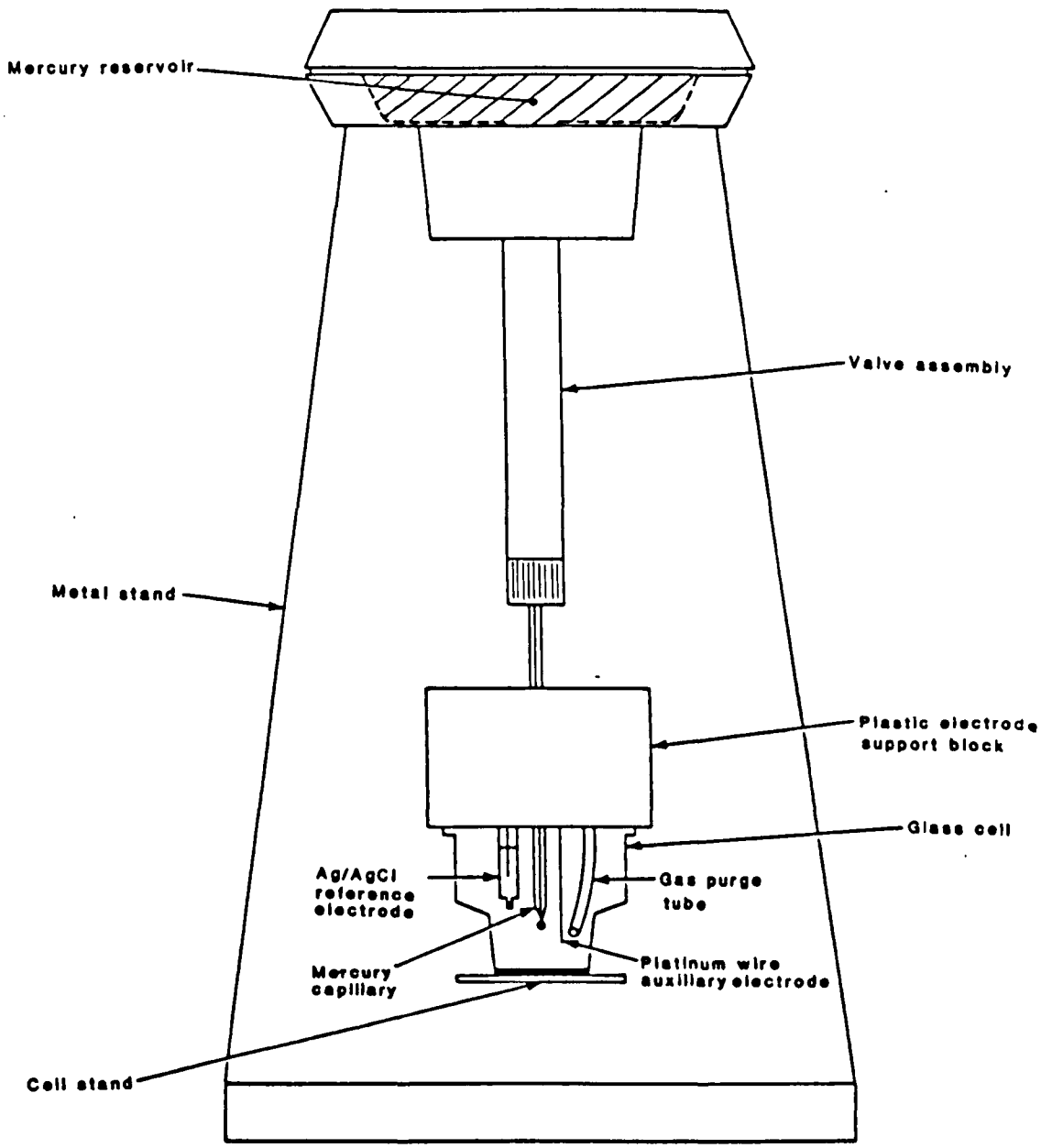

FIGURE 2.5 E.G. & G. PARC Model 303A static mercury drop electrode and cell.

and the cell components were attached. The cell, a glass cup of volume 20 cm^3, was located beneath an electrode support block which contained the various electrodes and the drop dislodge mechnanism. There was no requirement for a luggin capillary because of the low currents passed at the small area mercury drop. A plastic tube allowed solutions to be purged. In addition, the cell was automatically blanketed with nitrogen during measurements through a port in the electrode support block. The electrode had the facility to operate as a static mercury drop, dropping mercury or hanging mercury drop electrode.

The PARC design did, however, have some disadvantages. The mercury reservoir height could not be adjusted with loss of an important test for diffusion controlled reactions (i.e. diffusion controlled limiting currents are directly proportional to the square root of the mercury head height). The cell was also undivided allowing possible interference from oxidation product(s) at the mercury drop.

2.3.4 Coulometry Cell

The glass cell is shown in Figure 2.6. The geometrical area of the platinum foil auxiliary electrode (1.8 cm^2) was much greater than that of the rotating disc electrode (0.5 cm^2). The reference electrode was connected to less than 1 mm from the rotating disc electrode surface by a luggin capillary formed from a length of silicone rubber tubing attached to a glass end section, which was manufactured as an integral part of the catholyte chamber. Nafion 324 cationic ion-exchange membrane divided the cell. Efficient separation was important because of the long duration of experiments and the need to accurately determine the reactant and product concentrations after electrolysis. Electrolysis times were minimised by using a rotating disc electrode, rather than a stationary one, to provide efficient mass transport and by maximising the electrode area (0.50 cm^2)

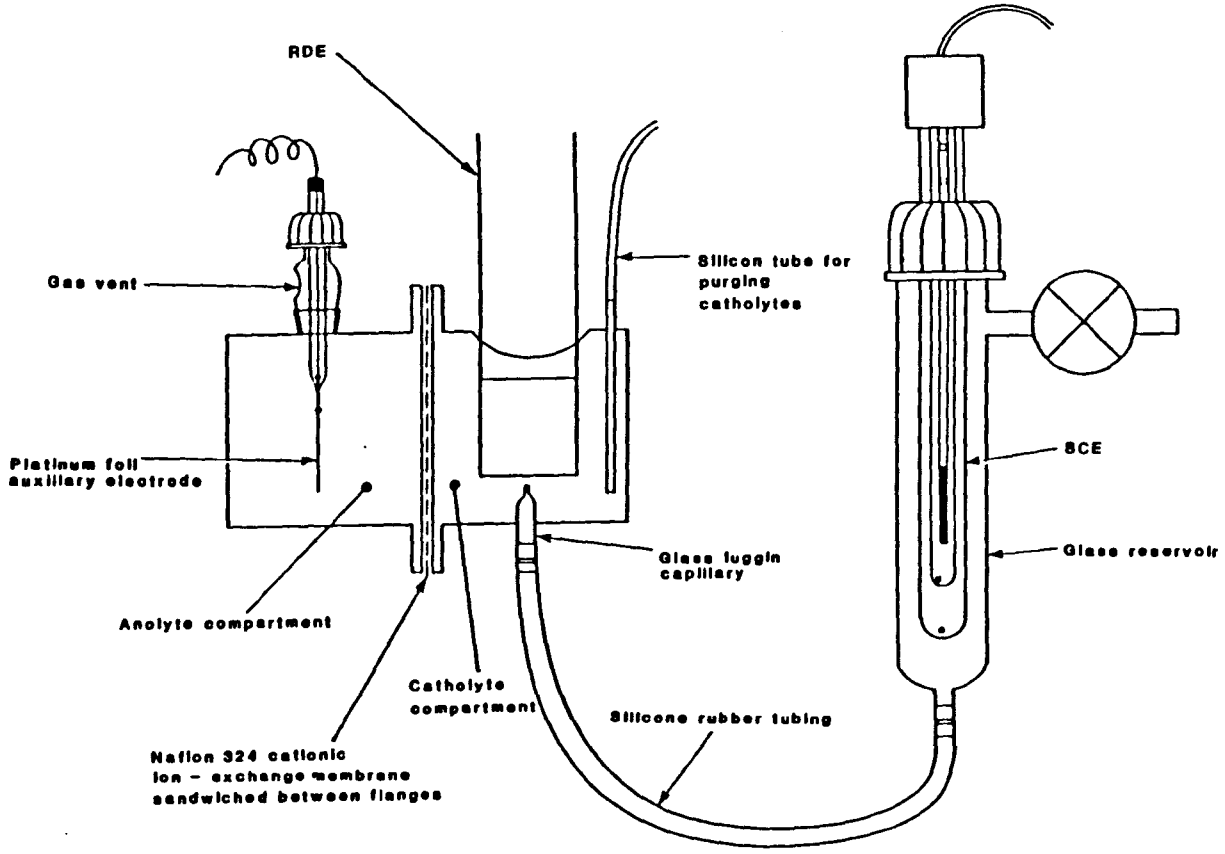

FIGURE 2.6 Coulometry cell.

to catholyte volume (25 cm^3) ratio. Even in the small catholyte compartment rotating disc electrode theory [1] was obeyed for the range of rotation rates investigated. Acceptable limiting current plateaus were obtained for ferricyanide reduction and ferrocyanide oxidation at a platinum rotating disc electrode. Diffusion coefficients of 6.3 x 10^{-10} m^2 s^{-1} for ferricyanide and 7.1 x 10^{-10} m^2 s^{-1} for ferrocyanide in aqueous 1.0 mol dm^{-3} potassium hydroxide, at 25°C, were determined in close agreement with the literature [3].

2.4 CHEMICALS AND SOLUTIONS

BDH Analar grade L-cystine and L-cysteine were used as supplied, at the concentrations indicated in Chapters 3 and 4. Most experiments were performed in aqueous 0.1 mol dm^{-3} or 2.0 mol dm^{-3} hydrochloric acid. In some experiments, aqueous 0.1 mol dm^{-3} nitric acid was used to examine the effect of chloride ions on the voltammograms. The effect of pH on the system was investigated using several different aqueous solutions of constant ionic strength and pH. Details of solution preparation was obtained from a collection of tables of buffer solutions [4]. The relevant details are summarised in Table 2.2.

2.5 PROCEDURES

2.5.1 Recording Voltammograms of L-Cystine Hydrochloride Reduction

(a) General Procedure

Steady state voltammograms were recorded by sweeping the electrode potential from the initial to the final potential limit and back to the initial potential (to check for hysteresis) at a rate of less than or equal to 2 mV s^{-1}. The current output was monitored with a Houston 2000 XY chart recorder or with a Keithly 178 digital multimeter connected across the current output terminals of the

TABLE 2.2 Preparation of solutions of constant ionic strength (0.5 mol dm^{-3}) and pH at 25°C.

Solution	pH	x	y	z
Hydrochloric Acid/Potassium Chloride Solutions	1.11	50.0	200.0	
Contain x cm^3 of 2.0 mol dm^{-3} hydrochloric	1.50	20.1	230.0	
acid and y cm^3 of 2.0 mol dm^{-3} potassium	2.00	6.5	243.5	
chloride diluted to 1.0 dm^3.	2.20	4.2	246.0	
	2.50	2.0	248.0	
McIlvaine Buffers	2.2	4.0	98.0	499.0
Contain x cm^3 of 1.0 mol dm^{-3} di-sodium	3.0	57.0	79.5	421.2
hydrogen orthophosphate ($Na_2HPO_4.12H_2O$),	4.0	77.1	61.4	342.1
y cm^3 of 1.0 mol dm^{-3} oxalic acid	5.0	103.0	48.5	244.1
($C_6H_8O_7.H_2O$) and z cm^3 of 1.0 mol dm^{-3}	6.0	126.2	36.8	155.6
potassium chloride diluted to 1.0 dm^3.	7.0	164.5	17.6	73.6
	8.0	194.3	2.8	0.0
Boric Acid/Sodium Hydroxide Buffers	8.00	3.9	223.0	
Contain 50 cm^3 of 1.0 mol dm^{-3} boric	9.02	23.6	213.0	
acid (H_3BO_3) in 1.0 mol dm^{-3} potassium	10.03	45.0	203.0	
chloride, x cm^3 of 1.0 mol dm^{-3} sodium				
hydroxide and y cm^3 of 2.0 mol dm^{-3}				
potassium chloride diluted to 1.0 dm^3.				
Sodium Hydroxide/Potassium Chloride Solutions	12.00	6.0	244.0	
Contain x cm^3 of 2.0 mol dm^{-3} sodium	13.00	66.0	184.0	
hydroxide and y cm^3 of 2.0 mol dm^{-3}				
potassium chloride diluted to 1.0 dm^3.				

All chemicals were BDH Analar grade apart from di-sodium hydrogen orthophosphate which was Fisons A.R. grade. Doubly distilled water was used as diluent.

potentiostat.

Linear sweep and cyclic voltammograms were recorded by sweeping the electrode potential linearly between the potential limits, at sweep rates of between 25 mV s^{-1} and 500 mV s^{-1}, and recording the current response on a Houston 2000 XY chart recorder.

All voltammograms were recorded at 25°C unless indicated otherwise and, at least, in triplicate. Electrolytes were deoxygenated with nitrogen for an hour prior to measurements and the cell blanketed with the gas during measurements to prevent air ingress.

(b) Mercury Electrodes

In chloride containing electrolytes, the electrode potential was maintained at least 50 mV cathodic of the potential required for calomel formation. For example calomel formation occurred at about +0.1 V (vs. SCE) in aqueous 0.1 mol dm^{-3} hydrochloric acid.

(c) Rotating Disc Electrodes

The electrodes were wet polished to a mirror finish with 1 μm, 0.5 μm and 0.05 μm alumina, in turn, on polishing cloths. After rinsing with absolute alcohol and doubly distilled water, the electrodes were ultrasonicated to remove any remaining alumina particles. The remaining procedure was dependent upon the electrode metal.

1) Mercury Plated Copper

The electrode was placed in the cell but maintained at lest 50 mV cathodic of the potential required for calomel formation and/or copper corrosion, which was about -0.2 V (vs. SCE) in aqueous 0.1 mol dm^{-3} hydrochloric acid.

2) Lead

The electrode was immersed in aqueous 1.0 mol dm^{-3} nitric acid for 15

seconds to remove surface oxides, rinsed with doubly distilled water and transferred to the cell under deoxygenated, distilled water to exclude air from the disc surface, since an oxide film formed quickly which might have been stable even at the cathodic potentials required for hydrogen evolution [5]. The electrode was immediately set at a cathode potential which produced a current density for hydrogen evolution of about 100 A m^{-2} (typically ca. -1.5 V (vs. SCE) in aqueous 0.1 mol dm^{-3} hydrochloric acid), and the disc rotated at 50 Hz to prevent gas blinding. Once the current had steadied (ca. 10 minutes) voltammograms were recorded. The lead electrode was maintained 100 mV cathodic of the open circuit potential (typically ca. -0.5 V (vs. SCE) in aqueous 0.1 mol dm^{-3} hydrochloric acid) at which corrosion occurred. In aqueous chloride electrolytes this produced a passivating lead chloride film [6].

3) Other Electrodes

At the remaining electrodes (titanium, tin, vitreous carbon, carbon paste, zinc, stainless steel, cadmium, copper, nickel and molybdenum) a number of separate procedures were adopted when the electrode was placed in the cell. The electrode was immediately potentiostated at a cathode potential producing a current density for hydrogen evolution of about 100 A m^{-2} and, after a few minutes, voltammograms were recorded by initially sweeping the electrode potential anodically. In separate experiments the electrode was potentiostated at the open circuit potential and at least 50 mV cathodic of the open circuit potential and voltammograms were recorded by initially sweeping the electrode potential cathodically. Maintaining the electrodes cathodic of the open circuit potential allowed examination for L-cystine hydrochloride reduction activity free from the influence of possible corrosion processes at the open circuit potential.

(d) Instrumentation

Voltammograms at the dropping, static or hanging mercury drop electrode were recorded with an E. G. & G. PARC Model 174A polarographic analyser. At the stationary mercury disc and rotating disc electrodes a PARC Model 371 potentiostat/galvanostat (capable of delivering 1 A at 30 V maximum) or Model 363 potentiostat/galvanostat (7 A at 20 V maximum) was used. Potential sweep rates were controlled using a Thompson DRG 16 sweep generator. Rotating disc electrodes were rotated with an Oxford Electrodes rotating disc assembly.

(e) Testing of Equipment

The polarographic equipment was tested with an aqueous mixture of copper(II), lead(II) and cadmium(II) ions in aqueous 0.1 mol dm^{-3} nitric acid. $E_{\frac{1}{2}}$ values from sampled d.c. polarograms of -0.08 V, -0.40 V and -0.60 V (vs. SCE) respectively, agreed with the published literature [7].

The rotating disc equipment was tested using a platinum rotating disc electrode and the ferricyanide/ferrocyanide redox couple in aqueous 1.0 mol dm^{-3} potassium hydroxide. The diffusion coefficients of ferricyanide and ferrocyanide (see Section 2.3.4), determined from Levich plots, were in close accord with the published literature [3].

2.5.2 Coulometry at Mercury Plated Copper and Lead Electrodes

L-Cystine hydrochloride reduction was examined using coulometry. The electrodes were pretreated as described in Section 2.5.1(c) to obtain surfaces equivalent to those in the voltammetry experiments. The lead electrode was pretreated in the rotating disc electrode cell then, avoiding contact with air, transferred to the coulometry cell. Immediately upon contacting the electrolyte the electrodes were set at the cathode potential for the electrolysis and the electrode rotation rate fixed. During electrolysis the charge passed and electrolysis

time were recorded. At the end of an experiment, voltammograms were recorded and the catholyte was analysed for L-cystine hydrochloride and L-cysteine hydrochloride concentrations by high performance liquid chromatography (see Section 2.6). Electrolytes were deoxygenated with nitrogen prior to electrolysis and a steady stream of the gas was passed over the catholyte during measurements to prevent air ingress.

An E. G. & G. PARC Model 173 potentiostat/galvanostat (1 A at 100 V maximum) with an E. G. & G. PARC Model 179 digital coulometer as a plug in accessory was used.

2.5.3 Measurement of Electrolyte Properties

Solution viscosity was determined by standard U-tubes in a Gallencamp viscometer bath. Solution density was determined using density bottles. A Corning 150 pH/Ion Meter and Ingold pH electrode were used to measure solution pH. Experiments were thermostated using a Townson and Mercer water bath linked to the cells by plastic tubing or, for those cells without water jackets, by immersion in a Haake L water bath.

2.6 ANALYSIS FOR L-CYSTINE HYDROCHLORIDE AND L-CYSTEINE HYDROCHLORIDE BY HIGH PERFORMANCE LIQUID CHROMATOGRAPHY

2.6.1 Introduction

An analytical technique was required to determine the change in L-cystine hydrochloride and L-cysteine hydrochloride concentrations during electrolysis experiments, in both the coulometry cell and in a large batch reactor. A literature survey indicated only a few methods have been developed for the determination of low concentrations (i.e. < 1 ppm) of disulphide and thiol

mixtures. Almost all were based upon high performance liquid chromatography (HPLC) with a strong cation exchange resin and utilised post- or pre- column derivatisation (e.g. see [8]).

A new method was developed, which avoided the complication of derivitisation, based upon HPLC with ultra violet (U.V.) detection. The U.V. spectra [9] of the amino acids suggested L-cystine and L-cysteine could be monitored spectrophotometrically, albeit with low sensitivity (i.e. the molar extinction coefficients are small). Indeed the low sensitivity of the technique promised to avoid large dilution factors in the determination of amino acid concentrations in batch reactor electrolyses.

2.6.2 Equipment and Procedure

A Hewlett Packard HP 1090 Series M Liquid Chromatographs system with autoinjector, 1040A diode array U.V. detector and computer control was used. The diode array, with 211 photodiodes read every 10 milliseconds, allowed simultaneous monitoring of different detection wavelengths and simultaneous recording of chromatograms and U.V. spectra. Low signal to noise ratios were possible by signal averaging which enabled low absorbances to be used. Peak purity was readily determined by comparing U.V. spectra with those for a standard sample.

A highly polar bonded amino phase column, Spherisorb S5NH$_2$ (25 x 0.46 cm, 5 μm particle diameter) from Anachem Ltd., capable of operating in normal, reverse or as a weak anion exchange phase was used. The mobile phase was aqueous 0.05 mol dm^{-3} potassium dihydrogen orthophosphate buffer solution (adjusted with potassium hydroxide to pH 6) together with methanol in a 60:40 ratio by volume. The eluent was degassed with helium and a flow rate of 1 cm^3 minute^{-1} used. Prior to use, the column had to be equilibriated with mobile

phase overnight to achieve reproducible results. Standards, prepared as mixtures of L–cystine hydrochloride and L–cysteine hydrochloride to highlight any synergistic effect, and electrolysis samples were prepared for injection by dilution with aqueous 2.0 mol dm^{-3} hydrochloric acid as required. The autoinjector was programmed to deliver 5 μdm^3 and to duplicate all injections. Standards were injected after every 5 samples. The column temperature was 40°C and the pressure 127 x 10^5 N m^{-2}. L–Cystine was determined at a wavelength of 241 nm where there was an absorbance maximum and a low possible contribution from L–cysteine to the signal. At all wavelengths, L–cystine was a stronger absorber of U.V. light than L–cysteine. Consequently the thiol was detected at the sensitive wavelength of 210 nm.

All chemicals were BDH Analar grade apart from hydrochloric acid (BDH Aristar) and methanol (Rathburn Chemicals HPLC grade). Only high quality water from an Elgastat UHQ was used.

2.6.3 Chromatography and Calibration Graphs

A typical chromatogram corresponding to detection at a wavelength of 210 nm is shown in Figure 2.7. Separation of the amino acids on the column was achieved, with L–cysteine eluted with a retention time of 3.4 minutes followed by L–cystine after 3.9 minutes. The U.V. spectra (Figure 2.8) recorded at the peak tops of the chromatogram shown in Figure 2.7, confirmed pure L–cysteine and pure L–cystine were present at the respective peak tops. They agreed with both the published spectra of the amino acids [9], and spectra obtained by injecting the pure materials onto the column. The mechnaism of separation was presumably anion exchange although adsorption and partitioning may have been important.

At the adjacent peak bases in the chromatograms, U.V. spectra indicated both L–cystine and L–cysteine contributed to the absorbance. Peak heights rather than

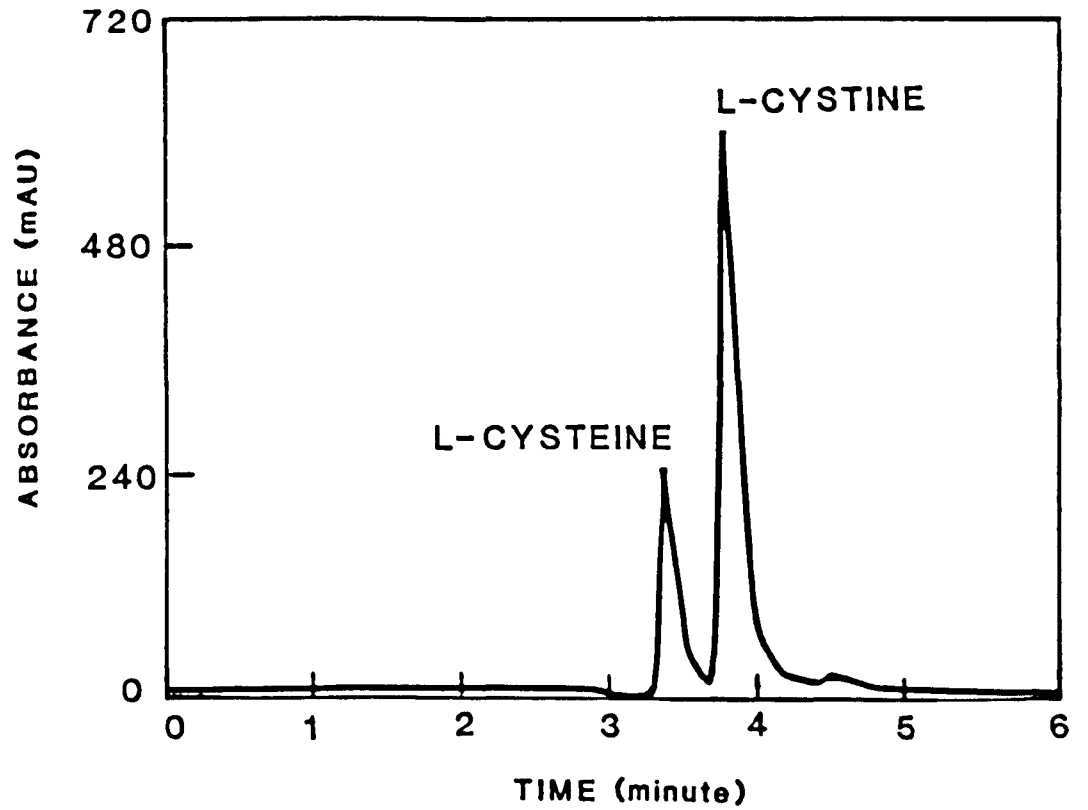

Solution	: Aqueous 25.0 mol m^{-3} L-cystine hydrochloride and 50.0 mol m^{-3} L-cysteine hydrochloride in 2.0 mol dm^{-3} HCl.
Column	: Spherisorb $S5NH_2$ (25 x 0.46 cm, 5 μm particle size) operated at 40°C and 127 x 10^5 N m^{-2}.
Eluent	: Aqueous 0.05 mol dm^{-3} $KHPO_4$ (pH 6; KOH)/CH_3OH in a ratio of 60:40 v/v.
Flow Rate	: 1 cm^3 $minute^{-1}$.
Detection	: U.V. at a wavelength of 210 nm.
Injection Volume	: 5 μdm^3.

FIGURE 2.7 Separation of L-cystine and L-cysteine by HPLC.

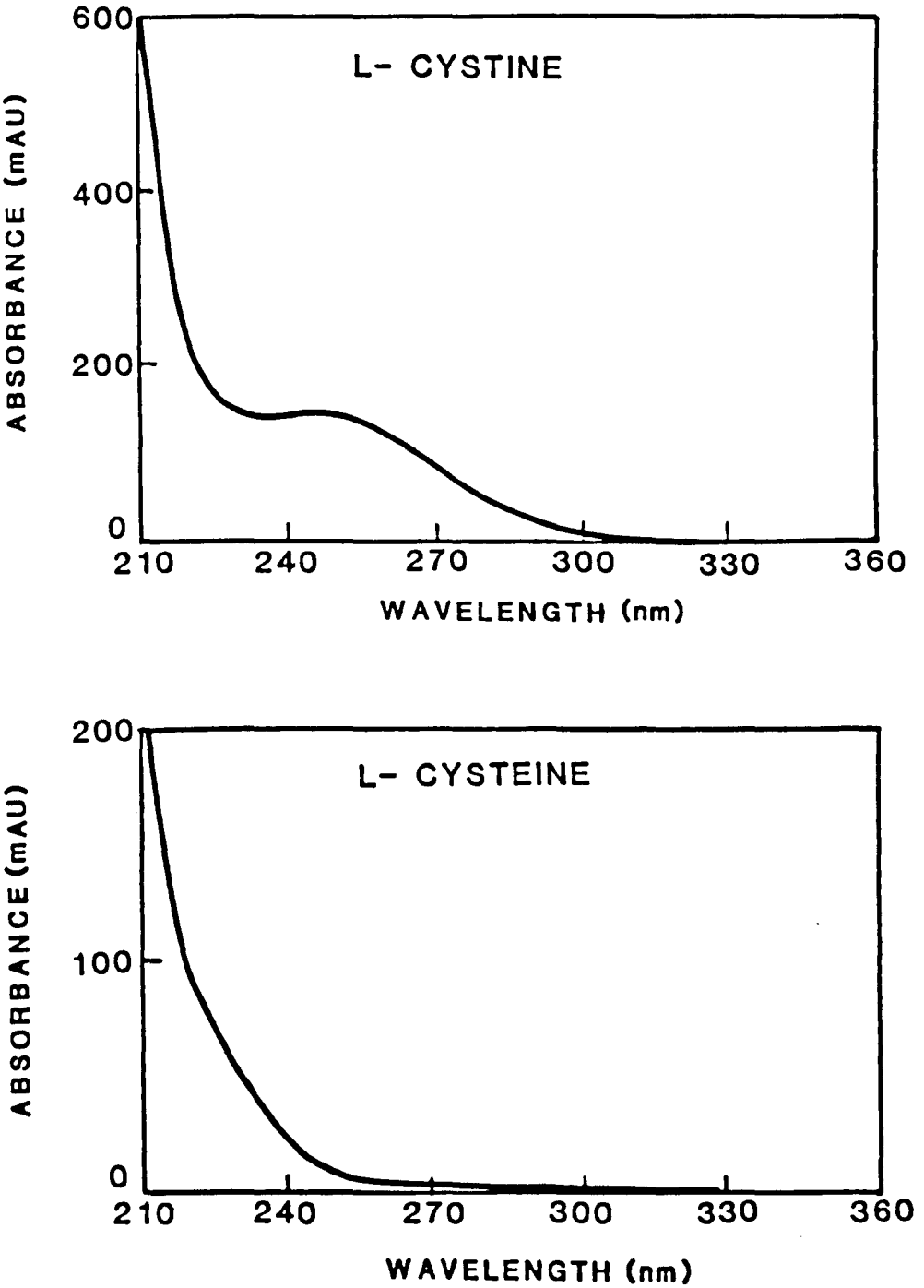

FIGURE 2.8 U.V. Spectra of L-cystine and L-cysteine recorded at the respective peak top of the chromatogram shown in Figure 2.7.

peak areas were consequently used to construct calibration graphs, from which the unknown amino acid concentrations were determined. Typical calibration graphs for L–cystine and L–cysteine are shown in Figure 2.9 and Figure 2.10 respectively. A slightly different linear response was obtained from day to day and with different columns. Correction was made for the absorbance of the mobile phase which was 2 mAU (absorbance units) at a wavelength of 210 nm and negligible at a wavelength of 241 nm. The sensitivity of the technique; defined as the concentration required to give 1% absorption (i.e. 4.4 mAU); was 0.85 mol m^{-3} (204 ppm) for L–cystine and 1.0 mol m^{-3} (121 ppm) for L–cysteine. The slopes of the calibration graphs i.e. 5.71 mAU/mol m^{-3} for L–cystine and 12.87 mAU/mol m^{-3} for L–cysteine highlighted the greater sensitivity of the technique for L–cysteine.

Although reproducible results were obtained, the analysis was problematical. Columns, even from the same batch, showed variable separating power and all took at least 12 hours to equilibriate. Most troublesome was the deterioration of column performance with complete loss of separation after, on average, only two weeks continuous use. Columns could not be rejuvenated and had to be replaced. The method is certainly not one which could be used routinely in an analytical laboratory.

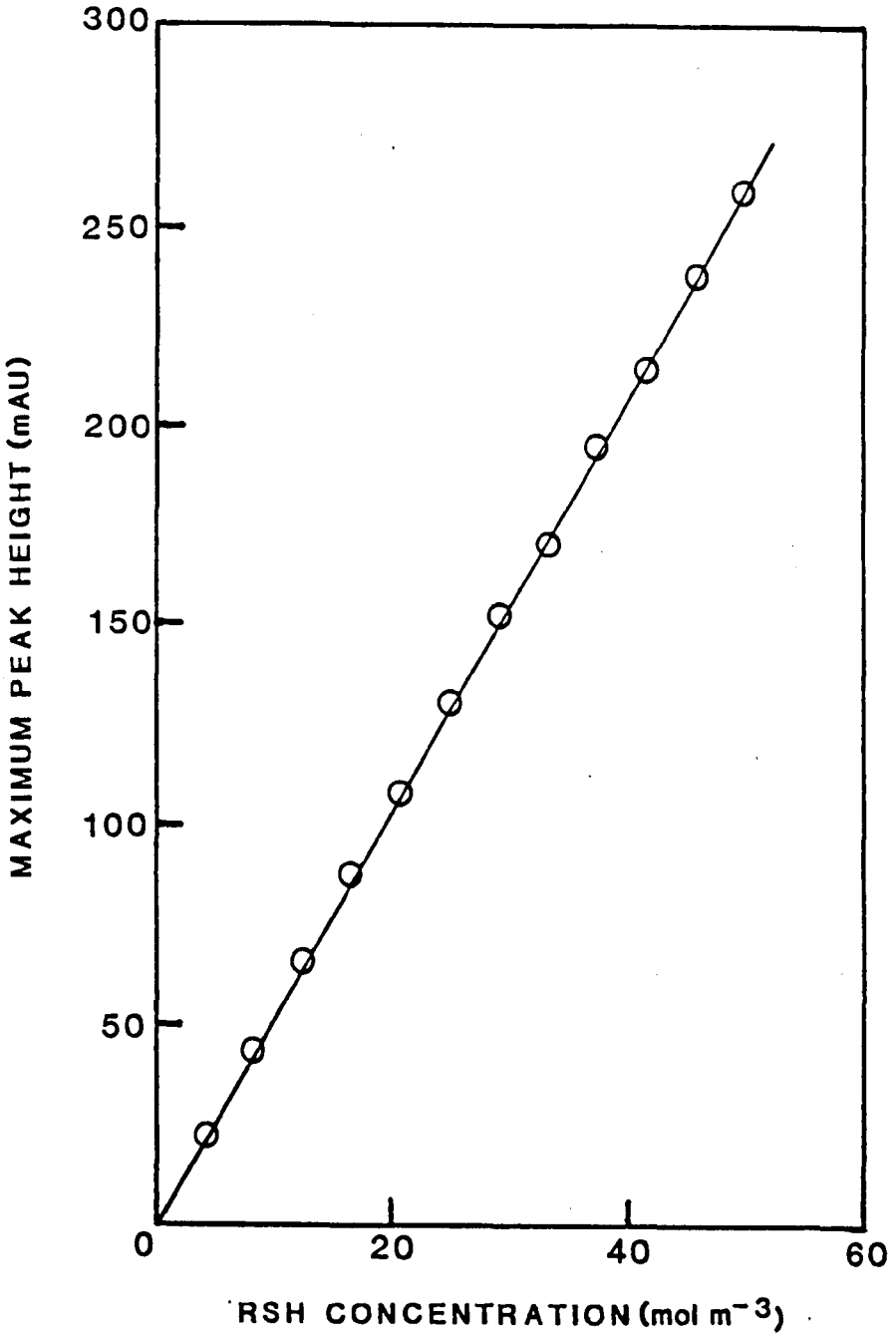

FIGURE 2.10 Calibration graph for L–cysteine with detection at a wavelength of 210 nm.

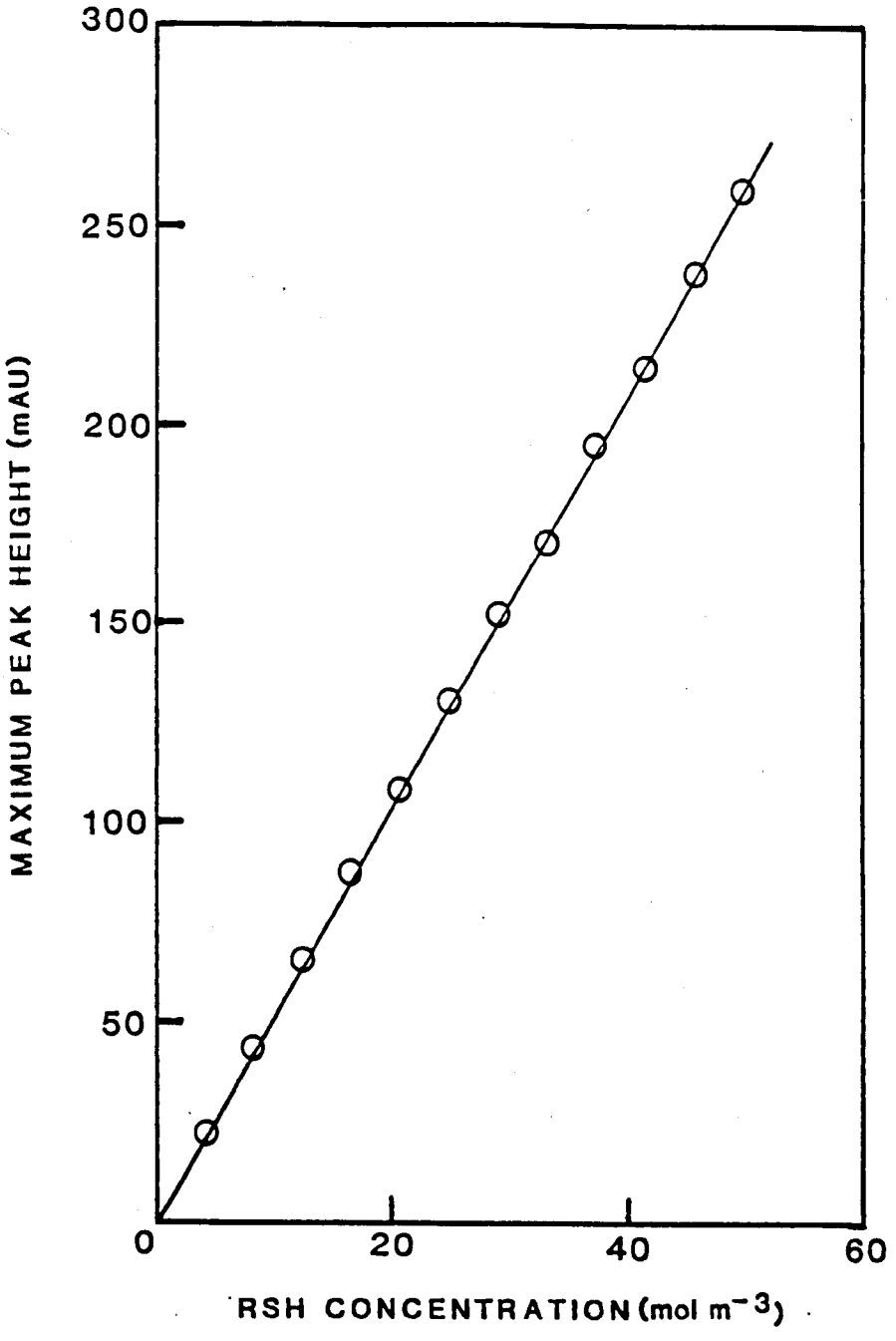

FIGURE 2.10 Calibration graph for L-cysteine with detection at a wavelength of 210 nm.

REFERENCES

1. Southampton Electrochemistry Group. "Instrumental Methods in Electrochemistry". Ellis Horwood Ltd., Chichester (1985). Chapter 4.

2. Daly P.J., Page D.J. & Compton R.G.; *Anal. Chem.* 55, 1191, (1983).

3. Ariva A.J., Marchiano S.L. & Podestá J.J.; *Electrochim. Acta* 12, 259, (1967).

4. Perrin D.D. & Dempsey B. "Buffers for pH and Metal Ion Control". Chapman and Hall Ltd., London (1974).

5. Kuhn A.T. in "Electrochemistry of Lead". Ed. Kuhn A.T., Academic Press, New York (1979). Chapter 14.

6. "Encyclopedia of Electrochemistry of the Elements". Ed. Bard A.J., Marcel Dekker, New York (1973). Vol. 1, pages 167, 250 and 404.

7. Hayes M. & Kuhn A.T. in "Electrochemistry of Lead". Ed. Kuhn A.T. Academic Press, New York (1979). Chapter 8.

8. Perrett D. in "Chemistry and Biochemistry of the Amino Acids". Ed. Barrett G.C., Chapman and Hall Ltd., London (1985). Chapter 15.

9. "Handbook of Biochemistry and Molecular Biology. Proteins". Ed. Fasman G.D., 3rd Edition, CRC Press Inc., Cleveland, Ohio (1976). Volume 1, pages 185, 186, 197 and 198.

CHAPTER 3

ELECTROCHEMICAL KINETICS AT MERCURY

3.1 INTRODUCTION

The available literature on L-cystine reduction at mercury (Section 1.4.2(a)) is restricted to conditions which are far from those used for the electrosynthesis of L-cystine hydrochloride. Reactant concentrations have been restricted to less than 0.4 mol m^{-3} and usually electrolytes other than aqueous hydrochloric acid have been used. Moreover, a comprehensive kinetic analysis is lacking. This chapter therefore examines the reduction under conditions more closely resembling those in the reactor and provides detailed kinetic information obtained from a variety of complementary techniques.

3.2 MERCURY PLATED COPPER RDE

Since the literature suggests mass transport of L-cystine hydrochloride is important and the plan is to examine the electrosynthesis in a batch reactor operating in the batch recycle mode, the RDE technique [1] was selected as a key method in the kinetic studies. Using this system not only can mass transport be varied in a controlled fashion but the transport rate can be calculated.

To enable the reduction to be studied at an RDE, a mercury plated copper RDE was prepared by the method of Daly et al [2]. There is always some concern over the purity of plated electrode surfaces. Both Daly et al [2] and Yoshida [2] suggested that electrode surfaces similar to those prepared in this study consisted of a mercury film, containing not more than 3 ppm copper, above a copper amalgam. After appoximately 24 hours, however, both authors observed dissolution of the mercury film in the underlying amalgam. Despite this evidence, two experiments were performed to determine whether the surface behaved essentially as a mercury film, or an amalgam, on the timescale of voltammetry ($<$ 30 minutes) and coulometry ($\leq$ 8 hours) experiments performed in this study.

3.2.1 Electrochemical Reduction of Fluorescein

At a fresh mercury plated surface the $E_{\frac{1}{2}}$ for the reversible reduction of fluorescein to semi-fluorescein (reaction 3.01) in aqueous 0.1 mol dm^{-3} sodium hydroxide was measured as −1.175 V (vs. SCE) in close accord with the $E_{\frac{1}{2}}$ of −1.168 V (vs. SCE) measured at a DME [2].

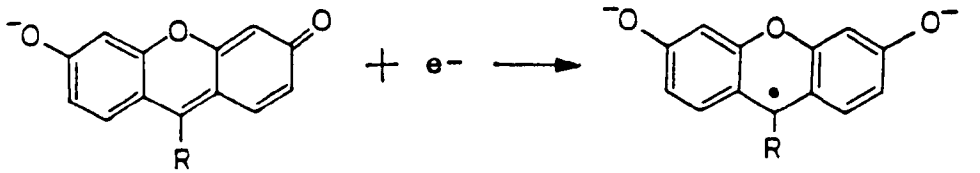

(3.01)

Fluorescein **Semi-fluorescein**

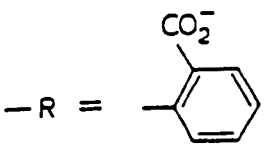

Further confirmation of a satisfactory mercury surface is provided by the accurate limiting currents obtained. From a Levich plot (Figure 3.1), using equation (3.02) for complete mass transport control at an RDE, the diffusion coefficient of fluorescein was measured as 3.0×10^{-10} m^2 s^{-1} in close agreement with the 3.2×10^{-10} $m^2 s^{-1}$ found using a channel electrode [4].

$$i_L = 0.62\ n\ F\ D^{2/3} \nu^{-1/6} c_b\ \omega^{1/2} \qquad (3.02)$$

where i_L is the limiting current density (A m^{-2}), n the number of electrons transferred per fluorescein molecule (n = 1), D is the diffusion coefficient of fluorescein (m^2 s^{-1}), ν the kinematic viscosity of the electrolyte (1.08×10^{-6} m^2 s^{-1} [5]), c_b the bulk concentration of fluorescein (5 mol m^{-3}) and ω the rotation rate of the electrode (s^{-1}).

Significantly there was no evidence of amalgam formation after 8 hours, which was the maximum time required for coulometry experiments. The mercury plated

copper RDE gave an unchanged $E_{\frac{1}{2}}$ for fluorescein reduction and an identical diffusion coefficient for the organic in the electrolyte.

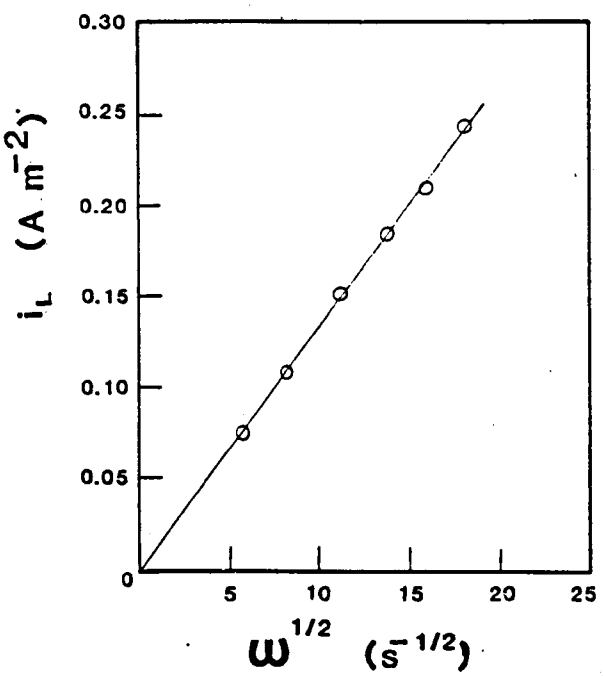

FIGURE 3.1 Levich plot for the reduction of fluorescein at a mercury plated copper RDE.

3.2.2 Hydrogen Evolution

The cathodic potential limit for hydrogen evolution from aqueous 0.1 mol dm^{-3} hydrochloric acid was measured. At a freshly plated surface a current density of 0.010 A m^{-2} at - 1.0 V (vs. SCE) was recorded. This is very close to the 0.008 A m^{-2} at the same potential recorded with a HMDE in this study. After 8 hours standing the current density at the plated electrode increased but only to 0.013 A m^{-2} at - 1.0 V (vs. SCE). It is likely that the electrodes prepared represent the optimum achievable by this method, in terms of hydrogen overpotential. Yoshida [3] noted that above 0.1 mg cm^{-2} of deposited mercury,

the hydrogen overpotential of the electrode is not improved. Around 150 mg cm^{-2} of mercury is deposited on the copper base metal in this study, and although some of this is wiped off with a tissue, there is well in excess of 0.1 mg cm^{-2} left on the surface.

3.2.3 Conclusions

All the evidence suggests that, on the timescale of both voltammetry and coulometry experiments, the surface is a mercury film and not an amalgam. After a period of 8 hours, there may be some increase in the copper concentration of the film but this effect does not greatly alter the hydrogen overpotential of the electrode. This is important to studies of L-cystine reduction in aqueous hydrochloric acid, where a major secondary reaction is hydrogen evolution.

The L-cystine/L-cysteine system differs from the above two reactions in one important respect. There is strong interaction between the amino acids and mercury (e.g. see Section 1.4.2(a)). Consequently a stationary mercury disc electrode of similar area to the RDE was prepared, to check the performance for the reduction of L-cystine hydrochloride. Figure 3.2 shows the main wave in linear sweep voltammograms for the reduction of dissolved L-cystine hydrochloride to L-cysteine hydrochloride in aqueous 0.1 mol dm^{-3} hydrochloric acid, at both the mercury plated copper and stationary mercury disc electrodes. Both the peak potential and peak current is unchanged at the two electrodes. This confirms that data recorded at the plated electrode is reliable for the electrosynthesis reaction.

3.3 ELECTROLYTE RESISTANCE AND THE KINETIC STUDIES

Often in kinetic studies it is necessary to correct the electrode potential for the electrolyte resistance between the tip of the luggin capillary and the working electrode. In this study, the resultant voltage drop is negligible and can be

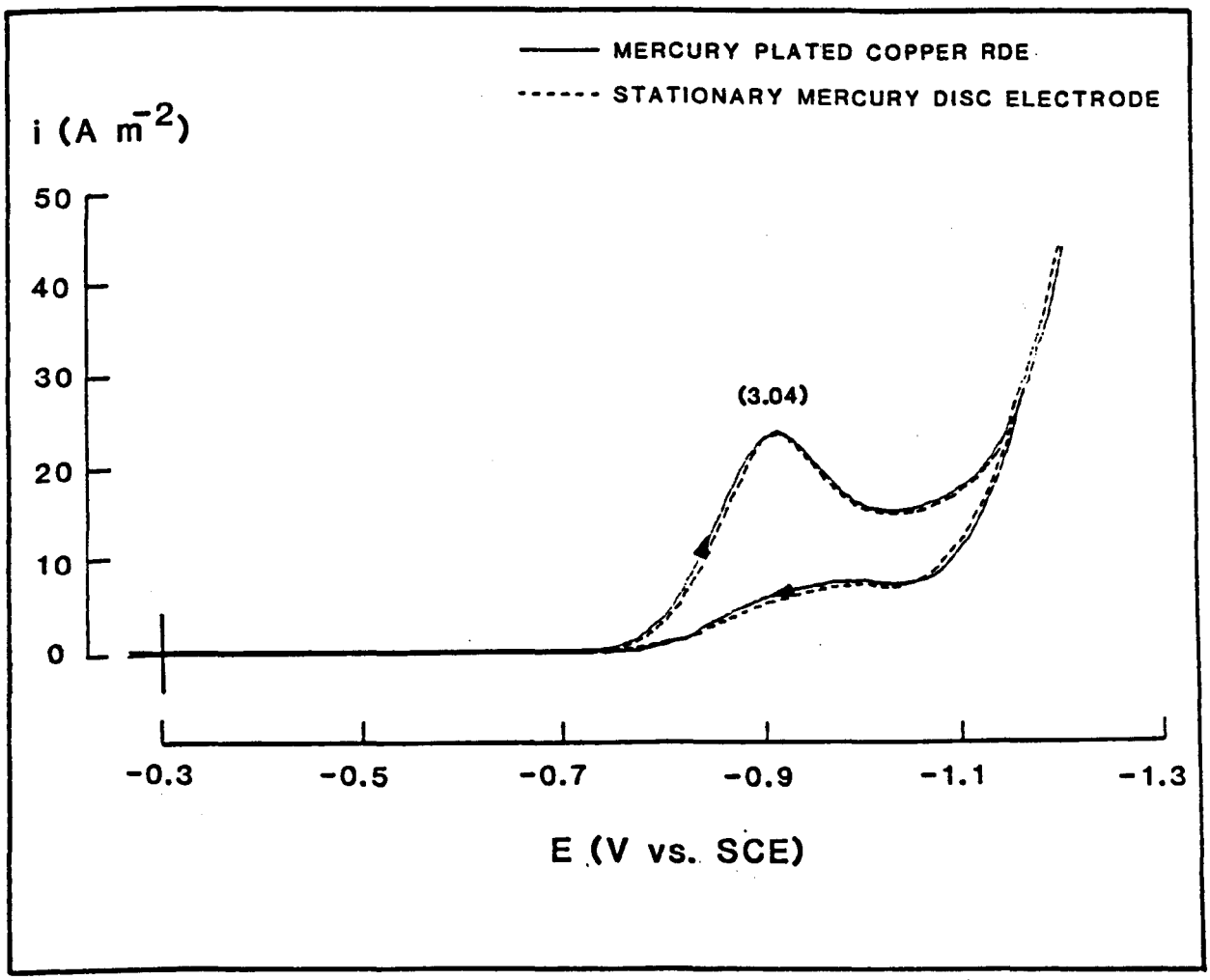

FIGURE 3.2 Cyclic voltammogram of 10 mol m^{-3} L-cystine hydrochloride in aqueous 0.1 mol dm^{-3} HCl at a mercury plated copper RDE and a stationary mercury disc electrode. Potential sweep rate 100 mV s^{-1}. Temperature 25°C. Electrolyte deoxygenated with N_2.

neglected. The electrolyte resistance was not measured, but an estimate of the maximum theoretical voltage drop in the glass cells used shows the minimal effect (Table 3.1).

The maximum theoretical voltage drop in Table 3.1 is calculated for the highest current encountered in the kinetic studies, performed in the least conductive hydrochloric acid electrolyte used (i.e. 0.1 mol dm^{-3}). For the RDE, stationary mercury disc and coulometry cells it is assumed the luggin capillary is the optimum 2d [6] from the working electrode surface where d is the outer diameter of the luggin capillary tip. Barnartt [7] has shown under such conditions the theoretical voltage drop is given by equation (3.03):

$$V_{DROP} = \frac{I\ (s/3.d)}{\kappa} = I\ R_{ELECTROLYTE} \qquad (3.03)$$

where κ is the specific conductivity of the electrolyte (0.039 $\Omega^{-1}\ cm^{-1}$ for aqueous 0.1 mol dm^{-3} hydrochloric acid [8]). To calculate the voltage drop in the mercury drop cell the 5/3d term in equation (3.03) was replaced by the distance between the reference and working electrodes (i.e. 1 cm) and a cross-sectional area for current flow of 1 cm^2 assumed.

3.4 CONSTANT POTENTIAL COULOMETRY AND L-CYSTINE HYDROCHLORIDE REDUCTION AT A MERCURY PLATED COPPER RDE

3.4.1 Examination of the Electrosynthesis Conditions

Concentrations of disulphide approaching those used in the electrosynthesis were problematical. Highly negative potentials (> -1.2 V vs. SCE) are required to achieve reasonable rates of reduction. At these negative potentials, however, rates of reduction are variable and current efficiencies no better than 80%. This

TABLE 3.1 Maximum theoretical voltage drop in glass cells used in the kinetic studies.

Cell	d (cm)	Electrolyte Resistance (Ω)	Maximum Current (mA)	Voltage Drop (mV)
RDE	0.024	1	5 3	5 (Polarisation curves) 3 (Linear sweep voltammograms)
Stationary Mercury Disc	0.027	1	5	5 (Linear sweep voltammograms)
Coulometry	0.1	4	8	16 (This error will fall as the current decays during electrolysis)
Mercury Drop	Not Applicable	26	5×10^{-3}	< 1

d is the outer diameter of the luggin capillary tip, measured using a micrometer gauge.

is most probably an effect of adsorption of the amino acids at the mercury surface. Figure 3.22 shows the large adsorption effects that the highest disulphide concentrations examined at a mercury drop, produce in voltammograms.

At much lower disulphide concentrations (e.g. 10 mol m^{-3}) in aqueous 2.0 mol dm^{-3} hydrochloric acid these effects are not observed. Not even an inflection is obtained, however, in steady state voltammograms at the mercury plated copper RDE. Constant potential coulometry at potentials on the voltammogram capable of giving acceptable reduction rates confirmed significant levels of hydrogen evolution. Current efficiencies are below 50% for L-cystine hydrochloride reduction. Consequently neither n nor the diffusion coefficient of L-cystine hydrochloride can be determined in aqueous 2.0 mol dm^{-3} hydrochloric acid.

3.4.2 Determination of n and the Reaction Order for L-Cystine Hydrochloride

In aqueous 0.1 mol dm^{-3} hydrochloric acid at the mercury plated copper RDE a large electrochemically irreversible wave is evident for the electrosynthesis reaction (reaction 3.04)

$$RSSR.2HCl + 2H^{+} + 2e^{-} \longrightarrow 2\ RSH.HCl \qquad (3.04)$$

Figure 3.3 shows the wave for 10 mol m^{-3} L-cystine hydrochloride at various electrode rotation rates. This disulphide concentration represents the experimentally determined solubility limit in aqueous 0.1 mol dm^{-3} hydrochloric acid. At electrode potentials which are more positive than - 0.7 V (vs. SCE) the rate of the reduction reaction is controlled completely by the kinetics of electron transfer. The current is therefore independent of the electrode rotation rate. At more negative electrode potentials there is an extensive region of mixed

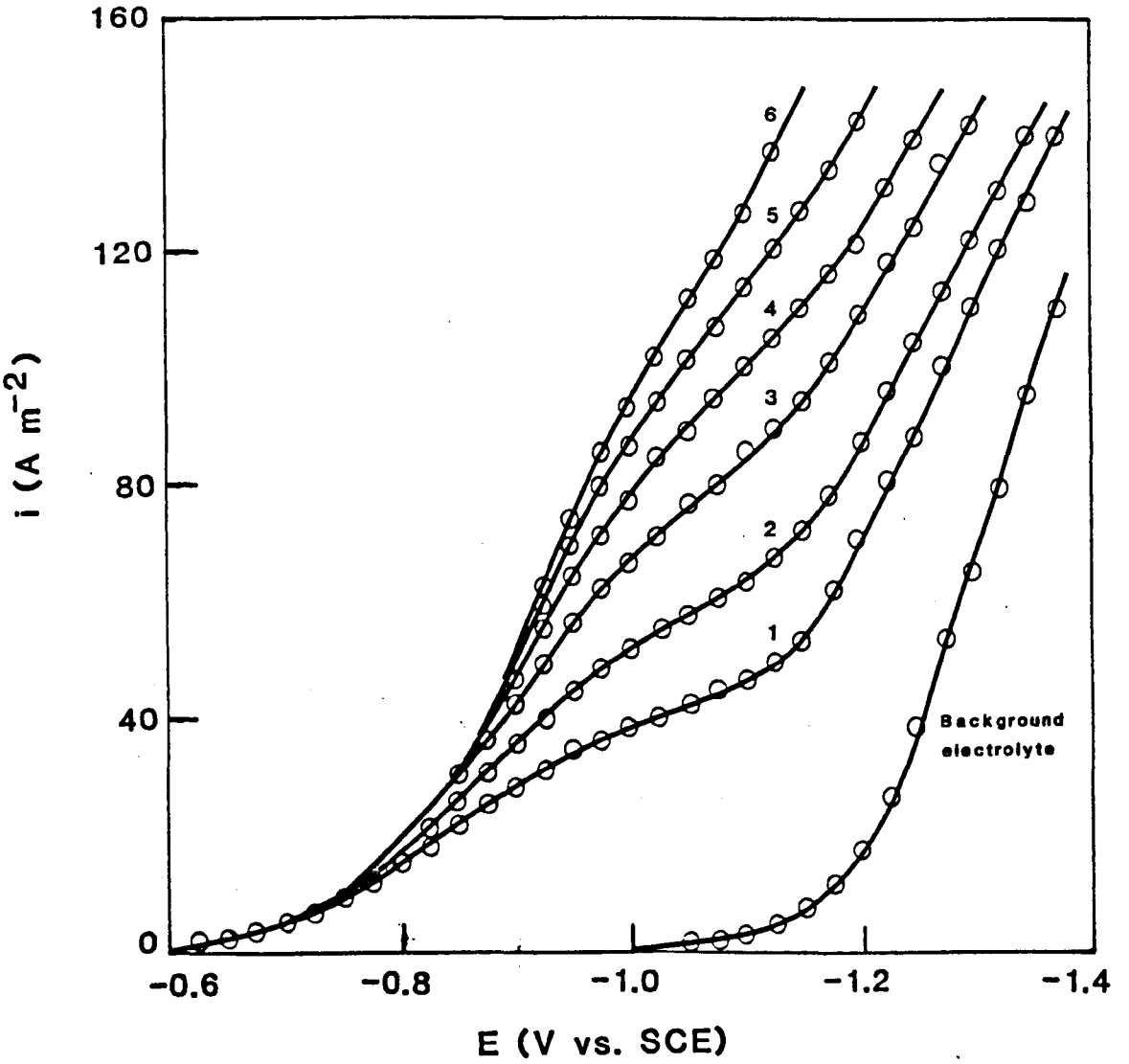

FIGURE 3.3 Steady state voltammograms of 10 mol m^{-3} L-cystine hydrochloride in aqueous 0.1 mol dm^{-3} HCl at a mercury plated copper RDE. Electrolyte deoxygenated with N_2. Temperature 25°C. Electrode rotation rates 1. 5 Hz 2. 10 Hz 3. 20 Hz 4. 30 Hz 5. 40 Hz and 6. 50 Hz.

kinetic–mass transport control. At values more negative than – 1.1 V (vs. SCE), an apparent convective–diffusion limited current is hidden by simultaneous hydrogen evolution from the background electrolyte. Plateau definition is increasingly lost at higher electrode rotation rates due to an extension of the mixed control region to progressively more negative potentials. This is a well established effect at an RDE for electrochemically irreversible systems [9].

Constant potential coulometry at the mercury plated copper RDE was performed with 10 mol m^{-3} L–cystine hydrochloride in aqueous 0.1 mol dm^{-3} hydrochloric acid. A cathode potential of –0.950 V (vs. SCE) and an electrode rotation rate of 50 Hz (to maximise the rate of reduction) was selected. Figure 3.3 suggests that the current efficiency for L–cystine hydrochloride reduction at this cathode potential should be 100%. Under these conditions, with a constant volume system, from Faraday's Laws

$$n = \frac{q}{\Delta c_t F V} \qquad (3.05)$$

where n is the number of electrons transferred in the overall electrode reaction, q is the charge passed, Δc_t is the change in bulk reactant concentration during electrolysis and V the electrolyte volume. Measurement of q and Δc_t thus provides a value for n and, indeed, this is the most frequently used technique for evaluating n. Table 3.2 shows values for q and Δc_t in addition to the concentration of L–cysteine hydrochloride produced for several disulphide electrolyses. Both reactant and product concentrations were determined by HPLC analysis. All electrolyses show the value for n is 2 in agreement with electrode reaction (3.04). In addition, the concentrations of reactant and product confirm 1 mol of disulphide is converted into 2 mol of thiol, within the confines of experimental error, again in agreement with electrode reaction (3.04). There is

no evidence for significant levels of alternative products.

TABLE 3.2 Constant potential coulometry at −0.950 V (vs.SCE) at a mercury plated copper RDE.

t (minute)	q (C)	RSSR.2HCl (mol m^{-3})	RSH.HCl (mol m^{-3})	Δc_t (RSSR.2HCl) (mol m^{-3})	n
0	0	10.0	0	0	-
63	3.412	9.3	1.4	0.7	2.02
129	6.862	8.6	2.7	1.4	2.03
186	9.313	8.1	3.9	1.9	2.01
288	13.741	7.2	5.7	2.8	2.04
381	17.011	6.5	6.9	3.5	2.02
480	20.662	5.8	8.4	4.2	2.04

It is also possible to determine the reaction order for L-cystine hydrochloride from the coulometry in the mixed control region, assuming the rate of hydrogen evolution is independent of the amino acid concentrations. For a first order reaction which is under mixed kinetic-mass transport control at an RDE [9]:

$$i = n F K_L (c_b - c^o) \qquad (3.06)$$

where K_L is the average mass transport coefficient, c_b the bulk and c^o the surface reactant concentration.

Since the diffusion limited current density is given by

$$i_L = n F K_L c_b \qquad (3.07)$$

equation (3.06) becomes

$$i = i_L - n F K_L c^o$$

or rearranging

$$\frac{c^o}{c_b} = \left(1 - \frac{i}{i_L} \right) \qquad (3.08)$$

Also for an electrochemically irreversible reaction the back reaction can be ignored since the electrode potential is relatively far from $E^{o'}$ and for first order kinetics [10]:

$$i = n F k_f c^o \qquad (3.09)$$

where k_f is the potential dependent, heterogeneous rate constant for electron transfer. This is given by [10]:

$$k_f = k_f^o \exp \left(- \frac{\alpha_c F}{RT} E \right) \qquad (3.10)$$

where k_f^o is the value of k_f at zero volts with respect to the reference electrode used, α_c is an empirical parameter called the transfer coefficient and E is the electrode potential.

Substituting for c^o from equation (3.08) into equation (3.09) gives

$$i = n F k_f c_b \left(1 - \frac{i}{i_L} \right) = i_k \left(1 - \frac{i}{i_L} \right) \qquad (3.11)$$

where i_k is the kinetic current density, which is a constant at a given electrode potential.

Rearranging equation (3.11) gives

$$\frac{1}{i} = \frac{1}{i_k} + \frac{1}{i_L} \qquad (3.12)$$

Now from equation (3.05)

$$- dc_t = \frac{q}{nFV} = \frac{I\,dt}{nFV} \qquad (3.13)$$

Substituting for i from equation (3.12) into equation (3.13) gives

$$- dc_t = \frac{\left[\frac{1}{I_k} + \frac{1}{I_L}\right]^{-1}_{t} dt}{nFV} \qquad (3.14)$$

Substituting into equation (3.14) using i_k from equation (3.11) and for i_L from equation (3.07) and rearranging gives

$$\frac{- dc_t}{c_b} = \frac{k_f K_L A}{(k_f + K_L)V} \cdot dt \qquad (3.15)$$

Integrating equation (3.15) with the boundary conditions

$t = 0$ and $t = t$

$c_b = c_o$ and $c_b = c_t$

gives

$$c_t = c_o \exp\left(-\frac{k_f K_L A}{(k_f + K_L) V} \cdot t\right) \qquad (3.16)$$

Taking natural logarithms

$$\ln c_t = \ln c_o - \frac{k_f K_L A}{(k_f + K_L)V} \cdot t \qquad (3.17)$$

Based upon equation (3.17) if the electrode reaction is first order in the reactant a plot of ln c_t against t should be a straight line with a slope dependent upon k_f and K_L. Figure 3.4 shows that between concentrations of 1.7 mol m^{-3} and 10 mol m^{-3} L-cystine hydrochloride the reduction is indeed first order with respect to the disulphide concentration. Disulphide concentrations below 1 mol m^{-3} were not examined since they are too close to the sensitivity limit of the HPLC technique (i.e. 0.85 mol m^{-3}). In any case these lower concentrations are even further removed from the electrosynthesis conditions.

3.4.3 Mass Transport Control and Determination of the Diffusion Coefficient of the Disulphide

A second series of constant potential electrolyses were peformed at -1.150 V (vs. SCE) with an electrode rotation rate of 5 Hz. Figure 3.3 shows under these conditions L-cystine hydrochloride reduction may be under complete mass transport control but this cannot be distinguished because of simultaneous hydrogen evolution. Assuming all current losses are due to hydrogen evolution and the current for this secondary reaction is independnent of the L-cystine hydrochloride and L-cysteine hydrochloride concentrations during electrolysis then from equation (3.12):

$$-dc_t = \frac{q_{(RSSR.\,2HCl)}}{nFV} = \frac{I_{L,t}\,dt}{nFV} \qquad (3.18)$$

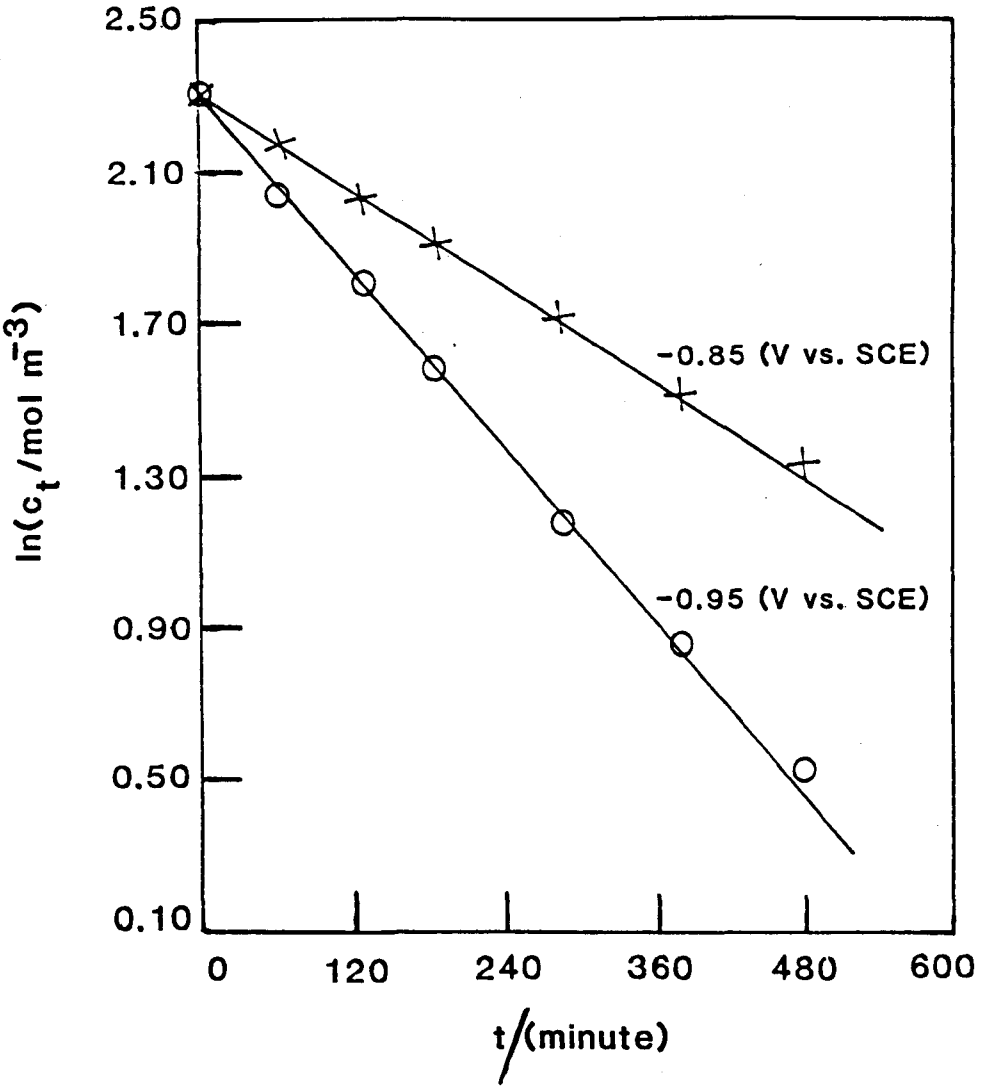

FIGURE 3.4 Dependence of ln c_t on time for L-cystine hydrochloride reduction occurring under mixed control at a mercury plated copper RDE. Rotation rate 50 Hz. The background electrolyte is aqueous 0.1 mol dm^{-3} HCl deoxygenated with N_2. Temperature 25°C.

For the RDE, the time dependent diffusion limited current density, (due to convective-diffusion) is given by equation (3.05). Substituting for $i_{L,t}$ from equation (3.07) into equation (3.18) gives

$$\frac{-dc_t}{c_b} = \frac{K_L A}{V} \cdot dt \qquad (3.19)$$

Integrating equation (3.19) with the boundary conditions

$t = 0$ and $t = t$

$c_b = c_o$ and $c_b = c_t$

gives

$$c_t = c_o \exp\left(-\frac{K_L A}{V} \cdot t\right) \qquad (3.20)$$

Taking natural logarithms

$$\ln c_t = \ln c_o - \frac{K_L A}{V} \cdot t \qquad (3.21)$$

Thus if L-cystine hydrochloride reduction is under complete mass transport control a plot of $\ln c_t$ against t should be a straight line with a slope of $K_L A/V$. Additionally for an RDE [11]

$$K_L = 0.62\, D^{2/3}\, \nu^{-1/6}\, \omega^{1/2} \qquad (3.22)$$

where D is the diffusion coefficient of the reactant, ν is the kinematic visocity of

the electrolyte and ω is the electrode rotation rate calculated using the formula $\omega = 2\pi f$ where f is the rotation rate in Hz, to give units of s^{-1}. Using equation (3.22) it is possible to determine the diffusion coefficient of the reactant from the slope of the ln c_t against t graph. This method has the particular advantage that neither n nor c_b are required (in contrast with voltammetric techniques), a fact which has been noted by Hitchman and Albery [12].

Figure 3.5 shows that a plot of ln c_t against t for L-cystine hydrochloride reduction at -1.150 V (vs. SCE) is indeed a straight line.

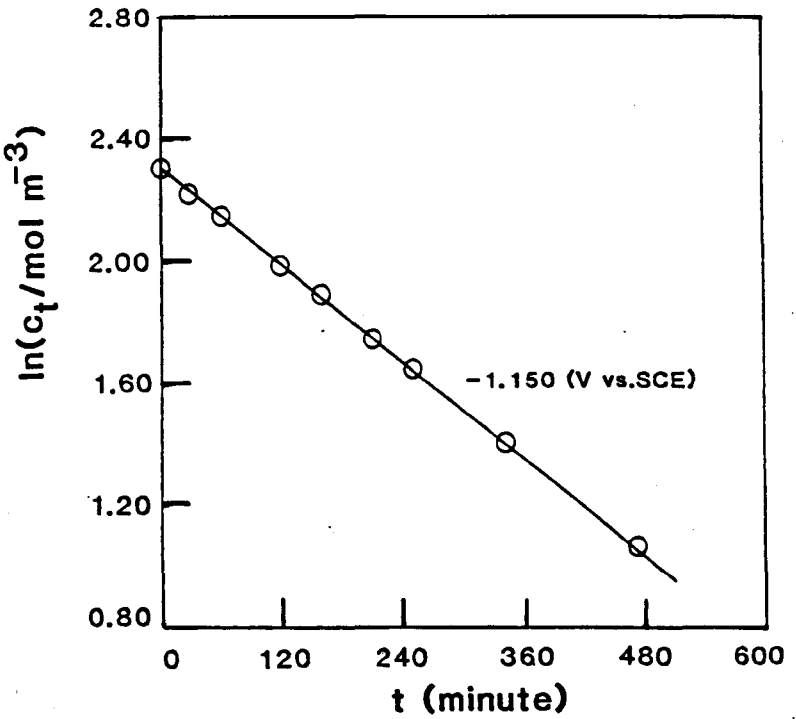

FIGURE 3.5 Dependence of ln c_t on time for complete mass transport controlled reduction of L-cystine hydrochloride at a mercury plated copper RDE. Rotation rate 5 Hz. The background electrolyte is aqueous 0.1 mol dm^{-3} HCl oxygenated with N_2. Temperature 25°C.

The determination of the diffusion coefficient of L-cystine hydrochloride from the slope of Figure 3.5 requires an accurate value for the kinematic viscosity

(dynamic viscosity/density) of the electrolyte as shown by equations (3.21) and (3.22). This was determined experimentally by measuring the solution density, using density bottles, and the dynamic viscosity in a viscometer bath (see Section 2.5.3). Table 3.3 lists the measured physical properties of several electrolytes of importance to the kinetic studies. The kinematic viscosity of aqueous 0.1 mol dm^{-3} hydrochloric acid was compared with available literature [13,14] to check the accuracy of the measured data. Figure 3.6, constructed from reference [13], gives a solution density of 998.8 kg m^{-3}. Note that although strictly not justified, the quoted density requires only a short extrapolation. From reference [14] the dynamic viscosity of aqueous 0.1 mol dm^{-3} hydrochloric acid is 1.007 ± 0.003 which from the listed dynamic viscosity of water (i.e. 8.949 x 10^{-4} kg m^{-1} s^{-1}) gives the viscosity of the acid as 9.012 x 10^{-4} kg m^{-1} s^{-1} at 25°C. The literature kinematic viscosity is therefore 9.0 x 10^{-7} m^2 s^{-1} in complete accord with Table 3.3.

Using the kinematic viscosity of 10 mol m^{-3} L-cystine hydrochloride in aqueous 0.1 mol dm^{-3} hydrochloric acid from Table 3.2 the diffusion coefficient of the disulphide is (4.85 ± 0.05) x 10^{-10} m^2 s^{-1} at 25°C. The error reflects the error of the slope in Figure 3.5 which is obtained from a least squares analysis. Agreement of this diffusion coefficient with the available literature values of 4.8 x 10^{-10} m^2 s^{-1} [15] and 5.3 x 10^{-10} m^2 s^{-1} [16] confirm pure mass transport control of the reduction at highly negative potentials.

TABLE 3.3 Measured physical properties of electrolytes at 25°C.

Solution	ρ (10^3 kg m^{-3})	μ (10^{-4} Kg m^{-1} s^{-1})	ν (10^{-7} m^2 s^{-1})
0.1 mol dm^{-3} HCl	1.000	9.0	9.0
10 mol m^{-3} RSSR.2HCl in 0.1 mol dm^{-3} HCl	1.010	9.2	9.1
2.0 mol dm^{-3} HCl	1.033	9.5	9.2
10 mol m^{-3} RSSR.2HCl in 2.0 mol dm^{-3} HCl	1.037	9.75	9.4

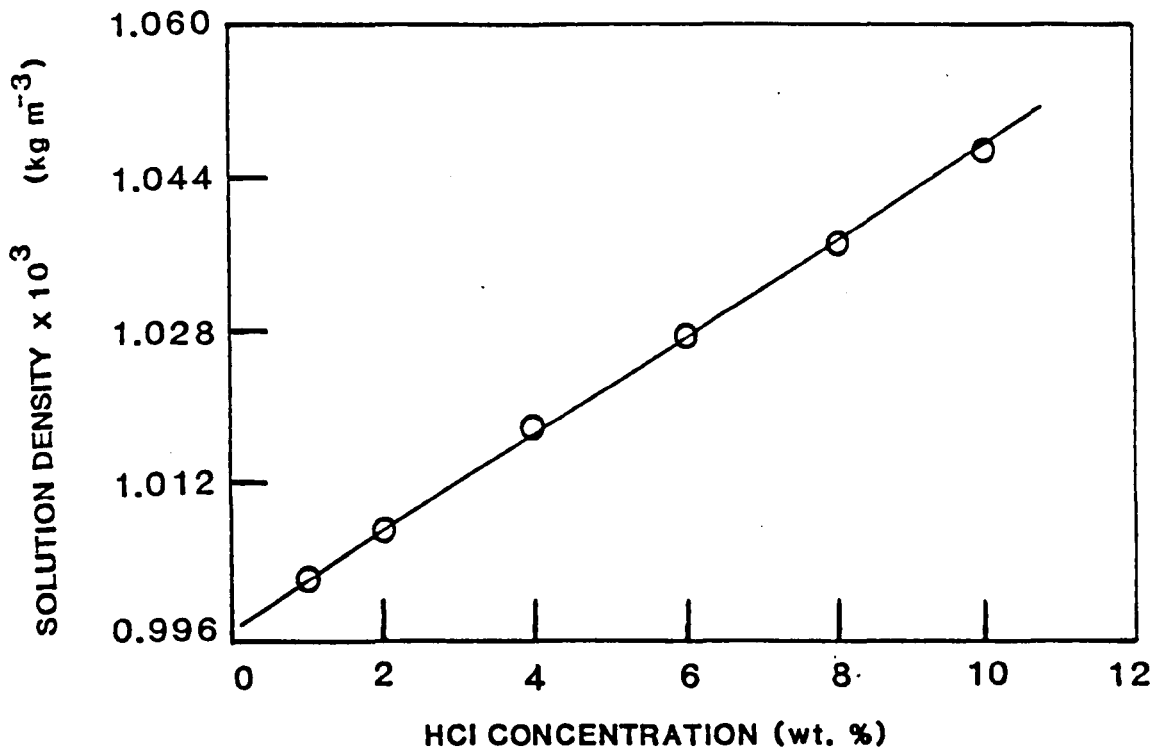

FIGURE 3.6 Dependence of solution density on HCl concentration at 25°C [13].

3.5 ANALYSIS OF THE STEADY STATE VOLTAMMOGRAMS FOR L-CYSTINE HYDROCHLORIDE REDUCTION AT A MERCURY PLATED COPPER RDE

The electrochemically irreversible waves due to L-cystine hydrochloride reduction, shown in Figure 3.3, can be analysed to obtain the important electrochemical kinetic parameters associated with electron transfer. For a first order reaction at those potentials where the reaction is under mixed kinetic-mass transport control

$$\frac{1}{i} = \frac{1}{i_k} + \frac{1}{i_L} \qquad (3.12)$$

Using equations (3.07) and (3.22) for i_L at the RDE and equation (3.11) for i_K this becomes

$$\frac{1}{i} = \frac{1}{nFk_f c_b} + \frac{1}{0.62n\ F\ D^{2/3}\ \nu^{-1/6}\ c_b\ \omega^{1/2}} \qquad (3.23)$$

Thus at a constant potential a plot of 1/i against $1/(\omega)^{\frac{1}{2}}$, which is often referred to as a Koutecky-Levich plot, is a straight line. The intercept (extrapolation of $\omega^{\frac{1}{2}} \longrightarrow \infty$ to yield $1/i_K$) gives the kinetic current and therefore the heterogeneous rate constant for electron transfer at the selected potential. The slope allows determination of the diffusion coefficient of the reactant, although this requires a knowledge of n and c_b. Figure 3.7 shows that at a range of electrode potentials, in the mixed control region of the irreversible waves in Figure 3.3, plots of 1/i against $1/(\omega)^{\frac{1}{2}}$ give, as predicted, a series of parallel straight lines. From the intercepts, k_f is calculated to increase from 2.4 x 10^{-5} m s^{-1} at -0.850 V (vs.

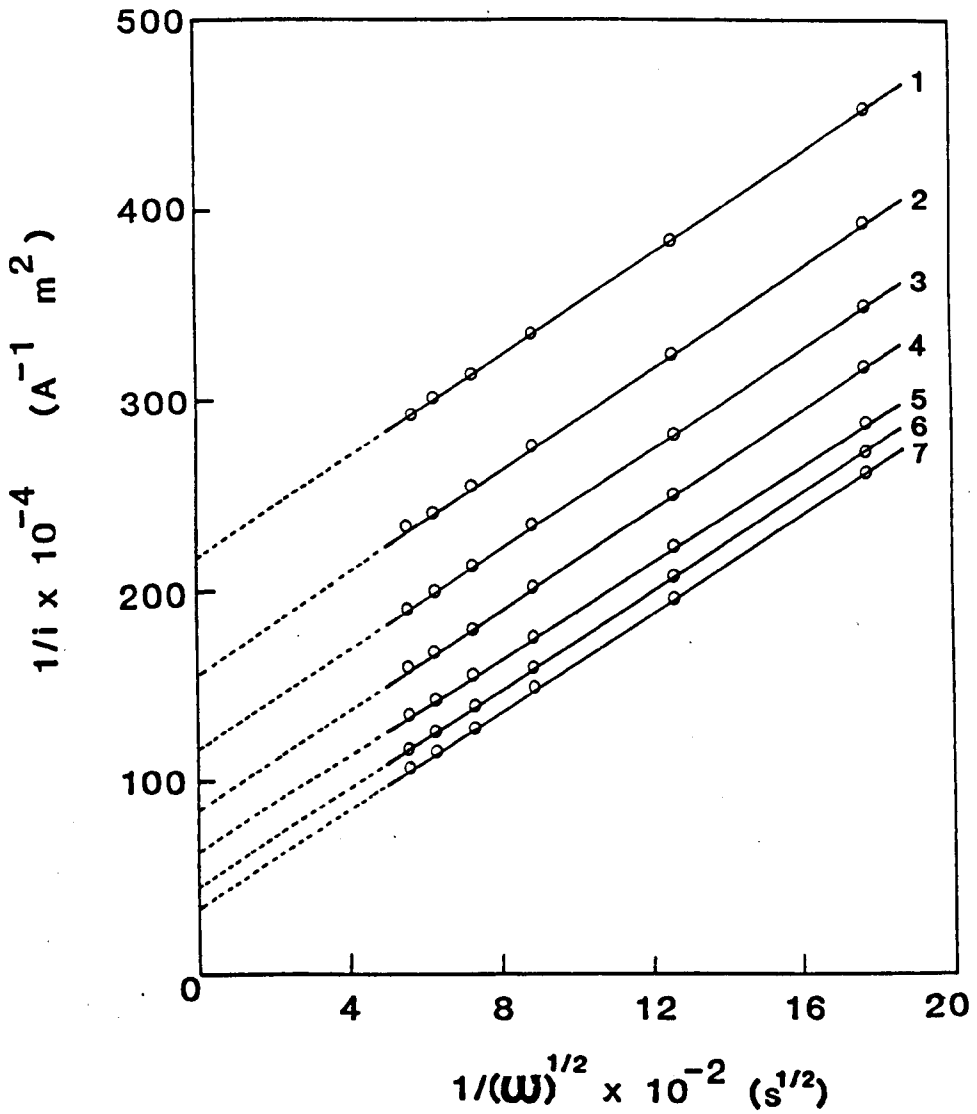

FIGURE 3.7 Plot of 1/i against $1/(\omega)^{\frac{1}{2}}$ for L-cystine hydrochloride reduction at a mercury plated copper RDE. 10 mol m^{-3} L-cystine hydrochloride in aqueous 0.1 mol md^{-3} HCl deoxygenated with N_2. Temperature 25°C. Electrode potentials 1. -0.850 V 2. -0.875 V 3. -0.900 V 4. -0.925 V 5. -0.950 V 6. -0.975 V and 7. -1.000 V (vs.SCE).

SCE) to 1.5 x 10^{-4} m s^{-1} at -1.000 V (vs. SCE). For n = 2 and a kinematic viscosity of 9.1 x 10^{-7} m^2 s^{-1} (Table 3.2) the diffusion coefficient of L-cystine hydrochloride is calculated as (5.01 ± 0.12) x 10^{-10} m^2 s^{-1} at 25°C. The error represents the spread of values obtained from all the straight lines in Figure 3.7, including the error in the slopes determined from a least squares analysis.

From the definition of the heterogeneous rate constant

$$k_f = k_f^o \exp\left(-\frac{\alpha_c F}{RT} E\right) \qquad (3.10)$$

Taking logarithms

$$\log k_f = \log k_f^o - \frac{\alpha_c F}{2.303\ RT} E \qquad (3.24)$$

Thus a plot of log k_f against E is a straight line the gradient of which yields the Tafel slope (2.303 RT/α_cF), and therefore α_c, and from the intercept k_f^o is obtained. The values of k_f from the intercepts in Figure 3.7 are plotted in the form of equation (3.24) in Figure 3.8. A good straight line is obtained from which the Tafel slope is (189 ± 1) mV/decade, α_c is (0.32 ± 0.01) and k_f^o is (7.0 ± 0.5) x 10^{-10} m s^{-1} for L-cystine hydrochloride reduction at 25°C. The relatively large error in k_f^o mainly reflects the long extrapolation to 0 V (vs. SCE).

There is an alternative method of determining the kinetic parameters from steady state voltammograms. From equation (3.12):

$$\frac{1}{i} - \frac{1}{i_L} = \frac{1}{i_k}$$

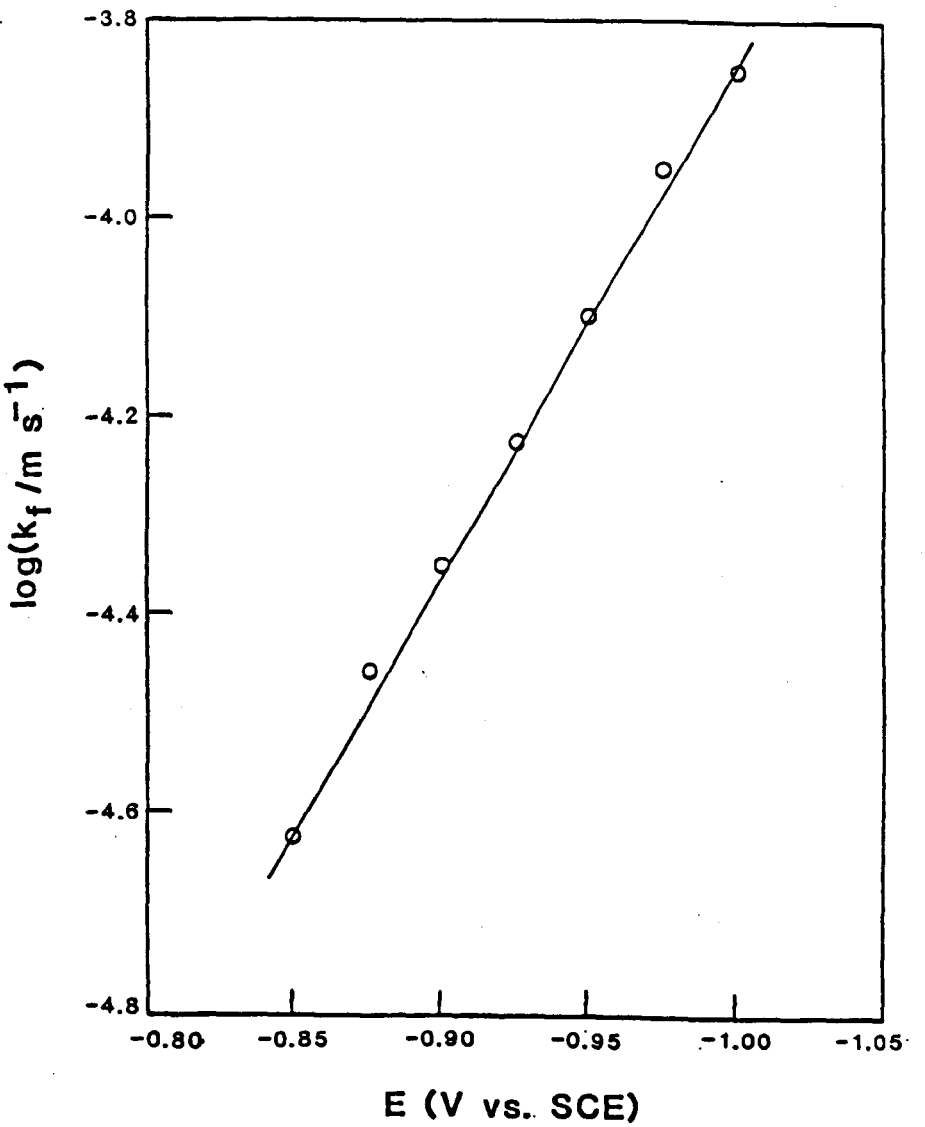

FIGURE 3.8 Plot of log k_f against E.

or substituting for i_k using equation (3.11), and k_f, using equation (3.09):

$$\frac{1}{i} - \frac{1}{i_L} = \frac{1}{nF\, k_f^o \exp(-\frac{\alpha_c F}{RT} E)\, c_b}$$

Taking logarithms

$$-\log\left[\frac{1}{i} - \frac{1}{i_L}\right] = -\frac{\alpha_c F}{2.303\, RT} E + \log (n F k_f^o c_b) \qquad (3.25)$$

Thus a plot of $-\log[1/i-1/i_L]$ against E is a straight line which yields from the gradient the Tafel slope and α_c, and from the intercept k_f^o. The use of $-\log[1/i - 1/i_L]$ corrects the normal Tafel plot (i.e. log i against E which applies for complete kinetic control) for the degree of mass transport control evident in the mixed control region of the voltammograms. This plot should be more accurate than the plot of log k_f against E, which is derived from Koutecky-Levich plots, since it uses the currents measured at the electrode directly. An accurate measurement of i_L is required, however, and as shown in Figure 3.3 this is not available for L-cystine hydrochloride reduction at mercury plated copper because of simultaneous hydrogen evolution. The problem may be solved by calculating the theoretical i_L using the Levich equation (i.e. equation 3.02), which is possible since the kinematic viscosity of the electrolyte and diffusion coefficient of the disulphide are known. Figure 3.9 shows the plot of $-\log[1/i - 1/i_L]$ against E for the voltammogram in Figure 3.3 recorded at an electrode rotation rate of 10 Hz. From this plot, at 25°C, the Tafel slope is (186 ± 2) mV/decade, α_c is (0.32 ± 0.01) and k_f^o (6.7 ± 0.5) x 10^{-10} m s^{-1}. These values are in close accord with those obtained from the plot of log k_f against E. The voltammograms for the other rotation rates in Figure 3.3 give essentially unchanged kinetic parameters.

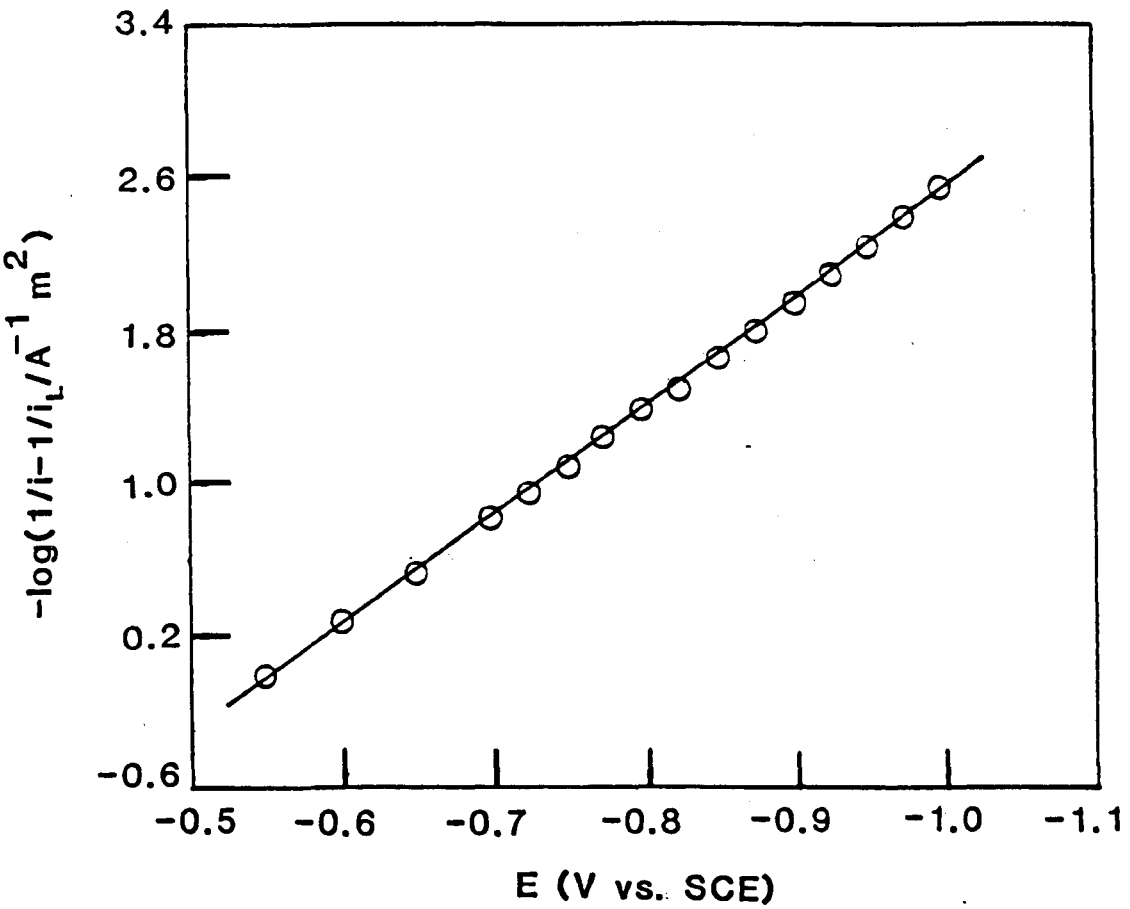

FIGURE 3.9 Mass transport corrected Tafel plot for L-cystine hydrochloride reduction at a mercury plated copper RDE. 10 mol m^{-3} L-cystine hydrochloride in aqueous 0.1 mol dm^{-3} HCl deoxygenated with N_2. Temperature 25°C.

It is worth considering the significance of the kinetic parameters. The Tafel slope and α_c determine the extent to which changes in the electrode potential alter the current density, which is a measure of the rate of an electrode reaction. The lower the Tafel slope (or conversely the higher α_c) the greater the increase in the current density for a unit change in the electrode potential. Consequently, an electrode material giving a low Tafel slope for an electrode reaction is strongly desired. The Tafel slopes observed for L-cystine hydrochloride reduction at mercury plated copper are high. It is difficult to justify a Tafel slope of greater than 120 mV/decade theoretically (e.g. see the consideration of the EE mechanism by Albery [17]).

In practice, however, there are a number of possible sources of high Tafel slopes. They can be attributed to a significant electrolyte resistance between the reference and working electrodes, to near-electrode pH changes for reactions which show a pH dependency, to the formation of resistive electrode films from sources other than the reactant and product and to the adsorption of reactants and/or products upon the electrode surface. For example Kuhn et al [18,19] have attributed Tafel slopes of about 700 mV/decade at a series of cathodes, for the electroreduction of glucose to sorbitol, to a near-electrode pH effect coupled with , at some metals, the formation of a resistive film (e.g. lead sulphate at lead cathodes in aqueous sulphate media).

In this study there is no effect from a resistive film formed by the components of the background electrolyte nor is there a significant contribution from a voltage drop in the electrolyte, as shown in Table 3.1. There may be an effect from a change in the near-electrode pH but the high Tafel slopes for L-cystine hydrochloride reduction are most probably the result of adsorption of the disulphide at the mercury surface. Under the experimental conditions there is

abundant voltammetric evidence of disulphide adsoprtion principally from HMDE studies (Sections 3.8.1 and 3.8.5).

A comparison between different electrode materials in terms of the kinetic facility of electron transfer during L-cystine hydrochloride reduction may be made by comparing k_f^o values. The larger k_f^o the faster the rate of electron transfer. A comparison with the kinetic rate of other electrode reactions cannot, however, be made. This requires the standard rate constant k^o which is the value of k_f at the $E^{o'}$ of a redox couple. Standard rate constants between 0.1 m s^{-1} and much lower than 10^{-11} m s^{-1} have been reported [10] with the faster associated with simple electron transfers (e.g. reduction and oxidation of aromatic aldehydes to anion and cation radicals respectively) and the more sluggish with significant molecular rearrangement upon electron transfer (e.g. oxygen reduction to hydrogen peroxide and water). By definition [10]:

$$k_f = k^o \exp\left(-\frac{\alpha_c F}{RT}\,[E - E^{o'}]\right) \qquad (3.26)$$

Taking logarithms

$$\log k_f = \log k^o - \frac{\alpha_c F}{2.303\ RT}\,[E - E^{o'}] \qquad (3.27)$$

Thus a plot of log k_f against $[E-E^{o'}]$ gives k^o from the intercept. To determine k^o therefore requires an accurate value of $E^{o'}$ which as shown in Section 3.8.3 is not available for the L-cystine/L-cysteine redox couple. Conseuqently k^o values are not reported for the reaction.

3.6 ANALYSIS OF THE MAIN PEAK FOR L-CYSTINE HYDROCHLORIDE REDUCTION IN LINEAR SWEEP VOLTAMMETRY

3.6.1 The Kinetic Parameters and Diffusion Coefficient of L-Cystine Hydrochloride

Linear sweep voltammograms show a large diffusion controlled peak for the irreversible reduction of L-cystine hydrochloride to L-cysteine hydrochloride (reaction 3.04). As shown in Figure 3.2 identical voltammograms were recorded at the mercury plated copper and the stationary mercury disc electrodes. Only the results recorded at the stationary mercury disc will be used in the following discussion.

It is possible to analyse linear sweep voltammograms to obtain the kinetic parameters for L-cystine hydrochloride reduction. The mathematics involved in determining the exact form of the voltammogram is quite complicated but it has been shown by Nicholson and Shain [20] that, for a first order, electrochemically irreversible reaction, assuming semi-infinite linear diffusion

$$i = n F c_b D^{1/2} v^{1/2} \left[\frac{\alpha_c F}{RT}\right]^{1/2} \pi^{1/2} \chi(bt) \qquad (3.28)$$

where c_b is the bulk reactant concentration, D the diffusion coefficient of the reactant, v the potential sweep rate and $\chi(bt)$ a tabulated current function which is dependent upon the electrode potential (i.e. see Table 3.4). $\Phi(bt)$, which is also shown in Table 3.4, is a current function which is a correction for spherical diffusion.

TABLE 3.4 Current function $\pi^{\frac{1}{2}}\chi(bt)$ for linear sweep voltammetry and irreversible charge transfer [20].

Potential (mV)	$\pi^{\frac{1}{2}}\chi(bt)$	$\Phi(bt)$	Potential (mV)	$\pi^{\frac{1}{2}}\chi(bt)$	$\Phi(bt)$
160	0.003		15	0.437	0.323
140	0.008		10	0.462	0.396
120	0.016		5	0.480	0.482
110	0.024		0	0.492	0.600
100	0.035		- 5	0.495	0.685
90	0.050		- 5.34	0.4958	0.694
80	0.073	0.004	-10	0.493	0.755
70	0.104	0.010	-15	0.485	0.823
60	0.145	0.021	-20	0.472	0.895
50	0.199	0.042	-25	0.457	0.952
40	0.264	0.083	-30	0.441	0.992
35	0.300	0.115	-35	0.423	1.00
30	0.337	0.154	-40	0.406	
25	0.372	0.199	-50	0.374	
20	0.406	0.253	-70	0.323	

The potential scale is $(E-E^{o'})\alpha_c + (RT/F)\ln\left[\left(\frac{\pi D\alpha_c Fv}{RT}\right)^{\frac{1}{2}}\frac{1}{k^o}\right]$

As shown in Table 3.4 $\chi(bt)$ goes through a maximum at $\pi^{\frac{1}{2}}\chi(bt) = 0.4958$. Introduction of this value into equation (3.28) gives for the peak current density

$$i_p = 0.4958\ n\ F\ c_b\ D^{1/2}\left[\frac{\alpha_c F}{RT}\right]^{1/2} v^{1/2} \qquad (3.29)$$

This value occurs when

$$\alpha_c\ (E_p - E^{o'}) + \frac{RT}{F}\ln\left[\left(\frac{\pi D\alpha_c Fv}{RT}\right)^{1/2}\frac{1}{k^o}\right] = -5.34\ mV$$

or

$$E_p = E^{o'} - \frac{RT}{\alpha_c F}\left[0.780 + 2.303\ \log\left(\frac{D^{1/2}}{k^o}\right) + 2.303\ \log\left(\frac{\alpha_c F v}{RT}\right)^{1/2}\right] \qquad (3.30)$$

Another equation sometimes employed in kinetic analyses can be obtained from equations (3.29) and (3.30). From equation (3.30):

$$\exp\left(\frac{\alpha_c F}{RT}\ [E - E^{o'}]\right) = 2.183\left(\frac{D\alpha_c F v}{RT}\right)^{1/2}\frac{1}{k^o}$$

Multiplying both sides by i_p, using equation (3.29), and rearranging gives

$$i_p = 0.227\ n\ F\ c_b\ k^o \exp\left(-\frac{\alpha_c F}{RT}\ [E_p - E^{o'}]\right) \qquad (3.31)$$

Taking logarithms

$$\log i_p = \log\ (0.227\ n\ F\ c_b\ k^o) - \frac{\alpha_c F}{2.303\ RT}\ [E_p - E^{o'}] \qquad (3.32)$$

To obtain the kinetic parameters either equation (3.30) or equation (3.32) can be used. Using equation (3.30) a plot of E_p against log v is a straight line which yields the Tafel slope and α_c from the slope and k^o (provided the diffusion coefficient of the reactant is known) from the intercept. Alternatively, as shown by equation (3.32), a plot of log i_p against $[E_p - E^{o'}]$ for different potential sweep rates is a straight line which yields the Tafel slope and α_c from the slope and k^o (provided n is known) from the intercept. The plot of log i_p against $[E_p - E^{o'}]$ might be expected to be the less accurate of the two plots since it requires the measurement of both i_p and E_p from the voltammogram rather than only E_p.

To obtain k_f° rather than k^o from equations (3.31) and (3.32) merely requires a value of zero volts to be assumed for $E^{o'}$.

Figure 3.10 shows the linear sweep voltammograms for reduction of 10 mol m^{-3} L-cystine hydrochlroide in aqueous 0.1 mol dm^{-3} hydrochloric acid at a range of potential sweep rates. The negative shift in E_p with increasing potential sweep rate is clearly evident. From the variation of E_p with log v (Figure 3.11), at 25°C, the Tafel slope is (185 ± 3) mV/decade, α_c is (0.32 ± 0.01) and k_f° (assuming D is 5.0 x 10^{-10} m^2 s^{-1}) is (6.7 ± 0.8) x 10^{-10} m s^{-1}. The plot of log i_p against [E_p - $E^{o'}$] (Figure 3.12), at 25°C, gives a Tafel slope of (185 ± 5) mV/decade, an α_c of (0.32 ± 0.02) and a k_f° (assuming n is 2) of (6.8 ± 1.4) x 10^{-10} m s^{-1}. As expected the errors are greater from this plot, although the difference between the two sets of errors is small. Strong evidence for the accuracy of the kinetic parameters is provided by the close comparison between the values obtained using linear sweep voltammetry and the RDE technique (see Table 3.5).

The diffusion coefficient of L-cystine hydrochloride can also be obtained from the linear sweep voltammetry by using equation (3.29). A plot of i_p against $v^{\frac{1}{2}}$ (a test of diffusion control) is a straight line through the origin from the slope of which the diffusion coefficient can be obtained provided n and α_c are known. A straight line plot through the origin is obtained for L-cystine hydrochloride reduction (Figure 3.13) from which (assuming n is 2 and α_c is 0.32) the diffusion coefficient of the disulphide is (5.1 ± 0.4) x 10^{-10} m^2 s^{-1} at 25°C.

There is one major difference between the RDE measurements and the linear sweep voltammetry. In aqueous 2.0 mol dm^{-3} hydrochloric acid a diffusion controlled peak is obtained in linear sweep voltammograms but in steady state measurements recorded at the RDE, L-cystine hydrochloride reduction is not

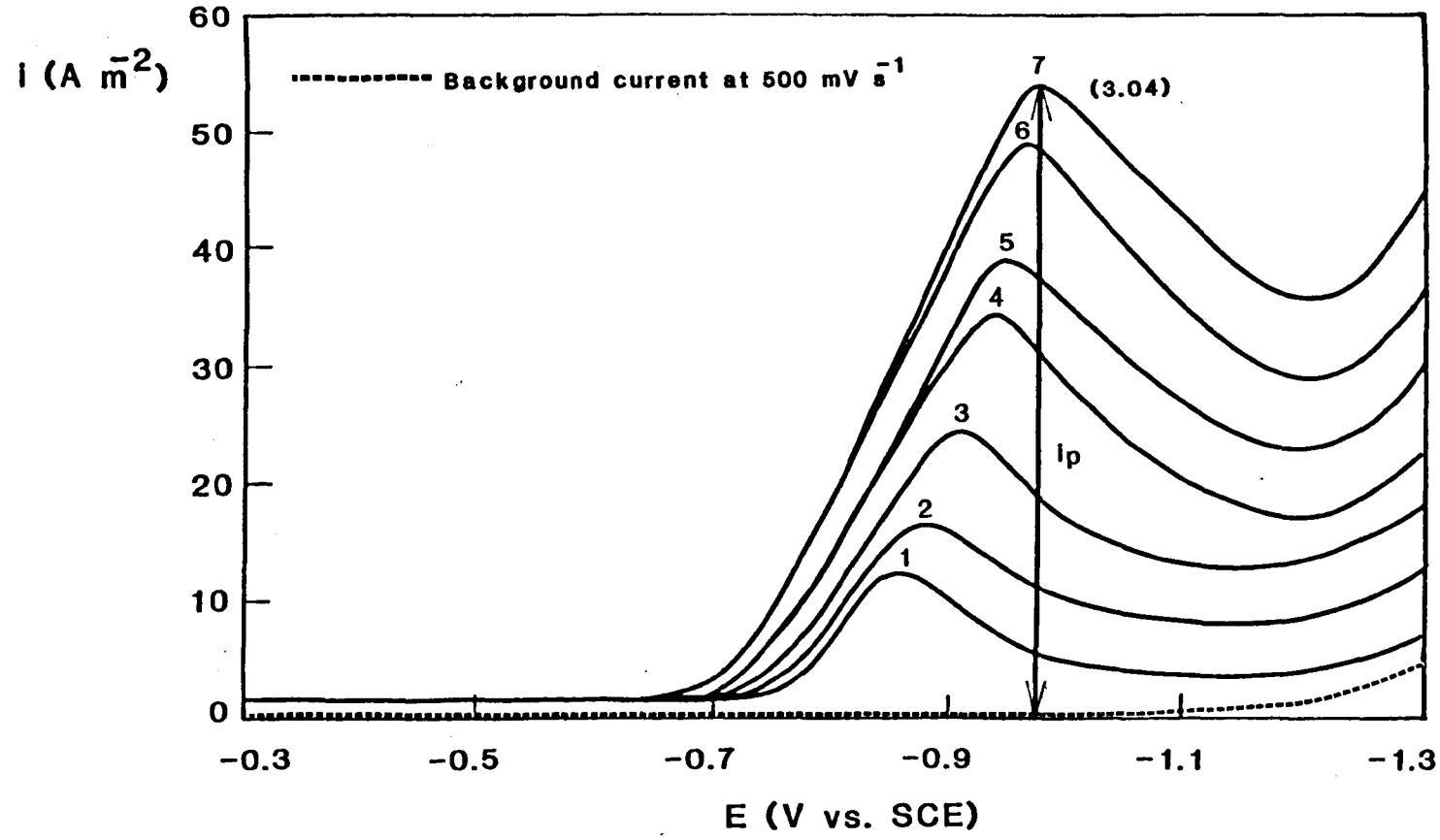

FIGURE 3.10 Linear sweep voltammetry of 10 mol m^{-3} L-cystine hydrochloride in aqueous 0.1 mol dm^{-3} HCl at the stationary mercury disc electrode. Electrolyte deoxygenated with N_2. Temperature 25°C. Potential sweep rate 1. 25 mV s^{-1} 2. 50 mV s^{-1} 3. 100 mV s^{-1} 4. 200 mV s^{-1} 5. 250 mV s^{-1} 6. 400 mV s^{-1} and 7. 500 mV s^{-1}. Peak currents were measured as shown for the voltammogram recorded at 500 mV s^{-1}.

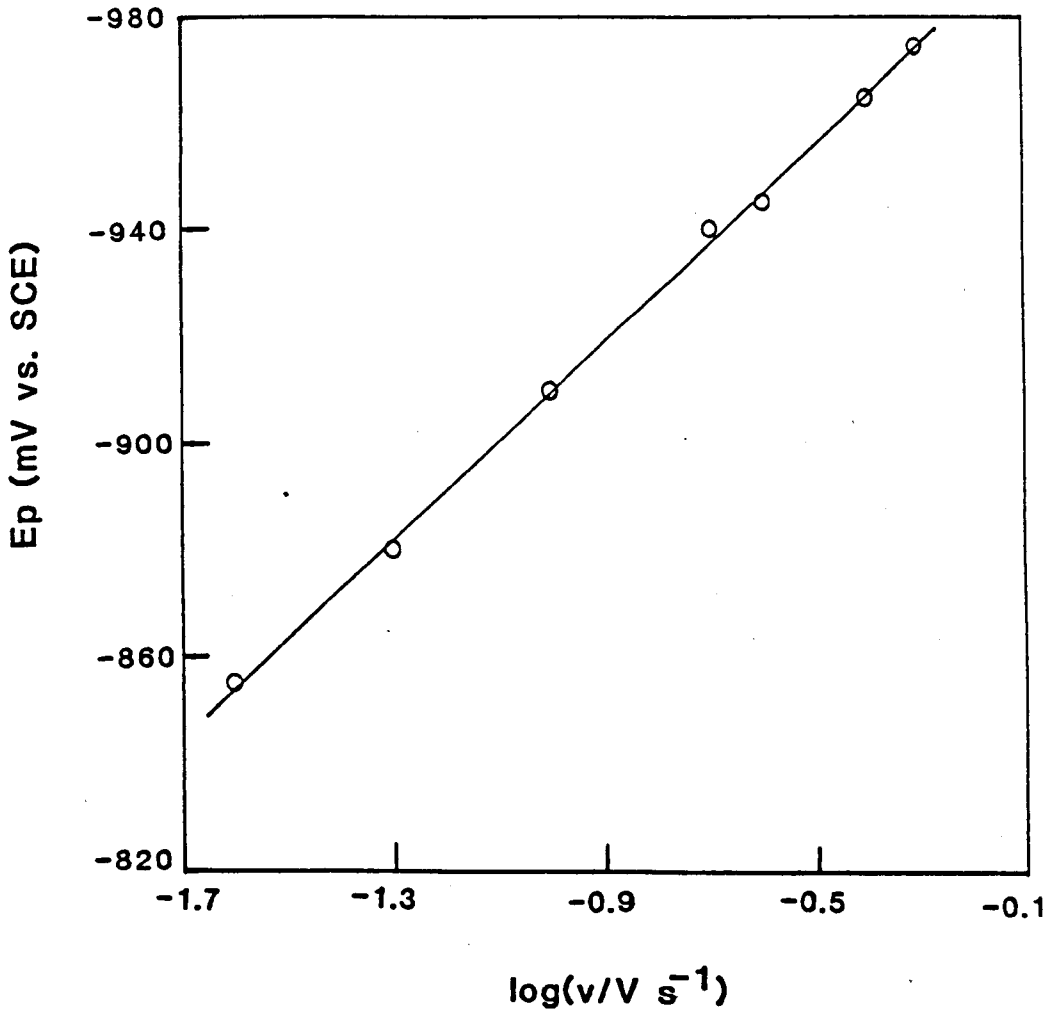

FIGURE 3.11 Dependence of E_p on log v in linear sweep voltammograms at a stationary mercury disc electrode. 10 mol m^{-3} L-cystine hydrochloride in aqueous 0.1 mol dm^{-3} HCl deoxygenated with N_2. Temperature 25°C. The points are the average of 5 separate measurements.

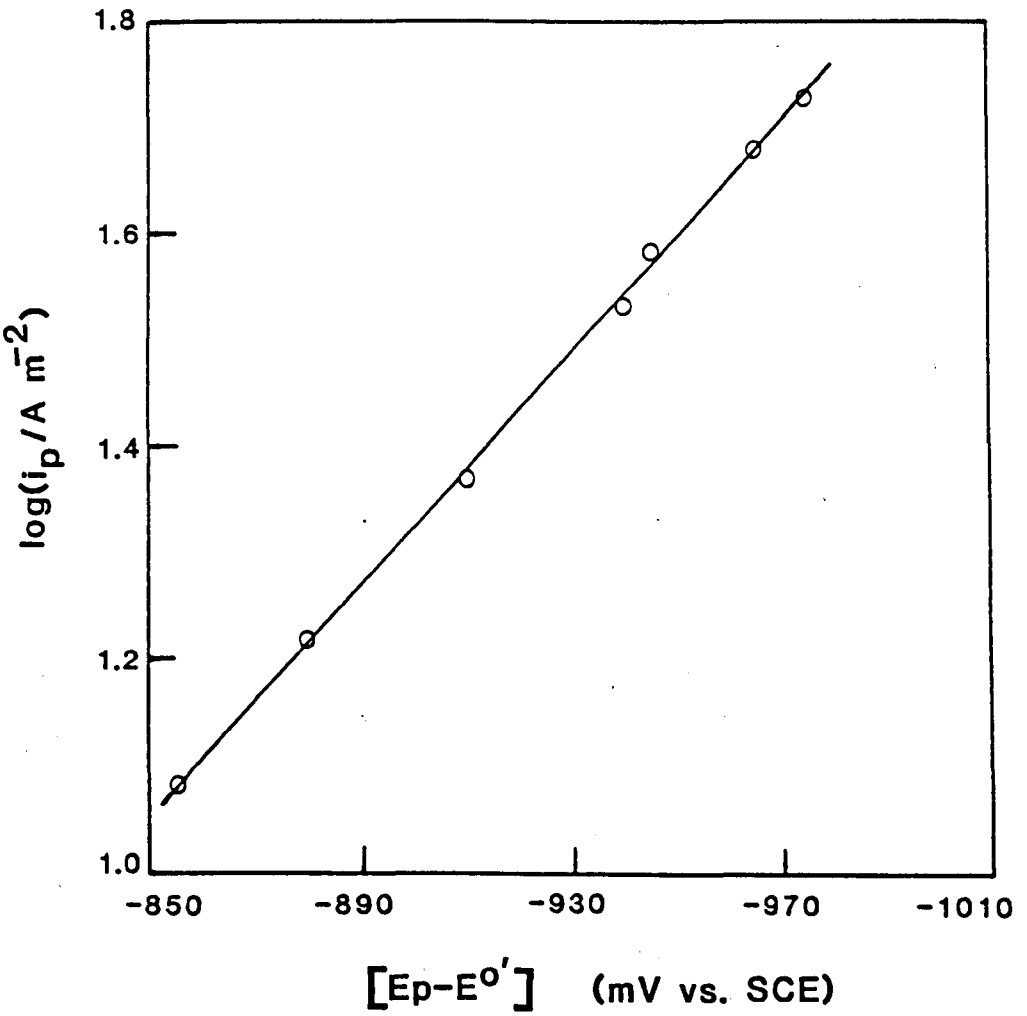

FIGURE 3.12 Dependence of log i_p on $[E_p - E^{o'}]$ in linear sweep voltammograms at a stationary mercury disc electrode. 10 mol m^{-3} L-cystine hydrochloride in aqueous 0.1 mol dm^{-3} HCl deoxygenated with N_2. Temperature 25°C. $E^{o'}$ was taken as 0 V (vs. SCE) to obtain k_f^o from the intercept. The points are the average of 5 separate measurements.

TABLE 3.5 Kinetic parameters from RDE and linear sweep voltammetry.

10 mol m^{-3} L-cystine hydrochloride in aqueous 0.1 mol dm^{-3} HCl at 25°C.

	RDE Technique		Linear Sweep Voltammetry	
Plot	log k_f vs E	$-\log[1/i-1/i_L]$ vs E	E_p vs log v	log i_p vs $[E_p-E^{o'}]$
Tafel Slope (mV/decade)	189±2	186±2	185±3	185±5
α_c	0.32±0.01	0.32±0.01	0.32±0.01	0.32±0.02
k_f^o (10^{-10} m s^{-1})	7.0±0.5	6.7±0.5	6.8±1.4	6.8±1.4

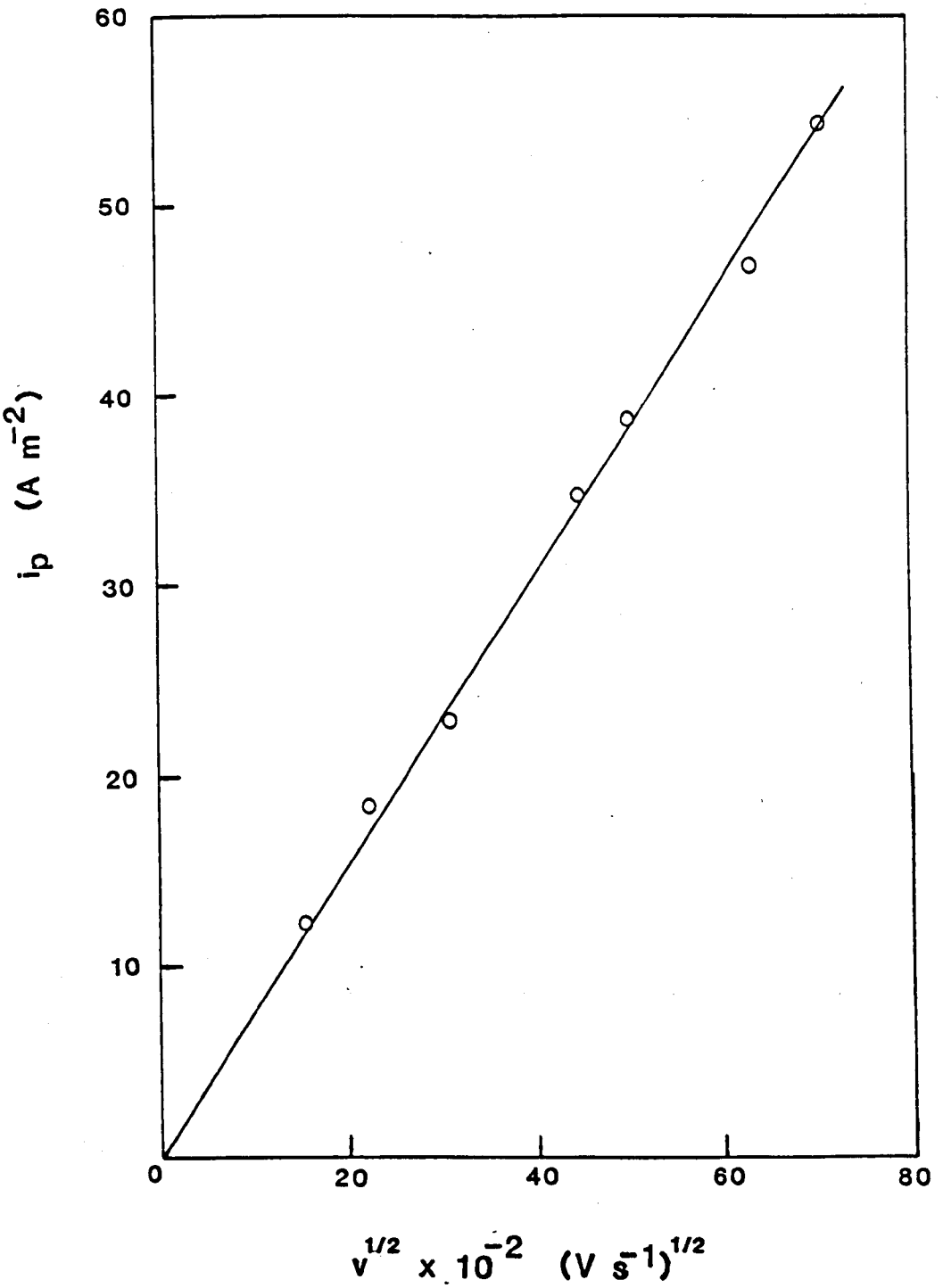

FIGURE 3.13 Dependence of i_p on $v^{\frac{1}{2}}$ in linear sweep voltammograms at a stationary mercury disc electrode. 10 mol m^{-3} L-cystine hydrochloride in aqueous 0.1 mol dm^{-3} HCl deoxygenated with N_2. Temperature 25°C. The points are the average of 5 separate measurements.

separated from hydrogen evolution. Not even an inflection is evident. This difference is probably the result of two effects. The peak potential for the reduction in linear sweep voltammograms occurs between -0.86 and -0.98 V (vs. SCE) (i.e. E_p is unchanged in 0.1 mol dm^{-3} and 2.0 mol dm^{-3} hydrochloric acid) which is positive of the hidden diffusion limited current in steady state voltammograms at the RDE. Also, the current increases over 10 seconds to a steady value in the steady state measurements. Consequently on the time scale of linear sweep voltammetry experiments the hydrogen evolution current is probably lower at a given electrode potential.

Analysis of the peak in linear sweep voltammograms for reduction of 10 mol m^{-3} L-cystine hydrochloride in aqueous 2.0 mol dm^{-3} hydrochloric acid indicates the kinetic parameters are unchanged from those measured in aqueous 0.1 mol dm^{-3} hydrochloric acid. The diffusion coefficient of L-cystine hydrochloride is lower in the more concentrated acid, however, as evidenced by a lower peak current at a given potential sweep rate. In aqueous 2.0 mol dm^{-3} hydrochloric acid from equation (3.29) (assuming n is 2 and α_c is 0.32) the diffusion coefficient of L-cystine hydrochloride is (4.0 ± 0.3) x 10^{-10} m^2 s^{-1} at 25°C.

3.6.2 Reaction Order for L-Cystine Hydrochloride

Kohler et al [21] have recently extended the theory for linear sweep voltammetry of irreversible electrode reactions to cover reaction orders other than 1. They defined the peak current as

$$i_p = n F c_b D^{1/2} \left[\frac{\alpha_c F}{RT}\right]^{1/2} \pi^{1/2} \Phi^{*.m} v^{1/2} \qquad (3.33)$$

where m is the reaction order and Φ^* is a function principally of m with a minor dependence upon the potential sweep rate. From equation (3.33) using Φ^* values calculated by Kohler et al and the relevant parameters for L-cystine hydrochloride

reduction it is possible to calculate the theoretical slope of the i_p against $v^{\frac{1}{2}}$ plot for various reaction orders. The theoretical slope for reaction orders between 0.5 and 3.0 are listed in Table 3.6.

The experimental slope in Figure 3.13 is 76 ± 3 A $m^{-2}/(V\ s^{-1})^{\frac{1}{2}}$. Comparison with Table 3.6 provides clear evidence that the reaction is first order in L-cystine hydrochloride. Furthermore, the reaction order does not change in aqueous 2.0 mol dm^{-3} hydrochloric acid.

3.7 CONCENTRATION DEPENDENCE OF THE MASS TRANSPORT CORRECTED TAFEL PLOTS FOR L-CYSTINE HYDROCHLORIDE REDUCTION AT A MERCURY PLATED COPPER RDE

Figure 3.14 shows the mass transfer corrected Tafel plots recorded at the mercury plated copper RDE for L-cystine hydrochloride concentrations between 0.4 mol m^{-3} and 10 mol m^{-3} in aqueous 0.1 mol dm^{-3} hydrochloric acid. At all disulphide concentrations the Tafel slope is (186 ± 3) mV/decade and α_c is (0.32 ± 0.01). From the Tafel plots it is possible to obtain the reaction order for L-cystine hydrochloride, by plotting $-\log[1/i - 1/i_L]$ against log (L-cystine hydrochloride concentration) at a constant cathode potential. Such plots, at a series of cathode potentials, are shown in Figure 3.15. Above 4 mol m^{-3} L-cystine hydrochloride, as expected, the reaction order is + 1 but at lower disulphide concentrations the kinetic currents are progressively higher than predicted for a first order reaction. This is confirmed by the progressively higher k_f^o values (Table 3.7) for L-cystine hydrochloride reduction as the reactant concentration decreases. The k_f^o values in Table 3.7 were determined from the intercepts of the Tafel plots in Figure 3.14.

TABLE 3.6 Reaction order dependence of the slope of the i_p against $v^{\frac{1}{2}}$ plot [21].

10 mol m^{-3} L-cystine hydrochloride in aqueous 0.1 mol dm^{-3} HCl. Temperature 25°C, n = 2, α_c = 0.32 and D = 5.0 x 10^{-10} m^2 s^{-1}.

m	[a] f	Φ^*	Theoretical Slope ($A\ m^{-2}/(V\ s^{-1})^{\frac{1}{2}}$)
0.5	4	0.1199	93.2
	7-10	0.1181	92.8
1.0	4	0.2817	76.0
	7-10	0.2797	75.5
1.5	4	0.3908	65.9
	7-10	0.3892	65.5
2.0	4	0.4678	59.1
	7-10	0.4665	58.7
2.5	4	0.5253	54.0
	7-10	0.5242	53.7
3.0	4	0.5701	50.0
	7-10	0.5692	49.8

a. f reflects the potential sweep rate dependence of Φ^*. As shown for $f > 7$ there is no effect on Φ^*.

$$f = \ln\left[\left[\pi D\left(\frac{\alpha_c F v}{RT}\right)\right]^{1/2} / k_{ch} (c_b)^{m-1}\right]$$

where k_{ch} is the chemical component of the heterogeneous rate constant for electron transfer at m = 1.0 .

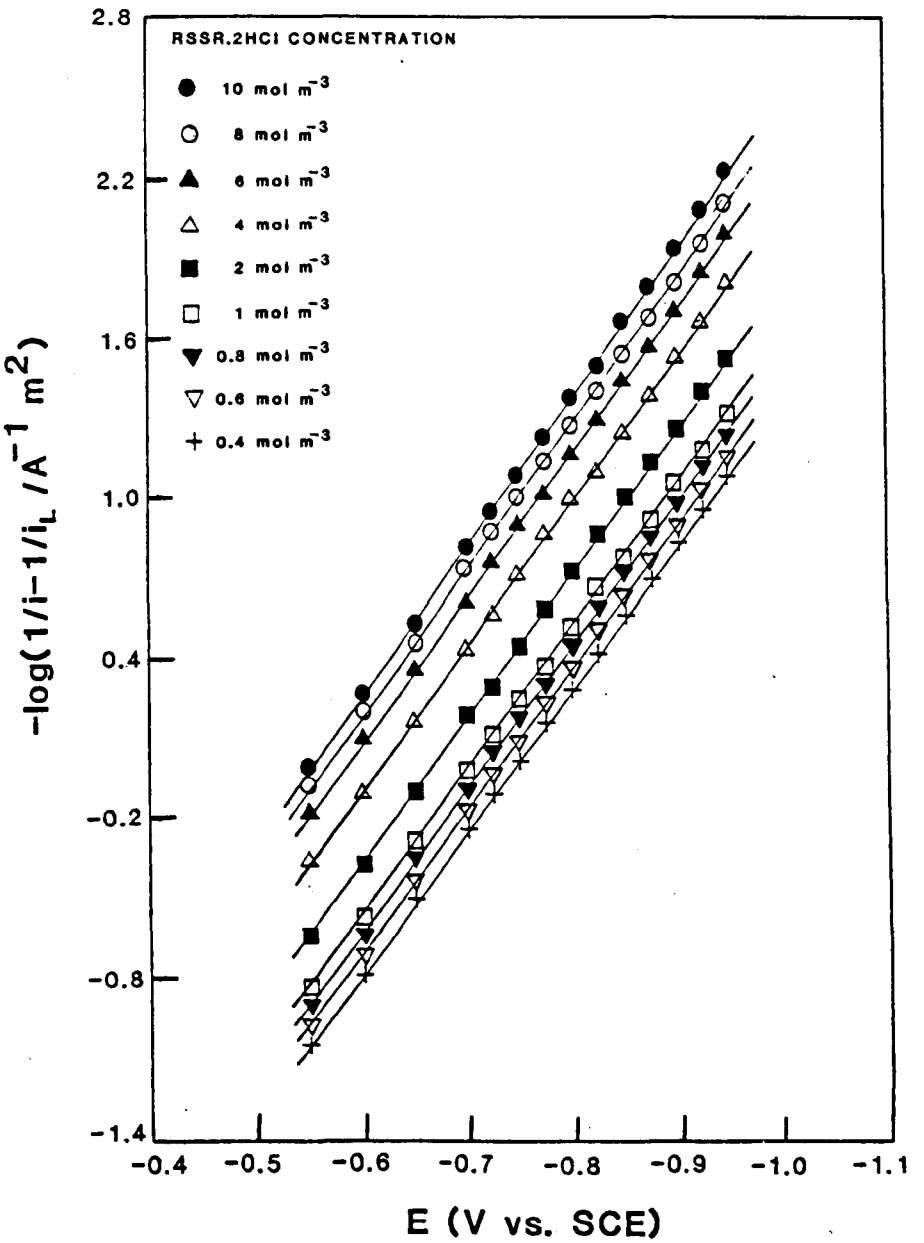

FIGURE 3.14 Mass transport corrected Tafel plots for a range of L-cystine hydrochloride concentrations at a mercury plated copper RDE. The background electrolyte is aqueous 0.1 mol dm^{-3} HCl deoxygenated with N_2. Temperature 25°C. Electrode rotation rate 10 Hz. The background current is subtracted.

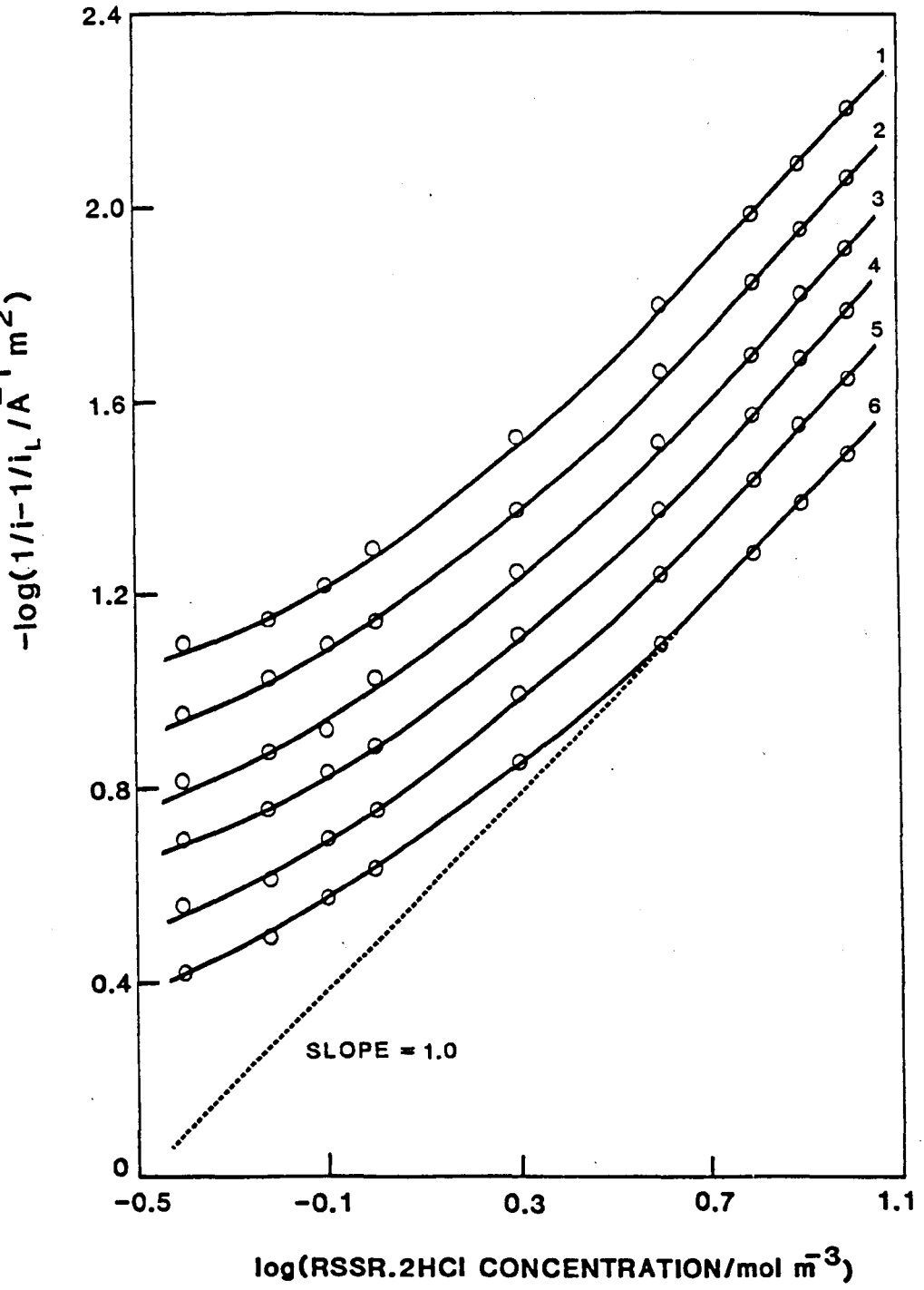

FIGURE 3.15 Plot of -log [1/i - 1/i] against log (RSSR.2HCl concentration). Cathode potentials 1. -0.950 V 2. -0.925 V 3. -0.900 V 4. -0.875 V 5. -0.850 V and 6. -0.825 V (vs. SCE).

TABLE 3.7 Concentration dependence of k_f for L-cystine hydrochloride reduction.

L-Cystine Hydrochloride Concentration (mol m^{-3})	k_f^o (10^{-10} m s^{-1})
10	6.6 ± 0.4
8	6.4 ± 0.5
6	6.4 ± 0.4
4	6.2 ± 0.4
2	7.2 ± 0.5
1	8.4 ± 0.4
0.8	9.5 ± 0.3
0.6	10.6 ± 0.3
0.4	14.8 ± 0.4

Confirmation of these k_f^o values is provided by linear sweep voltammetry. Plots of E_p against log v for 1.0 mol m^{-3} and 0.6 mol m^{-3} L-cystine hydrochloride (Figure 3.16) give from the intercept a k_f^o of (8.4 ± 0.7) x 10^{-10} m s^{-1} and (10.1 ± 0.8) x 10^{-10} m s^{-1} respectively (assuming a diffusion coefficient of 5.0 x 10^{-10} m^2 s^{-1}) in accord with Table 3.7.

This shows the importance of measuring the reaction order by varying the reactant concentration, which is the prescribed method (see e.g. [22]), rather than relying upon methods which utilise only a single reactant concentration. For example at each disulphide concentration in Table 3.7 the Koutecky-Levich plot, mass transport corrected Tafel plot and linear sweep voltammogram suggest the reaction is first order. The most likely source of the reduced rate of electron transfer at progressively higher disulphide concentrations up to 4 mol m^{-3}, is once again an effect of modification of the electrode surface by adsorption processes involving L-cystine hydrochloride. L-Cystine hydrochloride adsorption and the effect on k_f^o for the electrosynthesis reaction is discussed in detail in Section 3.8.5.

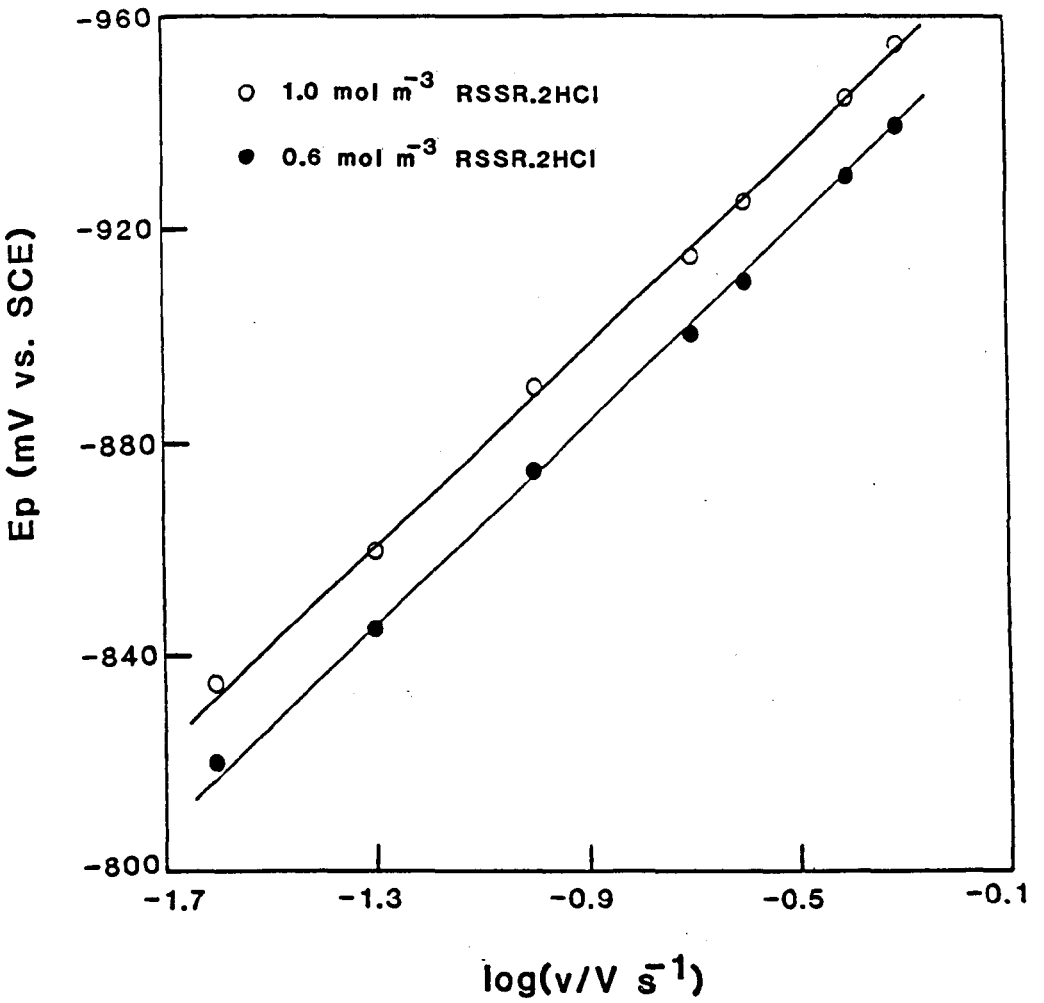

FIGURE 3.16 Dependence of E_p on log v in linear sweep voltammetry at a stationary mercury disc electrode. The background electrolyte is aqueous 0.1 mol dm^{-3} HCl deoxygenated with N_2. Temperature 25°C. The points are the average of 5 separate measurements.

3.8 L-CYSTINE HYDROCHLORIDE REDUCTION AT A MERCURY DROP ELECTRODE

3.8.1 Voltammograms

Cyclic voltammograms at a HMDE of 0.1 mol m^{-3} L-cystine hydrochloride (or below) in aqueous 0.1 mol dm^{-3} hydrochloric acid (Figure 3.17) are in accord with the literature for other electrolytes [23]. The peak at −0.125 V (vs. SCE) is due to the reduction of adsorbed L-cystine hydrochloride to L-cysteine hydrochloride (reaction 3.34). The reduction rate is controlled by the rate of adsorption of the reactant at the mercury surface based upon the linear dependence of the peak current on the potential sweep rate (Figure 3.18a)

$$RSSR.2HCl_{(ads.)} + 2H^+ + 2e^- \longrightarrow 2RSH.HCl \qquad (3.34)$$

The major peak at −0.450 V (vs. SCE) at a potential sweep rate of 100 mV s^{-1} corresponds to the irreversible, diffusion controlled electrosynthesis reaction (reaction 3.04). As expected i_p is directly proportional to $v^{\frac{1}{2}}$ (Figure 3.18b) and to the reactant concentration (Figure 3.19a). The L-cysteine hydrochloride produced in the cathodic potential scan is reversibly oxidised to mercury cysteinate (reactions 3.35 and 3.36) in the reverse anodic scan at a peak potential of −0.075 V (vs. SCE) at a potential sweep rate of 100 mV s^{-1}.

$$RS_2Hg_{2\,(ads)} + 4H^+ + Cl^- + 2e^- \rightleftharpoons 2RSH.HCl + 2Hg \qquad (3.35)$$

$$RS_2Hg_{(ads)} + 4H^+ + Cl^- + 2e^- \rightleftharpoons 2RSH.HCl + Hg \qquad (3.36)$$

The oxidation is diffusion controlled and i_p is directly proportional to $v^{\frac{1}{2}}$ (Figure

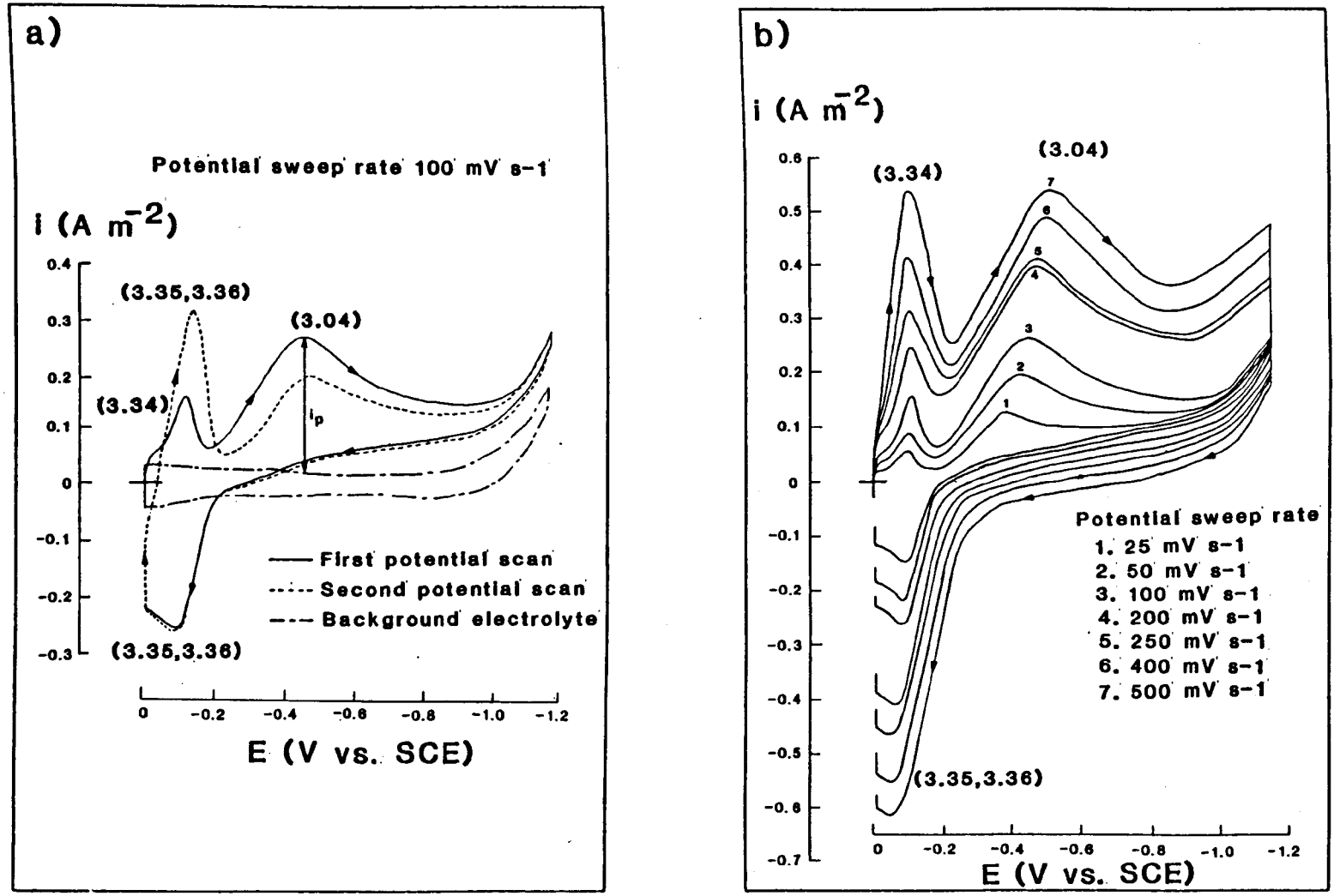

FIGURE 3.17 Cyclic voltammetry of 0.1 mol m^{-3} L-cystine hydrochloride in aqueous 0.1 mol dm^{-3} HCl showing a) multiple potential scan and b) potential sweep rate dependence of the initial potential scan at a HMDE. Electrolyte deoxygenated with N_2. Temperature 25°C.

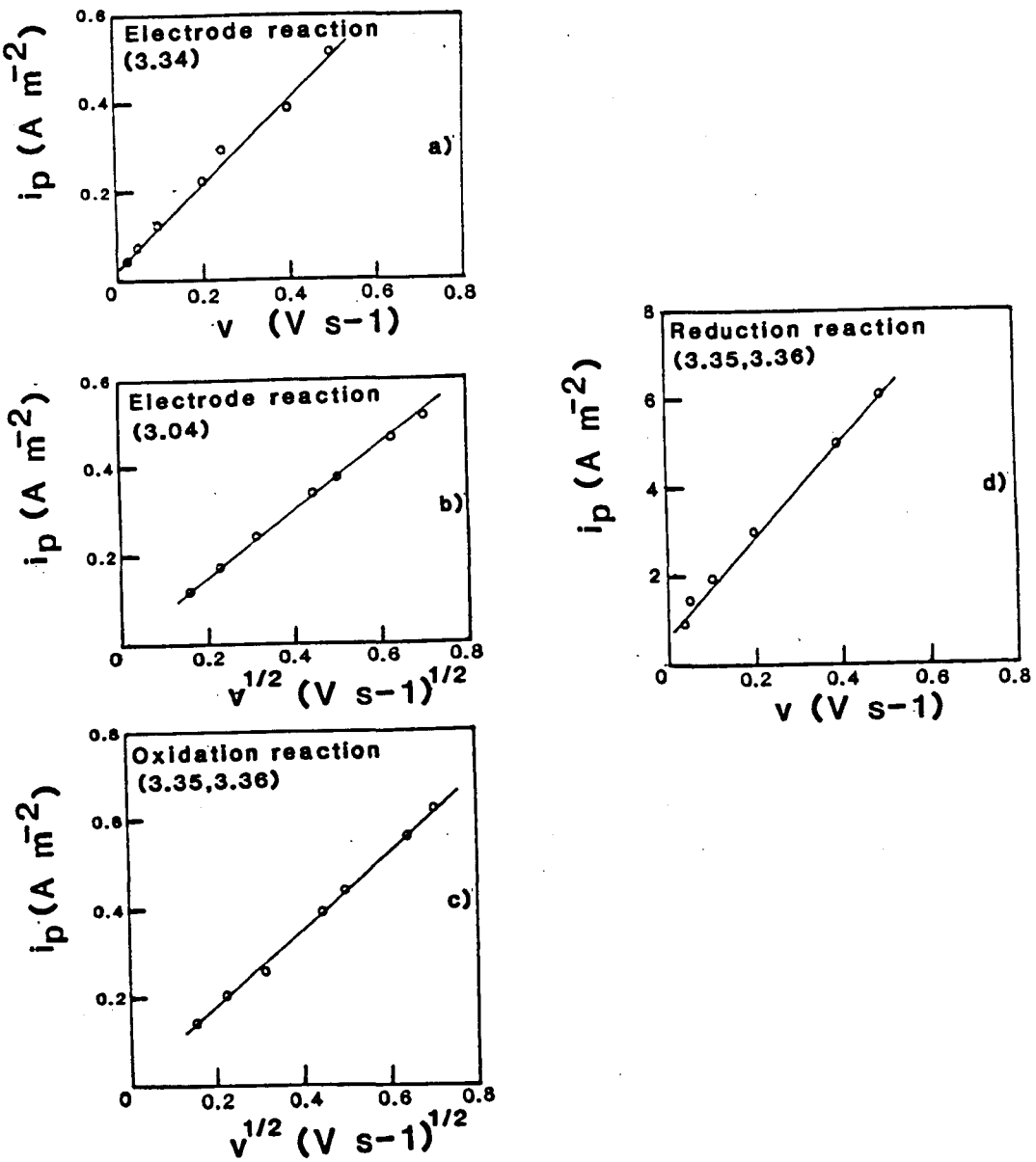

FIGURE 3.18 Sweep rate dependence of the peak currents in cyclic voltammograms at a HMDE. For a), b) and c) the electrolyte is 0.1 mol m^{-3} L-cystine hydrochloride in aqueous 0.1 mol dm^{-3} HCl and for d) 0.1 mol m^{-3} L-cysteine hydrochloride in aqueous 0.1 mol dm^{-3} HCl, both deoxygenated with N_2. Temperature 25°C.

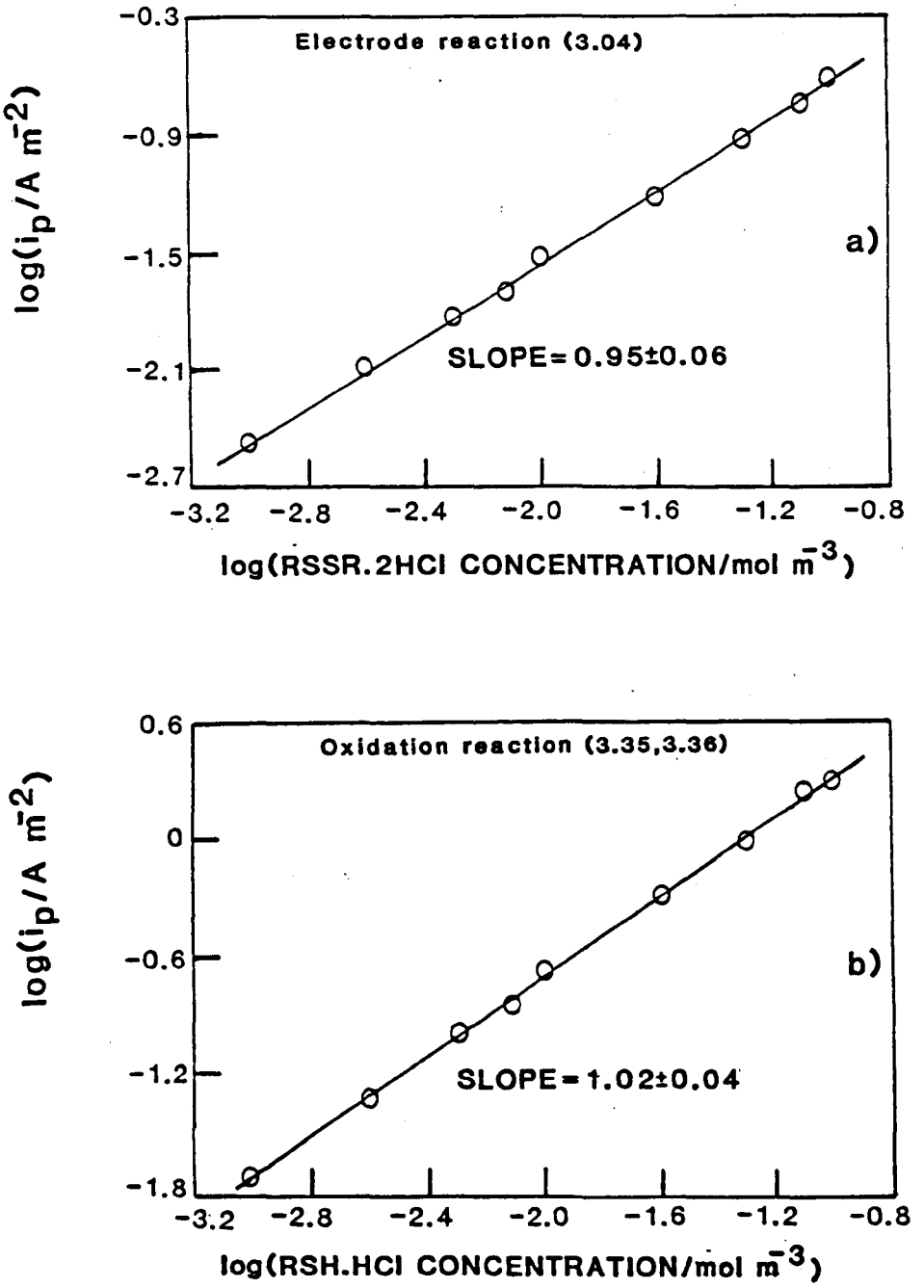

FIGURE 3.19 Concentration dependence of the peak currents in cyclic voltammograms at a HMDE. The background electrolyte is aqueous 0.1 mol dm^{-3} HCl deoxygenated with N_2. Temperature 25°C. Potential sweep rate 100 mVs^{-1}.

3.18c) and to the L-cysteine hydrochloride concentration (Figure 3.19b). In the second potential scan mercury cysteinate is reduced to L-cysteine hydrochloride (reactions 3.35 and 3.36) at a peak potential of -0.130 V (vs. SCE) at a potential sweep rate of 100 mV s^{-1}. The peak completely swamps the current for reduction of adsorbed L-cystine hydrochloride. For solutions of L-cysteine hydrochloride, at a concentration of 0.1 mol m^{-3} or below, i_p is directly proportional to v (Figure 3.18d) suggesting the rate of reduction is controlled by adsorption of mercury cysteinate at the electrode surface. At higher disulphide and thiol concentrations than 0.1 mol m^{-3} two cathodic and two anodic peaks are evident for electrode reactions (3.35) and (3.36) (Figure 3.20). This is presumeably due to the rearrangement of mercury cysteinate on the electrode surface, which Bard and Stankovich [23] have eluded to. They observed at pH 7.4, however, sharp spikes on the original peaks rather than an addition peak (Figure 1.3).

The differential pulse and sampled d.c. polarograms of 0.1 mol m^{-3} L-cystine hydrochloride in aqueous 0.1 mol dm^{-3} hydrochloric acid are shown in Figure 3.21. As expected from the cyclic voltammetry, differential pulse voltammograms show two peaks for reduction of adsorbed (E_p at -0.125 V vs. SCE) and dissovled (E_p at -0.450 V vs. SCE) L-cystine hydrochloride to L-cysteine hydrochloride. Sampled d.c. polarograms, however, appear to consist of a single irreversible wave. This highlights one of the dangers of d.c. polarography i.e. the complexity of systems may not be readily observed. The irreversible wave does show a well defined diffusion limited current above -0.5 V (vs. SCE) which is not evident at the mercury plated copper RDE with higher disulphide concentrtions. Below -0.5 V (vs. SCE) the reduction of dissolved L-cystine hydrochloride is under mixed kinetic-mass transport control followed by pure kinetic control at more positive

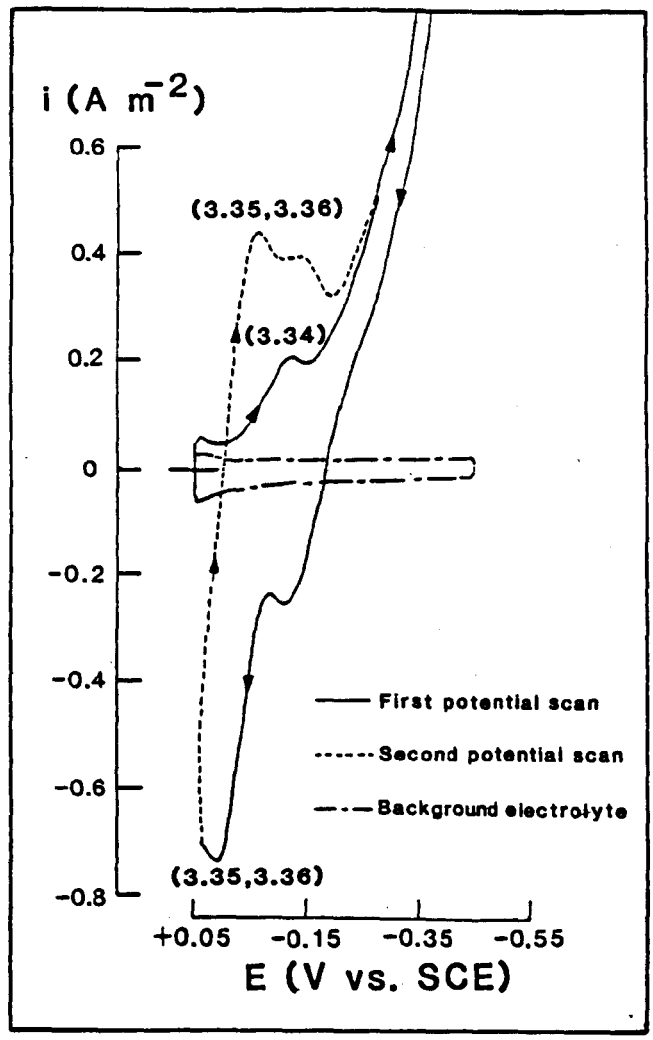

FIGURE 3.20 Cyclic voltammetry of 0.25 mol m^{-3} L-cystine hydrochloride in aqueous 0.1 mol dm^{-3} HCl at a HMDE. Potential sweep rate 100 mV s^{-1}. Electrolyte deoxygenated with N_2. Temperature 25°C.

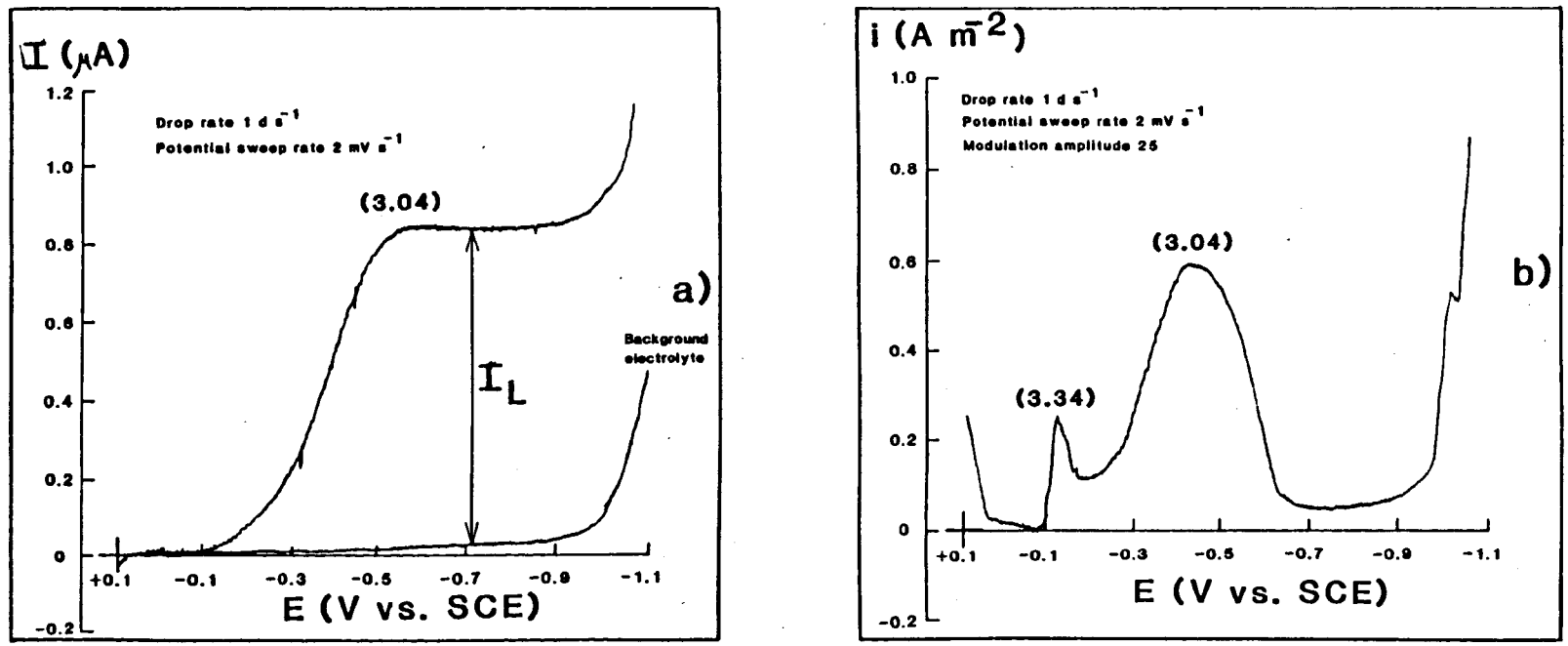

FIGURE 3.21 a) Sampled d.c. and b) differential pulse polarogram of 0.1 mol m^{-3} L-cystine hydrochloride in aqueous 0.1 mol dm^{-3} HCl deoxygenated with N_2. Temperature 25°C.

potentials.

At L-cystine hydrochloride concentrations higher than 0.1 mol m^{-3} cyclic voltammograms have not been reported in acid electrolytes. Figure 3.22a shows there is a complete blockage of the electrode surface by the amino acids on the cathodic potential scan and a sharp change in the current typical of adsorption phenomena in the return anodic scan. In agreement with the presence of adsorption phenomena sampled d.c. polarograms (Figure 3.22b) show a large capillary maximum and differential pulse polarograms (Figure 3.22c) show sharp changes in the current.

In aqueous 2.0 mol dm^{-3} hydrochloric acid, the reduction of adsorbed L-cystine hydrochloride (and the reversible reduction of mercury cysteinate in cyclic voltammograms) is obscured by the reduction of calomel (reaction 3.37).

$$Hg_2Cl_2 + 2e^- \rightleftharpoons 2Hg + 2Cl^- \qquad (3.37)$$

Cyclic voltammograms in the acid background electrolyte show the reported [24] reversible peaks for electrode reaction (3.37) in the critical potential range (Figure 3.23). The irreversible, diffusion controlled reduction of solution phase L-cystine hydrochloride to L-cysteine hydrochloride is still evident, however, in voltammograms (Figure 3.24). In aqueous 2.0 mol dm^{-3} hydrochloric acid cyclic voltammograms are recorded with an anodic limit of -0.2 V (vs. SCE) to ensure a calomel free electrode surface.

3.8.2 Kinetic Parameters

The sampled d.c. and cyclic voltammograms can be analysed to yield the kinetic parameters for the reduction of dissolved L-cystine hydrochloride (reaction 3.04).

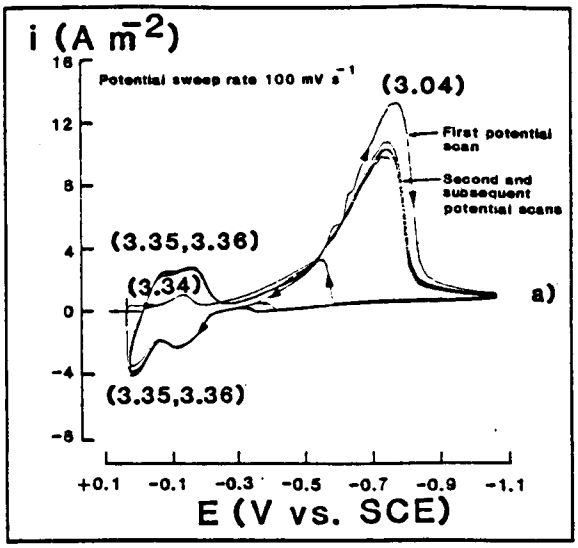

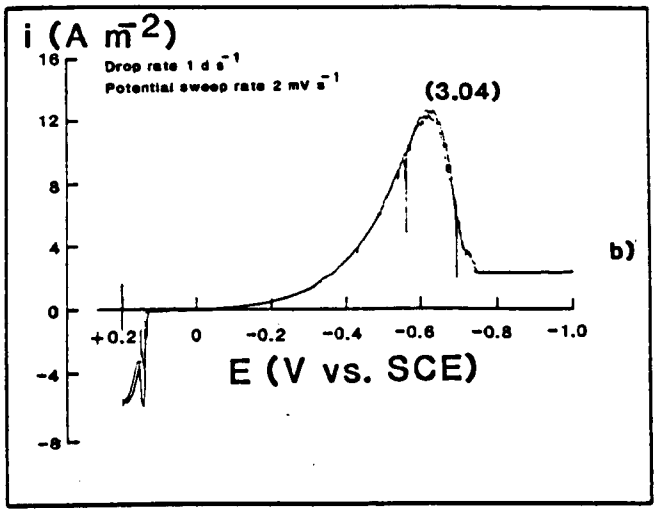

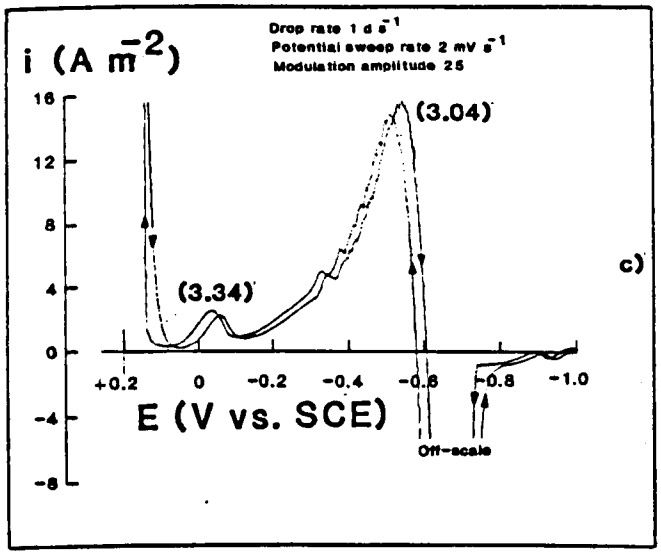

a) Cyclic voltammogram at a HMDE
b) Sampled d.c. polarogram at a SMDE
c) Differential pulse polarogram at a SMDE

FIGURE 3.22 Voltammograms of 0.75 mol m^{-3} L-cystine hydrochloride in aqueous 0.1 mol dm^{-3} HCl. Electrolyte deoxygenated with N_2 Tempearature 25°C.

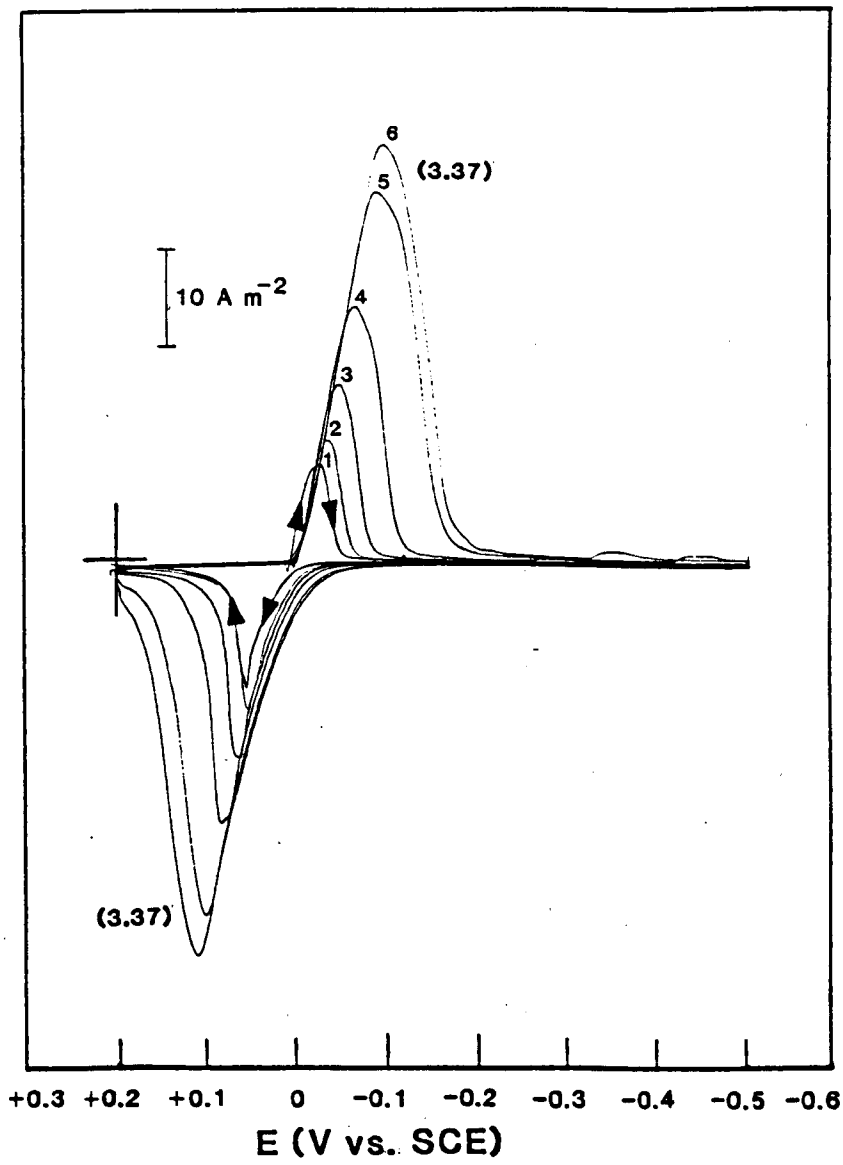

FIGURE 3.23 Cyclic voltammogram of aqueous 2.0 mol dm^{-3} HCl at a HMDE. Electrolyte deoxygenated with N_2. Temperature 25°C. Potential sweep rate 1. 25 mV s^{-1} 2. 50 mV s^{-1} 3. 100 mV s^{-1} 4. 200 mV s^{-1} 5. 400 mV s^{-1} and 6. 500 mV s^{-1}.

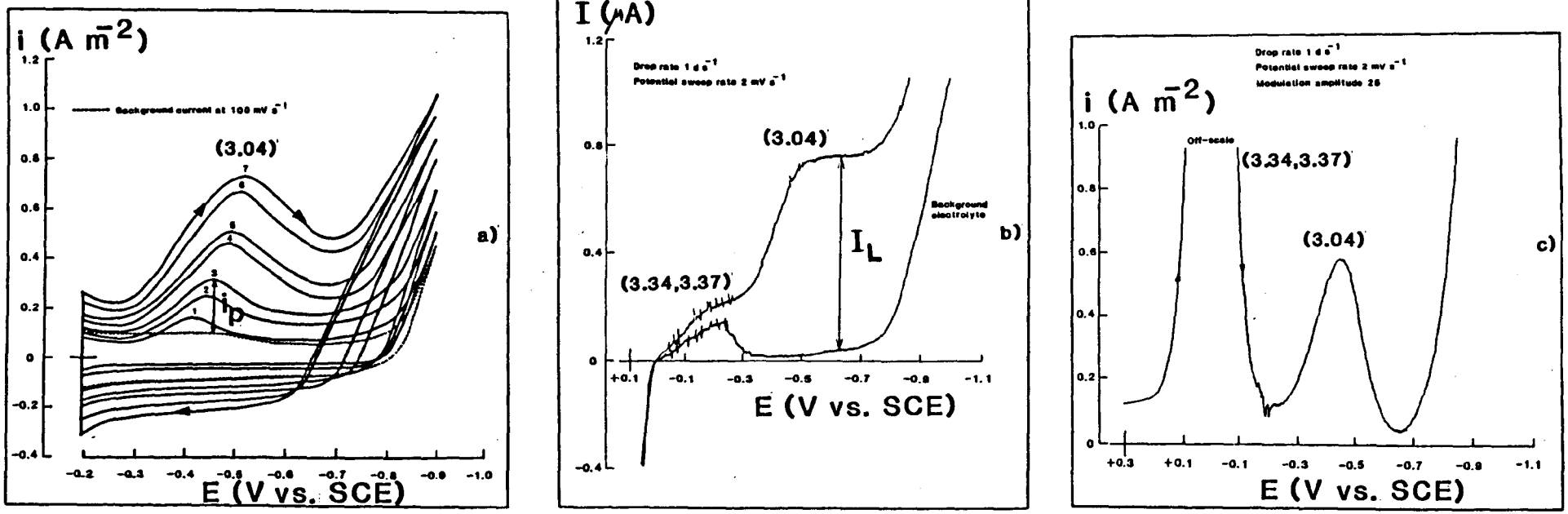

a) Sweep rate dependence of cyclic voltammograms at a HMDE. Potential sweep rates as for Figure 3.17. b) sampled d.c. polarogram at a SMDE and c) differential pulse polarogram at a SMDE.

FIGURE 3.24 Voltammograms of 0.1 mol m^{-3} L–cystine hydrochloride in aqueous 2.0 mol dm^{-3} HCl. Electrolyte deoxygenated with N_2. Temperature 25°C.

(a) Sampled d.c. Polarography

Equation (3.25) may be applied to sampled d.c. polarograms to yield the kinetic paramters [5].

$$-\log\left[\frac{1}{i}-\frac{1}{i_L}\right] = -\frac{\alpha_c F}{2.303\ RT}E + \log\left(n\ F\ k_f^o\ c_b\right) \qquad (3.25)$$

Figure 3.25 shows the mass transfer corrected Tafel plot for the polarogram in Figure 3.21, from which the diffusion limited current density was readily measured. A minor background current was subtracted at the limiting current as shown in Figure 3.21. From this Tafel plot, at 25°C, the Tafel slope is (183 ± 2) mV/decade, α_c is (0.32 ± 0.01) and k_f^o is (2.3 ± 0.2) x 10^{-7} m s^{-1}. The Tafel slope is similar to that measured with higher disulphide concentrations at the mercury plated copper RDE, but k_f^o is about 10^3 larger, reflecting much more facile kinetics of electron transfer.

There is an alternative method of obtaining the kinetic parameters. For an electrochemically, irreversible first order reaction, under mixed kinetic-mass transport control the time dependent current density is given by [25] (assuming semi-infinite linear diffusion):

$$i = n\ F\ k_f\ c_b \exp\left(\frac{k_f^2\ t}{D}\right)\ \operatorname{erfc}\left[k_f\left(\frac{t}{D}\right)^{1/2}\right] \qquad (3.38)$$

or

$$i = \left(\frac{n\ F\ D^{1/2}\ c_b}{t^{1/2}}\right)\lambda \exp\left(\lambda^2\right)\operatorname{erfc}\left(\lambda\right) \qquad (3.39)$$

where $\lambda = k_f t^{1/2}/D^{1/2}$

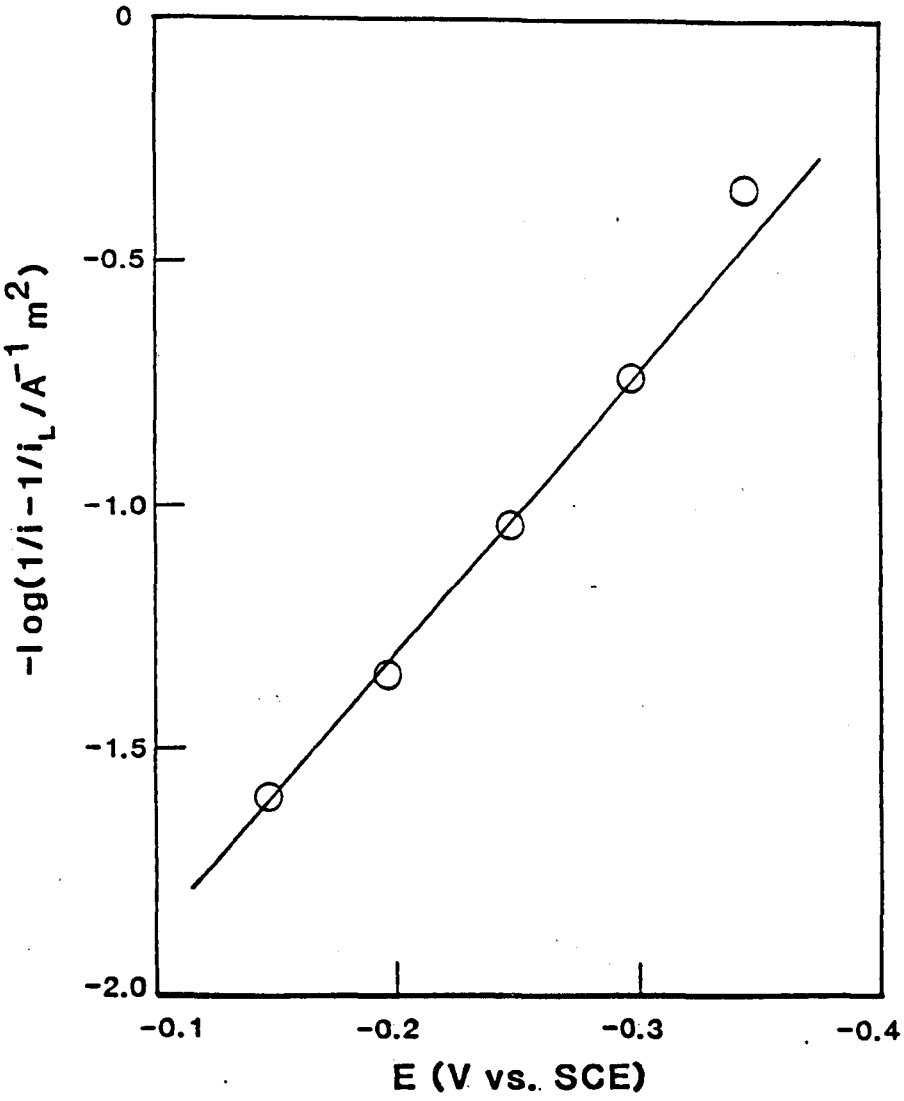

FIGURE 3.25 Mass transport corrected Tafel plot for L-cystine hydrochloride reduction at a SMDE. 0.1 mol m^{-3} L-cystine hydrochloride in aqueous 0.1 mol dm^{-3} HCl deoxygenated with N_2. Temperature 25°C. The background current is subtracted.

The diffusion limited current density is given by the Cottrell equation which is

$$i_L = \frac{n F D^{1/2} c_b}{(\pi t)^{1/2}} \qquad (3.40)$$

Combining equations (3.39) and (3.40) gives

$$\frac{i}{i_L} = \pi^{1/2} \lambda \exp(\lambda^2) \operatorname{erfc}(\lambda) \qquad (3.41)$$

This equation can be modified for a DME. The increasing electrode area during measurements, due to growth of the mercury drop, cancels out of the i/i_L ratio and need not be considered. The stretching effect (i.e. at any selected time expansion of the drop causes the thickness of the diffusion layer to be reduced so that larger currents flow) essentially increases the diffusion coefficient by 7/3 [25]. Introducing this correction into equation (3.41) gives

$$\frac{i}{i_L} \simeq \pi^{1/2} \left(\frac{3}{7}\right)^{1/2} \lambda \exp\left[\left(\frac{3}{7}\right) \lambda^2\right] \operatorname{erfc}\left[\left(\frac{3}{7}\right)^{1/2} \lambda\right]$$

or

$$\frac{i}{i_L} \simeq F_1\left(\frac{\chi}{2}\right) \qquad (3.42)$$

where $\chi = \left(\frac{12}{7}\right)^{1/2} \lambda$

Koutecky solved this problem more rigorously and expressed the result as [26,27]:

$$\frac{i}{i_L} = F_2(\chi) \qquad (3.43)$$

where $F_2(\chi)$ is a numeric function computed from a power series. Table 3.8 gives some representative values. Bard and Faulkner noted [25] equation (3.42) gives ratios consistently high, by margins ranging up to about 10%, compared with equation (3.43).

From a sampled d.c. polarogram measurement of i/i_L yields $F_2(\chi)$. Assuming the diffusion coefficient of the reactant is known (a disadvantage over the previous method) k_f is obtained (i.e. $\chi = (12/7)^{\frac{1}{2}} k_f t^{\frac{1}{2}}/D^{\frac{1}{2}}$) and from a plot of log k_f against E (see equation 3.24) the kinetic parameters are available.

Table 3.9 lists values of i/i_L (measured from the polarogram in Figure 3.21), the corresponding $F_2(\chi)$ value and the calculated k_f at the cathode potential corresponding to the current i (assuming the diffusion coefficient of L-cystine hydrochloride is 5.0×10^{-10} m^2 s^{-1} at 25°C). The large effect the cathode potential has on k_f is clearly evident.

TABLE 3.8 Shape function of a totally irreversible polarographic wave [20,21].

i/i_L	$F_2(\chi)$	i/i_L	$F_2(\chi)$
0.0428	0.05	0.5970	1.4
0.0828	0.1	0.6326	1.6
0.1551	0.2	0.6623	1.8
0.2189	0.3	0.6879	2.0
0.2749	0.4	0.7391	2.5
0.3245	0.5	0.773	3.0
0.3688	0.6	0.825	4.0
0.4086	0.7	0.8577	5.0
0.4440	0.8	0.9268	10.0
0.4761	0.9	0.9629	20.0
0.5050	1.0	0.9851	50.0
0.5552	1.2	1	∞

TABLE 3.9 Values of k_f from sampled d.c. polarography.

0.1 mol m^{-3} L-cystine hydrochloride in aqueous 0.1 mol dm^{-3} HCl. Temperature 25°C, D = 5.0 x 10^{-10} m^2s^{-1} and t = 1 d s^{-1}.

E (mV vs. SCE)	i/i_L	$F_2(\chi)$	k_f (m s^{-1})
-395	0.740	2.5	4.27×10^{-5}
-345	0.530	1.146	1.96×10^{-5}
-295	0.341	0.555	9.48×10^{-6}
-245	0.213	0.292	4.99×10^{-6}
-195	0.130	0.168	2.87×10^{-6}
-145	0.073	0.088	1.50×10^{-6}

The plot of log k_f against E is shown in Figure 3.26. As predicted by equation (3.24) a straight line relationship is obtained. From the gradient the Tafel slope is (183 ± 4) mV/decade and α_c is (0.32 ± 0.02) and from the intercept k_f^0 is (2.3 ± 0.3) x 10^{-7} m s^{-1}, using a least squares analysis. These values are identical, within the limit of experimental error, to those obtained from the mass transport corrected Tafel plot.

(b) Cyclic Voltammetry

The equations outlined in Section 3.5.1 have to be modified to take account of spherical diffusion to the HMDE. Nicholson and Shain [20] have shown

$$i = i_{(planar)} + i_{(spherical)} \qquad (3.44)$$

where

$$i_{(planar)} = n F c_b D^{1/2} v^{1/2} \left[\frac{\alpha_c F}{RT}\right]^{1/2} \pi^{1/2} \chi(bt)$$

$$i_{(spherical)} = n F c_b D \left[\frac{1}{r}\right] \Phi(bt)$$

where r is the drop radius and $\Phi(bt)$ is a current function which is listed in Table 3.4. Using equation (3.44), Table 3.10 shows for the conditions of L-cystine hydrochloride reduction the predicted effect of spherical diffusion on the current close to the peak potential in linear sweep voltammograms.

At potential sweep rates at, or above, 100 mV s^{-1} spherical diffusion has little effect upon Ep but at lower sweep rates E_p moves cathodically. Thus at the HMDE at these higher sweep rates, for L-cystine hydrochloride reduction equation (3.30) should still apply. Consequently a plot of Ep against log v should be a

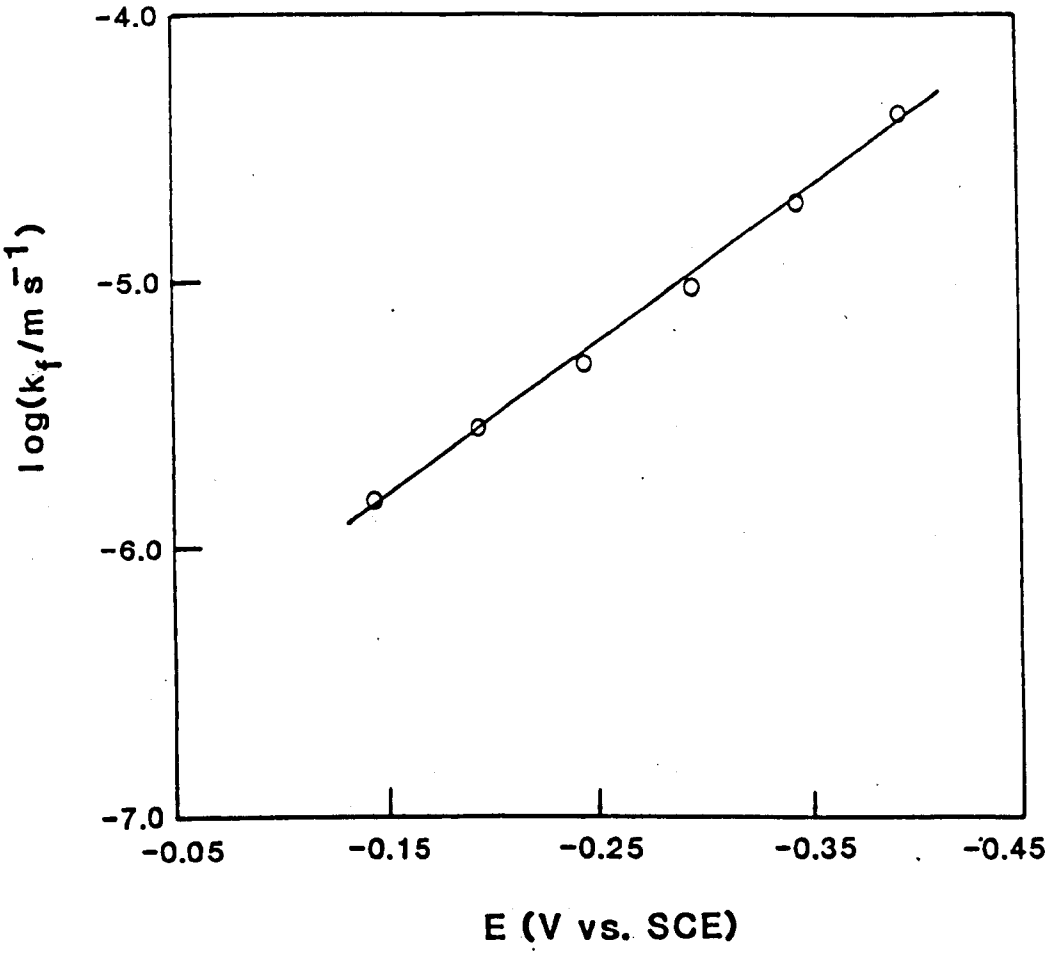

FIGURE 3.26 Plot of log k_f against E.

TABLE 3.10 The effect of spherical diffusion on the reduction of L-cystine hydrochloride in linear sweep voltammetry.

$A = 2.1 \times 10^{-6}$ m^2 ($r = 4.09 \times 10^{-4}$ m), $n = 2$, $C_b = 0.1$ mol m^{-3} $\alpha_c = 0.32$ and $D = 5.0 \times 10^{-10}$ m^2 s^{-1} at 25°C.

The current functions $\pi^{\frac{1}{2}}\chi(bt)$ and $\Phi(bt)$ are listed in Table 3.4.

Electrode Potential (mV)	v (mV s^{-1})	$\pi^{\frac{1}{2}}\chi(bt)$	I(PLANE) (μA)	$\Phi(bt)$	I(SPHERICAL) (μA)	I(TOTAL) (μA)
E_p	25	0.4958	0.2508	0.694	0.0344	0.2852
(E_p-10)		0.493	0.2494	0.755	0.0374	0.2868
(E_p-15)		0.485	0.2453	0.823	0.0408	0.2861
E_p	50	0.4958	0.3546	0.694	0.0344	0.3890
(E_p-10)		0.493	0.3526	0.755	0.0374	0.3900
(E_p-15)		0.485	0.3469	0.823	0.0408	0.3877
E_p	100	0.4958	0.5015	0.694	0.0344	0.5359
(E_p-10)		0.493	0.4987	0.755	0.0374	0.5361
(E_p-15)		0.485	0.4906	0.823	0.0408	0.5314
E_p	200	0.4958	0.7092	0.694	0.0344	0.7436
(E_p-10)		0.493	0.7052	0.755	0.0374	0.7426
E_p	400	0.4958	1.0030	0.694	0.0344	1.0374
(E_p-10)		0.493	0.9974	0.755	0.0374	1.0348
E_p	500	0.4958	1.1214	0.694	0.0344	1.1558
(E_p-10)		0.493	1.1151	0.755	0.0374	1.1525

straight line and yield the Tafel slope, α_c and k_f^o. At lower sweep rates deviation from a straight line is expected. Figure 3.27 shows a typical plot of E_p against log v for L-cystine hydrochloride reduction at the HMDE. The cathodic shift in E_p at potential sweep rates below 100 mV s^{-1} is evident. From a least squares analysis of the remaining points the Tafel slope is (187 ± 6) mV/decade, α_c is (0.32 ± 0.02) and k_f^o is (1.9 ± 0.2) x 10^{-7} m s^{-1} (assuming D is 5.0 x 10^{-10} m^2 s^{-1} at 25°C). Strong evidence for the accuracy of the kinetic parameters is provided by the close comparison between the values obtained using linear sweep voltammetry and sampled d.c. polarography (see Table 3.11). For 0.1 mol m^{-3} L-cystine hydrochloride in aqueous 2.0 mol dm^{-3} hydrochloric acid all the plots listed in Table 3.11 show the kinetic parameters for the reduction are unchanged. Together with an identical finding for 10 mol m^{-3} L-cystine hydrochloride using linear sweep voltammetry at the mercury disc electrode (see Section 3.6.1), this provides confidence in the applicability of the measured values for the electrosynthesis conditions.

TABLE 3.11 Kinetic parameters from sampled d.c. and linear sweep voltammetry at the mercury drop.

0.1 mol m^{-3} L-cystine hydrochloride in aqueous 0.1 mol dm^{-3} HCl at 25°C.

	Sampled d.c. Polarography		Linear Sweep Voltammetry
Plot	log k_f vs E - log[1/i-1/i_L]vs E		E_p vs log v
Tafel slope (mV/decade)	183 ± 4	183 ± 2	187 ± 6
α_c	0.32 ± 0.02	0.32 ± 0.01	0.32 ± 0.02
k_f^o (10^{-7} m s^{-1})	2.3 ± 0.3	2.3 ± 0.2	1.9 ± 0.2

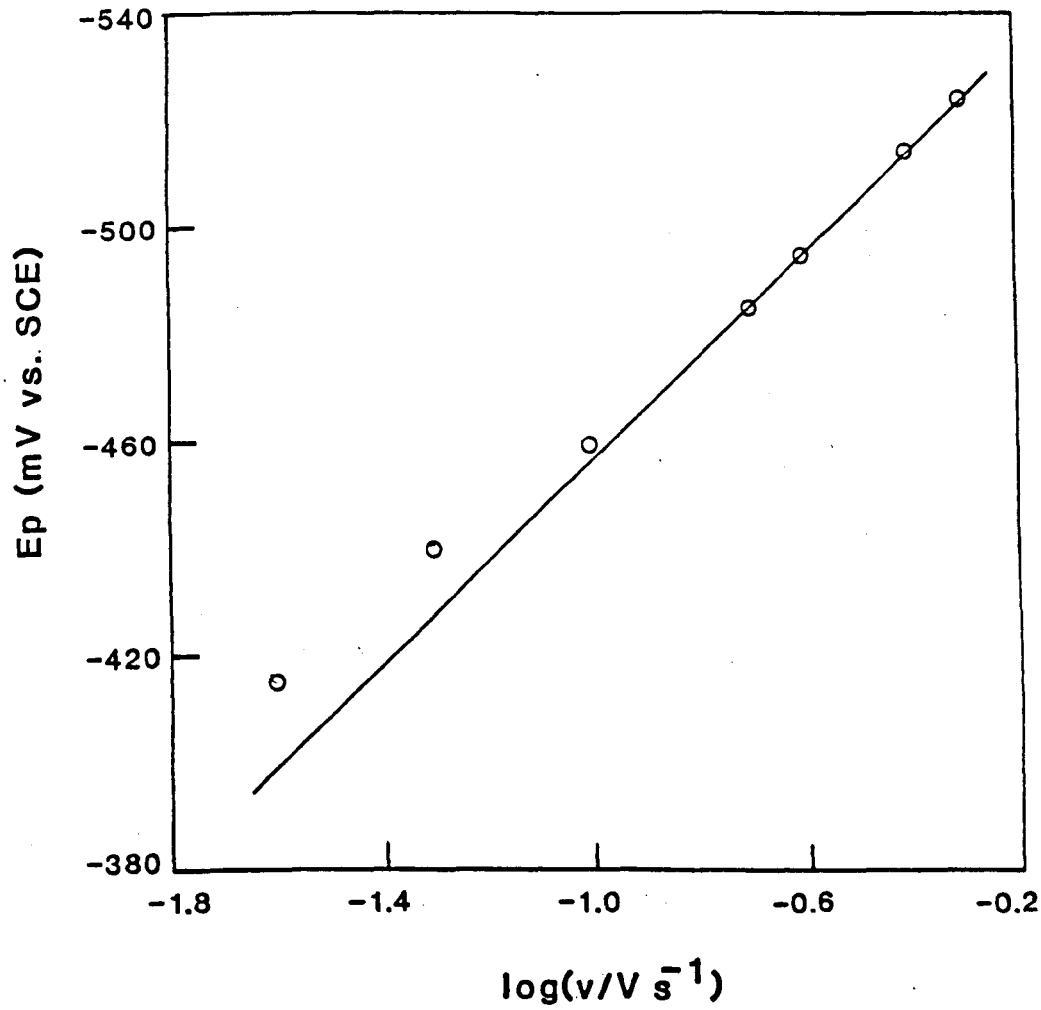

FIGURE 3.27 Dependence of E_p on log v in linear sweep voltammograms at a HMDE. 0.1 mol m^{-3} L-cystine hydrochloride in aqueous 0.1 mol dm^{-3} HCl deoxygenated with N_2. Temperature 25°C. The points are the average of 5 separate measurements.

3.8.3 Accuracy of the Available $E^{o'}$ Values for the L-Cystine/L-Cystine Redox Couple

Table 1.1 lists the reported $E^{o'}$ values for the couple. Using $E^{o'}$ it is possible to determine k^o from the sampled d.c. and cyclic voltammograms in Figures 3.21 and 3.17 respectively. For sampled d.c. polarography equation (3.25) can be written in the form

$$-\log\left[\frac{1}{i}-\frac{1}{i_L}\right] = -\frac{\alpha_c F}{2.303\ RT}\left[E - E^{o'}\right] + \log\left(n\ F\ k^o\ c_b\right) \qquad (3.45)$$

From equation (3.45) a plot of $-\log[1/i - 1/i_L]$ against $[E-E^{o'}]$ should be a straight line which gives k^o from the intercept. In Section 3.5.1 the linear sweep voltammetry equations are written in terms of k^o. From equation (3.30) a plot of E_p against log v should give k^o from the intercept provided the diffusion coefficient of L-cystine hydrochloride is known.

$$E_p = E^{o'} - \frac{RT}{\alpha_c F}\left[0.780 + 2.303\ \log\left(\frac{D^{1/2}}{k^o}\right) + 2.303\ \log\left(\frac{\alpha_c F v}{RT}\right)^{1/2}\right] \qquad (3.30)$$

From Table 1.1 the most likely value of $E^{o'}$ appears to be +0.08 V (vs. NHE) at pH 0. This is equivalent to -0.22 V (vs. SCE) at pH 1.0 (i.e. close to pH 1.1 of aqueous 0.1 mol dm^{-3} hydrochloric acid). Using this $E^{o'}$ from the plot of $-\log[1/i - 1/i_L]$ against E for the sampled d.c. polarogram in Figure 3.21 a k^o value of $(3.2\pm0.2) \times 10^{-6}$ m s^{-1} is obtained. The plot of E_P against log v for

the cyclic voltammograms in Figure 3.17, assuming the diffusion coefficient of the disulphide is 5.0×10^{-10} m^2 s^{-1} at 25°C, gives a k^o value of $(3.7 \pm 0.2) \times 10^{-6}$ m s^{-1}.

Electrochemical reactions can be termed electrochemically reversible, quasi-reversible or irreversible. For the L-cystine/L-cysteine couple to be reversible would require the concentration of the amino acids at the electrode surface to be constant, as given by the Nernst equation (equation 3.46), for each potential on the current-potential curve.

$$E = E^{o'} - \frac{RT}{2F} \ln \frac{[RSH]^2}{[RSSR]\,[H^+]^2} \qquad (3.46)$$

This holds rigorously only when k^o is infinitely large, but in practice k^o must only be large enough to keep the concentrations close to those predicted by equation (3.46) during the experiment. Simply put, in a long experiment, the redox system has a long time to attain equilibrium. The shorter the experiment, the greater the chance of viewing quasi-reversible and irreversible behaviour. Indeed in cyclic voltammetry studies as the potential sweep rate is changed over several orders of magnitude, a process may appear reversible at low potential sweep rates but irreversible at much higher sweep rates [28]. The commonly accepted range of rate constants for the various classes of behaviour, expected using the techniques employed in this section of the thesis to obtain k^o, are given in Table 3.12.

TABLE 3.12 Relationship between k^o and electrochemical reversibility for polarography and cyclic voltammetry.

Technique	Electrochemical Reversibility	k^o (m s^{-1})	
Polarography [Ref. 30,31]	Reversible	$>2\times10^{-4}$	
	Quasi-reversible	2×10^{-4} to 5×10^{-7}	
	Irreversible	$<5\times10^{-7}$	
Cyclic Voltammetry [Ref.28,29]		Values at 10 mV s^{-1}	500 mV s^{-1}
	Reversible	$>3\times10^{-4}$	$>2\times10^{-3}$
	Quasi-reversible	3×10^{-4} to 2×10^{-8}	2×10^{-3} to 1.5×10^{-7}
	Irreversible	$<2\times10^{-8}$	$<1.5\times10^{-7}$

On this basis of Table 3.12 the measured k^o for L-cystine hydrochloride reduction suggests the reaction is quasi-reversible. That the reduction is <u>not</u> quasi-reversible is confirmed by sampled d.c. polarography. Addition of up to 0.1 mol m^{-3} L-cysteine hydrochloride to 0.1 mol m^{-3} L-cystine hydrochloride in aqueous 0.1 mol dm^{-3} hydrochloric acid has no effect on the measured reduction current even at potentials corresponding to the bottom of the reduction wave. If the reaction is quasi-reversible the back reaction (i.e. L-cysteine hydrochloride oxidation to L-cystine hydrochloride) should progressively reduce the measured current at a given potential, as the thiol concentration is increased.

To obtain a k^o value of about 5×10^{-7} m s^{-1} (the maximum value associated with an irreversible reaction in Table 3.12) from equation (3.45) or

equation (3.30) requires an $E^{o'}$ of ca. +0.24 V (vs. NHE) at pH 0. To obtain a smaller k^o requires a more positive $E^{o'}$. Inspection of Table 1.1 shows all $E^{o'}$ values are negative of + 0.191 V (vs. NHE) at pH 0. This shows an accurate $E^{o'}$ is not available for the L-cystine/L-cysteine redox couple in hydrochloric acid media.

3.8.4 The Diffusion Coefficient of L-Cystine Hydrochloride from Sampled d.c. Polarography

Ilkovic derived [25] for a diffusion limited current in sampled d.c. polarograms at 25°C

$$I_L = 708\ n\ D^{1/2}\ c_b\ m_{Hg}^{2/3}\ t^{1/6} \qquad (3.47)$$

where I_L is in μA, D in $cm^2\ s^{-1}$, c_b in mol m^{-3}, m_{Hg} is the mass flow rate of mercury in mg s^{-1} (determined by weighing a measured number of mercury drops) and t is the drop time in s. Measurement of I_L allows determination of D provided n and c_b are known. From equation (3.47) the diffusion coefficient of L-cystine hydrochloride in aqueous 0.1 mol dm^{-3} hydrochloric acid is 5.3×10^{-10} $m^2\ s^{-1}$ at 25°C. In more concentrated aqueous 2.0 mol dm^{-3} hyrochloric acid the diffusion coefficient is reduced to 4.2×10^{-10} $m^2\ s^{-1}$ at 25°C.

3.8.5 Effect of Adsorption of L-Cystine Hydrochloride at the Mercury Surface on the Electrode Kinetics of the Electrosynthesis Reaction

The peak for reduction of adsorbed L-cystine hydrochloride in cyclic voltammograms indicates the disulphide is adsorbed at mercury at potentials just positive of the main reduction wave for dissolved L-cystine hydrochloride. If the adsorption process can be described by the Langmuir adsorption isotherm there are a number of assumptions which must be satisfied. These are;

1. There are a fixed number of adsorption sites. At equilibrium at a given temperature and concentration a fraction θ is occupied and $(1-\theta)$ unoccupied i.e. the coverage is less than monolayer.
2. Each site can accommodate only one adsorbed molecule.
3. The heat of adsorption is the same for all sites and does not depend upon θ.
4. There is no interaction between molecules on different sites.

It has been shown [30] that for this isotherm

$$\frac{1}{\tau} = \frac{1}{\tau_s} + \frac{1}{\tau_s \beta' c_b} \qquad (3.48)$$

where τ is the surface excess of adsorbent, τ_s the surface excess corresponding to saturation coverage, β' the adsorption coefficient and c_b the bulk concentration of adsorbent. For L-cystine hydrochloride adsorption at mercury τ can be calculated from the peak in cyclic voltammograms, since by definition

$$\tau = \frac{q}{n F A} \qquad (3.49)$$

where q is the charge under the peak in the voltammogram.

From equation (3.48) a plot of $1/\tau$ against $1/c_b$ is a straight line from which τ_s can be calculated from the intercept. Figure 3.28 shows at the HMDE a plot of $1/\tau$ against $1/c_b$ is a straight line for adsorption of L-cystine hydrochloride. From the intercept, using a least squares analysis, τ_s is estimated to be $(2.7 \pm 0.8) \times 10^{-7}$ moles m^{-2}. Based upon this saturation coverage the surface coverage increases from 0.01 to 0.68 as the bulk disulphide concentration is raised from 0.025 mol m^{-3} to 0.1 mol m^{-3}.

Bard and Stankovich [23] constructed a model of L-cystine and calculated monolayer coverage, with the disulphide bond orientated on the electrode surface,

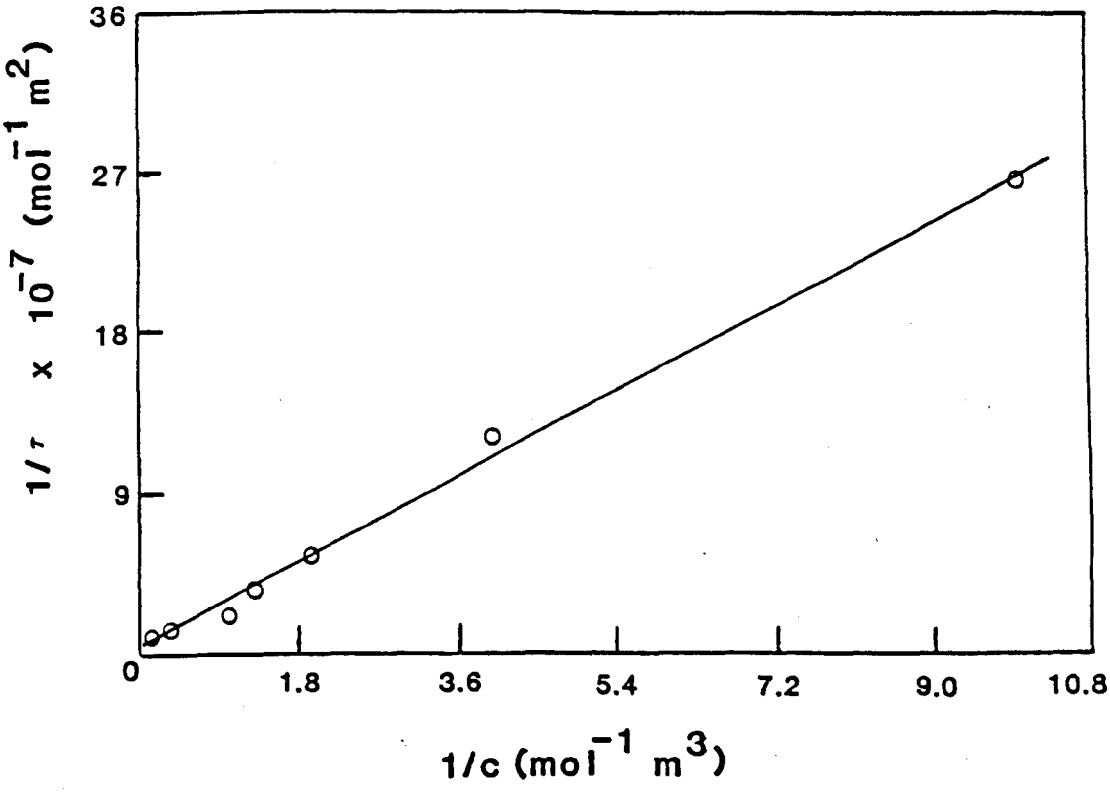

FIGURE 3.28 L-Cystine hydrochloride adsorption from aqueous 0.1 mol dm^{-3} HCl at a HMDE.

corresponded to 2.3 x 10^{-6} mol m^{-2}. They confirmed this value from the constant peak area in cyclic voltammograms recorded at pH 7 at bulk disulphide concentrations of 0.05 mol m^{-3} and above, which yielded a τ_S of 2.2 x 10^{-6} mol m^{-2}. This is a factor of 10 larger than the saturation coverage, τ_S, with adsorption from aqueous 0.1 mol dm^{-3} hydrochloric acid. There may be several reasons why monolayer coverage is achieved at pH 7 but not in acid media. There may be an effect linked directly to the concentration of protons in the double layer. Perhaps the L-cystine molecule must replace protons in the double layer to itself adsorb at the electrode surface and at lower pH there are more protons to displace. The ionised forms of L-cystine at a given solution pH, shown in Figure 1.2, may also help to partially explain the effect. In hydrochloric acid, the protonated amino groups of the L-cystine molecule have an associated hydrogen chloride molecule which must be accommodated. In buffered media at pH 7, not only are the hydrogen chloride molecules absent but the carboxyl groups are deprotonated and there is a resultant attraction to the positively charged amino groups. These effects may reduce, somewhat, the surface area occupied by the disulphide molecule.

Examination of much higher disulphide concentrations at the larger area stationary mercury disc electrode is illuminating. Between 4 mol m^{-3} and 10 mol m^{-3} L-cystine hydrochloride a large current spike is present on the peak for reduction of the adsorbed material (Figure 3.29). This is most likely due to rearrangement of L-cystine hydrochloride on the electrode surface after saturation coverage (as discussed earlier in Section 3.8.1 for mercury cysteinate reduction). Determination of the charge passed under the adsorption peak (ignoring the current spike) yields a saturation coverage of 3.1 x 10^{-7} mol m^{-2} in accord with the value derived from Figure 3.28. At disulphide concentrations below 4 mol m^{-3}

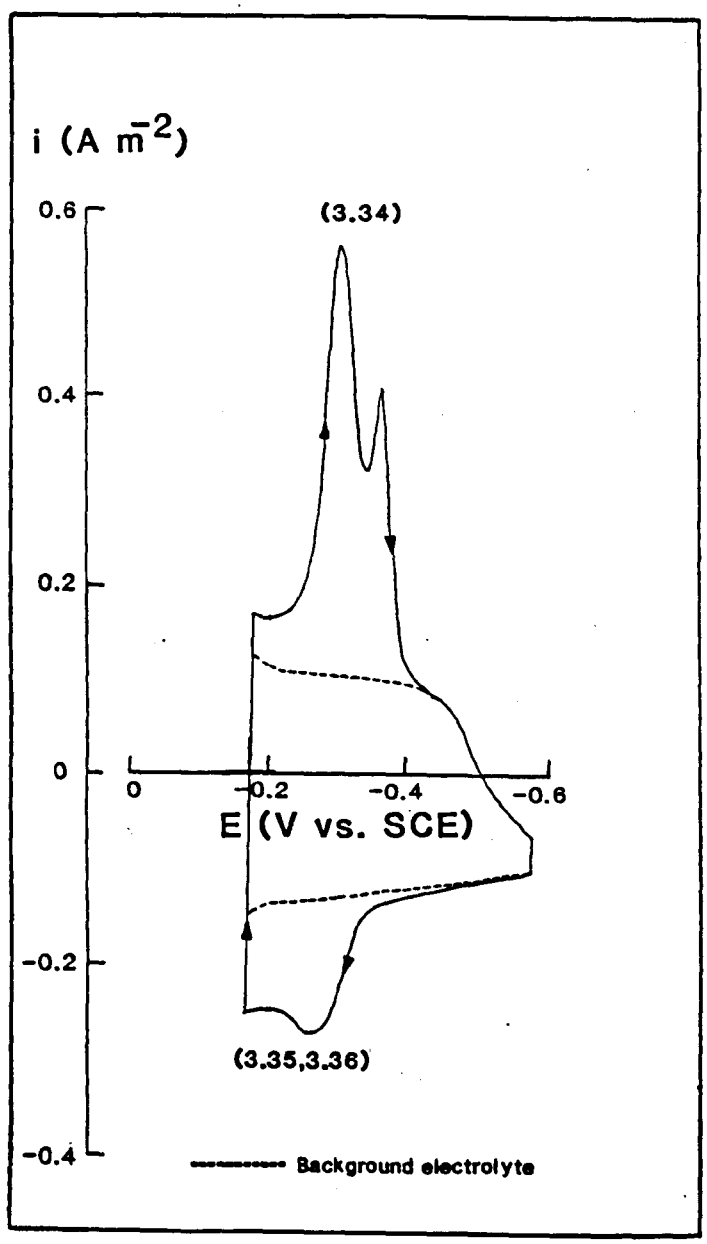

FIGURE 3.29 Cyclic voltammetry of 10 mol m^{-3} L-cystine hydrochloride in aqueous 0.1 mol dm^{-3} HCl showing disulphide adsorption peaks at a stationary mercury disc electrode. Potential sweep rate 100 mV s^{-1}. Electrolyte deoxygenated with N_2. Temperature 25°C.

the current spike is removed from the adsorption peak and the surface coverage is calculated to vary from 1.0 down to 0.90 at a bulk concentration of 0.4 mol m^{-3}. At these high coverages the Langmuir adsorption isotherm is not obeyed probably because of interaction between adjacent disulphide molecules on different sites.

Correlation of this adsorption data with the electrode kinetics of the electrosynthesis reaction does indicate there is a relationship. At the HMDE for θ between 0.01 and 0.68 values of $-\log[1/i - 1/i_L]$ at various electrode potentials (taken from mass transport correct Tafel plots) plotted against log (L-cystine hydrochloride concentration), are shown in Figure 3.30. The plot indicates the reaction is first order in the disulphide. Consequently over this range of surface coverage k_f^o and the electrode kinetics are unaltered. At $0.92 < \theta < 1.0$, however, the $-\log[1/i - 1/i_L]$ against log (L-cystine hydrochloride concentration) plot, shown in Figure 3.15, indicates the electrode kinetics become progressively more sluggish as the surface coverage increases which is reflected by ever decreasing k_f^o values (Table 3.7). At $\theta = 1$ the reaction is again first order in L-cystine hydrochloride and k_f^o and the electrode kinetics are independent of the reactant concentration.

The observed correlation might not be expected since the adsorbed disulphide is reduced prior to the reduction wave for the electrosynthesis reaction. The most likely explanation is further adsorption of the disulphide at electrode potentials on the main irreversible wave, with the adsorption strength sufficient to prevent reduction until potentials negative of the main irreversible wave are reached. Any adsorption post-peak may be hidden by copious hydrogen evolution from the background electrolyte. Strongly adsorbed reactants are known to give a post-peak in cyclic voltammograms [32]. Certainly the pure diffusion control of the reduction of dissovled L-cystine hydrochloride at potentials close to the peak in

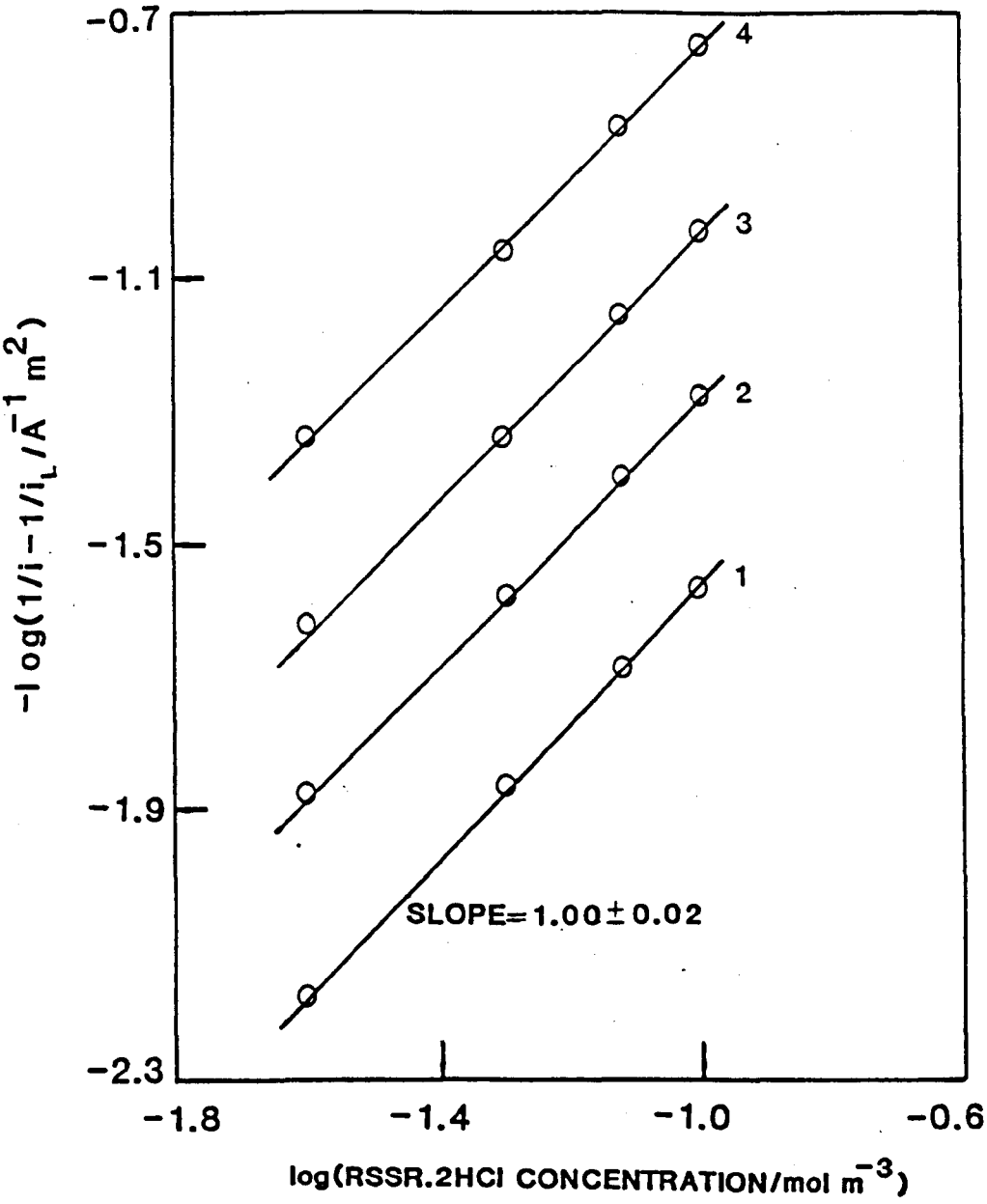

FIGURE 3.30 Plot of $-\log [1/i - 1/i_L]$ against log (RSSR.2HCl concentration) derived from sampled d.c. polarograms. Cathode potential 1. -0.145 V 2. -0.195 V 3. -0.245 V and 4. -0.295 V (vs. SCE).

cyclic voltammograms (e.g. as shown by the plot of i_p against $v^{\frac{1}{2}}$ (Figure 3.13) and the constant potential coulometry studies in Section 3.4.2) there is little reduction of adsorbed disulphide in this potential region. Also the disulphide molecule has a double positive charge in acid electrolyte which purely on an electrostatic basis suggests adsorption will be stronger at more negative potentials. There is some evience to support this argument from studies at the mercury drop electrode. At high disulphide concentrations there is evidence of strong adsoprtion phenomena in voltammograms and the irreversible wave for reduction of dissolved L-cystine hydrochloride is shifted to more negative potentials (see Figure 3.22). If this explanation is correct the unchanged k_f^o for $\theta = 1$ indicates reduction of dissolved L-cystine hydrochloride occurs through the adsorbed disulphide film.

3.8.6 Effect of pH on the Voltammograms

This will only be considered briefly since it is not of prime importance to the electrosynthesis and, in any case, in higher pH media there exists in the literature an extensive body of information from sampled d.c., differential pulse and cyclic voltammetry. This is reviewed in Section 1.4.2a.

The low solubility of the disulphide above pH 2 (i.e. about 0.5 mol m^{-3}) restricts studies to the mercury drop. At the larger area mercury plated copper rotating disc and stationary mercury disc electrodes the measured currents are barely above the level of the background at these disulphide concentrations. L-cystine reduction at the mercury drop, in the electrolytes listed in Table 2.2 (i.e. pH 1 to 13), produces similar sampled d.c., differential pulse and cyclic voltammograms to those previously published in the literuature [Chapter 1, references 20 to 23]. There are two clear, separate current responses for reduction of adsorbed and dissolved L-cystine, even in sampled d.c. polarograms above pH 2. Indeed the current plateau for reduction of the adsorbed material becomes

progressively more visible at higher pH (Figure 3.31). As predicted by the electrode reactions, shown below, both reduction waves shift cathodically as the pH is increased.

$$RSSR_{(ads.)} + 2H^+ + 2e^- \longrightarrow 2RSH \qquad (1.12)$$

$$RSSR + 2H^+ + 2e^- \longrightarrow 2RSH \qquad (1.04)$$

For the reduction of adsorbed L-cystine the Nernst equation (equation 3.46) predicts a shift of -59 mV/pH unit for the reversible reduction reaction. Figure 3.32 shows the variation of E_p for the reduction peak in cyclic voltammograms (this can be measured more accurately than the $E_{\frac{1}{2}}$ in sampled d.c. polarograms) with the electrolyte pH. Between pH 1 and 7 the predicted shift of -59 mV/pH unit is observed in support of electrode reaction (1.12). Also the higher saturation coverage of L-cystine at pH 7 compared with pH 1, eluded to earlier, is clearly evident.

Considering the more important reduction of dissolved L-cystine, at least in terms of the electrosynthesis, there is a particular piece of important information lacking in the literature - the reaction order with respect to protons. This can be measured from sampled d.c. polarograms, recorded at a constant L-cystine concentration in aqueous background electrolytes with a range of constant pH and a constant ionic strength (to negate possible salt and double layer effects). By definition [22] the proton reaction order for reduction of dissolved L-cystine is given by

$$m_{H^+} = \left[\frac{\partial \ -\log[1/i - 1/i_L]}{\partial \log c_b\,(H^+)} \right]_{E, c_b\,(RSSR)} \qquad (3.50)$$

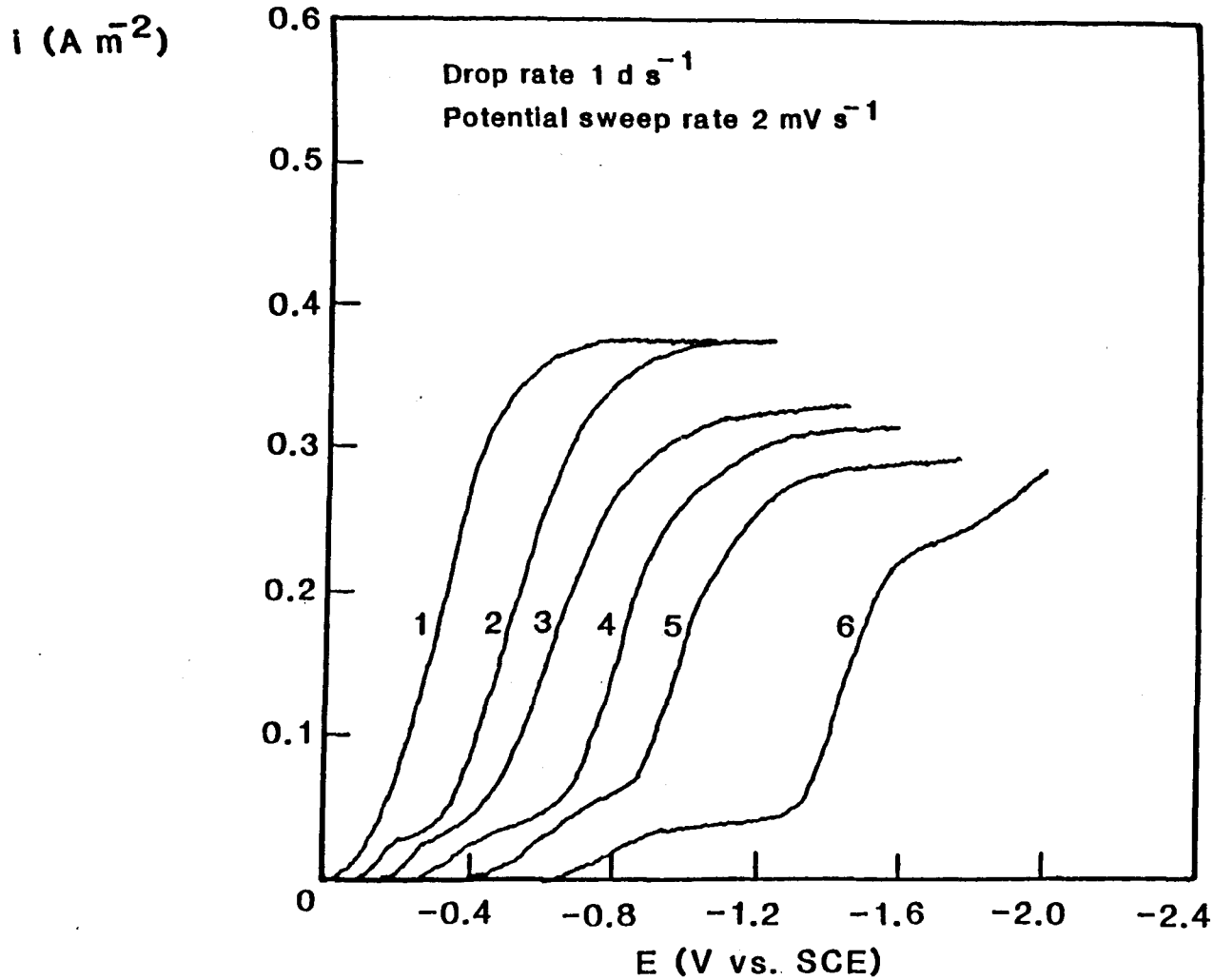

FIGURE 3.31 Variation of sampled d.c. polarograms with electrolyte pH. 0.1 mol m^{-3} L-cystine hydrochloride in various electrolytes of constant ionic strength (0.5 mol dm^{-3}) and pH prepared as detailed in Table 2.2. Electrolytes deoxygenated with N_2. Temperature 25°C. 1. pH 1.1 2. pH 2.0 3. pH 4.0 4. pH 6.0 5. pH 9.0 and 6. pH 13.0.

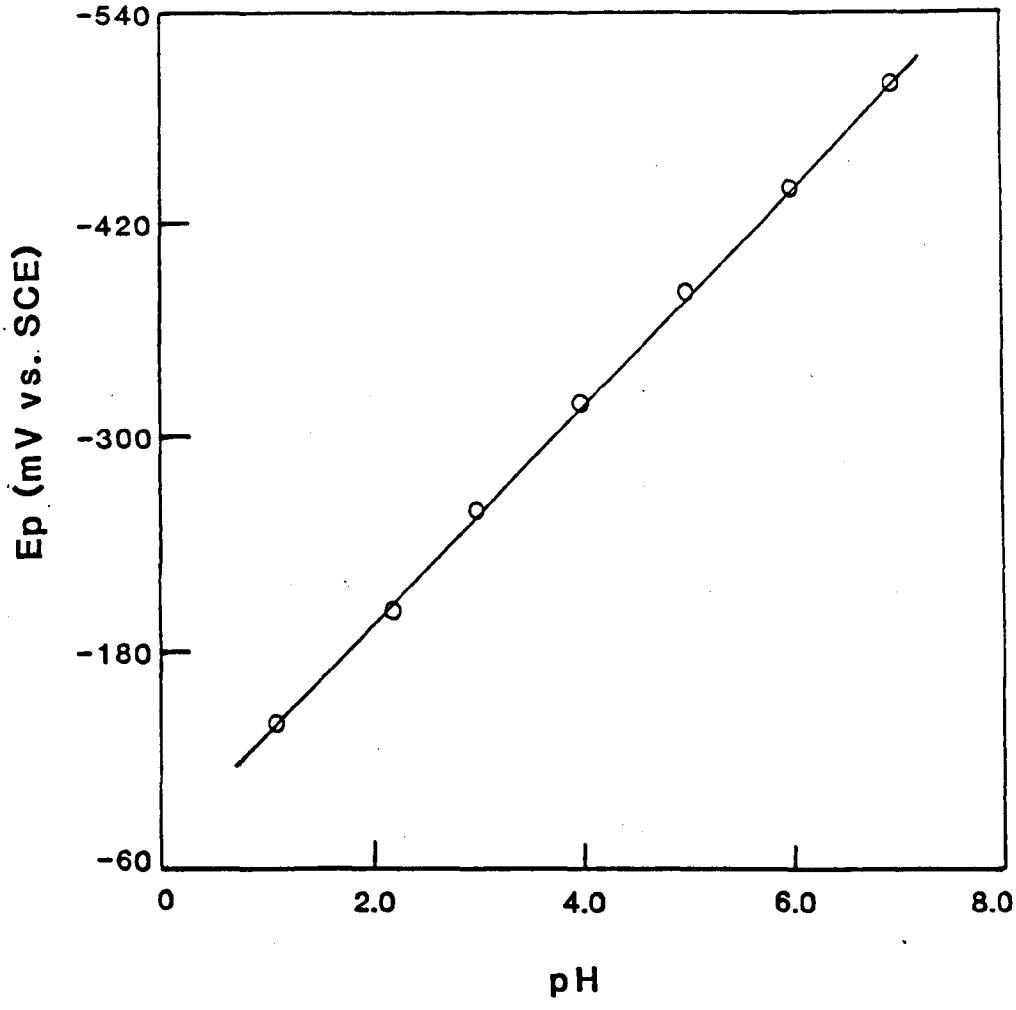

FIGURE 3.32 Variation with electrolyte pH of the peak potential for reduction of adsorbed L-cystine in cyclic voltammograms at a HMDE. 0.1 mol m^{-3} L-cystine in aqueous solutions of constant pH and ionic strength (0.5 mol m^{-3}) as detailed in Table 2.2. Temperature 25°C. Potential sweep rate 100 mV s^{-1}.

where $-\log[1/i - 1/i_L]$ is the mass transport corrected kinetic current for L-cystine reduction, $c_{b(H^+)}$ is the bulk proton concentration, $c_{b(RSSR)}$ the bulk concentration of L-cystine and E the electrode potential. A plot of $-\log[1/i - 1/i_L]$ against log $c_{b(H+)}$ should be a straight line with a slope equal to the desired reaction order. In practice it was necessary to restrict the range of pH to between 1.1 and 2.5. At higher pH values a constant electrode potential cannot be choosen at which the reduction current does not have some contribution from the reduction of adsorbed L-cystine (e.g. see Figure 3.31). An optimum cathode potential of -0.295 V (vs. SCE) is necessary to obtain even this limited range of pH. The resultant plot of $-\log[1/i - 1/i_L]$ against electrolyte pH is shown in Figure 3.33. In the narrow pH range the proton reaction order is +1.

3.9 MECHANISM OF THE ELECTROSYNTHESIS OF L-CYSTEINE HYDROCHLORIDE FROM L-CYSTINE HYDROCHLORIDE

Listed in Table 3.13 are a number of possible mechanisms for the reduction. Two reasonable assumptions have been used in compiling the list, namely that proton transfers are assumed to be faster than electron transfers [17] and electrons are assumed to be transferred one at a time [e.g. 29]. In order to distinguish between the mechanisms, for each possible pathway predicted values for the reaction order for L-cystine hydrochloride, the reaction order for protons and the cathodic transfer coefficient are given in the Table. The cathodic transfer coefficients were obtained from equation (3.55) which applies for multistep electrode processes [33].

$$\alpha_c = \frac{\gamma_c}{\nu} + r\,\beta \qquad (3.55)$$

In equation (3.55) γ_c is the number of electrons preceeding the RDS, ν (the

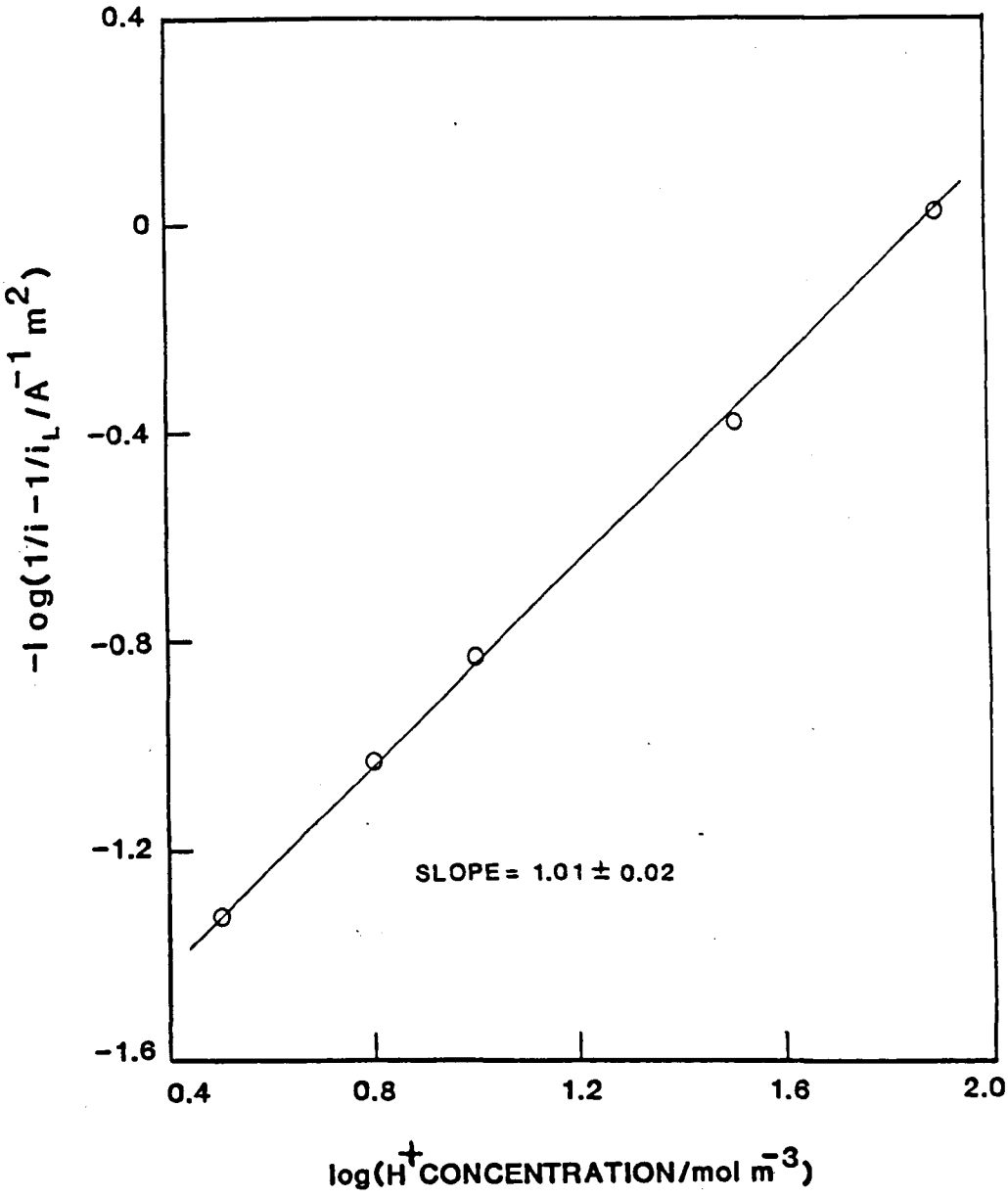

FIGURE 3.33 Plot of $-\log [1/i - 1/i_L]$ against log (H^+ concentration) derived from sampled d.c. polarograms. 0.1 mol m^{-3} L-cystine in aqueous HCl and KCl solutions of constant pH and ionic strength as detailed in Table 2.2. Temperature 25°C. Cathode potential -0.295 V (vs. SCE).

TABLE 3.13 Possible mechanisms for L-cystine hydrochloride reduction and their associated reaction orders and transfer coefficient.

	Mechanism	Reaction Order RSSR.2HCl	Reaction Order H^+	α_c
(3.51)	$RSSR.2HCl + H^+ + e^- \xrightarrow{RDS} RSH.HCl + RS^{\bullet}.HCl$ $RS^{\bullet}.HCl + H^+ + e^- \rightleftharpoons RSH.HCl$	+ 1	+ 1	β
(3.52)	$RSSR.2HCl + e^- \xrightarrow{RDS} RS^-.HCl + RS^{\bullet}.HCl$ $RS^-.HCl + H^+ \rightleftharpoons RSH.HCl$ $RS^{\bullet}.HCl + H^+ + e^- \rightleftharpoons RSH.HCl$	+ 1	0	β
(3.53)	$RSSR.2HCl + H^+ + e^- \rightleftharpoons RSH.HCl + RS^{\bullet}.HCl$ $RS^{\bullet}.HCl + H^+ \rightleftharpoons \overset{+}{R}SH.HCl$ $\overset{+}{R}SH.HCl + e^- \xrightarrow{RDS} RSH.HCl$	+ 1	+ 2	$1 + \beta$
(3.54)	$RSSR.2HCl + H^+ + e^- \rightleftharpoons RSH.HCl + RS^{\bullet}.HCl$ $RS^{\bullet}.HCl + e^- \xrightarrow{RDS} RS^-.HCl$ $RS^-.HCl + H^+ \rightleftharpoons RSH.HCl$	+ 1	+ 1	$1 + \beta$

stoichiometric coefficient) is the number of times the RDS has to be repeated to give the overall electrode reaction, r is the number of electrons in the RDS and β is the symmetry factor for the RDS.

The experimental reaction order of +1 for L-cystine hydrochloride (certainly at the higher reactant concentrations examined, which more closely resemble the electrosynthesis conditions) and +1 for protons reduces the number of possible mechanisms from Table 3.13 to two. Either the first electron transfer controls the rate of reduction and $\alpha_c = \beta$ (mechanism 3.51) or the second electron transfer is rate determining and $\alpha_c = 1 + \beta$ (mechanism 3.52).

β, the symmetry factor, applicable to the single electron transfer RDS, whilst having the same practical effect as α_c (i.e. it determines the extent to which changes in the cathode potential alter the current density for L-cystine hydrochloride reduction) has a fundamental significance in the study of electrode kinetics. Consider the reaction

$$Ox + e^- \longrightarrow Red$$

and the effect of a change in the electrode potential from 0 V to < 0 V (vs. a selected reference electrode) on the free energy-reaction coordinate profiles, assuming they are linear close to the activated complex. The effect is shown schematically in Figure 3.34. At 0 V, $\Delta G^{\neq}_{f(o)}$ and $\Delta G^{\neq}_{b(o)}$ are the cathodic and anodic activation energies respectively. A shift in the electrode potential to < 0 V changes the energy of the electron on the electrode by -nFE, and the ($Ox + e^-$) curve moves by this amount. This ignores any charge on Ox and Red. It is readily apparent that the barrier for oxidation, $\Delta G^{\neq}_{b(E)}$, is now greater than $\Delta G^{\neq}_{b(o)}$ by a fraction of the total energy change. This fraction is $(1 - \beta)$. Conversely the barrier to reduction, $\Delta G^{\neq}_{f(E)}$, is now less thant $\Delta G^{\neq}_{f(o)}$ by a fraction β. Thus,

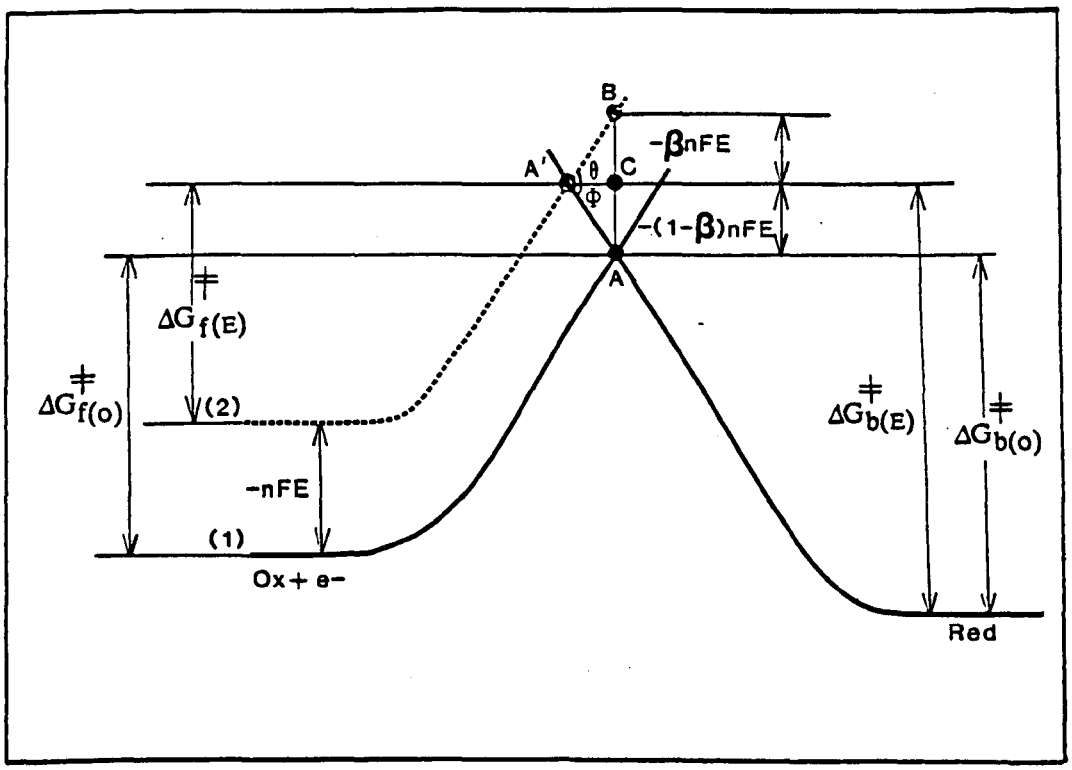

FIGURE 3.34 Schematic representation of the effect of a change in the electrode potential on the free energy–reaction coordinate curves.

$$\Delta G^{\ddagger}_{f(E)} = \Delta G^{\ddagger}_{f(o)} + \beta\, nFE$$

$$\Delta G^{\ddagger}_{b(E)} = \Delta G^{\ddagger}_{b(o)} - (1 - \beta)\, nFE$$

Consequently β must lie between 0 and 1. Consideration of Figure 3.34 shows that β is in fact a measure of the symmetry of the energy barrier for the reaction and

$$\tan \theta = \frac{\beta nFE}{A'C}$$

$$\tan \Phi = \frac{(1-\beta)nFE}{A'C}$$

and therefore

$$\beta = \frac{\tan \theta}{\tan \Phi + \tan \theta} \qquad (3.56)$$

From equation (3.56) if the intersection is symmetrical at the cross-over points, A and A' (as drawn in Figure 3.34), then $\Phi = \theta$ and $\beta = \frac{1}{2}$. This is found for many 'simple' electron transfer reactions (e.g. Table 3.14). Otherwise the intersection is not symmetrical, as shown in Figure 3.35, and either $0 < \beta < \frac{1}{2}$ or $\frac{1}{2} < \beta < 1$.

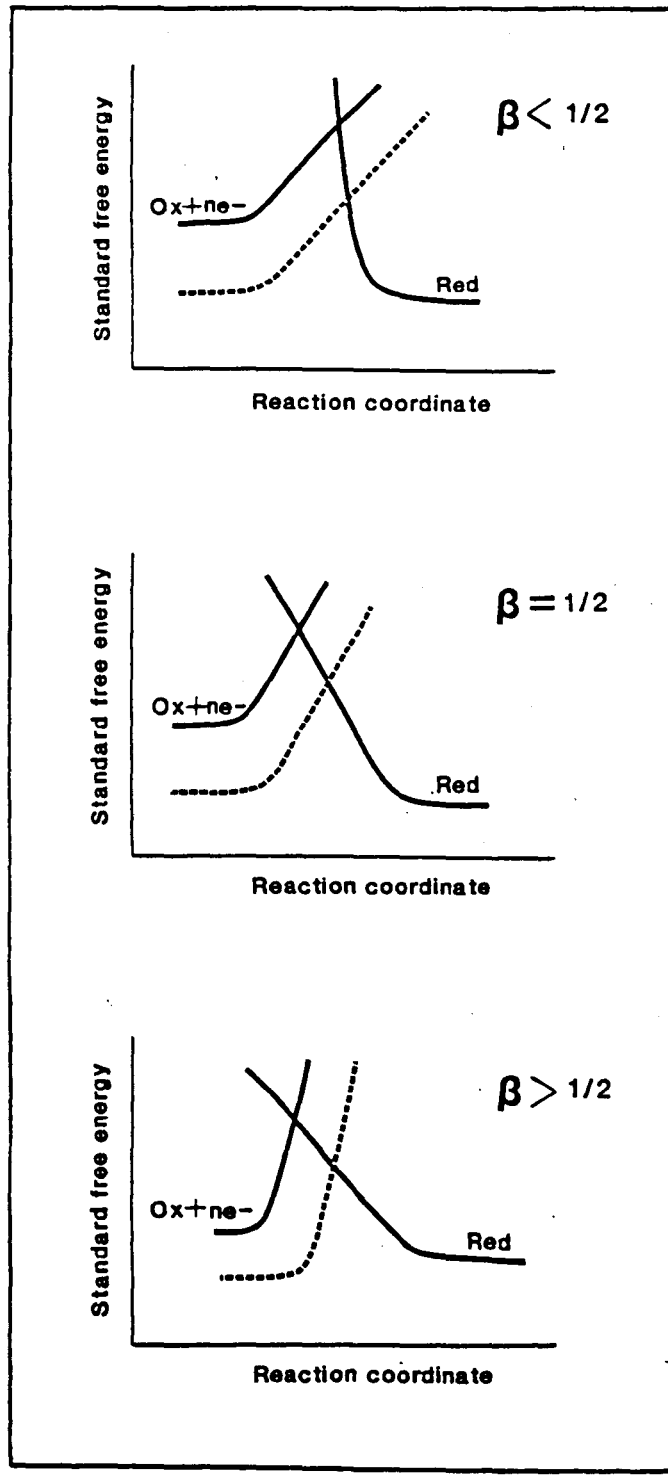

FIGURE 3.35 The symmetry factor as an indicator of the symmetry of the barrier to reaction.

TABLE 3.14 Value of β for some electrode reactions [34].

Metal	Electrode Reaction	β
Platinum	$Fe^{3+} + e^- \longrightarrow Fe^{2+}$	0.58
Mercury	$Ti^{4+} + e^- \longrightarrow Ti^{3+}$	0.42
Mercury	$2H^+ + 2e^- \longrightarrow H_2$	0.50
Silver	$Ag^+ + e^- \longrightarrow Ag$	0.55

For L-cystine hydrochloride reduction since β must lie between 0 and 1, for mechanism (3.51) α_c must have a value of between 0 and 1, but for mechanism (3.52) α_c must take a value of between 1 and 2. The experimentally determined value of α_c is 0.32. Consequently only mechanism (3.51) is consistent with all the measured parameters at mercury.

$$\text{RSSR.2HCl} + H^+ + e^- \xrightarrow{\text{RDS}} \text{RSH.HCl} + \text{RS}^{\bullet}\text{.HCl}$$

$$\text{RS}^{\bullet}\text{.HCl} + H^+ + e^- \longrightarrow \text{RSH.HCl} \qquad (3.51)$$

The first electron transfer to L-cystine hydrochloride controls the rate of reduction. Proton transfer may either preceed or occur simultaneously with the first electron transfer. For the RDS the value for β (equal to α_c) of 0.32 indicates the activated complex of this step is further from the electrode surface than for a 'simple' electron transfer reaction for which β is $\frac{1}{2}$ (see Figure 3.35). The link between β and the molecular properties of the reactants and products of the RDS lies in the dependency of the slopes of the free energy-reaction coordinate curves upon

quantities such as the force constants of the molecular bonds involved. Since adsorption of L-cystine hydrochloride and to a lesser degree L-cysteine hydrochloride, occurs at mercury, it is perhaps understandable that β is not $\frac{1}{2}$.

3.10 CONCLUSIONS

The reduction of dissolved L-cystine hydrochloride to L-cysteine hydrochloride is chemically and electrochemically irreversible at mercury. In aqueous 0.1 mol dm^{-3} hydrochloric acid there is no evidence of alternative products and the only current losses are due to hydrogen evolution from the background electrolyte. In contrast to steady state measurements at a SMDE, which show a diffusion limited current starting at ca. -0.5 V (vs. SCE) which is well separated from hydrogen evolution, with higher disulphide concentrations at a mercury plated copper RDE the reduction wave shifts cathodically and the limiting current at above ca. -1.1 V (vs. SCE) is hidden by simultaneous hydrogen evolution. It appears the principal reason for the large shift is strong adsorption of L-cystine hydrochloride at the electrode surface, through which the reduction reaction must occur. At surface coverages of $0.92 < \theta < 1.0$ the kinetics of the first electron transfer to the disulphide molecule (i.e. the RDS) is hindered although the symmetry factor is unaltered. For $\theta = 1$ the adsorbed disulphide layer has no additional effect upon the kinetics of the electrosynthesis reaction.

Thus for conditions most closely resembling those used in the electrosynthesis on average the Tafel slope is 185 mV/decade, α_c is 0.32 and k_f^o is 6.7×10^{-10} m s^{-1}. Significantly these kinetic parameters are unaltered in aqueous 2.0 mol dm^{-3} hydrochloric acid. The close agreement obtained for the kinetic parameters using RDE, cyclic voltammetry and sampled d.c. measurements shows the high degree of accuracy that is possible with voltammetry techniques. The first electron transfer

to L–cystine hydrochloride is the RDS (mechanism 3.51) with the Tafel slope (and α_c) modified by disulphide adsorption at the mercury surface.

The sampled d.c. polarography at the SMDE suggests from the measured k^o that the literature $E^{o'}$ values for the L–cystine/L–cysteine couple (Table 1.1) are all erroneous for the electrosynthesis conditions. All are at least 50 mV too negative and $E^{o'}$ is > + 0.24 V (vs. NHE) at pH 0. As discussed in Section 1.4.1 this is not surprising for the values measured by potentiometry, because of the adsorption effects at the indicator electrodes used. This now provides evidence that the $E^{o'}$ values measured using the Fe(II)/Fe(III) and various dye redox couples are also erroneous when extrapolated to pH 0. Examination of other redox couples to elucidate the $E^{o'}$ value of the L–cystine/L–cysteine couple is an area which merits further study. A redox couple capable of reacting with the amino acid system in hydrochloric acid media would be particularly valuable, since $E^{o'}$ could be established for the electrosynthesis conditions.

The diffusion coefficients of L–cystine hydrochloride in aqueous hydrochloric acid determined from the voltammetry studies, are listed in Table 3.15. These coefficients are in accord with the available literature values of 4.8 x 10^{-10} m^2 s^{-1} [15] and 5.3 x 10^{-10} m^2 s^{-1} [16] in aqueous 0.1 mol dm^{-3} hydrochloric acid at 25°C. The literature values were measured by polarography using the Ilkovic equation (equation 3.47). Of the techniques used in this study it is generally accepted [35] that the RDE is capable of determining diffusion coefficients with a precision of better than ± 1% whilst linear sweep voltammetry often produces values no better than ± 20% in practice. The poor performance of linear sweep voltammetry has been attributed not only to the difficulty of accurately measuring the peak current but to the uncertainty in the theoretical equation for this current. Some evidence for this is presented by the results in

TABLE 3.15 Diffusion coefficients of L-cystine hydrochloride in aqueous hydrochloric acid at 25°C obtained from the kinetic studies.

Technique	Equation Used	Assumptions Required	Electrolyte	Diffusion Coefficient (10^{-10} m^2 s^{-1})
Constant Potential Coulometry Mercury Plated Copper RDE	(3.21) and (3.22)	None	0.1 mol dm^{-3} HCl	4.85 ± 0.05
Koutecky-Levich Plot Mercury Plated Copper RDE	(3.23)	n = 2	0.1 mol dm^{-3} HCl	5.02 ± 0.12
Linear Sweep Voltammetry Mercury Plated Copper RDE Stationary mercury disc	(3.29)	n = 2 and α_c = 0.32	0.1 mol dm^{-3} HCl	5.1 ± 0.4
			2.0 mol dm^{-3} HCl	4.0 ± 0.3
Sampled d.c. Polarography SMDE	(3.47)	n = 2	0.1 mol dm^{-3} HCl	5.3
			2.0 mol dm^{-3} HCl	4.2

this study. Linear sweep voltammetry gives an error of ± 8% whilst the RDE gives an error of only ± 2.5% from Koutecky-Levich plots and ± 1% from constant potential coulometry studies. The diffusion coefficients obtained from sampled d.c. polarography are slightly higher than those from the above techniques. These utilised, however, a 100 fold lower concentration of L-cystine hydrochloride. The increased diffusion coefficient probably represents the effect of this reduced concentration of disulphide.

REFERENCES

1. Albery W.J. & Hitchman M.L. "Rotating Ring-Disc Electrodes". Clarendon Press, Oxford (1971).
2. Daly P.J., Page D.J. & Compton R.G.; *Anal. Chem.* 55, 1191, (1983).
3. Yoshida Z.; *Bull. Chem. Soc. Jpn.* 54, 562, (1981).
4. Coles B.A. & Compton R.G.; *J. Electroanal. Chem.* 144, 87, (1983).
5. Albery W.J. "Electrode Kinetics". Clarendon Press, Oxford (1975). Chapter 3.
6. Barnartt S. *J.*; *Electrochem. Soc.* 99, 549, (1952).
7. Barnartt S. *J.*; *Electrochem. Soc.* 108, 102, (1961).
8. "Handbook of Chemistry and Physics". Eds. Weast R.C. & Astle M.J., 61st. Edition, CRC Press, Florida (1980-81). Page D-171.
9. Brett C.M.A. & Brett A.M.C.F.O. in "Comprehensive Chemical Kinetics". Eds. Bamford C.H. & Compton R.G., Elsevier, Amsterdam (1986). Volume 26, Chapter 5.
10. Bard A.J. & Faulkner L.R. "Electrochemical Methods Fundamentals and Applications". John Wiley & Sons, New York (1980). Chapter 3.
11. Levich V.G. "Physiochemical Hydrodynamics". Prentice Hall, New Jersey (1962).
12. Hitchman M.L. & Albery W.J.; *Electrochim. Acta* 17, 787, (1972).
13. "International Critical Tables of Numerical Data Physics, Chemistry and Technology". Eds. Washburn E.W., West C.J., Dorsey N.E., Bichowsky F. & Ring M.D. McGraw-Hill, New York (1929). Volume 3, page 54.
14. "International Critical Tables of Numerical Data Physics, Chemistry and Technology". Eds. Washburn E.W., West C.J., Dorsey N.E., Bichowsky F. & Ring M.D. McGraw-Hill, New York (1929). Volume 5, pages 10 and 12.

15. Issa I.M., Samahy A.A.El, Issa R.M. & Temerik Y.M.; *Electrochim. Acta*, 17, 1615, (1972).

16. Kolthoff I.M. & Barnum C.; *J. Am. Chem. Soc.* 63, 520, (1941).

17. Albery W.J. "Electrode Kinetics". Clarendon Press, Oxford (1975). Chapter 5.

18. Kassim A. Bin, Kuhn A.T. & Rice C.L.; *Electrochim. Acta* 26, 1047, (1981).

19. Kassim A. Bin, Kuhn A.T. & Rice C.L.; *J. Chem. Soc. Faraday Trans. I* 77, 683, (1981).

20. Nicholson R.S. & Shain I.; *Anal. Chem.* 36, 706, (1964).

21. Kohler H., Piron D.L. & Belanger G.; *J. Electrochem. Soc.* 134, 120, (1987).

22. Bockris J.O'M. & Reddy A.K.N. "Modern Electrochemistry". Plenum Press, New York (1970). Volume 2, page 1008.

23. Stankovich M.T. & Bard A.J.; *J. Electroanal. Chem.* 75, 487, (1977).

24. Fleischman M. & Thirsk H.R.; *Electrochim. Acta.* 9, 757, (1964).

25. Bard A.J. & Faulkner L.R. "Electrochemical Methods Fundamentals and Applications". John Wiley & Sons, New York (1980). Chapter 5.

26. Koutecky J.; *Collect. Czech. Chem. Commun.* 18, 597, (1953).

27. Weber J. & Koutecky J.; *Collect. Czech. Chem. Commun.* 20, 980, (1955).

28. Southampton Electrochemistry Group "Instrumental Methods In Electrochemistry". Ellis Horwood Ltd., Chichester (1985). Chapter 6.

29. Heinze J.; *Angw. Chem.* 23, 831, (1984).

30. Delahay P.; *J. Am. Chem. Soc.* 75, 1430, (1953).

31. Matsuda H. & Ayabe Y.; *Z. Elektrochem.* 63, 1164, (1959).

32. Wopschall R.H. & Shain I.; *Anal. Chem.* 39, 1514, (1967).

33. Bockris J.O'M. & Reddy A.K.N. "Modern Electrochemistry". Plenum Press, New York (1970), Volume 2, page 1007.

34. Bockris J.O'M. & Reddy A.K.N. "Modern Electrochemistry". Plenum Press, New York (1970). Volume 2, page 918.

35. Adams R.N. "Electrochemistry at Solid Electrodes". Marcel Dekker, New York (1969). Chapter 8.

CHAPTER 4

ELECTROCHEMICAL KINETICS AT SOLID ELECTRODES

4.1 INTRODUCTION

Kinetic studies are difficult at titanium, tin, cadmium, copper, zinc, stainless steel, nickel, platinum, molybdenum, vitreous carbon and carbon paste rotating disc electrodes. In steady state or linear sweep voltammograms L-cystine hydrochloride reduction and hydrogen evolution cannot readily be separated in aqueous hydrochloric acid catholytes. This perhaps accounts for the real dearth of voltammetric literature at solid electrodes. At lead, however, it is possible to more easily separate the two reactions and perform a thorough kinetic analysis.

4.2 KINETICS AT LEAD

4.2.1 Importance of Electrode Preparation

The initial results at a lead RDE were not promising. A polished electrode treated with aqueous 1.0 mol dm^{-3} nitric acid for 15 seconds, rinsed, then immediately immersed in aqueous 0.1 mol dm^{-3} or 2.0 mol dm^{-3} hydrochloric acid, to prevent surface oxide formation, and allowed to sit at the open circuit voltage showed large anodic and cathodic currents in cyclic voltammograms (Figure 4.1). The currents are due to formation and reduction of lead chloride on the electrode surface (equation 4.01), which is the major corrosion product.

$$Pb + 2Cl^- \rightleftharpoons \underset{(ads.)}{PbCl_2} + 2e^- \qquad (4.01)$$

This system has been studied extensively and the available literature reviewed by Kuhn [1]. The cyclic voltammograms in Figure 4.1 are in complete agreement with the findings of Barradas et al [2]. In aqueous 0.1 mol dm^{-3} hydrochloric acid, where the solubility of lead chloride is relatively high, the surface growth of lead chloride is limited by diffusion of chloride ions and passivation of the electrode surface is not observed since the growth rate is low compared to the rate

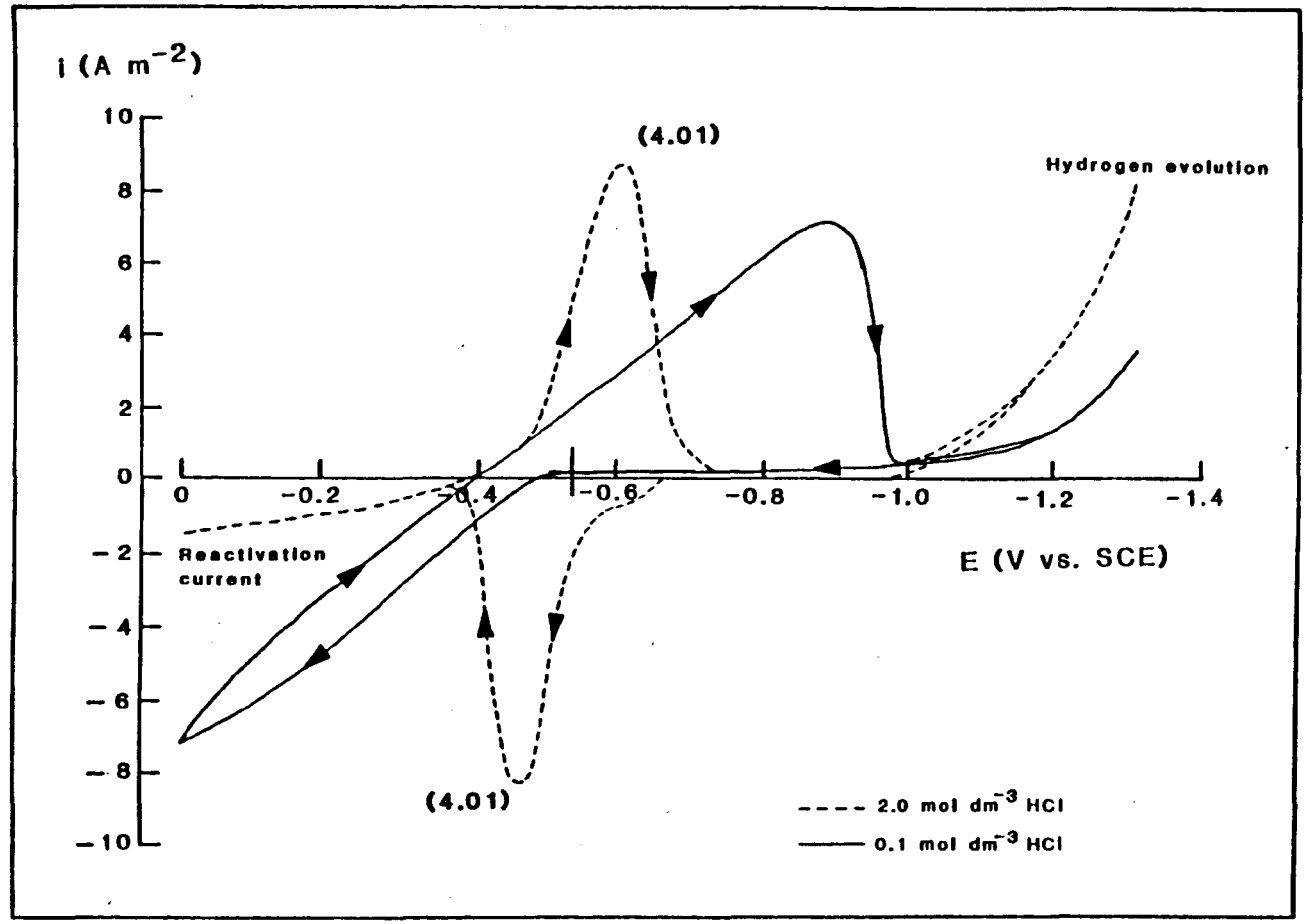

FIGURE 4.1 Cyclic voltammetry of hydrochloric acid solutions at a lead RDE. Electrolyte deoxygenated with N_2. Temperature 25°C. Potential sweep rate 25 mV s^{-1}.

of lead chloride dissolution. At higher concentrations of chloride ions the solubility of lead chloride is still relatively high but the rate of surface growth is no longer determined by chloride ion diffusion and the electrode readily passivates. Evidence for chemical dissolution of the lead chloride film is provided by the large reactivation current in aqueous 2.0 mol dm^{-3} hyrochloric acid.

Lead chloride formation is confirmed by two other factors. The open circuit voltage of −0.510 V (vs. SCE) at 25°C in aqueous 0.1 mol dm^{-3} hydrochloric acid is close to the reported [3] $E^{o'}$of −0.513 V (vs. SCE) for the lead/lead chloride system under these conditions. Also, extensive potential cycling between 0 V and −1.0 V (vs. SCE) produced a white deposit on the electrode surface which was identified as lead chloride by ex−situ XRD analysis [4].

Significantly L−cystine hydrochloride reduction at the lead chloride contaminated surface could not be separated from hydrogen evolution in steady state or linear sweep voltammograms. Gas bubbles on the electrode surface clearly identified the onset of hydrogen evolution. The lead electrode surface can, however, be 'cleaned' by the additional procedures outlined in Section 2.5.1(c) (i.e. using hydrogen evolution to remove residual oxide and not allowing the electrode potential to become anodic of −0.6 V vs. SCE). At a 'cleaned' surface it is possible to separate reduction of the amino acid in a background electrolyte of aqueous 0.1 mol dm^{-3} hydrochloric acid and therefore conduct a detailed kinetic analysis. Separation is due to a much reduced background current, rather than enhanced L−cystine hydrochloride reduction, with the lower background current due principally to a suppression of hydrogen evolution with perhaps a minor contribution from diminished reduction currents for lead chloride and possibly other, soluble, lead corrosion species. In the more concentrated acid used in the electrosynthesis, however, rates of hydrogen evolution are sufficiently enhanced that

a distinct L-cystine hydrochloride reduction current is not evident, even at the 'cleaner' lead electrode. A kinetic analysis cannot be performed under these conditions.

4.2.2 Constant Potential Coulometry

Figure 4.2 shows the electrochemically irreversible waves for reduction of L-cystine hydrochloride to L-cysteine hydrochloride in aqueous 0.1 mol dm^{-3} hydrochloric acid at a selection of rotation rates of a lead RDE. Current measurements were made by manual adjustment of the electrode potential followed by continuous monitoring of the cell current, since approximately 20 seconds is required to achieve steady state. The current-potential curves show at electrode potentials positive of -0.925 V (vs. SCE) the current density is independent of the electrode rotation rate, indicating the reduction is controlled purely by the kinetics of electron transfer. At more negative potentials there is a large region of mixed kinetic-mass transport control until at about -1.35 V (vs. SCE) where simultaneous hydrogen evolution from the background electrolyte masks a probable convective-diffusion limiting current for pure mass transport controlled reduction of the disulphide. Progressive extension of the mixed control region at higher electrode rotation rates, observed at mercury plated copper (Figure 3.3), is clearly evident at lead.

Constant potential coulometry with a lead RDE was performed at potentials in both the mixed and probable mass transport controlled regions. The initial aim of the coulometry was to confirm the irreversible waves are, indeed, due to L-cystine hydrochloride reduction since there is no literature evidence to support this electrochemistry. At the termination of electrolyses current-potential curves of the electrolysed solutions showed progressively diminished curves as the concentration of L-cystine hydrochloride presumeably reduced. Subsequent HPLC analysis of the

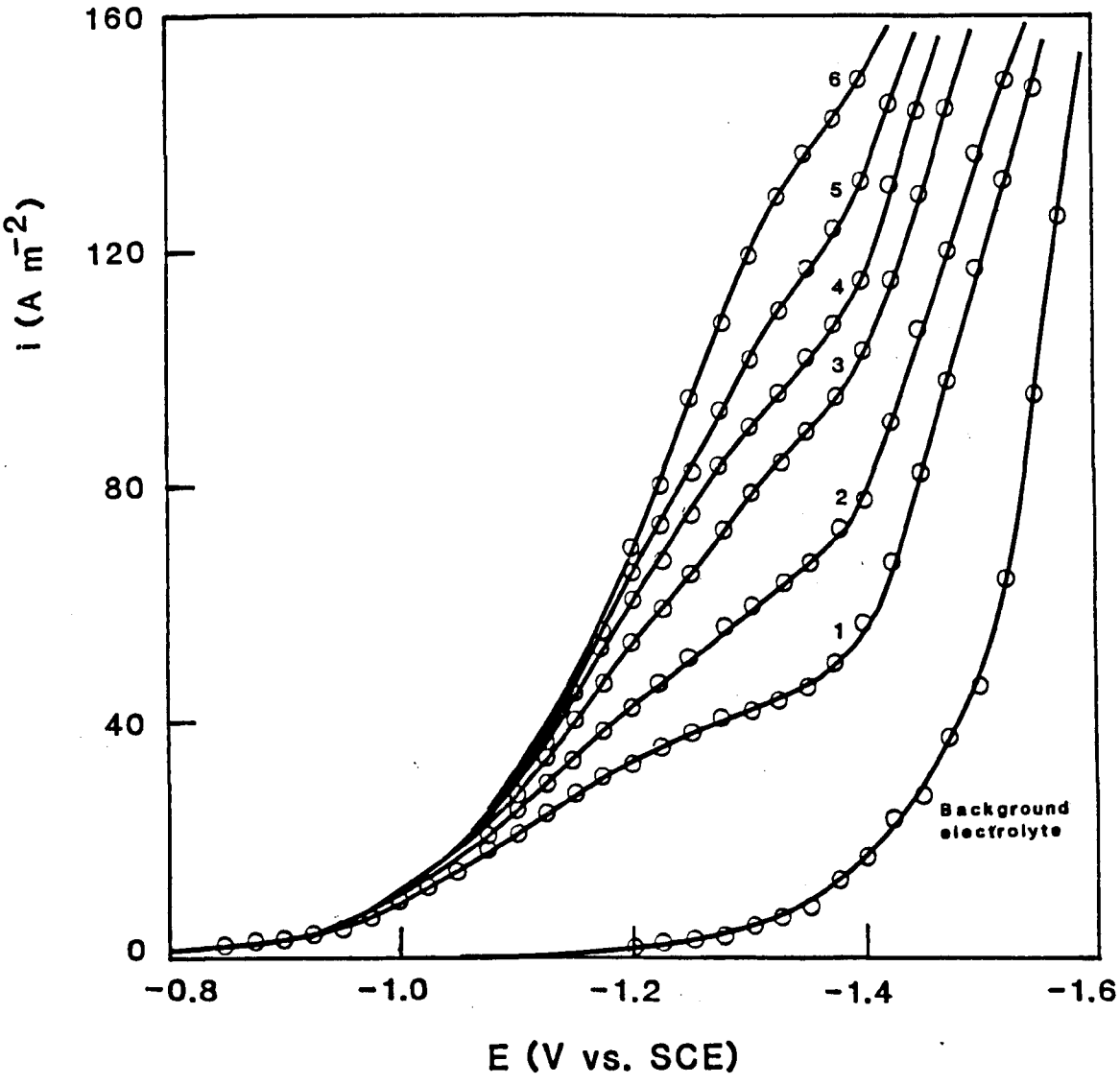

FIGURE 4.2 Steady state voltammograms at a lead RDE. 10 mol m^{-3} L–cystine hydrochloride in aqueous 0.1 mol dm^{-3} hydrochloric acid deoxygenated with N_2. Temperature 25°C. Electrode rotation rate 1. 5 Hz 2. 10 Hz 3. 20 Hz 4. 30 Hz 5. 40 Hz and 6. 50 Hz.

electrolysed solution confirmed the conversion of disulphide into thiol.

The results of constant potential coulometry at −1.1 V (vs. SCE) are summarised in Table 4.1.

TABLE 4.1 Constant potential coulometry at −1.1 V (vs. SCE) at a lead RDE.

t (minute)	q (C)	RSSR.2HCl (mol m^{-3})	RSH.HCl (mol m^{-3})	Δc_t (RSSR.2HCl) (mol m^{-3})	n
0	0	10.0	0	0	-
61	5.386	8.9	2.2	1.1	2.03
122	10.384	7.9	4.2	2.1	2.05
179	14.130	7.1	5.8	2.9	2.02
280	20.262	5.8	8.4	4.2	2.00
375	24.710	4.8	10.4	5.2	1.97
480	28.251	3.9	12.2	6.1	1.92

From equation (3.05) (i.e. $n = q/\Delta c_t FV$) the measured charge passed for a measured change in reactant concentration gives n = 2. HPLC analysis confirms 1 mol of the disulphide is converted into 2 mol of thiol, all in agreement with the proposed electrosynthesis reaction (reaction 3.04).

$$RSSR.2HCl + 2H^+ + 2e^- \longrightarrow 2\ RSH.HCl \qquad (3.04)$$

The accurate value for n requires the current efficiency for the synthesis to be

100%. There appear to be no current losses due to formation of organic by-products. Current losses at more negative electrode potentials than -1.1 V (vs. SCE) are most likely due exclusively to hydrogen evolution from the background electrolyte. Figure 4.2 shows excessive gas evolution commences just cathodic of -1.1 V (vs. SCE) in the absence of the disulphide.

In constant potential coulometry experiments where L-cystine hydrochloride reduction is under mixed kinetic-mass transport control, if the reaction is first order in the disulphide a plot of ln c_t against t should be a straight line. This is shown by equation (3.17) which is derived in Section 3.4.

$$\ln c_t = \ln c_o - \frac{k_f K_L A}{(k_f + K_L) V} \cdot t \qquad (3.17)$$

Figure 4.3 shows the relevant plots for electrolysis at -1.1 V and -1.2 V (vs. SCE) at a lead RDE rotated at 50 Hz. Mixed control at these potentials is confirmed in Figure 4.2. The straight line plots obtained indicate between 1.4 mol m^{-3} and 10 mol m^{-3} L-cystine hydrochloride the reduction is first order in the disulphide. At -1.2 V (vs. SCE) towards the end of electolysis the interval current efficiency is only about 80%. The current losses are ascribed to hydrogen evolution. The lack of deviation from the straight line relationship in Figure 4.3 under these conditions suggests the assumption implicit in the derivation of equation (3.17), namely that the change in amino acid concentrations during electrolysis has no effect upon the rate of hydrogen evolution, is valid.

At -1.3 V (vs. SCE) at an electrode rotation rate of 5 Hz Figure 4.2 indicates L-cystine hydrochloride reduction at lead is probably controlled completely by the rate of mass transport. Constant potential coulometry at this potential produced a straight line plot of ln c_t against t (Figure 4.4). From equations (3.21) and (3.22), derived in Section 3.2,

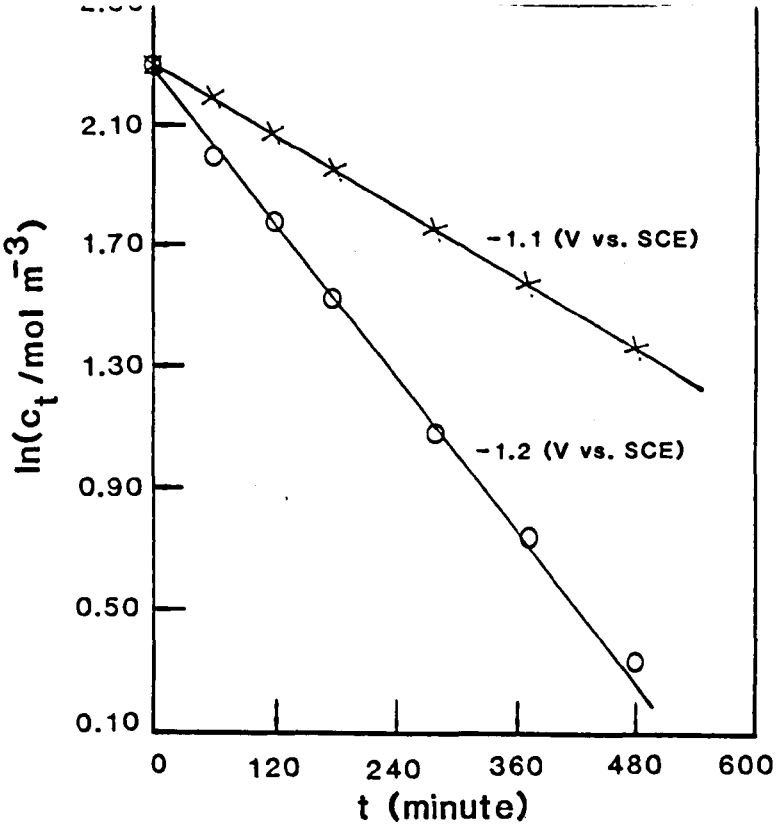

FIGURE 4.3 Dependence of ln c_t on time for reduction of L-cystine hydrochloride occuring under mixed control at a lead RDE. Rotation rate 50 Hz. The background electrolyte is aqueous 0.1 mol dm^{-3} HCl deoxygenated with N_2. Temperature 25°C.

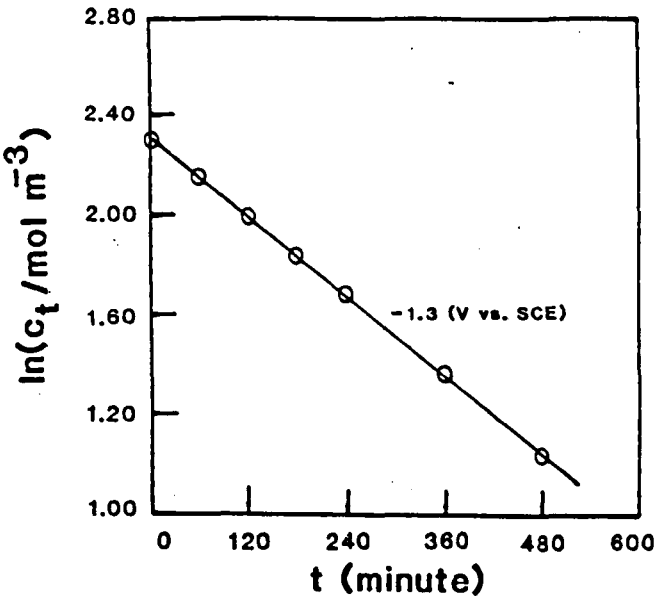

FIGURE 4.4 Dependence of ln c_t on time for complete mass transport controlled reduction of L-cystine hydrochloride at a lead RDE. Rotation rate 5 Hz. The background electrolyte is aqueous 0.1 mol dm^{-3} HCl deoxygenated with N_2. Temperature 25°C.

$$\ln c_t = \ln c_o - \frac{K_L A}{V} \cdot t \qquad (3.21)$$

$$K_L = 0.62\, D^{2/3}\, \nu^{-1/6}\, \omega^{1/2} \qquad (3.22)$$

the slope of this straight line gives the diffusion coefficient of L-cystine hydrochloride as (4.95 ± 0.06) x 10^{-10} m^2 s^{-1} at 25°C.

The close agreement of this value with the available literature [5,6] and the values measured in this study at mercury (Table 3.15) confirm the complete mass transport control of L-cystine hydrochloride reduction. Towards the end of the electrolysis, the interval current efficiency is probably less than 50%, due to simultaneous hydrogen evolution from the background electrolyte. Lack of deviation from a straight line at longer times in Figure 4.4. provides further evidence that over this concentration range, changes in the amino acid concentration have no effect upon the rate of hydrogen evolution.

In all these constant potential electrolyses, even after 8 hours, there is no visual evidence of lead chloride formation on the electrode surface. Further evidence of, at least, minimal lead chloride contamination is provided by the straight line plots of Figure 4.3 and 4.4. As discussed in Section 4.2.1 current-potential curves recorded at lead chloride contaminated, and cleaned lead electrode surfaces suggest lead chloride enhances the rate of hydrogen evolution at lead. This would reduce the rate of L-cystine hydrochloride reduction at any constant potential where the two reactions occur simultaneously.

4.2.3 Kinetic Parameters for L-Cystine Hydrochloride Reduction

(a) Steady state voltammograms

The steady state voltammograms of L-cystine hydrochloride reduction at a lead RDE (e.g. Figure 4.2) can be analysed to obtain the kinetic parameters for the

reduction. For a first order reaction at the RDE equation (3.23) is derived in Section 3.5.

$$\frac{1}{i} = \frac{1}{nFk_f c_b} + \frac{1}{0.62n\ F\ D^{2/3}\ \nu^{-1/6}\ c_b\ \omega^{1/2}} \qquad (3.23)$$

Figure 4.5 shows the straight line plots of $1/i$ against $1/(\omega)^{\frac{1}{2}}$ at a series of cathode potentials where the disulphide reduction is under mixed kinetic-mass transport control at the RDE. For n = 2 and a kinematic viscosity of 9.1×10^{-7} $m^2\ s^{-1}$ (Table 3.2) the diffusion coefficient of L-cystine hydrochloride is calculated as $(4.80 \pm 0.11) \times 10^{-10}$ $m^2\ s^{-1}$ at 25°C. The error represents the spread of values obtained from the set of essentially parallel straight lines in Figure 4.5.

From the intercepts in Figure 4.5 k_f is calculated to increase from 2.1×10^{-5} m s^{-1} at -1.100 V (vs. SCE) to 1.0×10^{-3} m s^{-1} at -1.225 V (vs. SCE). A plot of log k_f against E is shown in Figure 4.6. The straight line relationship confirms the applicability of the fundamental equation for the kinetics of electron transfer (equation 3.10) to L-cystine hydrochloride reduction at lead.

$$k_f = k_f^o \exp\left(-\frac{\alpha_c F}{RT} E\right) \qquad (3.10)$$

From Figure 4.6 the Tafel slope is (183 ± 4) mV/decade, α_c is (0.32 ± 0.01) and k_f^o is $(2.2 \pm 0.3) \times 10^{-11}$ m s^{-1}. The relatively large error in k_f^o mainly reflects the long extrapolation involved. As discussed for mercury cathodes in Section 3.5 the high Tafel slope for L-cystine hydrochloride reduction is indicative of modification of the electrochemical kinetics of electron transfer by disulphide adsorption at the electrode surface. At lead, however, there is no additional voltammetry evidence to support adsorption of the amino acid at the cathode.

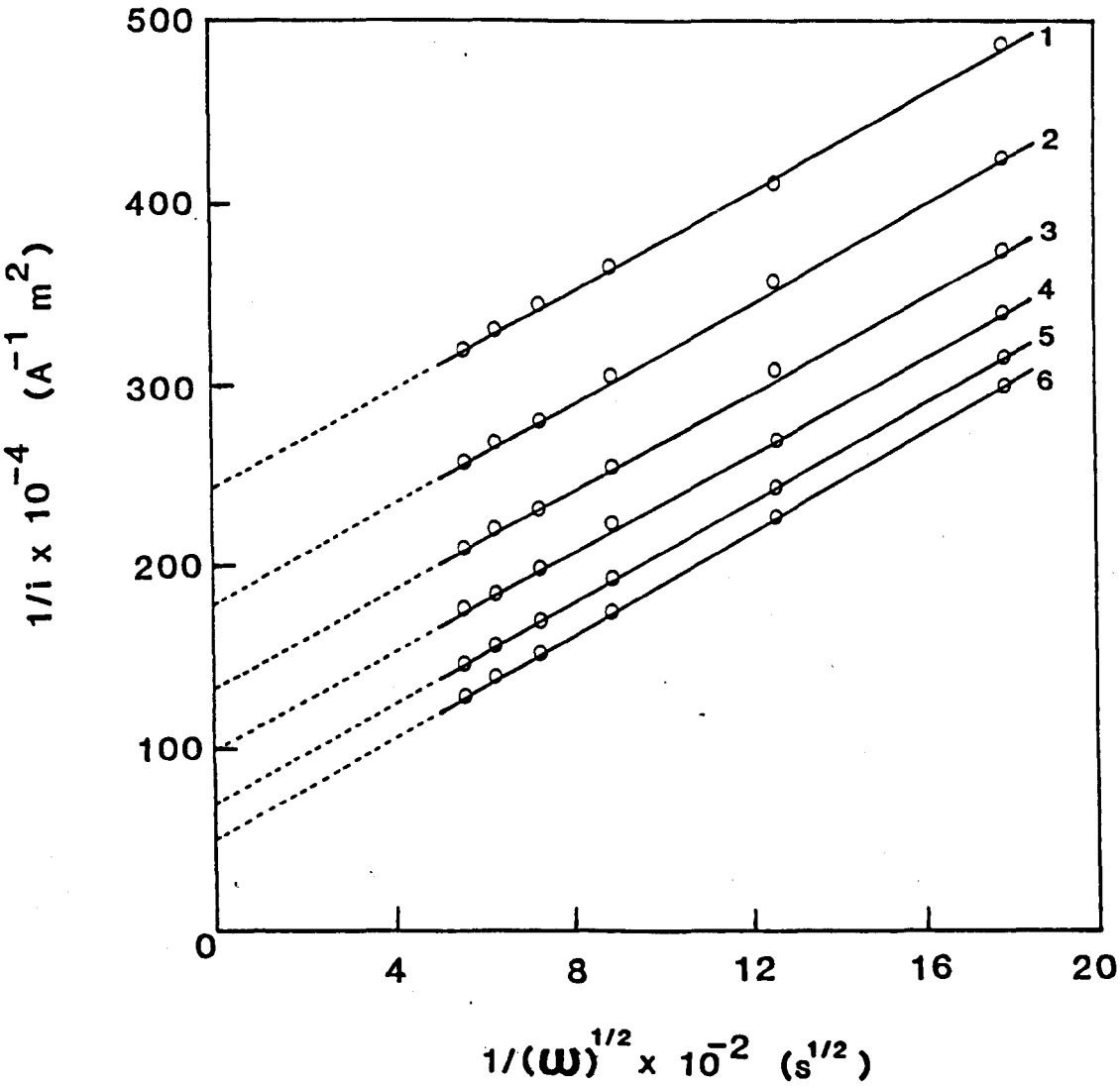

FIGURE 4.5 Plot of 1/i against $1/(\omega)^{\frac{1}{2}}$ for L-cystine hydrochloride reduction at a lead RDE. 10 mol m^{-3} L-cystine hydrochloride in aqueous 0.1 mol dm^{-3} HCl deoxygenated with N_2. Temperature 25°C. Electrode potentials 1. -1.100 V 2. -1.125 V 3. -1.150 V 4. -1.175 V 5. -1.200 V and 6. -1.225 V (vs. SCE). The background current has been subtracted where necessary.

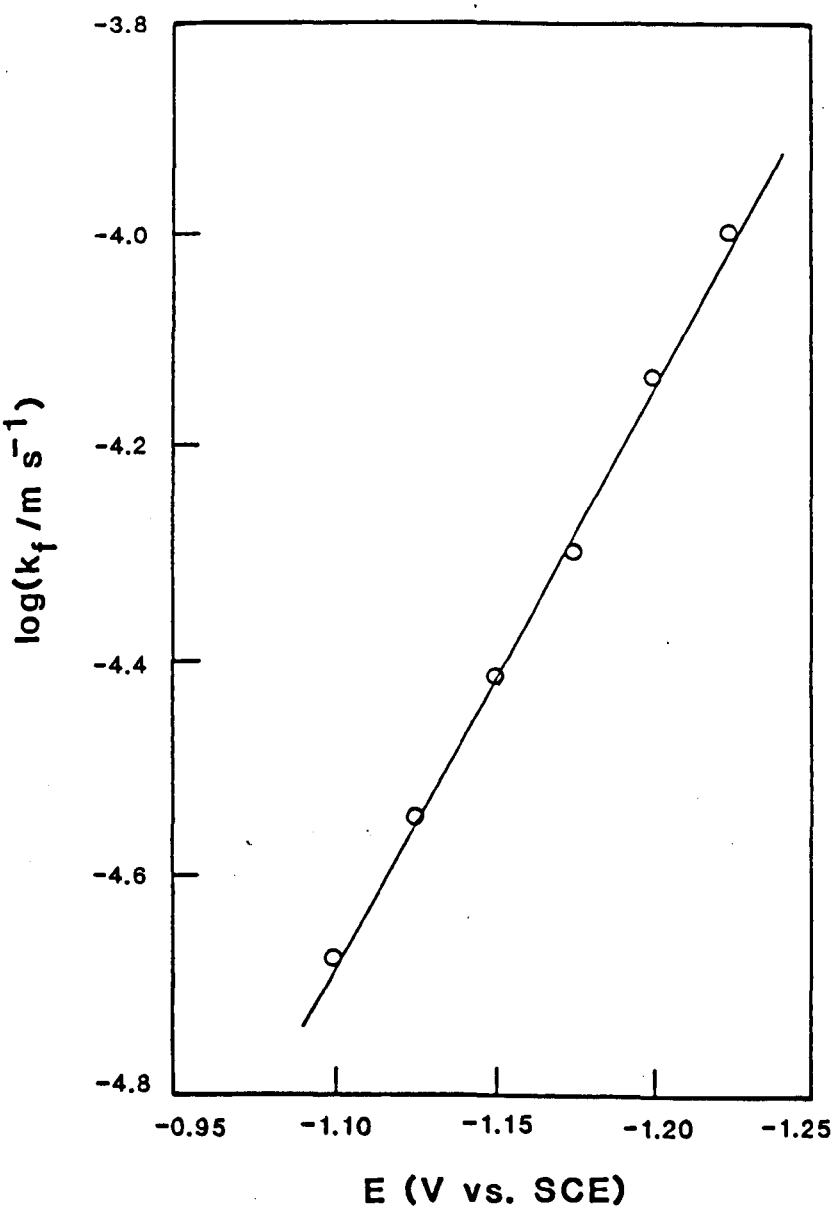

FIGURE 4.6 Plot of log k_f against E.

The kinetic parameters may also be obtained directly from the currents at the RDE by using equation (3.25).

$$- \log\left[\frac{1}{i} - \frac{1}{i_L}\right] = - \frac{\alpha_c F}{2.303\ RT}\ E + \log\ (nF\ k_f^o\ c_b) \qquad (3.25)$$

Figure 4.7 shows the plot of $-\log[1/i-1/i_L]$ against E for L-cystine hydrochloride reduction at a lead RDE. The steady state voltammograms shown in Figure 4.2, which are recorded at electrode rotation rates of between 5 and 50 Hz, all collapse onto the two straight lines in Figure 4.7 as required of data which is corrected for mass transport. The diffusion limited currents required in the calculation of $-\log[1/i-1/i_L]$ could not be mesured directly from the current-potential curves due to simultaneous hydrogen evolution. They were calculated using the Levich relationship (eqaution 3.02). The major Tafel region above -0.850 V (vs. SCE) has a slope of (182 ± 4) mV/decade which corresponds to an α_c of (0.32 ± 0.02). Extrapolation to 0 V (vs. SCE) gives a k_f^o of (2.6 ± 0.3) x 10^{-11} m s^{-1}. These values are in close accord with those from the plot of log k_f against E (Figure 4.6). The Tafel region of high slope (i.e. 470 mV/decade) at low currents, is most likely due to a change in the electrode surface. A similar effect has been observed for hydrogen evolution at lead [7,8], with the effect attributed to an oxide film formed by trace quantities of oxygen in the deoxygenated catholytes. At more cathodic potentials the film was presumed to be reduced and a 'normal' Tafel slope of 120 mV/decade recorded. Such an oxide film may also retard the rate of L-cystine hydrochloride reduction, particularly if adsorption of the disulphide plays a significant role in the electrode reaction.

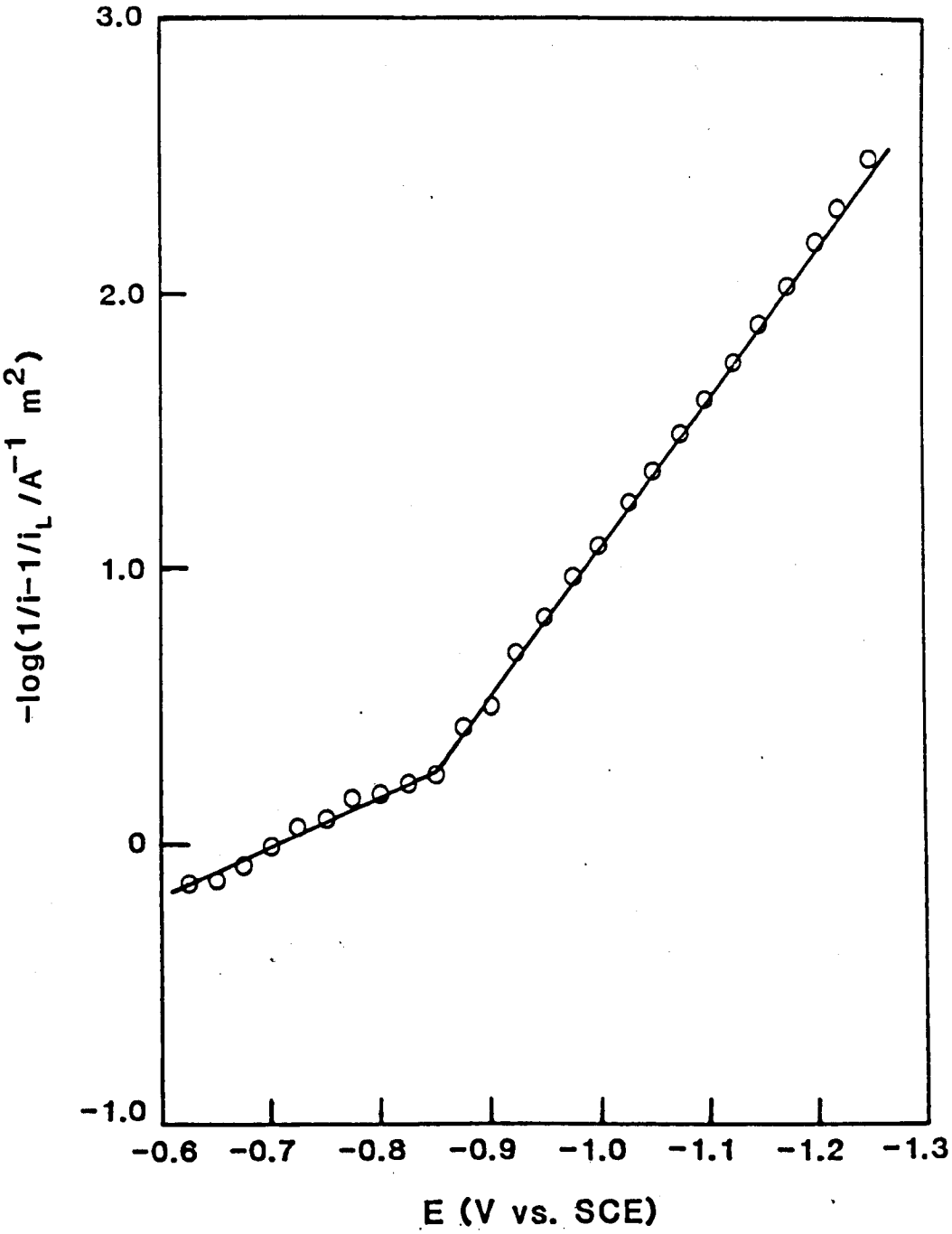

FIGURE 4.7 Mass transport corrected Tafel plot for L-cystine hydrochloride reduction at a lead RDE. 10 mol m^{-3} L-cystine hydrochloride in aqueous 0.1 mol dm^{-3} HCl dexoygenated with N_2. Temperature 25°C. The background current is subtracted.

(b) Linear Sweep Voltammetry

Figure 4.8 shows the linear sweep voltammograms at a range of potential sweep rates for reduction of L-cystine hydrochloride in aqueous 0.1 mol dm^{-3} hyrochloride acid, at lead. The theoretical equations from which the kinetic parameters for the reduction are obtained are reviewed in Section 3.6.1 and listed below.

$$i_p = 0.4958\ n\ F\ c_b\ D^{1/2} \left[\frac{\alpha_c F}{RT}\right]^{1/2} v^{1/2} \qquad (3.29)$$

$$E_p = E^{o'} - \frac{RT}{\alpha_c F}\left[0.780 + 2.303\ \log\left(\frac{D^{1/2}}{k^o}\right) + 2.303\ \log\left(\frac{\alpha_c F v}{RT}\right)^{1/2}\right] \qquad (3.30)$$

$$\log\ i_p = \log\ (0.227\ n\ F\ c_b\ k^o) - \frac{\alpha_c F}{2.303\ RT}\ [E_p - E^{o'}] \qquad (3.32)$$

They all assume the reaction is first order with respect to the reactant and semi-infinite linear diffusion is the mode of mass transport to the electrode surface. Confirmation that the reduction of L-cystine hydrochloride is first order under the experimental conditions of Figure 4.8 is provided by appiying an extension to the above theory by Kohler et al, to cover a wide range of reaction orders (see Section 3.6.2). They predicted the change in the slope of the straight line plot of i_p against $v^{\frac{1}{2}}$ as the reaction order changed. Figure 4.9 shows this plot for the voltammograms in Figure 4.8. The slope of (74 ± 3) A m^{-2} (V

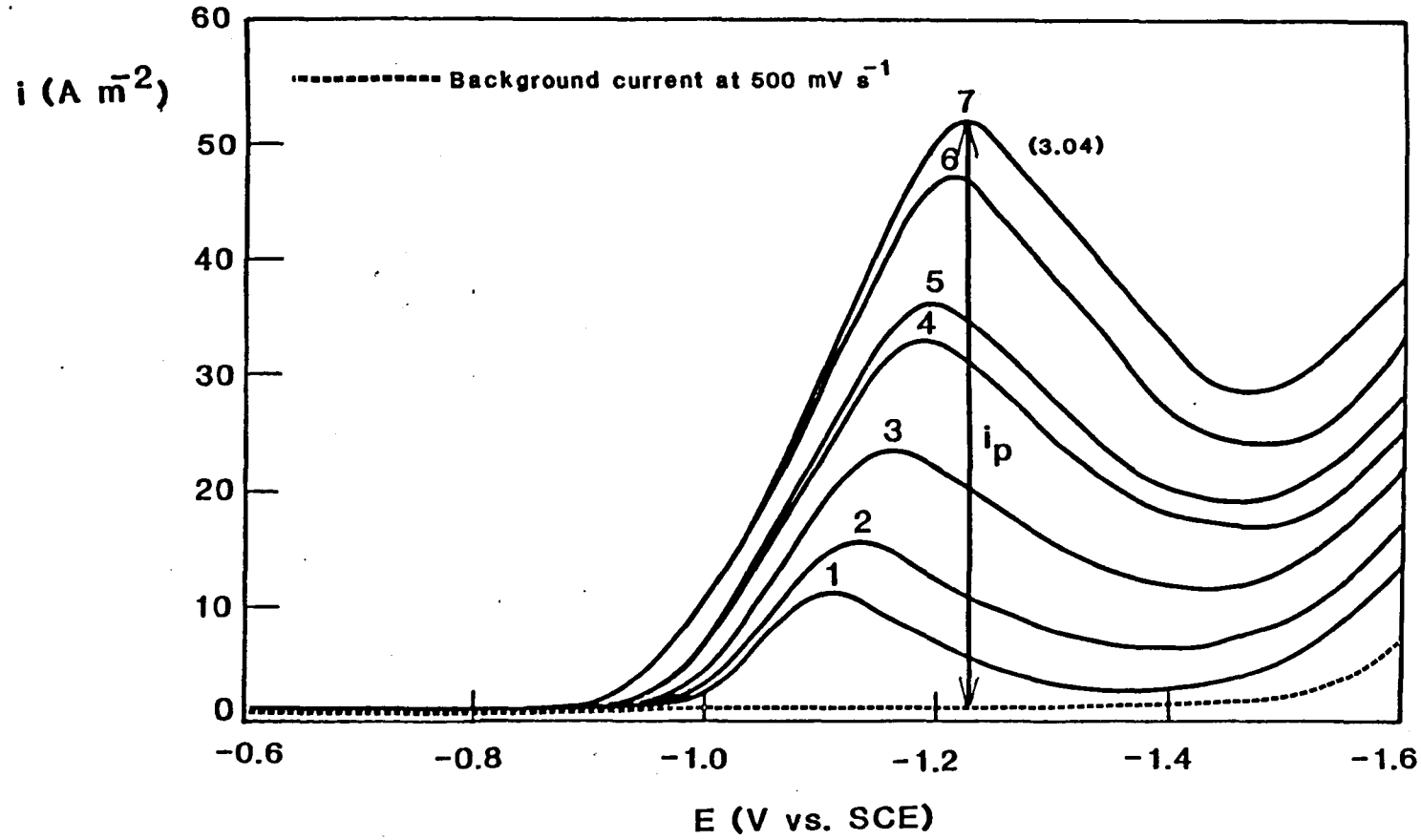

FIGURE 4.8 Linear sweep voltammetry of 10 mol m^{-3} L–cystine hydrochloride in aqueous 0.1 mol dm^{-3} HCl at lead. Electrolyte deoxygenated with N_2. Temperature 25°C. Potential sweep rate 1. 25 mV s^{-1} 2. 50 mV s^{-1} 3. 100 mV s^{-1} 4. 200 mV s^{-1} 5. 250 mV s^{-1} 6. 400 mV s^{-1} and 7. 500 mV s^{-1}. The peak current was measured as shown for the voltammogram recorded at 500 mV s^{-1}.

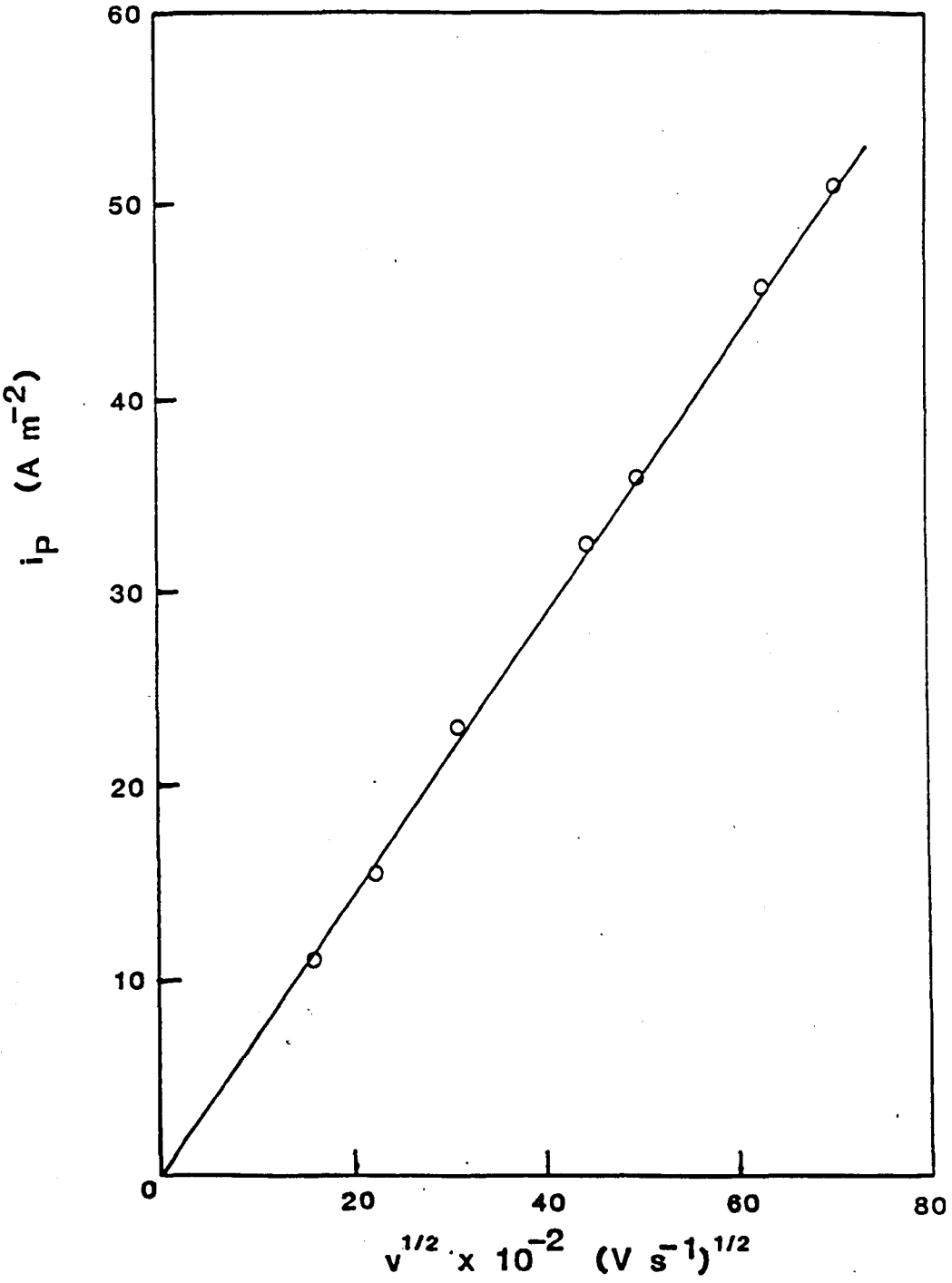

FIGURE 4.9 Dependence of i_p on $v^{\frac{1}{2}}$ in linear sweep voltammograms at lead. 10 mol m^{-3} L-cystine hydrochloride in aqueous 0.1 mol dm^{-3} HCl deoxygenated with N_2. Temperature 25°C. The points are the average of 5 separate measurements.

$s^{-1})^{-\frac{1}{2}}$ agrees with the slope predicted by Kohler et al for a first order reaction (see Table 3.6). This plot also confirms reduction of the disulphide is diffusion controlled and from the slope, assuming n is 2 and α_c is 0.32, from equation (3.29) the diffusion coefficient of L-cystine hydrochloride is (4.8 ± 0.4) x 10^{-10} m^2 s^{-1} at 25°C.

The kinetic parameters for L-cystine hydrochloride reduction may be obtained from a plot of E_p against log v (equation 3.30) or from a plot of log i_p against $[E_p - E^{o'}]$ (equation 3.32). These plots, derived from the voltammograms in Figure 4.8, are shown in Figures 4.10 and 4.11 respectively. From the plot of E_p against log v the Tafel slope is (178 ± 3) mV/decade, α_c is (0.33 ± 0.01) and k_f^o is (1.7 ± 0.2) x 10^{-11} m s^{-1} (assuming D is 5.0 x 10^{-10} m^2 s^{-1} at 25°C). The kinetic parameters from the plot of log i_p against $[E_p - E^{o'}]$, as found in the mercury studies, are less accurate since both i_p and E_p must be measured from the voltammogram. Figure 4.11 gives a Tafel slope of (175 ± 6) mV/decade, α_c is (0.34 ± 0.02) and k_f^o is (1.3 ± 0.3) x 10^{-11} m s^{-1}.

There is reasonable agreement between the kinetics parameters obtained using the RDE and linear sweep voltammetry apart from those obtained using the log i_p against $[E_p - E^{o'}]$ plot, as shown in Table 4.2. It is much more difficult, however, to ensure a reproducible surface condition with solid electrodes than with mercury (see e.g. [9]). Indeed a major advantage of polarography is continuous renewal of the electrode surface. Considering the possible surface contaminants at lead in the acid electrolyte (e.g. lead chloride, lead oxide, other heavy metals) it is perhaps surprising that such a close range of kinetic parameters are obtained. A variation in electrode surface condition is most probably the reason for the slightly adrift kinetic parameters from linear sweep voltammetry and particularly the log i_p against $[E_p - E^{o'}]$ plot.

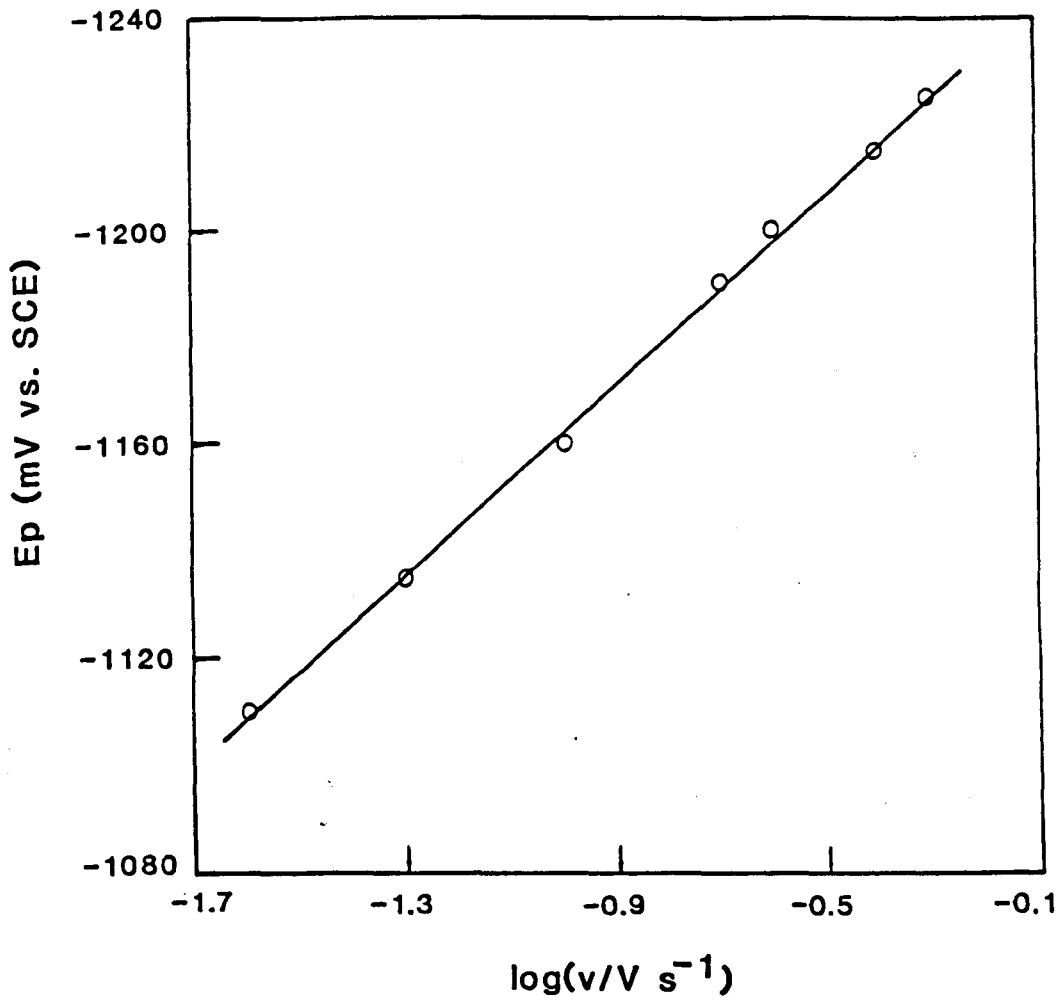

FIGURE 4.10 Dependence of E_p on log v in linear sweep voltammograms at lead. 10 mol m^{-3} L-cystine hydrochloride in aqueous 0.1 mol dm^{-3} HCl deoxygenated with N_2. Temperature 25°C. The points are the average of 5 separate measurements.

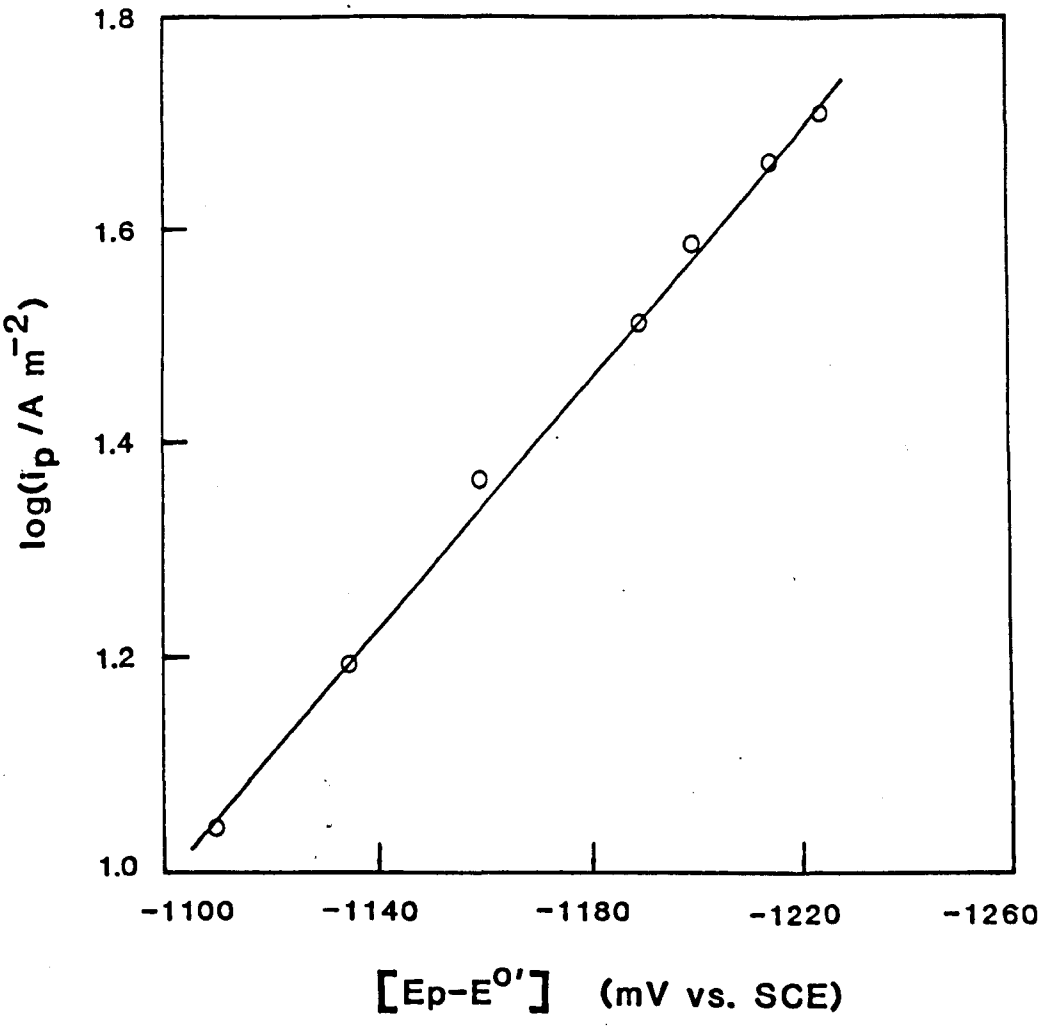

FIGURE 4.11 Dependence of log i_p on $[E_p - E^{o'}]$ in linear sweep voltammograms at lead. 10 mol m^{-3} L-cystine hydrochloride in aqueous 0.1 mol dm^{-3} HCl deoxygenated with N_2. Temperature 25°C. $E^{o'}$ was taken as 0 V to obtain k_f^o from the intercept. The points are the average of 5 separate measurements.

TABLE 4.2 Kinetic parameters from RDE studies and linear sweep voltammetry.

10 mol m^{-3} L-cystine hydrochloride in aqueous 0.1 mol dm^{-3} HCl at 25°C.

	RDE Technique		Linear Sweep Voltammetry	
Plot	log k_f vs E	$-\log[1/i-1/i_L]$ vs E	E_p vs log v	log i_p vs $[E_p-E^{o'}]$
Tafel slope (mV/decade)	183±4	182±4	178±3	175±6
α_c	0.32±0.01	0.32±0.02	0.33±0.01	0.34±0.02
k_f (10^{-11}m s^{-1})	2.2±0.3	2.6±0.3	1.7±0.2	1.3±0.3

(c) Concentration Dependence of the Kinetic Parameters

Although the analysis in Sections 4.2.3(a) and 4.2.3(b) focused on the voltammetry of 10 mol m^{-3} L-cystine hydrochloride, steady state and linear sweep voltammograms at a lead RDE were recorded down to a disulphide concentration of 0.1 mol m^{-3}. There is no increase in k_f^o with reduced disulphide concentration as observed at mercury. Indeed all of the kinetic parameters are independent of the reactant concentration in this range.

4.2.4 Mechanism of the Electrosynthesis of L-Cysteine Hydrochloride from L-Cystine Hydrochloride

To aid in the elucidation of the reduction mechanism the reaction order for L-cystine hydrochloride and protons was determined. Although the voltammetric evidence suggests the reaction order for L-cystine hydrochloride is +1, based on the experience of the mercury studies (Section 3.7) determination by varying the reactant concentration is justified. Steady state voltammograms at a lead RDE were recorded for disulphide concentrations of between 0.5 and 10 mol m^{-3} in aqueous 0.1 mol dm^{-3} hydrochloric acid. At lower reactant concentrations the level of the reduction current is not much above the background. The electrode rotation rate was fixed at 30 Hz as a compromise between maximising the current at the electrode and approximate identification of the convective-diffusion limiting current (see e.g. Figure 4.2). Reasonable agreement between the visual estimate of the limiting current and that calculated from the Levich relationship (equation 3.02) was obtained. The mass transport corrected Tafel plots, derived from the voltammograms, are shown in Figure 4.12. There is no change in the Tafel slope, and therefore α_c, for L-cystine hydrochloride reduction over the range of disulphide concentrations. From Figure 4.12 the relationship between the kinetic current for L-cystine hydrochloride reduction and the L-cystine hydrochloride

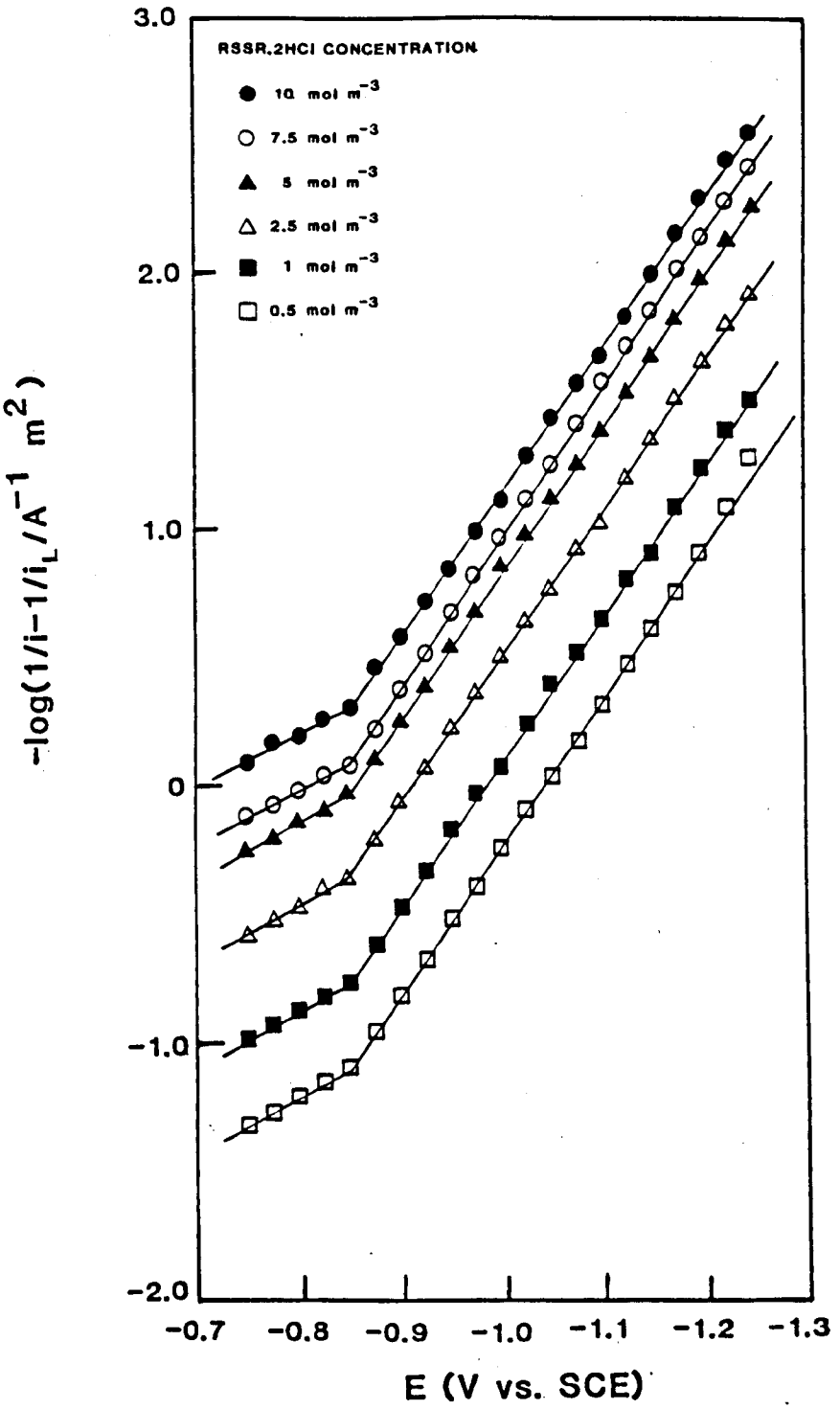

FIGURE 4.12 Mass transport corrected Tafel plots for L-cystine hydrochloride reduction at a lead RDE for a range of disulphide concentrations. The background electrolyte is aqueous 0.1 mol dm^{-3} HCl deoxygenated with N_2. Temperature 25°C. Electrode rotation rate 30 Hz. The background current is subtracted.

concentration, at a series of cathode potentials, is shown in Figure 4.13. The slope of the straight line plots in Figure 4.13, gives the disulphide reaction order at the specified cathode potential. At all potentials examined

$$m_{RSSR} = \left[\frac{\delta\ -\log[1/i\ -\ 1/i_L]}{\delta\ \log\ c_{b(RSSR)}}\right]_{E,c_{b(H^+)}} = +\ 1$$

Determination of the reaction order for protons required experimental care. The study was restricted to a narrow pH range because of the limited solubility of the disulphide above pH 2 (e.g. 0.46 mol m^{-3} in water at 25°C [10]). At such a low reactant concentration the reduction current is not sufficiently large with respect to the background. Hydrochloric acid and potassium chloride solutions (Table 2.2) of constant pH between 1.18 and 2.44 and constant ionic strength (i.e. 0.5 mol dm^{-3}) to preclude possible salt and double layer effects, were utilised. To maximise currents a concentration of 1 mol m^{-3} L-cystine hydrochloride was used which represents close to the maximum reactant solubility at pH 2.5 at 25°C. Steady state voltammograms were recorded at a lead RDE at an electrode rotation rate of 30 Hz which was again selected for the reasons expressed earlier in the determination of the disulphide reaction order. Again, reasonable agreement was obtained between the experimental and calculated convective-diffusion limiting currents. The resultant mass transport corrected Tafel plots are shown in Figure 4.14. The Tafel slope and α_c are invariant over the range of electroiyte pH. The plot of $-\log[1/i - 1/i_L]$ against log (H^+/mol m^{-3}) at a series of cathode potentials is shown in Figure 4.15. At all potentials from the slope of the straight lines,

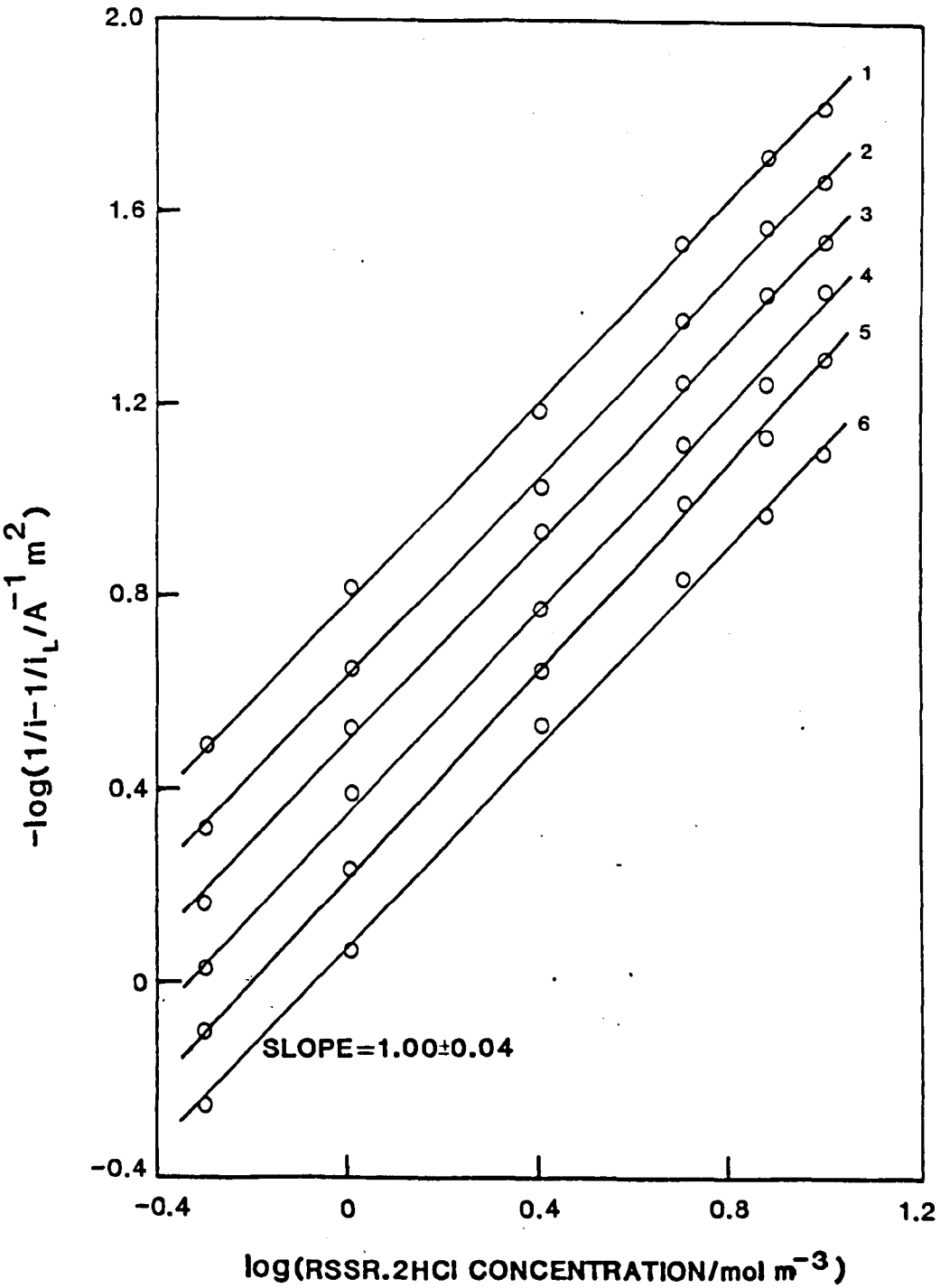

FIGURE 4.13 Plots of $-\log(1/i - 1/i_L)$ against log(RSSR.2HCl concentration) at a selection of cathode potentials. Cathode potentials are 1. −1.125 V 2. −1.100 V 3. −1.075 V 4. −1.050 V 5. −1.025 V and 6. −1.000 V (vs. SCE).

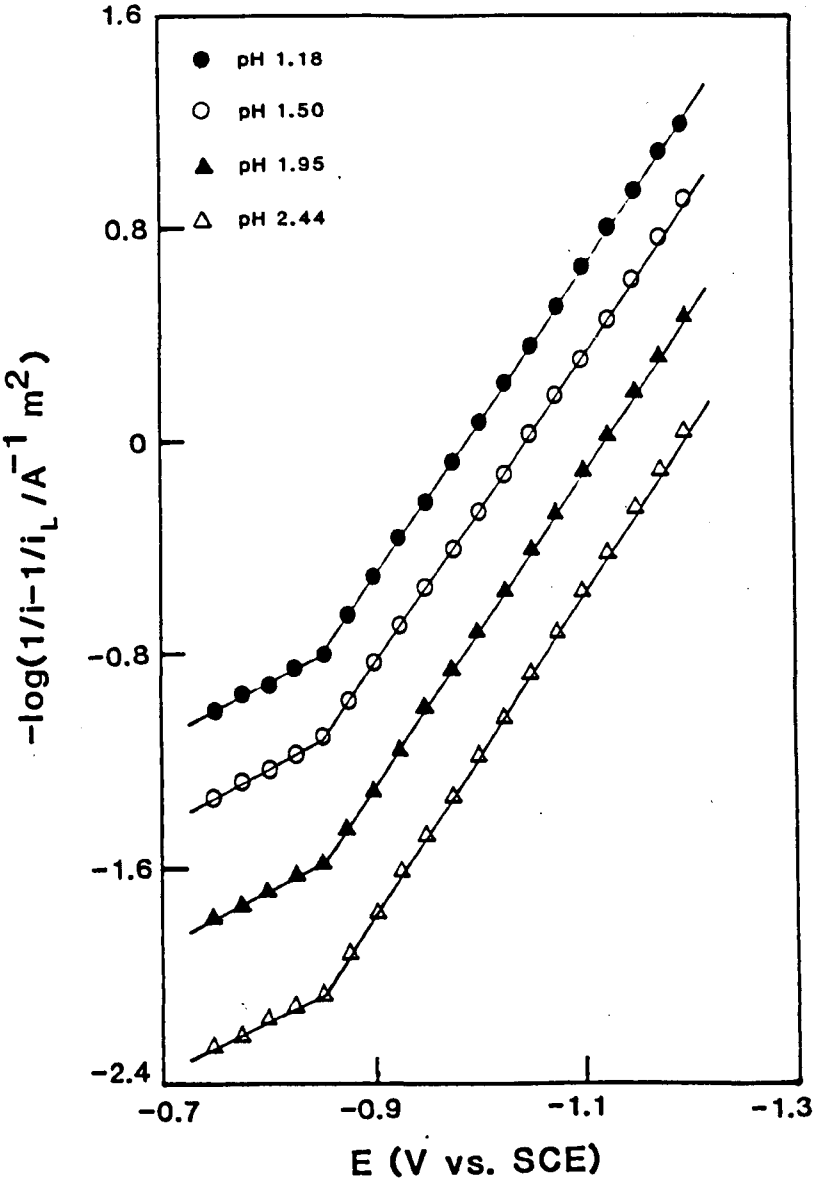

FIGURE 4.14 Variation of mass transport corrected Tafel plots for L-cystine hydrochloride reduction with electrolyte pH at a lead RDE. 1 mol m^{-3} L-cystine hydrochloride in HCl and KCl solutions of constant ionic strength (0.5 mol dm^{-3}) and pH prepared as detailed in Table 2.2. Electrolyte deoxygenated with N_2. Temperature 25°C. Electrode rotation rate 30 Hz. The background current is subtracted.

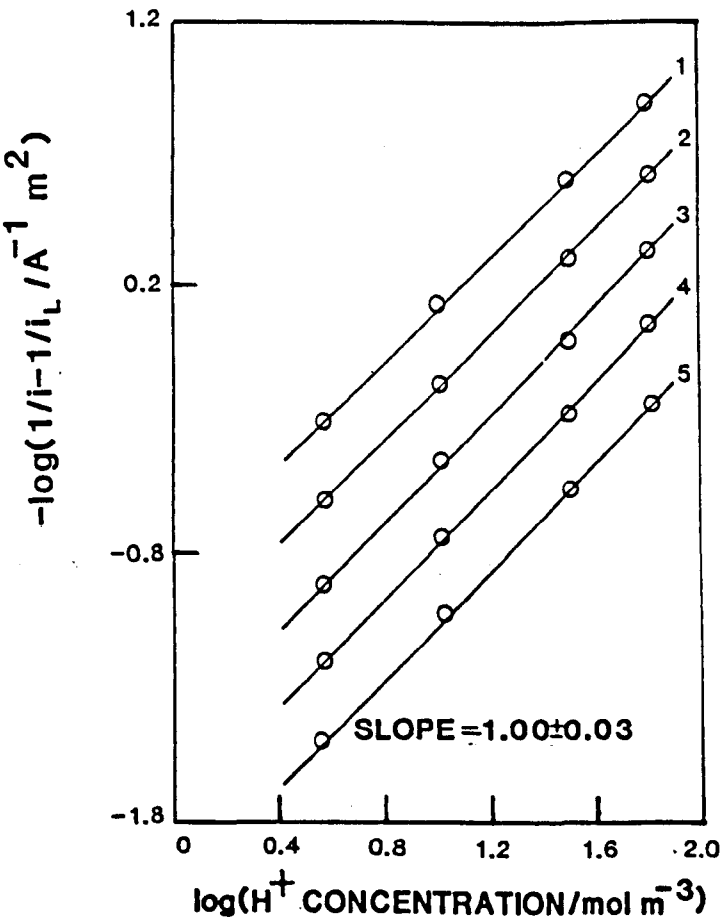

FIGURE 4.15 Plots of $-\log(1/i - 1/i_L)$ against $\log(H^+$ concentration) at a selection of cathode potentials. Cathode potentials are 1. -1.150 V 2. -1.100 V 3. -1.050 V 4. -1.000 V and 5. -0.950 V (vs. SCE).

$$m_{H^+} = -\left[\frac{\delta \log[1/i - 1/i_L]}{\delta \log c_{b(RSSR)}}\right]_{E, c_{b(RSSR)}} = +1$$

A list of plausible mechanisms for L-cystine hydrochloride reduction to L-cysteine hydrochloride is given in Table 3.13. The above reaction orders coupled with a value of 0.32 for α_c, following the arguments of Section 3.9, suggest the mechanism is

$$\begin{aligned} RSSR.2HCl + H^+ + e^- &\xrightarrow{RDS} RSH.HCl + RS^{\bullet}.HCl \\ RS^{\bullet}.HCl + H^+ + e^- &\rightleftharpoons RSH.HCl \end{aligned} \qquad (4.02)$$

The first electron transfer controls the rate of reduction with β for the RDS equal to 0.32. The low symmetry factor perhaps reflects the effect of adsorption of the disulphide at the lead surface upon the kinetics of electron transfer. Proton transfer may either preceed or occur simultaneously with the first electron transfer.

4.3 CONCLUSIONS

On the sole basis of the kinetic studies it might be expected that mercury and lead will be the most efficient cathodes for the electrosynthesis of L-cysteine hydrochloride At the other cathodes the reduction cannot be separated from hydrogen evolution even in aqueous 0.1 mol dm^{-3} hydrochloric acid.

Many of the features of the kinetics of L-cystine hydrochloride reduction at mercury are mirrored at lead. The reduction is electrochemically irreversible, there is no evidence of alternative products and current losses are due exclusively to hydrogen evolution. Steady state voltammograms, in aqueous 0.1 mol dm^{-3} hydrochloric acid, show the reduction commences just positive of hydrogen

evolution and the convective-diffusion limiting current is hidden by gas evolution. From an analysis of the mixed kinetic-mass transport controlled region the Tafel slope is 182 mV/decade, α_c is 0.32 and k_f^o 2.5 x 10^{-11} m s^{-1} (Table 4.2). Similar kinetic parameters were obtained from linear sweep voltammetry (Table 4.2). The high Tafel slope probably reflects the effect of adsorption of the disulphide at the lead surface at the cathode potentials where the amino acid is reduced. There is, however, no direct voltammetric evidence to compare with the adsorption peak in cyclic voltammograms at mercury, to confirm reactant adsorption at lead. Reaction orders of +1 for L-cystine hydrochloride and protons are measured. The mechanism of reduction is, as far as can be ascertained, equivalent at mercury (reaction 3.51) and lead (reaction 4.02).

The diffusion coefficients from the kinetic studies at lead are listed in Table 4.3. These agree well with those recorded with mercury electrodes (Table 3.15 and [5,6]). The greater accuracy of the RDE techniques compared with linear sweep voltammetry, observed at mercury, is reinforced by the coefficients measured at lead. The steady state techniques give an error of less than 3% compared with an error of about 20% from linear sweep voltammetry.

TABLE 4.3 Diffusion coefficients of L-cystine hydrochloride in aqueous 0.1 mol dm^{-3} HCl at 25°C.

Technique	Diffusion Coefficient (10^{-10} m^2 s^{-1})
Constant Potential Coulometry	4.95 ± 0.06
Koutecky-Levich Plot	4.80 ± 0.11
Linear Sweep Voltammetry	4.8 ± 0.4

REFERENCES

1. Kuhn, A.T. in "Electrochemistry of Lead", Ed. Kuhn A.T., Academic Press, New York (1979). Chapter 14.
2. Barradas R. G., Belinko K. & Ambrose J.; *Can. J. Chem.* 53, 389, (1975).
3. von Fraunhofer J.A.; *Anticorrosion*, December (1968). Page 5.
4. Kelly E.H.; *Electricity Research and Development Research Report 0273*, April (1988).
5. Issa I. M., Samahy A. A. El, Issa R.M. & Temerik Y.M.; *Electrochim. Acta* 17, 1615, (1972).
6. Kolthoff I. M. & Barnum C.; *J. Am. Chem. Soc.* 63, 520, (1941).
7. Hayes M. & Kuhn A.T. in "Electrochemistry of Lead". Ed. Kuhn A.T., Academic Press, New York (1979). Chapter 8.
8. Baugh I. M. & Bladen K. L.; *J. Electroanal. Chem.* 145, 325, (1983).
9. Adams R.N. "Electrochemistry at Solid Electrodes". Marcel Dekker, New York (1969).
10. Dawson R.M.C., Elliott D.C., Elliott W.H. & Jones K.M. "Data for Biochemical Research". Clarendon Press, Oxford (1986). Pages 12 and 13.

CHAPTER 5

EXPERIMENTAL FOR BATCH REACTOR STUDIES

5.1 ELECTRODES

5.1.1 Material and Electrode Specifications

The specification of the metals employed are listed in Table 5.1. Planar sheet electrodes were used which had active areas of (10 x 10) cm^2 when sealed within the batch reactor. An aluminium backing plate was used with tin, nickel and molybdenum electrodes to provide electrical contact since they were too short to contact directly.

5.1.2 Mercury Plated Copper Cathode

A mercury plated copper electrode was prepared by the method detailed in Section 2.1.3 [1]. A copper electrode was cleaned with wire wool, degreased with absolute alcohol and pickled in aqueous 2.0 mol dm^{-3} hydrochloric acid for 60 seconds. After rinsing thoroughly with doubly distilled water the electrode was placed in a 'beaker' cell fitted with a silicone rubber gasket cell top and a platinised titanium anode. Electroplating was performed in aqueous 0.15 mol dm^{-3} mercuric nitrate and 0.12 mol dm^{-3} potassium cyanide (1 dm^3) previously de-oxygenated with nitrogen, which was passed over the electrolyte during electrolysis to prevent air ingress. A constant current of 5 A was passed for 10 minutes, using a Farnell L12-10C power supply, with the rate of mass transport of mercuric ions enhanced by use of a magnetic stirrer. After plating, the mercury surface was rinsed with doubly distilled water and wiped with a tissue to give a mirror finish.

5.1.3 Amalgamated Copper Cathode

A copper electrode was cleaned with wire wool, degreased with absolute alcohol and pickled in aqueous 2.0 mol dm^{-3} hydrochloric acid for 10 minutes. After rinsing thoroughly with doubly distilled water the electrode was submerged in a bath of mercury (triply distilled) for 24 hours. On removal excess mercury was wiped off with cotton wool previously soaked in mercury, using a circular motion.

TABLE 5.1 Specification of the electrode materials employed in the batch reactor.

Metal	Source	Specification
Mercury	Belgrave Mercury Ltd.	Polarographic Grade BM3. Triply distilled.
Copper	Imperial Metal Industries	99.0 + % w/w Copper Pb 0.005 % w/w, Bi 0.001 % w/w.
Lead	Associated Lead Manufacturers (Chester)	99.90 + % w/w Lead Bi < 0.005 % w/w, (Fe,Cu) < 0.003 % w/w,(Sb,Ag,Zn) < 0.002 % w/w, (Ni+Co) < 0.001 % w/w, (Sn,Cd,As,S) trace.
Titanium	Imperial Metal Industries	99.08 + % w/w Titanium Fe < 0.20 % w/w, 0_2 < 0.18 % w/w, C < 0.10 % w/w,(Pd,Mo,Ni) each < 0.1 % w/w & total < 0.4 % w/w, N_2 < 0.03 % w/w, H_2 < 0.015 % w/w.
Carbon	Cramhill & Percy Ltd.	99.4 + % w/w Carbon Ash 0.4 % w/w, Fe 0.1 % w/w, (Ca,Si) 0.04 % w/w, S 200 ppm, Al 50-100 ppm, (Cr,V,Ba,Ni,Ti) 10-50 ppm, (Sr,Mo,B,Hg,Mo) 1-10 ppm, (Co,Zr,Sn,Cu,Pb,Ag,Be,La) < 0.1 ppm.
Tin	Goodfellow	98.8 + % w/w Tin Sb 1.1 % w/w, Pb 600 ppm, Cu 100 ppm, As 20 ppm, (Ag,Bi,Cd,Fe,Ni,Zn) 10 ppm.
Nickel	Goodfellow	99.98 + % w/w Nickel C 70 ppm, (Cu,Fe,Mg,Mn,Ti,S) 10 ppm, (Co,Cr,Si) 8 ppm.
Molybdenum	Goodfellow	99.9 + % w/w Molybdenum (Si,Fe,Cr) < 50 ppm, C 40 ppm, (Pb,Ti) < 30 ppm, 0_2 30 ppm, (Al,Ca,Cu,Mg) < 20 ppm, (W,N_2) 10 ppm, H_2 5 ppm, K < 2 ppm.
Stainless steel	Imperial Metal Industries	Cr 17-20 % w/w, Ni 7-10 % w/w, Mn < 2 % w/w, C < 1500 ppm, Ti 4 x C ppm, Fe balance.
Platinised Titanium	Imperial Metal Industries	Coating thickness 2.5 μm.

5.2 ELECTROCHEMICAL CELL DESIGN AND ANCILLARY EQUIPMENT

The parallel plate cell design is shown in Figure 5.1 and the important cell dimensions given in Table 5.2.

TABLE 5.2 Electrochemical reactor cell dimensions.

Parameter	Dimension
Cathode area	(10 x 10)cm^2
Anode area	(10 x 10)cm^2
Cathode to membrane gap	2.0 cm
Anode to membrane gap	1.2 cm
Interelectrode gap	3.2 cm
Catholyte compartment	
- Width	2.0 cm
- Length parallel to the electrolyte flow	10.0 cm
- Length perpendicular to the electrolyte flow	10.0 cm
- Volume	200 cm^3
- Internal diameter of the electrolyte ports	0.80 cm
Anolyte compartment	
- Width	1.2 cm
- Length parallel to the electrolyte flow	10.0 cm
- Length perpendicular to the electrolyte flow	10.0 cm
- Volume	120 cm^3
- Internal diameter of the electrolyte ports	0.60 cm

The cell housing, end plate and cell frames were constructed from PVC. The complete assembly was sealed by tightening a screw which was fixed within an end section of the housing, whilst disc spring compressors located in grooves at the top of the cell maintained an even pressure across the cell. PTFE tape, (1 cm^2 cross-sectional area), at both sides of each cell frame was used as sealant.

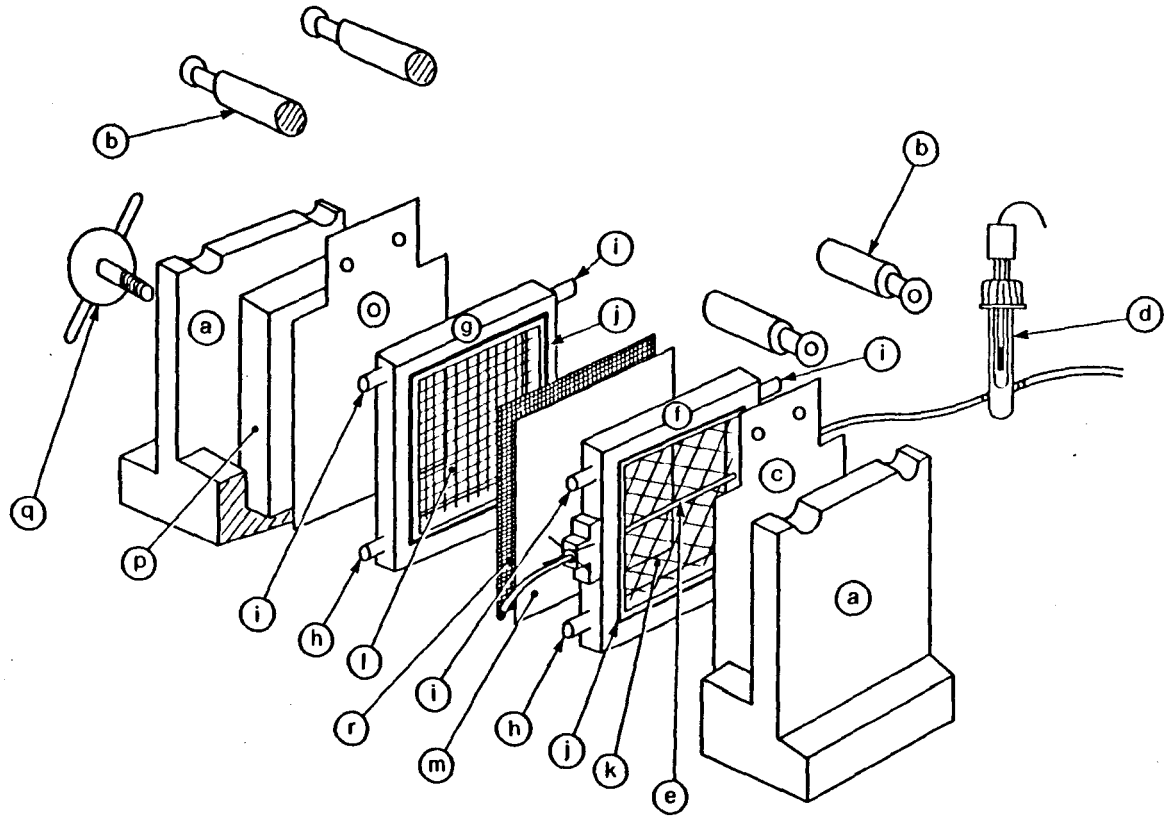

a) cell housing b) disc spring compressors c) cathode d) glass reservoir containing SCE e) PTFE luggin capillary f) catholyte cell frame g) anolyte cell frame h) electrolyte inlet ports i) electrolyte outlet ports j) PTFE sealant k) turbulence promoter (variety used) l) Netlon garden mesh m) Nafion 324 cationic ion-exchange membrane n) nylon mesh o) anode p) end plate q) screw to press assembly together.

FIGURE 5.1 Exploded view of the parallel plate electrochemical reactor.

Nafion 324 cationic ion–exchange membrane divided the cell, with several sections of 125 μm thick nylon mesh and Netlon garden mesh (1 cm^2 gap area) used to reinforce its anodic face. This reduced membrane movement which was important in mass transport measurements. The performance of a range of Netlon turbulence promoters was examined in the catholyte chamber. The chamber was completely filled with the required number of (10 x 10) cm^2 sections of promoter. In large cells reference electrodes are often prone to gas blockages. The cell was consequently fitted with a 'flowing' reference electrode consisting of a glass reservoir, containing an SCE, connected to a luggin capillary formed from PTFE tubing (3 mm o.d.) with a 1 mm diameter hole drilled in its surface. The hole was centered on the cathode, 3 mm from the electrode surface, by locking screws on either side of the catholyte cell frame and electrolyte flowed through the glass reservoir and luggin capillary into the catholyte compartment at a uniform flow rate of 0.25 cm^3 $minute^{-1}$ using principally a Gilson Model 301 HPLC pump although a perastaltic pump was used in a few experiments. Some experiments employed a reference electrode in the anolyte compartment. A length of PTFE tubing (3 mm o.d.) was pushed into the compartment through one of the electrolyte output ports and located close to the anode by attachment to the Netlon garden mesh. The opposite end of the tubing was connected to a glass reservoir, containing an SCE, and the anolyte level maintained by balancing the hydrostatic head. This arrangement was, however, prone to gas blockages.

Separate flow loops (Figure 5.2) provided batch recycle operation for the catholyte and anolyte. The reservoirs, which had a maximum capacity of 6 dm^3, and the associated plumbing to the flow control values were constructed from PVC. Connections from the cell to the flow control valves were made with silicone rubber tubing. Magnetically coupled, Totton EMP 50/7 pumps (rated at 50 cm^3

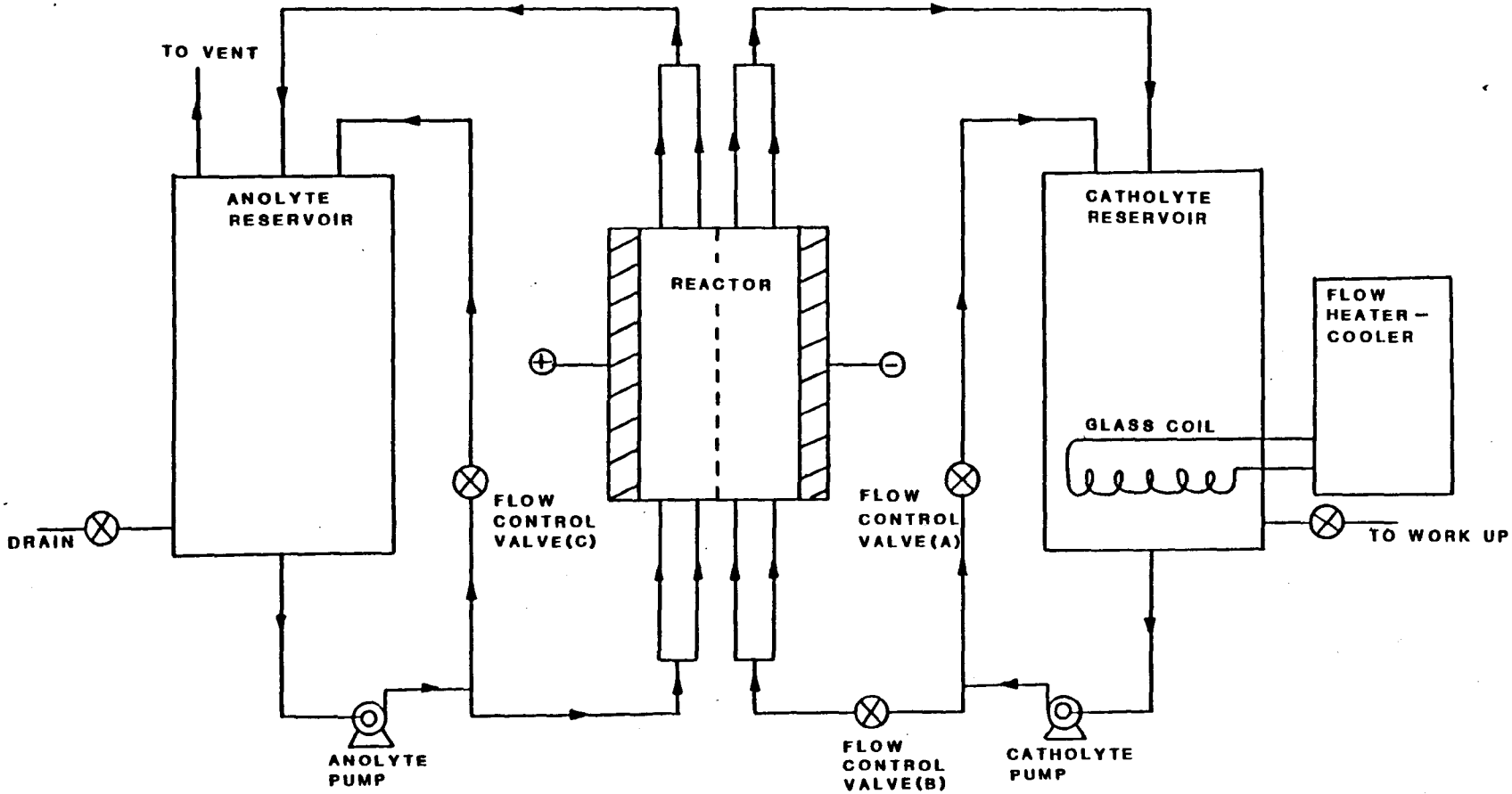

FIGURE 5.2 Flow schematic for batch recycle operation of the parallel plate electrochemical reactor.

minute^{-1} maximum) recycled the electrolytes between the reservoirs and the cell. A more powerful Iwaki pump (rated at 70 dm^3 minute^{-1} maximum) provided greater catholyte flow rates. The range of flow rates obtained was restricted by a large pressure drop in the system, not only through the cell, but between the cell and reservoirs. This was principally due to the difference in the internal diameter of the silicone rubber (0.9 cm) and PVC (3 cm) plumbing. The catholyte and anolyte flow rates were controlled by the flow control valves which were calibrated. The catholyte temperature in the reservoir was held constant with a Grant FC25 or Haake L flow heater-cooler linked to a glass coil in the reservoir. Thermocouples located within the reservoir and at the reservoir inlet monitored the temperature. A length of PVC tubing from the anolyte reservoir provided a gas vent.

Constant currents were supplied by type H60/50 (capable of delivering 50A at 60 V maximum), L12-10C (10 A at 12V maximum) and L30-5C (5 A at 30 V maximum) Farnell stabilised power supplies. Shunts of value 2 A/75 mV, 5 A/50 mV and 20 A/200 mV (all with a precision of ± 0.1%) connected between the anode and the power supply allowed measurement of the current passed. Thandar TM 451 or Keithly 178 high impedance digital multimeters placed directly across the cathode and reference electrode, the cathode and anode and the shunt monitored continuously the cathode potential, cell voltage and cell current respectively. The pilot plant is shown in Plate 5.1.

5.3 CHEMICALS AND SOLUTIONS

5.3.1 L-Cystine Hydrochloride Solutions

All experiments used aqueous 2.0 mol dm^{-3} hydrochloric acid background electrolyte with the L-cystine hydrochloride concentrations indicated in Chapters 7 and 8. Lancaster Syntheses reagent grade L-cystine, BDH Analar grade acid and

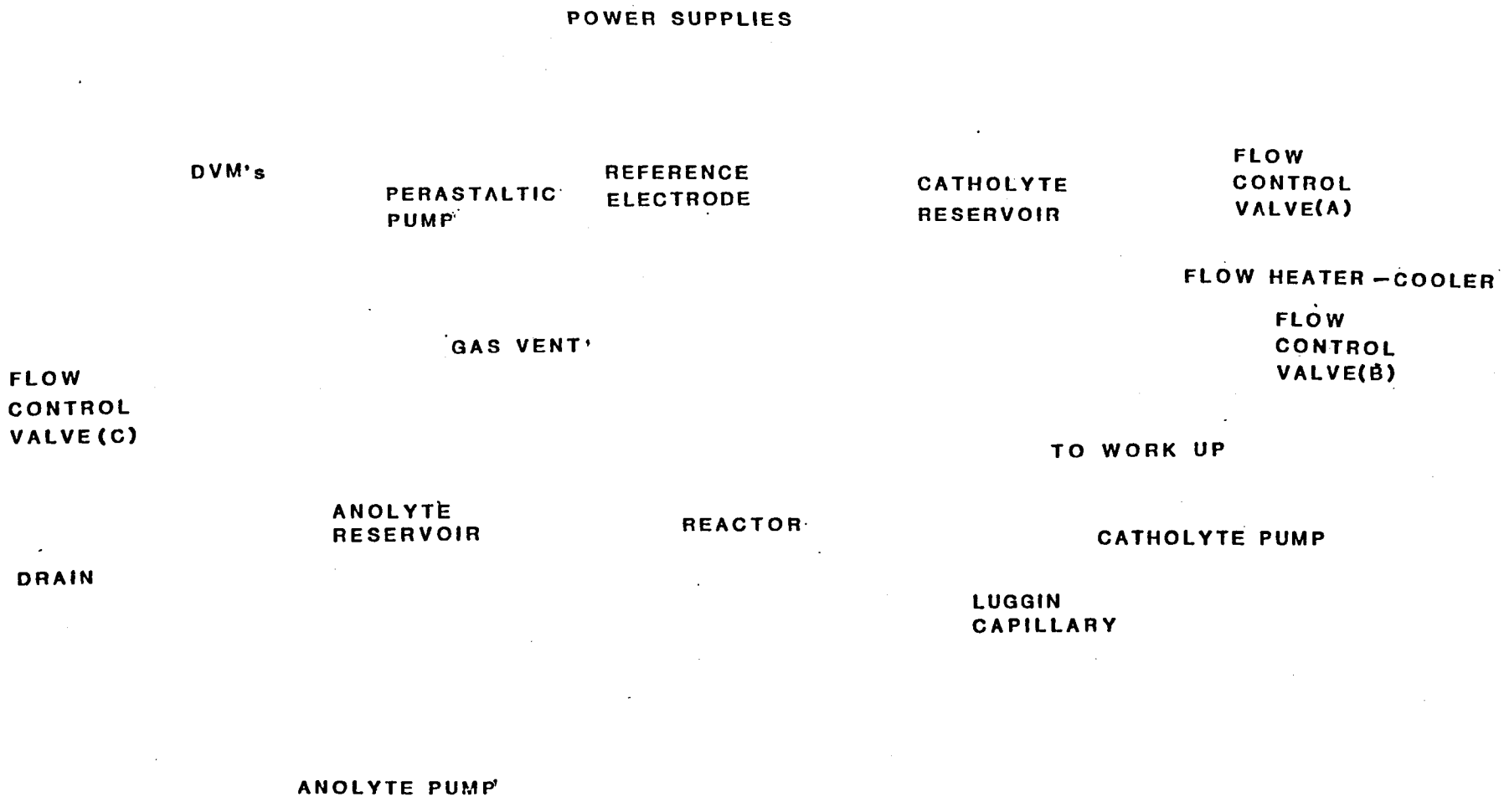

PLATE 5.1 Pilot plant

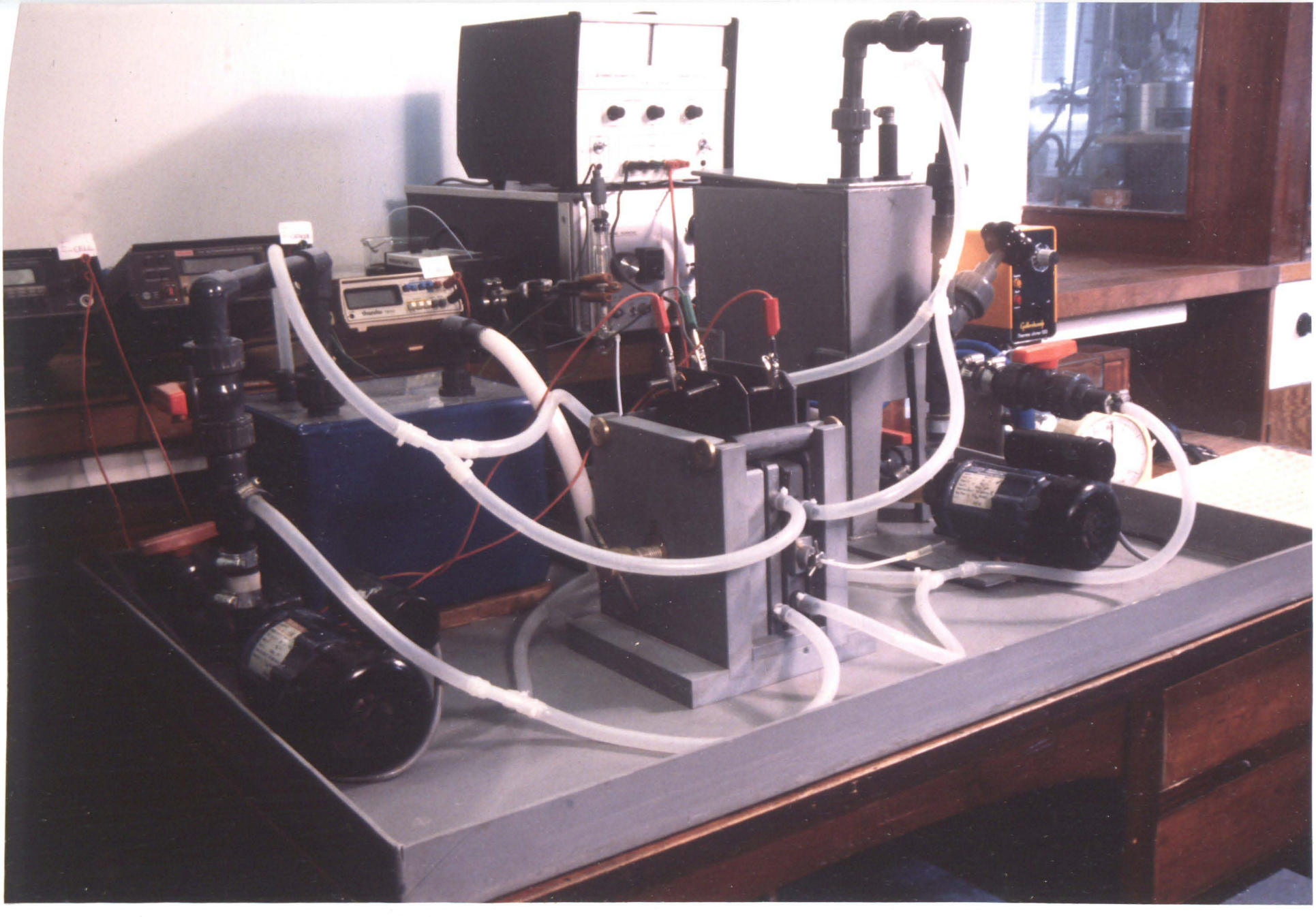

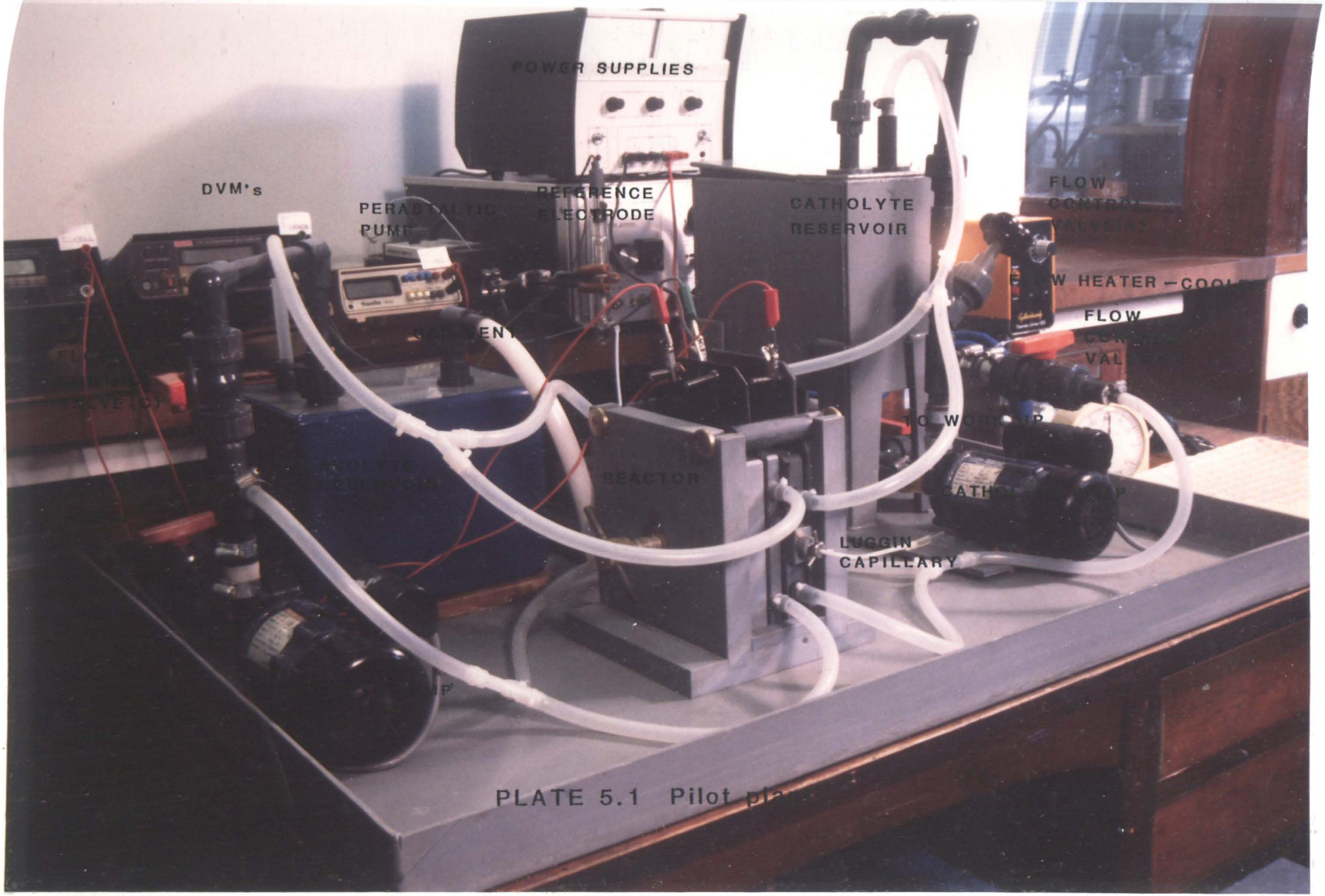

PLATE 5.1 Pilot pla

doubly distilled water were used.

5.3.2 Ferricyanide and Ferrocyanide Solution

An aqueous 0.05 mol dm^{-3} potassium ferricyanide, 0.05 mol dm^{-3} potassium ferrocyanide and 1.0 mol dm^{-3} potassium hydroxide solution was employed in mass transport measurements. The physical properties of this solution have been well documented [2]. BDH Analar grade chemicals and doubly distilled water were used.

5.4 PROCEDURES

5.4.1 Calibration of Electrolyte Flow Rates

Table 5.3 shows the type of pump used and the position of the flow control valves required to obtain a given electrolyte flow rate or average linear velocity (defined as the electrolyte flow rate divided by the cross-sectional area of the cell perpendicular to the direction of electrolyte flow) through the cell. Flowmeters could not be incorporated into the catholyte and anolyte plumbing. They severely restricted the flow rate. Flow rates were measured by determining the time taken to pump 5 dm^3 of electrolyte from the reservoir, through the cell and into a measuring cylinder. At each flow rate three individual measurements were taken and the average value used.

5.4.2 Determination of the Average Mass Transport Coefficient using the Diffusion Limited Current Technique

The electroreduction of ferricyanide at a platinised titanium cathode was used. The transparent sections of the catholyte plumbing were masked with black tape to avoid photochemical decomposition of the reactant [3]. The platinised titanium cathode and a nickel anode were polished with fine emery paper and washed in absolute alcohol followed by distilled water. After the cell had been assembled,

TABLE 5.3 Calibration of the flow control valves in the pilot plant.

CATHOLYTE				
Pump	Flow Rate ($10^{-6}m^3s^{-1}$)	Average Linear Velocity ($10^{-3}m\ s^{-1}$)	Flow Control Valve Position	
			Valve(A)	Valve(B)
Totton EMP 50/7	246	123	Closed	Open
	176	88	2 Turns	"
	130	65	4 Turns	"
	94	47	6 Turns	"
	66	33	Open	"
	50	25	"	1 Turn
	40	20	"	2 Turns
	30	15	"	3 Turns
	22	11	"	4 Turns
	14	7	"	5 Turns
	10	5	"	6 Turns
Iwaki	412	206	Closed	Open
	366	183	2 Turns	"
	328	164	4 Turns	"
	272	136	6 Turns	"
	204	102	OPEN	"

ANOLYTE			
Pump	Flow Rate ($10^{-6}m^3s^{-1}$)	Average Linear Velocity ($10^{-3}m^3s^{-1}$)	Flow Control Valve Position Valve (C)
Totton.	246	126	Closed
EMP 50/7	131	109	4 turns
	67	56	Open

The flow control valves are identified in Figure 5.2. A single turn of the flow control valve corresponds to 90°.

the cathode was further preconditioned by evolving hydrogen gas at a constant current density of 200 A m^{-2}, for 15 minutes, from aqueous 1.0 mol dm^{-3} potassium hydroxide electrolyte [3]. The cell was charged with 2 dm^3 of catholyte (aqueous 0.05 mol dm^{-3} potassium ferricyanide, 0.05 mol dm^{-3} potassium ferrocyanide and 1.0 mol dm^{-3} potassium hydroxide) and 2 dm^3 of anolyte (aqueous 1.0 mol dm^{-3} potassium hydroxide). The catholyte was purged with nitrogen for an hour before measurements were taken, and the gas passed into the reservoir for the duration of the experiment to reduce air ingress. At average linear catholyte velocities of 0.033 m s^{-1}, 0.123 m s^{-1} and 0.206 m s^{-1} current-voltage curves were recorded. The cell current was increased in small increments and the cathode potential and cell voltage recorded when they steadied. This took, on average, 10 seconds. At all other average linear catholyte velocities examined, since the current-voltage curves indicated ca. -0.5 V (vs. SCE) corresponded to the centre of the limiting current plateau, the current was adjusted from zero, in a single step, to a value which produced this cathode potential and the limiting current recorded when steady. Three separate measurements of limiting current were obtained for each average linear catholyte velocity. The temperature of the catholyte in the reservoir was maintained at 25.0 ± 0.5°C.

5.4.3 Constant Current Batch Electrolysis of L-Cystine Hydrochloride

L-Cystine hydrochloride reduction was performed at a selection of cathode materials (i.e. mercury plated copper, amalgamated copper, lead, titanium, tin, carbon, stainless steel, copper, nickel and molybdenum). All experiments employed a platinised titanium anode and a 2 dm^3 volume of aqueous 2.0 mol dm^{-3} hydrochloric acid anolyte. The catholyte was a 2 dm^3 volume of aqueous 700 mol m^{-3} or 250 mol m^{-3} L-cystine hydrochloride in 2.0 mol dm^{-3} hydrochloric acid, which was maintained at a temperature of 25.0 ± 0.5°C in the

reservoir.

The electrodes were conditioned prior to electrolysis. All electrodes were polished with fine emery paper, degreased with absolute alcohol and rinsed with doubly distilled water. This was the only pretreatment for titanium, carbon and platinised titanium electrodes. The lead electrode was further treated by immersion in aqueous 1.0 mol dm^{-3} nitric acid for 15 seconds to remove surface oxides. After rinsing with doubly distilled water the electrode was sealed within the cell and a cathodic potential imposed prior to catholyte contacting its surface. This minimised corrosion. Similarily a cathodic potential was imposed upon mercury plated copper, amalgamated copper, tin, stainless steel, copper, nickel and molybdenum electrodes before the cell was charged with catholyte.

After the reservoirs were charged, the catholyte and anolyte flow rates were fixed and a selected constant current applied to the cell. At measured time intervals, 3 cm^3 samples of catholyte were withdrawn from the reservoir and retained for HPLC analysis (see Section 2.6) to determine the L-cystine hydrochloride and L-cysteine hydrochloride concentrations. Simultaneously, the cathode potential, cell voltage and catholyte temperature were recorded. At the end of an electrolysis the catholyte and anolyte volumes were measured to give an estimate of the quantity of solvent transported through the membrane.

5.4.4 Cathode Stability Test for Mercury Plated Copper, Lead and Titanium

(a) Procedure

Electrolysis at a constant current density of 500 A m^{-2} and electrolyte flow rate of 246 x 10^{-6} m^3 s^{-1} was performed for 48 hours at mercury plated copper and 168 hours at lead and titanium without cleaning the electrode surfaces. The catholyte had to be replenished every 12 hours. Concentrated hydrochloric acid was added to the anolyte periodically to maintain the acid concentration.

(b) X-ray Diffraction (XRD) of the Lead Electrode

After stability testing XRD photographs of the lead and titanium electrode surface were taken with 114.83 mm diameter Debye-Scherrer cameras, using nickel filtered copper K-alpha radiation with the X-ray tube operating at 45 kV and 30 mA. All the hardware employed was manufactured by Philips.

Compound(s) on the electrode surface were identified by comparing the diffraction pattern to standard patterns in a data base supplied by the Joint Committee on Powder Diffraction Standards of Swarthmore, Pennsylvania, USA.

(c) Inductively Coupled Plasma - Mass Spectroscopy (ICP-MS)

Samples of product taken from the several batches produced during the stability testing were analysed for metal impurities (especially the cathode metal) using ICP-MS. The product was obtained from the treated catholyte by rotary evaporation at 90°C. The solid L-cysteine hydrochloride was dried to constant weight in a vacuum oven at 75°C and then dissolved (1.0 g) in aqueous 2.0 mol dm^{-3} hydrochloric acid (100 cm^3). The solution was introduced into the plasma of the VG Elemental PlasmaQuad PQ2. The instrument was capable of determining simultaneously a wide range of elements down to ppb levels using a standard solution of 6 to 8 elements. The trace metals present in 2.0 mol dm^{-3} hydrochloric acid were determined and subtracted from the response obtained with the solutions of L-cysteine hydrochloride.

5.4.5 Current-voltage curves for L-Cystine Hydrochloride Reduction

Current-voltage curves of L-cystine hydrochloride reduction were recorded at all cathodes, pretreated as detailed in Section 5.4.3, using a platinised titanium anode and a 2 dm^3 volume of aqueous 2.0 mol dm^{-3} hydrochloric acid anolyte. The catholyte was a 2 dm^3 volume of aqueous 250 mol m^{-3} or 50 mol m^{-3} L-cystine hydrochloride in 2.0 mol dm^{-3} hydrochloric acid. The reservoirs were

charged and the catholyte deoxygenated with nitrogen for an hour before measurements were taken. Whilst current–voltage curves were recorded nitrogen was passed into the catholyte reservoir, to reduce air ingress, and the catholyte temperature was maintained at 25.0 ± 0.5°C. The cell current was increased in small increments and the cathode potential and cell voltage recorded when steady. The reverse current–voltage curve from the final to zero current was obtained to check for hysteresis. Experiments were performed in triplicate.

5.4.6 Specific Rotation of L–Cysteine Hydrochloride

The specific rotation of L–cysteine hydrochloride produced in the batch electrolyses was measured and compared with standard values [4]. The product, obtained from the catholyte after batch electrolysis as detailed in Section 5.4.4(c), was dissolved to give an aqueous solution containing 670 mol m^{-3} of the amino acid in 1.0 mol dm^{-3} hydrochloric acid. The specific rotation of the solution was measured at 20°C with the D line of a sodium lamp in a Hilger and Watts polarimeter. For comparison, the specific rotation of an identical solution prepared from BDH Analar grade L–cysteine hydrochloride was measured.

REFERENCES

1. Daly P.J., Page D.J. & Compton R.G.; *Anal. Chem.* 55, 1191, (1983).

2. Ariva A.J., Marchiano S.L. & Podestá J.J.; *Electrochim. Acta* 12, 259, (1967).

3. Berger F.P. & Ziai A.; *Chem. Eng. Research and Design* 61, 377, (1983).

4. Itoh T. in "Synthetic Production and Utilisation of Amino Acids". Eds. Kaneko T., Izumi Y., Chibata I. & Itoh T., Halsted Press, New York (1974). Chapter 5.

CHAPTER 6

MASS TRANSPORT IN THE ELECTROCHEMICAL REACTOR USING THE DIFFUSION LIMITED CURRENT TECHNIQUE

6.1 INTRODUCTION

The average mass transport coefficient (K_L) in the reactor was determined by the diffusion limited current technique. The range of usable catholyte flowrates, both in the empty catholyte channel and in the presence of turbulence promoters, was examined. The study had three objectives:

1) To determine the applicability of the simple models outlined in Section 7.3 to the electrosynthesis of L-cysteine hydrochloride in the reactor. K_L is obtained from the models but an independent determination is required to test the validity of the results.
2) To contrast the reactor performance with other parallel plate cell designs in terms of mass transport.
3) To establish some criteria for the selection of turbulence promoters in the reactor. There is scant information in the literature in this area.

6.2 MASS TRANSPORT RATES IN FLOW CELLS BY THE DIFFUSION LIMITED CURRENT TECHNIQUE

6.2.1 The Technique

A number of monographs and review articles (e.g. [1-3]) have been devoted to the subject. Only a brief outline will be given here.

For an electrode reaction which is controlled by convective - diffusion of the reactant the limiting current is defined by equation (6.01).

$$I_L = n F A K_L c_b \qquad (6.01)$$

where A is the active electrode area and c_b is the bulk concentration of the reactant. Consequently, measuring the potential independent limiting current

plateau of electrochemical reactions, from steady state current versus electrode potential graphs, provides a value for K_L providing n, A and c_b are known. Useful electrochemical reactions have, however, to satisfy a number of criteria:

1) The reaction must be diffusion controlled.

2) The reaction stoichiometry must be known (i.e. n is established) and must take place with 100% current efficiency.

3) The limiting current plateau must have adequate width (e.g. about 100 mV) and minimum inclination. For aqueous solutions the achievement of adequate width is aided by facile electrochemical kinetics and an equilibrium electrode potential for the reaction well separated from hydrogen (for cathodic reactions) or oxygen (for anodic reactions) evolution potentials. Plateau inclination results if there is an increase in the electrode surface area or a decrease in the bulk concentration of the reactant during measurements. The former is common if metal deposition reactions are used. The latter requires the reactant to be chemically stable, and, in addition, electrolysis times to be minimised during the recording of current-voltage curves. Often more problematical in terms of a large plateau inclination, however, is a non-uniform current distribution which can be particularly evident if large electrode areas or complex cell designs are used.

The above criteria are met by a variety of reactions [1,3] of which the ferricyanide/ferrocyanide redox couple (reaction 6.02) is the best behaved and therefore the most frequently adopted.

$$[Fe(CN)_6]^{3-} + e^- \longrightarrow [Fe(CN)_6]^{4-} \qquad (6.02)$$

Since the system was used in this study it is worth considering the conditions under which it should be used [4]. A platinum or nickel electrode is employed to provide acceptable reaction reversibility and reproducible limiting currents, after suitable conditioning of the electrode surface. The background electrolyte is normally 1 to 3 mol dm^{-3} sodium or potassium hydroxide in which the redox couple is stable. The system is, however, prone to slow photolytic decomposition (reaction 6.03), but in practice the use of freshly prepared solutions stored in darkness overcomes the problem.

$$[Fe(CN)_6]^{4-} + H_2O \underset{\text{Dark}}{\overset{\text{Light}}{\rightleftharpoons}} [Fe(CN)_5]^{3-} + CN^- \qquad (6.03)$$

$$CN^- + H_2O \rightleftharpoons HCN + OH^-$$

Important to mass transport studies the diffusion coefficients of ferricyanide and ferrocyanide and the density and the dynamic viscosity of solutions of the redox couple in the favoured background electrolytes, are available in tabular form [5]. Oxygen is normally removed from solution to eliminate a background oxygen reduction current. Finally care should be taken to avoid rate control from the secondary electrode reaction particularly in cells with electrodes of equal area. In undivided cells equimolar solutions of the redox couple should be avoided and in divided cells, if a common reservoir is not used, a judicious selection of the anode and anolyte is required.

In this study, as stated, only macroscopic, averaged mass transport coefficients were measured. Local mass transport coefficients can be measured by using an array of microelectrodes or segmenting the electrode.

6.2.2 Dimensionless Group Correlations

Mass transport relationships, because of the large number of variables involved, are normally expressed in terms of dimensionless group correlations. The theory of the technique [6] and the application to electrochemical systems [7] has been discussed. For forced convection in a channel the general case is a dimensionless group correlation in terms of four dimensionless groups (i.e. the Sherwood number (Sh), Reynolds number (Re), Schmidt number (Sc) and Le group):

$$Sh = a\ Re^b\ Sc^c\ Le^d \qquad (6.04)$$

where a, b, c and d are constants. Sh describes the rate of mass transport. $(Re)^b$, $(Sc)^c$ and $(Le)^d$ describe the dependence of the rate of mass transport on the fluid flow, on the transport properties of the electrolyte and on the channel length in the direction of electrolyte flow respectively. By definition

$$Sh = K_L d_e/D \qquad (6.05)$$

$$Re = \bar{v} d_e/\nu \qquad (6.06)$$

$$Sc = \nu/D \qquad (6.07)$$

$$Le = d_e/L \qquad (6.08)$$

where the hydraulic diameter (d_e = 4 x [channel cross-sectional area perpendicular to flow]/wetted perimeter) is the characteristic length (the usual choice), $\bar{v}$ is the average, linear electrolyte velocity (electrolyte flow rate/channel cross-sectional

area), ν (dynamic viscosity/density) is the electrolyte kinematic viscosity and L is the channel length in the direction of electrolyte flow. By definition, therefore, Le is a dimensionless length.

In many mass transport studies (as in this study) the reactor dimensions are not varied. Under this condition equation (6.04) is modified to

$$Sh = a' Re^b Sc^c \qquad (6.09)$$

where $a' = a(Le)^d$ is a constant for a given reactor.

For such empirical mass transport correlations the most satisfactory way of determining a', b and c is to take logarithms of equation (6.09) and perform a multiple regression analysis. Less rigorous but usual in practice a value is assumed for c, which is normally 1/3 based upon practical experience (see e.g. [2]), and Sh is plotted against Re on log-log axes and a simplified regression analysis is applied. Clearly a dimensionless group correlation is by nature an averaged experession over a certain range of experimental conditions and extrapolation outside this range should be undertaken with caution.

6.3 MASS TRANSPORT CORRELATIONS FOR PARALLEL PLATE ELECTROCHEMICAL REACTORS

One of the objectives of the study is to contrast the mass transport in the reactor with other parallel plate cell designs. Consequently this section considers some relevant mass transport correlations available in the literature.

6.3.1 Theoretical Correlations

Two fundamental equations are used to obtain theoretical mass transport correlations. Assuming migration can be neglected, which is arranged

experimentally by using a large excess of indifferent electrolyte, mass transport occurs by convective-diffusion which is described by

$$\frac{\partial c}{\partial t} = -D \nabla^2 c + v \nabla c \qquad (6.10)$$

where c is the reactant concentration, v the linear electrolyte velocity and D the diffusion coefficient of the reactant. Before the convective-diffusion equation can be solved the velocity distribution must be known. It is, in principle, possible to determine the velocity distribution from the Navier-Stokes equation. For incompressible Newtonian fluids

$$\frac{\partial c}{\partial t} + (v \nabla) v = - \nabla p + \mu \nabla^2 v + f \qquad (6.11)$$

where the left hand side represents the product of mass and acceleration per unit volume and the right hand side represents the forces acting on the volume element (i.e. p is the pressure, $\mu \nabla^2$ v represents fractional forces and f is the force per unit volume exerted by gravity).

Theoretical solution of the convective-diffusion equation via solution of the Navier-Stokes equation, to obtain the rate of mass transport, is however only possible for laminar flow. Turbulent flow is characterised by random time dependent velocity fluctuations superimposed on time independent mean velocities. Application of the Navier-Stokes equation to such a flow produces terms involving these fluctuations which can only be accounted for empirically.

In the case of laminar flow two theoretical mass transport correlations are often quoted [1-3, 9]:

$$Sh = 1.85\ (Re\ Sc\ Le)^{1/3} \qquad (6.12)$$

(valid for $Re\ Sc\ Le > 10^4$ and $L/d_e < 35$)

$$Sh = 1.85\chi(Re\ Sc\ Le)^{1/3} \qquad (6.13)$$

(valid for the conditions of equation 6.10)

Equation (6.12) applies to a reactor with infinitely wide electrodes and fully developed flow. The details of the derivation from equations (6.10) and (6.11) are given by Pickett [9] and are worth consulting for the insight they provide. The correlation was modified by Rousar et al [8] for a reactor of finite width and equation (6.13) obtained. The parameter, χ, is a correction factor which is dependent upon the aspect ratio of the channel as shown in Table 6.1 (i.e. γ = channel height/channel width perpendicular to the direction of electrolyte flow) . Clearly for reactors with a small aspect ratio equation (6.12) is a good approximation to equation (6.13).

TABLE 6.1 Correction factor χ in equation (6.13) after Rousar et al [8].

γ	χ
0.05	0.9829
0.10	0.9671
0.20	0.9388
0.33	0.9071
0.5	0.8760
1.0	0.8214

6.3.2 Empirical Correlations

A multitude of empirical mass transport correlations have been reported for parallel plate cells (e.g. [9–15]). The vast majority consider channel flow where a large 'calming section' is built into the cell to encourage full development of the flow prior to the electrode zone. A comprehensive review of this data is given by Pickett [9]. For example for fully developed laminar flow in a reactor with an aspect ratio of 0.175 or 0.167 Pickett et al [9] found

$$Sh = 2.54\ (Re\ Sc\ Le)^{0.3} \qquad (6.14)$$

(valid for $58 < Re < 2{,}000$, $2{,}850 < Sc < 5{,}140$ and $0.08 < Le < 5.95$)

Equation (6.14) shows rates of mass transport broadly similar to the theoretical predictions of equations (6.12) and (6.13) although there appears to be a trend away from the one third power on the (Re Sc Le) group.

The same workers [9] found for fully developed turbulent flow the mass transport coefficient was independent of Le in a reactor with $L/d_e > 12.5$ (i.e. the reactant concentration distribution is fully developed)

$$Sh = 0.023\ Re^{0.8}\ Sc^{1/3} \qquad (6.15)$$

(valid for $2{,}000 < Re < 20{,}000$ and $L/d_e > 12.5$)

Only at shorter electrodes (i.e. $L/d_e < 7.5$) did Pickett et al [9] observe length dependence. They obtained for such a reactor

$$Sh = 0.145\ Re^{2/3}\ Sc^{1/3}\ Le^{1/4} \qquad (6.16)$$

(valid for $2{,}000 < Re < 20{,}000$ and $L/d_e < 7.5$)

Contrasting these results with the predicted length dependency for $L/d_e < 35$ in laminar flow (equations 6.12 and 6.13) highlights the much shorter distances over which fully developed concentration distributions are obtained in turbulent flow.

In contrast to this extensive literature there is a real scarcity of published work relevant to pilot plant and larger indusrial cells [12], which have no deliberate calming section. Mass transport correlations have, however been published for the FM21-SP and FM01-LC reactors [13], marketed by ICI, and the ElectroSyn cell [14] supplied by the Swedish National Development Corporation. The results of Goodridge et al [15] and Wragg et al [16], who working independently examined the empty and baffled channel of a small cell with approximately double the electrode area of the reactor using in this study, are also of interest. Significantly Goodridge et al examined the effect of scaling up the baffled reactor by a factor of 10 and Wragg et al examined the result of removing the baffles from the reactor. Mass transport correlations obtained in these practical reactors are listed in Table 6.2 together with the others discussed in this section.

6.4 MASS TRANSPORT IN THE PARALLEL PLATE ELECTROCHEMICAL REACTOR

6.4.1 The System

Ferricyanide reduction (equation 6.25) at a platinised titanium cathode with a catholyte equimolar in ferricyanide and ferrocyanide was used.

TABLE 6.2 Selected mass transport correlations for the parallel plate geometry.

Equation	Sh = a Re^b Sc^c Le^d				Conditions	Reference
	a	b	c	d		
(6.12)	1.85	1/3	1/3	1/3	Theoretically derived for fully developed laminar flow assuming infinitely wide electrodes. Re $Sc(d_e/L) > 10^4$ and $L/d_e < 35$.	[9]
(6.13)	1.85χ	1/3	1/3	1/3	χ corrects the above correlation for a finite width between the electrodes. Re $Sc(d_e/L) > 10^4$ and $L/d_e < 35$.	[9]
(6.14)	2.54	0.3	0.3	0.3	Fully developed laminar flow. $58 < Re < 2,000$, $2,850 < Sc < 5,140$ $0.17 < L/d_e < 12.5$ and $\gamma = 0.167$ or 0.175.	[9]
(6.15)	0.023	0.8	1/3	minimal	Fully developed turbulent flow. $2,000 < Re < 20,000$ and $L/d_e < 12.5$.	[9]
(6.16)	0.145	2/3	1/3	1/4	Fully developed turbulent flow. $2,000 < Re < 20,000$ and $L/d_e < 7.5$.	[9]
	Sh = a' Re^b Sc^c					
	a'	b	c			
(6.17)	0.125	0.66	1/3		FM21-SP Reactor. $65 < Re < 450$. Sc constant and 1/3 power assumed. L/d_e = 94 cm/ 1.02 cm = 92. Electrode area, 2,250 cm^2.	[13]
(6.18)	0.174	0.68	1/3		FM01 - LC Reactor. $120 < Re < 450$. Sc constant and 1/3 power assumed. L/d_e = 16 cm/0.967 cm = 16.5. Electrode area 64 cm^2.	
(6.19)	0.39	0.58	1/3		ElectroSyn Cell. empty channel.	[14]
(6.20)	5.57	0.40	1/3		SU grid turbulence promoter. $70 < Re < 800$. Sc = 1572 and 1/3 power assumed. L/d_e = 28 cm/2.2 cm = 13. Electrode area 440 cm^2.	
(6.21)	0.38	0.68	1/3		Baffled parallel plate cell. electrode area 225 cm^2 L/d_e = 15 cm/ 2.3 cm = 6.5.	[15]
(6.22)	0.20	0.63	1/3		electrode area 2,025 cm^2 L/d_e = 45 cm/ 2.4 cm = 19. $3,000 < Re < 15,000$. Sc constant and 1/3 power assumed. L/d_e calculations assume the cathode is square.	
(6.23)	0.46	0.66	1/3		Small parallel plate cell used in [15]. empty channel $1,250 < Re < 6,897$.	[16]
(6.24)	0.18	0.75	1/3		baffled cell $3,000 < Re < 15,000$. Sc constant and 1/3 power assumed.	

$$[Fe(CN)_6]^{3-} + e^- \longrightarrow [Fe(CN)_6]^{4-} \qquad (6.25)$$

Aqueous 1.0 mol dm^{-3} potassium hydroxide anolyte ensured the anode reaction, oxygen evolution at a nickel anode, did not become rate controlling during measurements.

6.4.2 Current-Voltage Curves

The shape of the current-cathode potential curves (Figure 6.1) indicates the rate of the cathode reaction is controlled by convective-diffusion of the reactant at all measured currents. A distinct limiting current plateau is obtained at all average, linear catholyte velocities in the empty channel and with the channel filled by any one of a range of turbulence promoters. With increasing catholyte velocities although the plateau shortens (e.g. from 1000 mV at 0.033 m s^{-1} to 500 mV at 0.206 m s^{-1}) there is little change in the inclination which is small. A background current density of about 2.0 A m^{-2} at the limiting current density (which was subtracted from the limiting current density) is due to hydrogen evolution and oxygen reduction. It is difficult to completely remove dissolved oxygen from a large volume of catholyte.

Measurement of cell voltage, rather than cathode potential, also produces a limiting current plateau (Figure 6.2). The plateau length and inclination is comparable to that obtained with cathode potential values. This may be particularly valuable for measuring mass transport rates in reactors where the incorporation of a reference electrode and luggin capillary is not straightforward and can inadvertedly alter the hydrodynamics. Consideration of the components of cell voltage (E_{CELL}, equation 6.26) perhaps helps to explain why a plateau is obtained under limiting current conditions.

$$E_{CELL} = E_e^C - E_e^A - |\eta^C| - |\eta^A| - IR_{CELL} - IR_{CIRCUIT} \qquad (6.26)$$

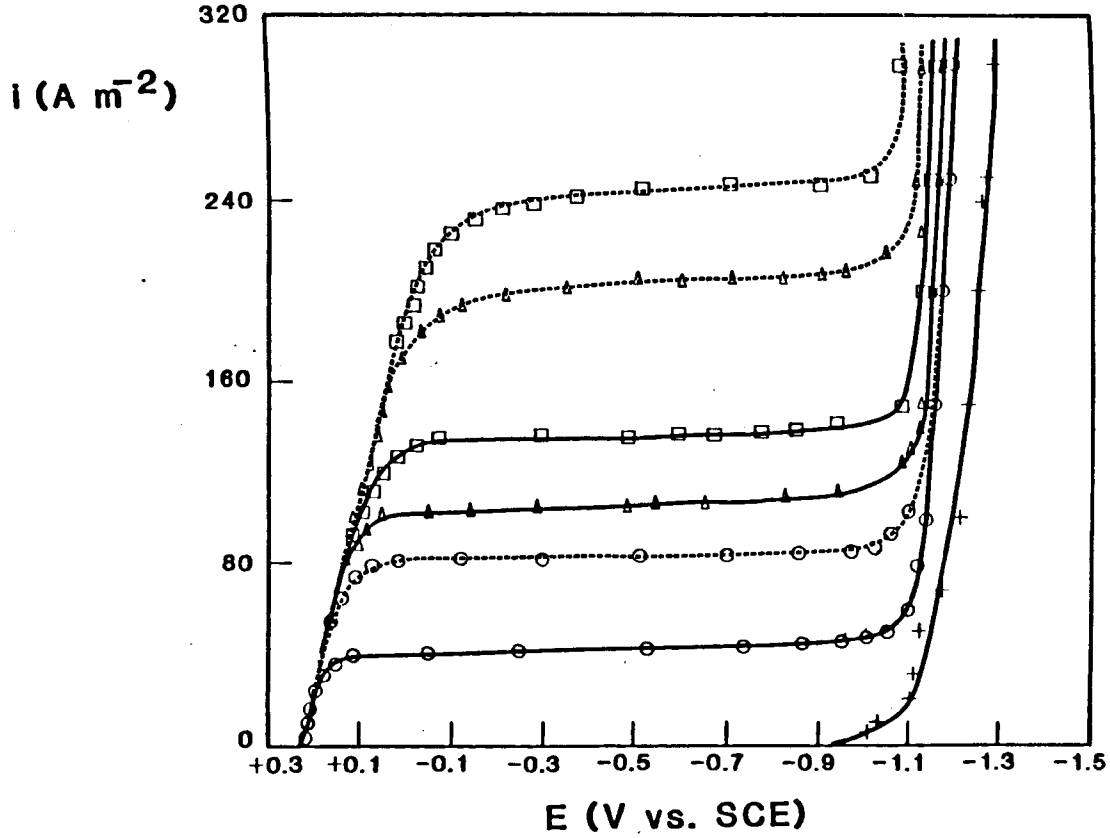

——— empty channel - - - - - - - channel filled with Expamet turbulence promoter (orientation A)
O $\bar{v}$ = 0.033 m s^{-1} Δ $\bar{v}$ = 0.123 m s^{-1} □ $\bar{v}$ = 0.206 m s^{-1} + background electrolyte at all $\bar{v}$.

FIGURE 6.1 Current–cathode potential curves for ferricyanide reduction at platinised titanium. 0.05 mol dm^{-3} potassium ferricyanide and 0.05 mol dm^{-3} potassium ferrocyanide in aqueous 1.0 mol dm^{-3} potassium hydroxide. Electrolyte purged with N_2 for an hour. Temperature 25°C.

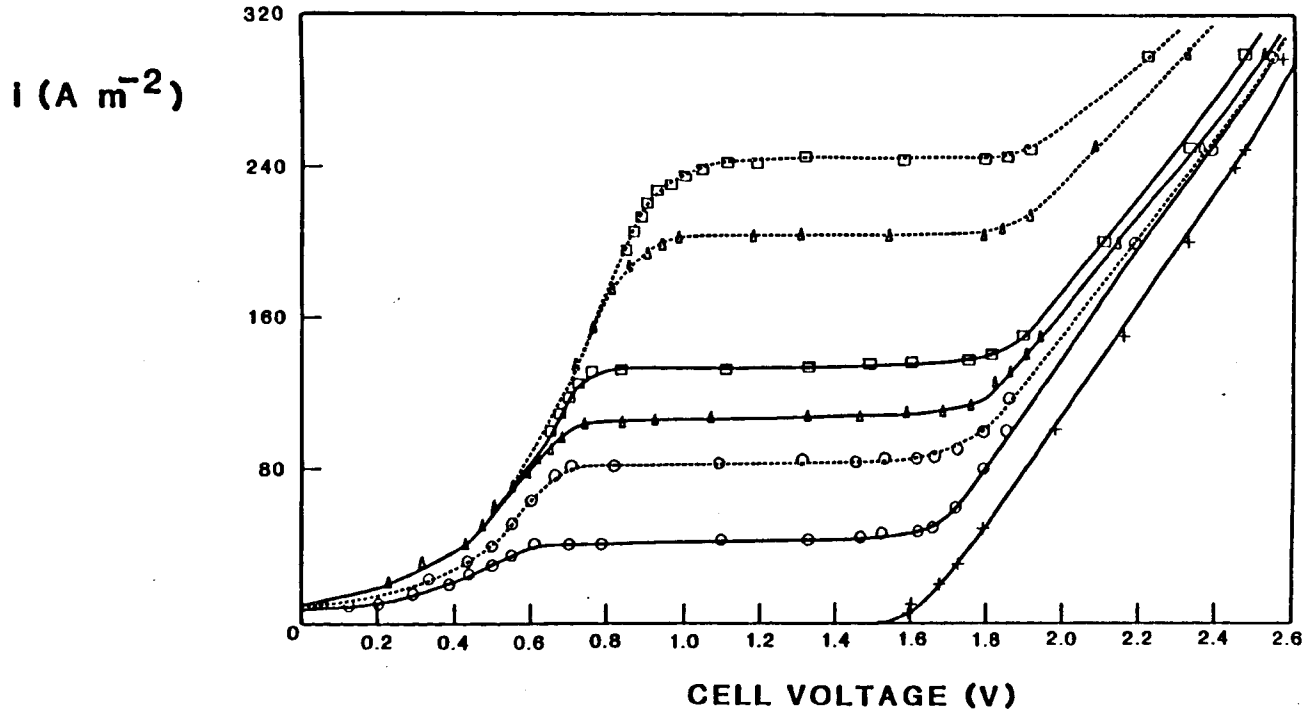

———— empty channel . -------- channel filled with Expamet turbulence promoter (orientation A)
O $\bar{v}$ = 0.033 m s^{-1} Δ $\bar{v}$ = 0.123 m s^{-1} □ $\bar{v}$ = 0.206 m s^{-1} + background electrolyte at all $\bar{v}$.

FIGURE 6.2 Current against cell voltage relationship for ferricyanide reduction at platinised titanium. 0.05 mol dm^{-3} potassium ferricyanide and 0.05 mol dm^{-3} potassium ferrocyanide in aqueous 1.0 mol dm^{-3} potassium hydroxide. Electrolyte purged with N_2 for an hour. Temperature 25°C.

where the superscripts represent anode (A) or cathode (C) component, E_e^C and E_e^A are the reversible potentials, η^C and η^A the overpotentials and IR_{CELL} and $IR_{CIRCUIT}$ the cell and circuit resistance respectively. The reversible potentials are fixed by thermodynamics. At constant current (e.g. the limiting current) the resistance terms are constant. The anodic overpotential is activation controlled and changes little with time as shown by the shape of the current density against cell voltage graphs below the limiting current density (Figure 6.2). At low current densities the curve is exponential as expected of kinetic control and at higher current densities there is a mixed kinetic-mass transport controlled region. The kinetic control must be due to the secondary electrode reaction since ferricyanide reduction is mass transport controlled at all current densities. Consequently under limiting current conditions changes in the cell voltage essentially reflect changes in the cathode potential. Equation (6.26) also suggests the use of cell voltage may produce longer limiting current plateaus than the cathode potential if electrochemical systems with a high cell and circuit resistance and high counter electrode overpotential are used.

6.4.3 Mass Transport in the Empty Catholyte Channel

By combining equations (6.05) to (6.09), for ferricyanide reduction in the reactor

$$K_L = k\,\bar{v}^b \qquad (6.27)$$

where k is a constant $\left(\text{i.e. } k = \frac{a'(Le)^{d_D}}{d_e}\left(\frac{d_e}{\nu}\right)^b\left(\frac{\nu}{D}\right)^c\right)$

Figure 6.3 shows the variation, on log-log axes, of the average mass transport

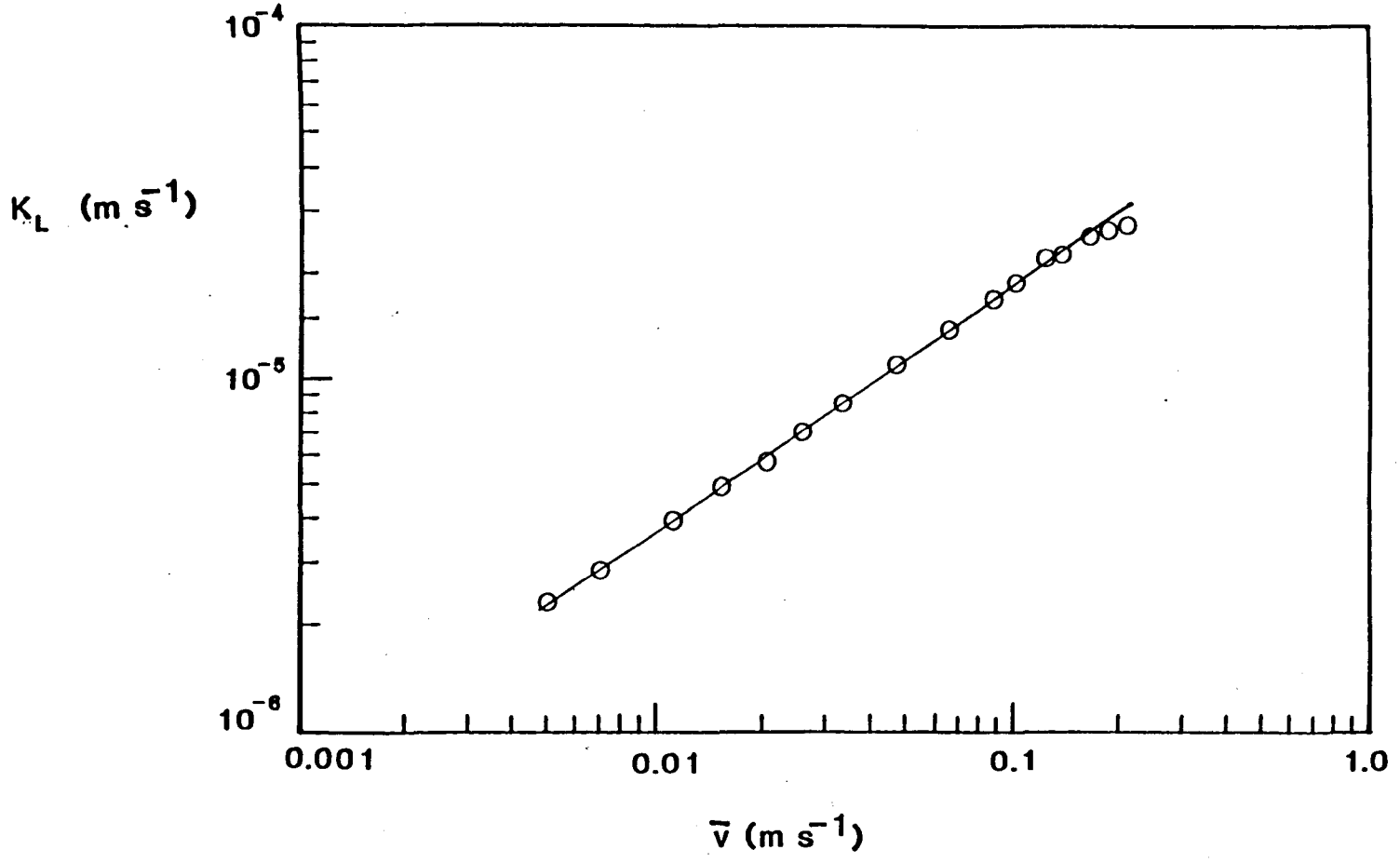

FIGURE 6.3 Variation of the average mass transport coefficient with the nominal, average linear catholyte velocity in the empty channel of the reactor.

coefficient with the nominal, average linear catholyte velocity in the empty channel of the cell. The average mass transport coefficient increases from 2.3 x 10^{-6} to 2.7 x 10^{-5} m s^{-1} over the useable range of catholyte flowrates. At linear velocities below 0.16 m s^{-1} a straight line relationship is obtained which is described by equation (6.28) with a correlation coefficient of 0.9998. At higher velocities there is some evidence of channeling.

$$K_L = (9.4 \times 10^{-5}\ \bar{v}^{0.70})\ m\ s^{-1} \qquad (6.28)$$

Converting equation (6.28) to the form of a mass transport correlation, with the hydraulic diameter of the reactor (3.33 cm) as the characteristic length, allows comparison with some of the literature correlations of Table 6.2. Comparison of mass transport correlations which are not based upon an identical characteristic length is a common error. For the empty catholyte channel

$$Sh = 0.28\ Re^{0.70}\ Sc^{1/3} \qquad (6.29)$$

(valid for 148 < Re < 6,109 and Sc = 1,588 calculated from [5] with ν = 1.123 x 10^{-6} m^2 s^{-1} and D = 7.07 x 10^{-10} m^2 s^{-1} with the 1/3 power dependency assumed *a priori*).

Figure 6.4 shows equation (6.29) and the mass transport correlations in Table 6.2 as plots of Sh against Re on log-log axes. In Figure 6.4 equations (6.12 to 6.16) are calculated using the Le group of the reactor used in this study. The transition from laminar to turbulent flow in parallel plate reactors with fully developed flow normally occurs at a Reynolds number of around 2,300 [9]. For the reactor used in this study there is no apparent transition in the nature of the electrolyte flow between Reynolds numbers of 150 and 6,000. The flow appears

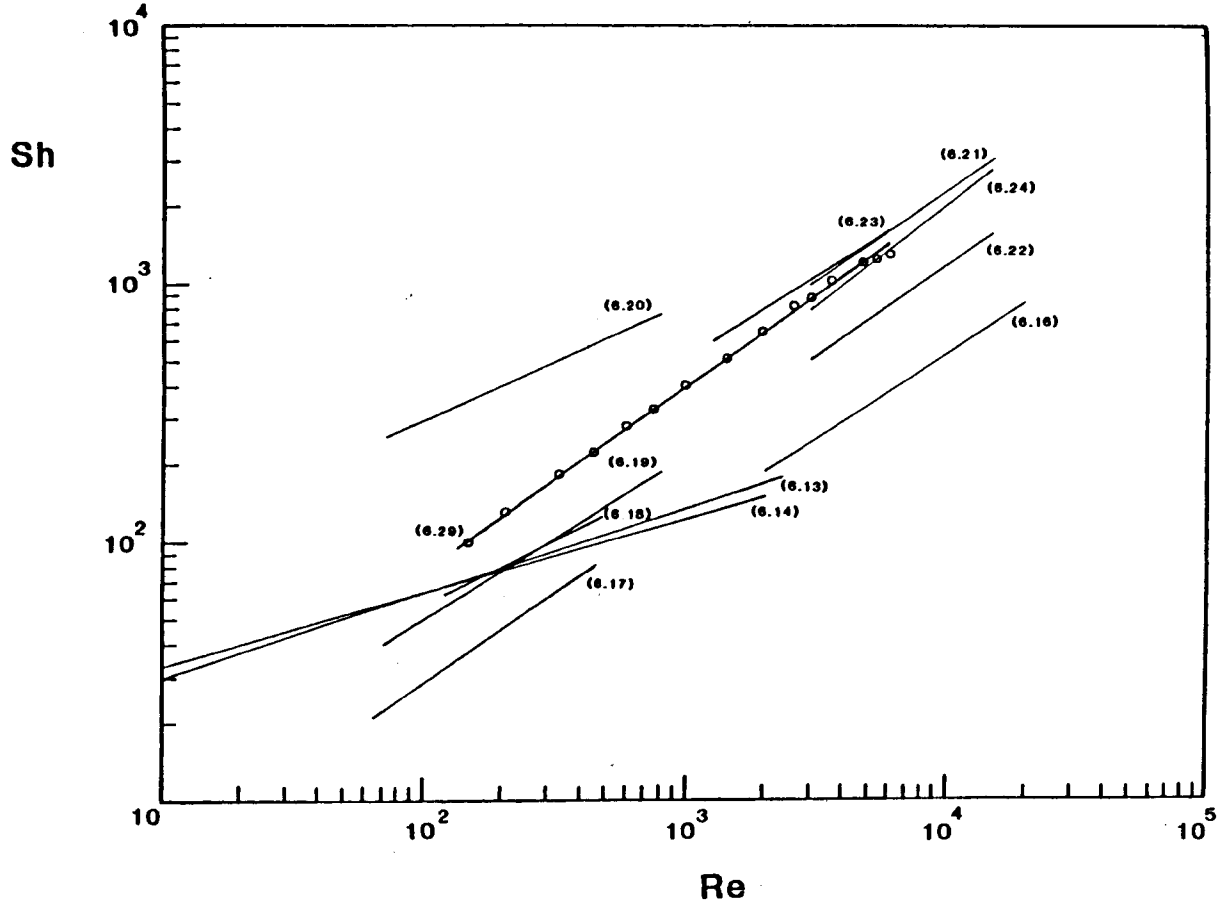

FIGURE 6.4 Mass transport correlation in the empty channel of the reactor together with those of Table 6.2.

turbulent even at the lowest Reynolds numbers. The Reynolds exponent of 0.70 is close to the 2/3 measured for fully developed turbulent flow in a reactor with $L/d_e < 7.5$ (equation 6.16), which contrasts with an exponent close to 0.3 (e.g. equation 6.14) expected for fully developed laminar flow. Similarly, Reynolds exponents of between 0.58 and 0.68 are obtained in the empty channel of the ElectroSyn (equation 6.19), FM21-SP (equation 6.17) and FM01-LC (equation 6.18) reactors at Reynolds numbers where laminar behaviour might be expected. The effect is almost certainly due to the direct transfer of electrolyte from the reactor plumbing into the electrode compartment.

Not surprisingly a direct result of this entrance effect is higher rates of mass transport in these reactors than predicted by the mass transport correlations for fully developed laminar flow (Figures 6.4 and 6.5). For the reactor used herein and the empty channel of the similarly small reactor examined by Wragg et al [16], however, the rates of mass transport are also higher than predicted for fully developed turbulent flow (Figure 6.4 and 6.5). Goodridge et al [15] have shown that for such small reactors high rates of mass transport are achieved due to domination of the entire electrode surface by the entrance effect. They measured local mass transport coefficients in both the small and large baffled reactor by segmenting the working electrodes. In the larger cell the coefficients were much higher at the electrolyte inlet with the remainder of the electrode showing reasonably uniform rates of mass transport. High local mass transport coefficients, comparable with those at the entrance of the large reactor, were measured over the complete electrode surface in the smaller reactor. This produced average mass transport coefficients about 2 fold higher at a given nominal, average linear electrolyte velocity in the small reactor which is reflected in the mass transport correlations (equations 6.21 and 6.22) for the reactors when d_e for the reactors

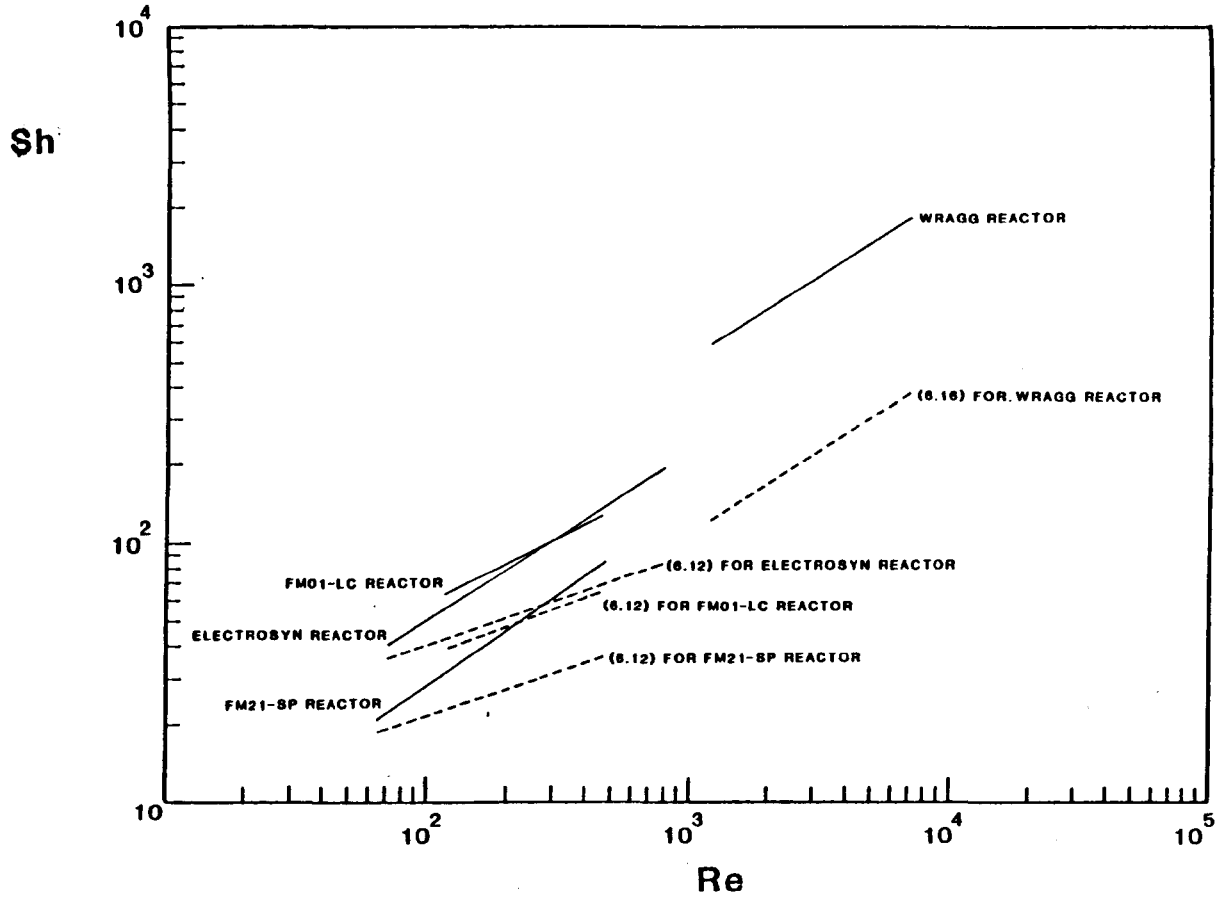

FIGURE 6.5 Comparison of mass transport correlations for reactors with predicted behaviour for fully developed laminar or turbulent flow.

(Table 6.2) are taken into account. Significantly Wragg et al [16] showed the high rates of mass transport in the small reactor examined by Goodridge et al are not due to the baffles which they found reduced the rate of mass transport. This is also reflected in the relevant mass transport correlations (equation 6.23 and 6.24) which assume d_e is not altered by the baffles.

The comparison between the range of achievable Reynolds numbers in the ElectroSyn, FM21-SP and FM01-LC reactors and the reactors used by Goodridge et al, Wragg et al and in this study is enlightening. Much lower Reynolds numbers are achieved in the former reactors (Figure 6.4). This arises because the interelectrode gap is much smaller in these reactors (ca. 0.5 cm compared with 1.5 to 2.0 cm) and therefore the pressure drop through the reactor is correspondingly larger at a given volumetric flowrate. This restricts the upper limit of achievable Reynolds numbers. Of course the lower interelectrode gap has the advantage of reducing the cell voltage, which may be of prime importance, particularly in poorly conductive electrolytes.

6.4.4 Performance of a Range of Turbulence Promoters

A wide selection of turbulence promoters with a large variety of geometrical characteristics were examined in the reactor. Sufficient sections of promoter to completely fill the catholyte channel were used. The promoters are shown in Plate 6.1 and the dimensions used to characterise the materials identified. The promoter dimensions are listed in Table 6.3.

The initial experiments focused upon the effect of promoter orientation. Both Expamet PV876 and Netlon CE121 were examined with CD and LD parallel to the direction of electrolyte flow. Whilst there is no measureable dependence of the rate of mass transport upon promoter orientation with Netlon CE121 with Expamet PV876 a 12% enhancement in mass transport is achieved over the range

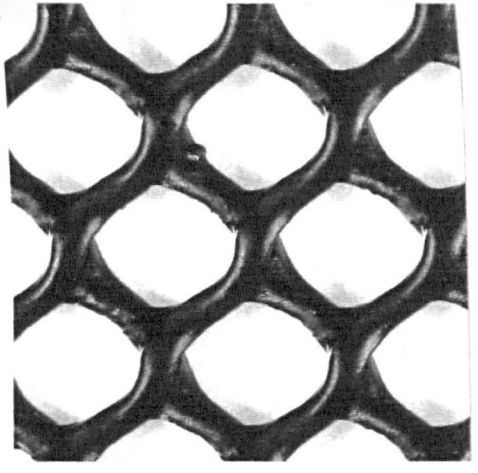

NETLON CE121

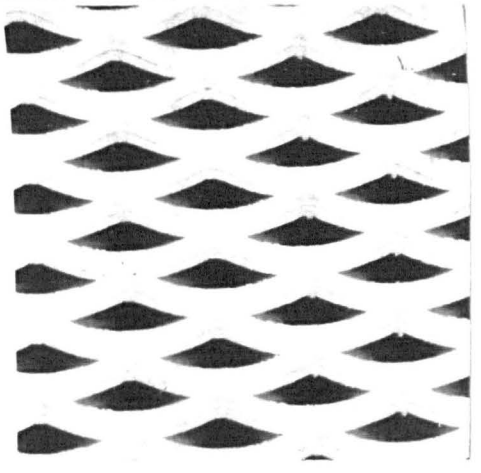

EXPAMET PV876

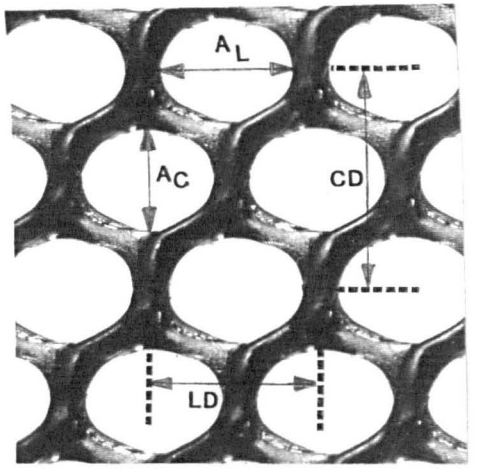

NETLON CE111

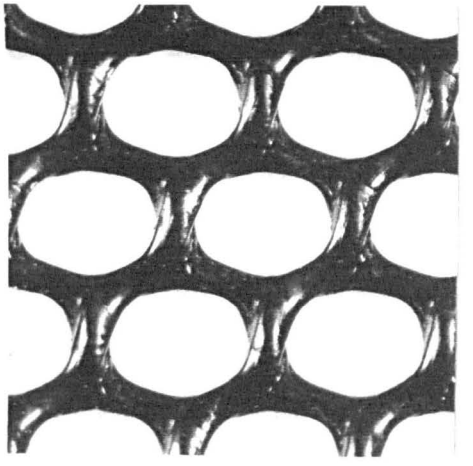

NETLON STR7017

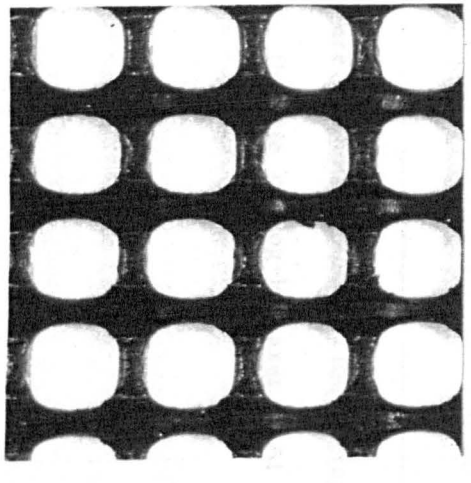

NETLON CLADDING

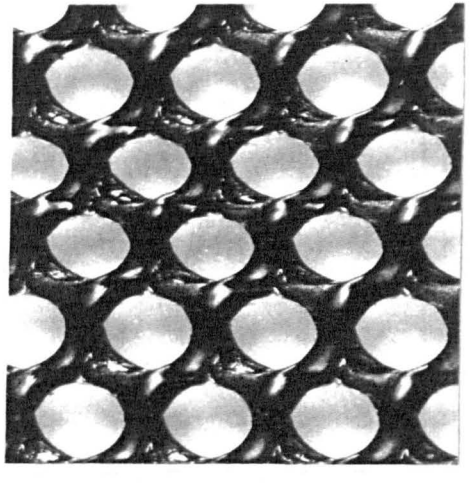

NETLON STR7005

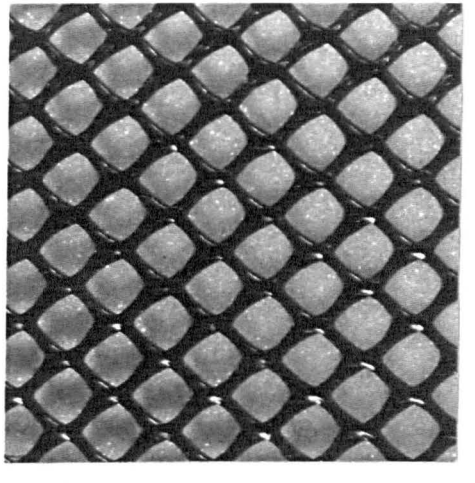

NETLON GREENHOUSE SHADING

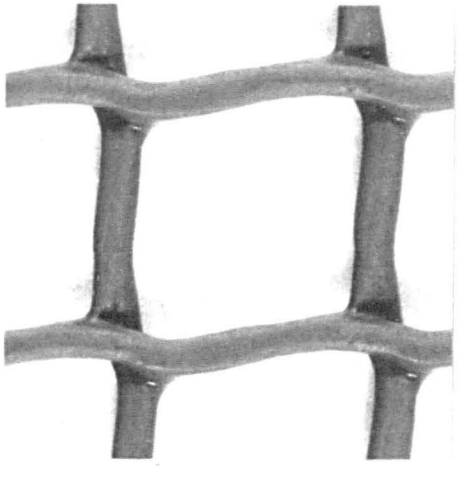

NETLON GARDEN MESH

PLATE 6.1 FRONT FACE OF TURBULENCE PROMOTERS PROJECTED AT THE CATHODE (MAGNIFICATION X 2).

of catholyte flowrates with CD rather than LD parallel to the direction of electrolyte flow. This is shown in Figure 6.6. Fortuitously, in the electrosynthesis experiments described in Chapter 7 and 8 the CD dimension (refered to as orientation A) was used exclusively. This orientation effect with Expamet agrees with the findings of Coeuret et al [17] who examined in a parallel plate reactor, four different Expamet metal meshes of similar design to the plastic mesh used herein. Visual inspection of all the promoters suggests Expamet PV876 offers the largest difference in profile with changing promoter orientation. Although, as observed with Netlon CE121, orientation effects may be small with the remaining promoters, to provide uniformity in the study all were examined with CD parallel to the direction of electrolyte flow.

TABLE 6.3 Characteristic dimensions of the turbulence promoters.

Promoter	A_L (cm)	A_C (cm)	LD (cm)	CD (cm)	Thickness (cm)
Netlon CE121	0.93	0.83	1.20	1.55	0.32
Expamet PV864	0.75	0.20	1.20	0.50	0.22
Netlon CE111	0.88	0.65	1.10	1.40	0.21
Netlon STR7017	0.90	0.70	1.15	1.55	0.21
Netlon cladding	0.60	0.45	0.85	1.15	0.15
Netlon greenhouse shading	0.38	0.35	0.65	0.48	0.05
Netlon STR7005	0.55	0.53	0.75	0.70	0.12
Netlon garden mesh	1.40	1.40	1.70	1.70	0.20

Figure 6.7 shows for the range of turbulence promoters plots of the average mass transport coefficient against the volumetric flowrate on log-log axes. At a

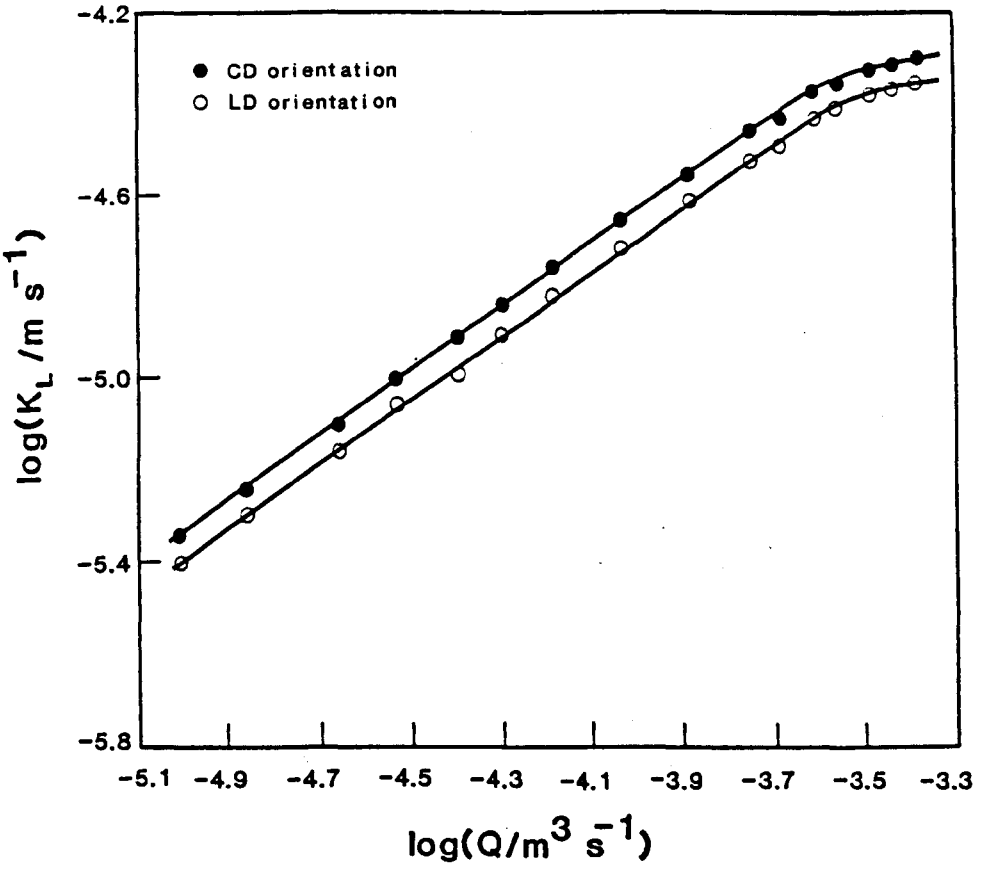

FIGURE 6.6 Dependence of the average mass transport coefficient upon the orientation of Expamet PV876.

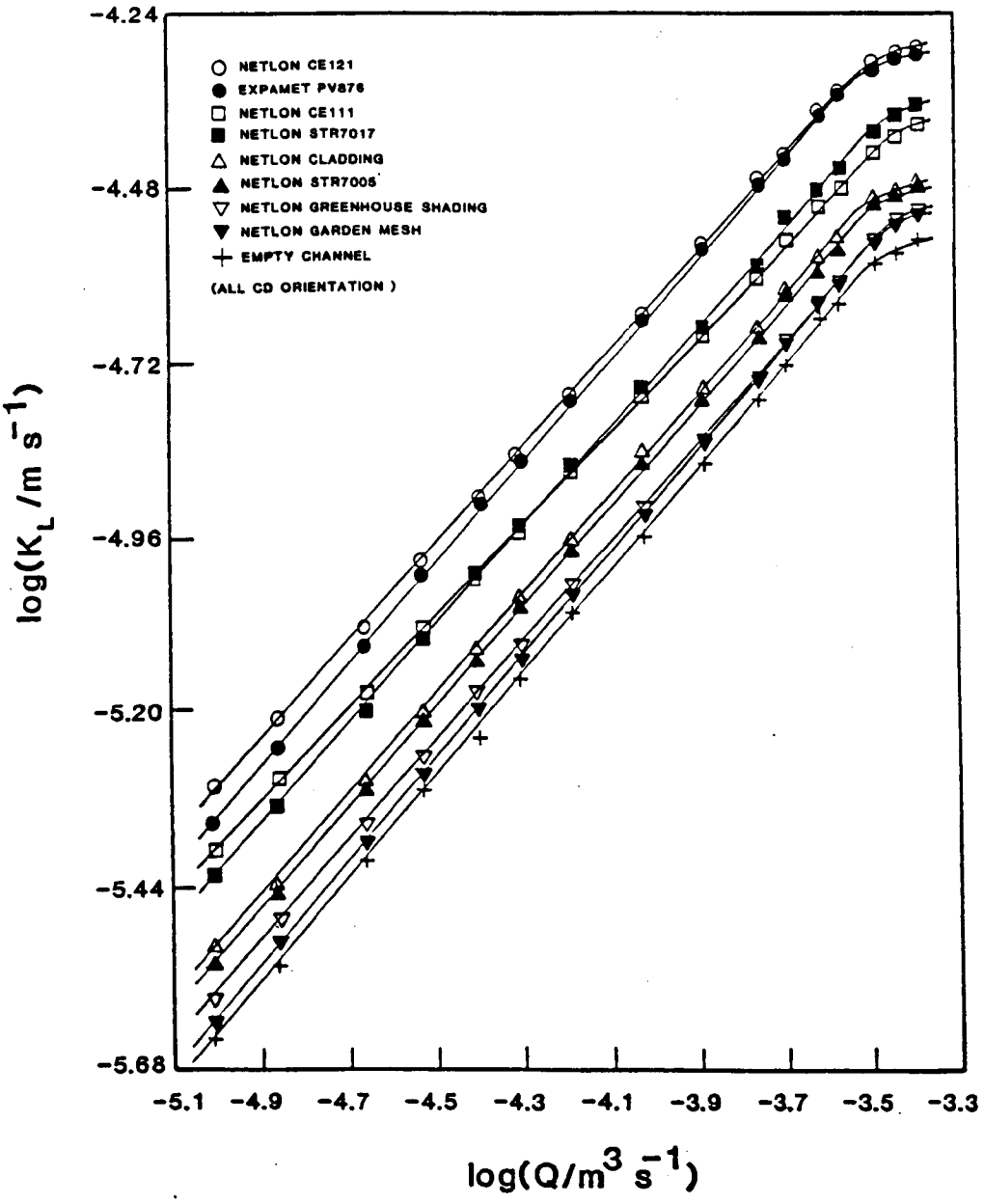

FIGURE 6.7 Variation of the average mass transport coefficient with the volumetric flowrate of the catholyte for all turbulence promoters.

given electrolyte flowrate all promoters produce at least some enhancement in the rate of mass transport. For the promoters we can define the enhancement factor, γ, as

$$\gamma = \frac{K_{L(P)}}{K_{L(E)}} \qquad (6.30)$$

where $K_{L(E)}$ is the average mass transport coefficient in the empty channel and $K_{L(P)}$ the value for the channel filled with promoter. Figure 6.8 shows the plots of γ against the volumetric flowrate for all promoters. The graph readily allows the promoters to be graded in terms of mass transport enhancement at a given volumetric flowrate. The order of performance is Netlon CE121 > Expamet PV876 > Netlon CE111 > Netlon STR7017 > Netlon cladding > Netlon STR 7005 > Netlon greenhouse shading > Netlon garden mesh.

The most efficient promoter, Netlon CE121, produces an approximate doubling of the rate of mass transport at a given volumetric flowrate. That higher γ values are not achieved is perhaps not surprising since, as shown in Section 6.4.3, the flow appears turbulent even in the empty catholyte channel. Certainly the Reynolds exponents, derived from the log K_L against log Q plot, are very similar for the empty channel and all promoters (Table 6.4) as reflected by the essentially parallel straight lines in Figure 6.7.

The usual mechanism of mass transport enhancement by turbulence promoters is via eddy formation as the electrolyte weaves through the expanded plastic mesh (see e.g [10]). This produces an increase in the normal velocity component of the electrolyte at the electrode surface which by the conservation of momentum must product an identical reduction in the electrolyte velocity component parallel to the electrode. Of course part of the enhancement effect observed with the

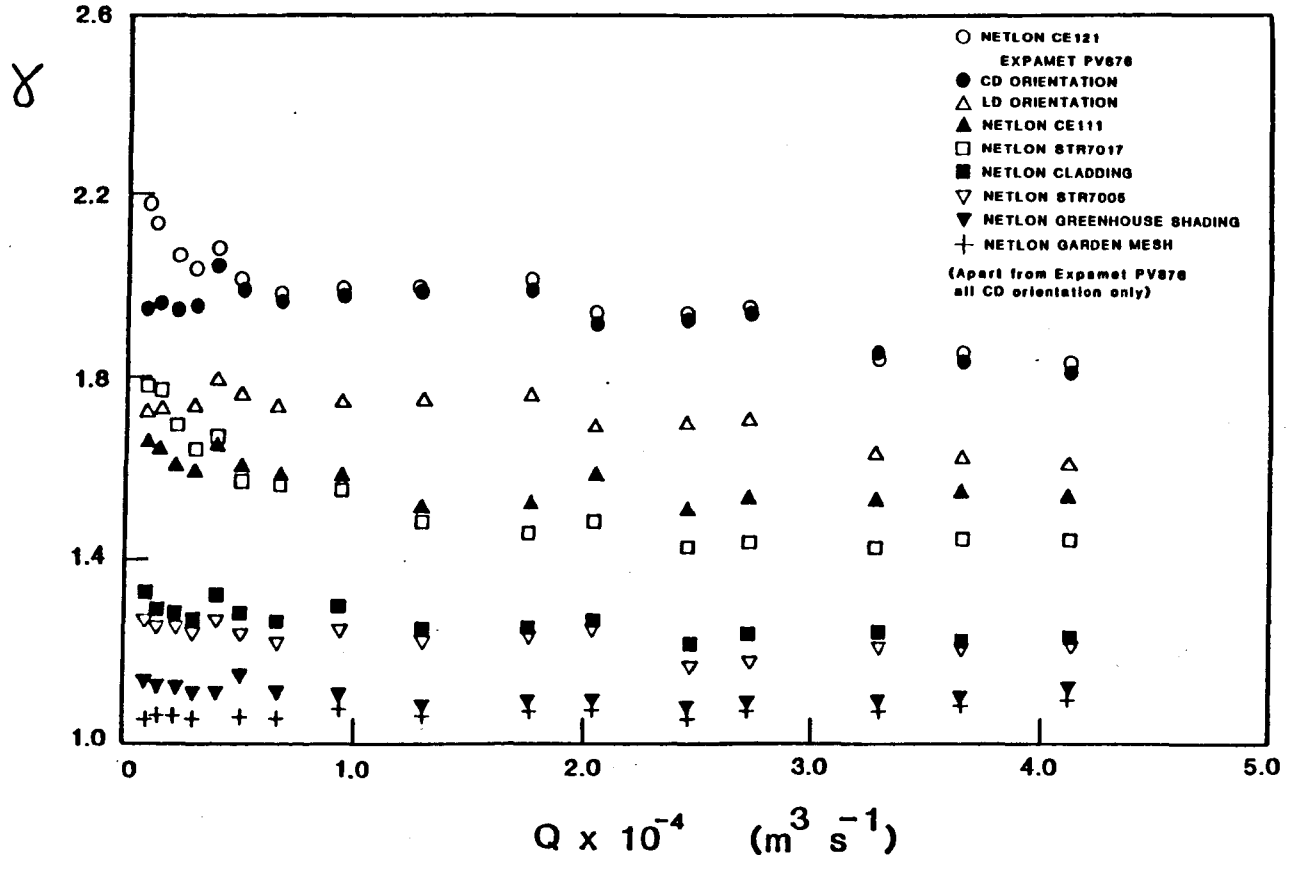

Figure 6.8 The enhancement factor for the turbulence promoters as a function of the volumetric flowrate of the catholyte.

TABLE 6.4 Reynolds exponents for the promoters and empty reactor channel from the slope of the log K_L against log Q plots in Figure 6.7. From equation (6.27) $K_L = k''Q^b$ where b is the Reynolds exponent and k'' is a constant.

Promoter	$k'' \times 10^{-3}$	Reynolds Exponent
Netlon CE121	11.1	0.67
Expamet PV876	14.3	0.70
Netlon CE111	5.8	0.63
Netlon STR7017	9.7	0.68
Netlon cladding	7.5	0.69
Netlon STR 7005	7.3	0.69
Netlon greenhouse shading	7.5	0.68
Netlon garden mesh	8.9	0.71
Empty channel	7.3	0.70

turbulence promoters may be due to blockage of the catholyte channel which will increase the nominal, average linear electrolyte velocity at a given volumetric flowrate. It is likely, however, that the effect, at least for the four most efficient promoters, will be similar since the materials have similar porosities (Table 6.5). Further, Netlon cladding, Netlon greenhouse shading and Netlon STR7005 are significantly less porous than these more efficient turbulence promoters (Table 6.5). Based upon channel blockage alone higher γ factors would be expected. Clearly eddy formation is favoured by certain geometrical characteristics of the promoters.

TABLE 6.5 Porosity of the turbulence promoters.

Promoter	[a] ρ ($g\ cm^{-3}$)	Porosity
Netlon CE121	0.51	0.590
Expamet PV876	1.62	0.510
Netlon CE111	0.40	0.500
Netlon STR7017	0.41	0.400
Netlon cladding	0.58	0.245
Netlon STR7005	0.45	0.205
Netlon greenhouse shading	0.56	0.205
Netlon garden mesh	1.07	0.780

[a]The density values were determined by the displacement method. This allowed the porosity to be calculated by weighing a single promoter and, from the density, obtaining the volume occupied by the promoter. Comparison with the volume occupied by a solid piece of plastic having the same volume gives the porosity.

Attempts to find a simple characteristic length were not successful. For materials which have many geometrical characteristics this is perhaps not unexpected and the situation is probably further complicated by a complex electrolyte flow pattern in the reactor. For example the γ factors are not related to A_L, A_C, LD, CD, thickness or simple ratios thereof for the range of turbulence promoters. It does appear, however, that the γ values are related to the promoter surface area shown schematically in Figure 6.9, calculated only for the promoter closest to the electrode surface per geometrical unit area of the electrode. Plate 6.2 attempts to show the key promoter surface area pictorially. Accurate determination of the relevant promoter surface areas is difficult. High magnification photographs were used. The surface areas are listed in Table 6.6. Figure 6.10 shows the plot of γ factors against this promoter surface area per unit electrode area. Considering the errors involved in the measurements the relationship is a fairly convincing one. That the enhancement is restricted to the turbulence promoter closest to the electrode surface is perhaps not unreasonable since it might be expected that only this promoter would be effective in reducing the boundary layer at the electrode surface. When only a single section of Netlon CE121 was used in the reactor, however, γ fell to ca. 1.5. This is not necessarily inconsistent with the arguments above. The reduction in the rate of mass transport may be due to electrolyte channeling effects.

Figure 6.10 does suggest that for the reactor used in this study, increasing the surface area of the promoters in the regions identified in Figure 6.9 should further enhance the rate of mass transport. That the observed relationship in Figure 6.10 is not universal, however, is shown by the orientation effect with Expamet PV876. There is little change in the calculated promoter surface area between the CD and LD orientations (Table 6.6) but γ falls from ca. 2.0 to 1.8

DIAMOND SHAPED PROMOTERS

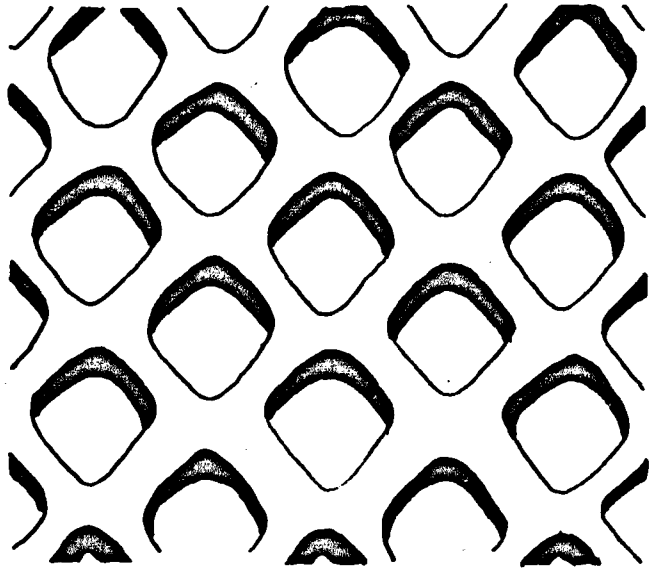

SQUARE SHAPED PROMOTERS

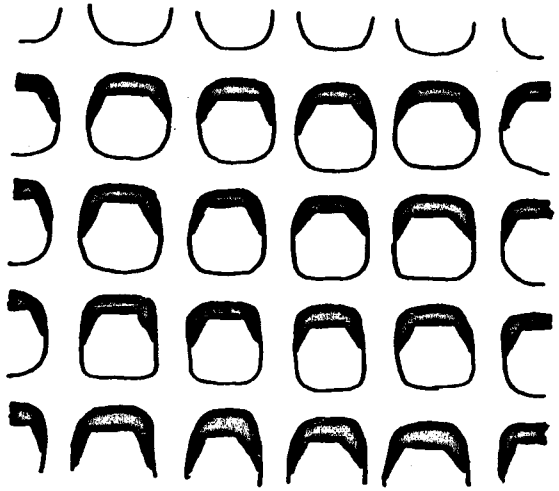

FIGURE 6.9 Schematic showing electrode face of promoter tilted at an angle to highlight the surface area responsible for mass transport enhancement. The key surface area is that shaded.

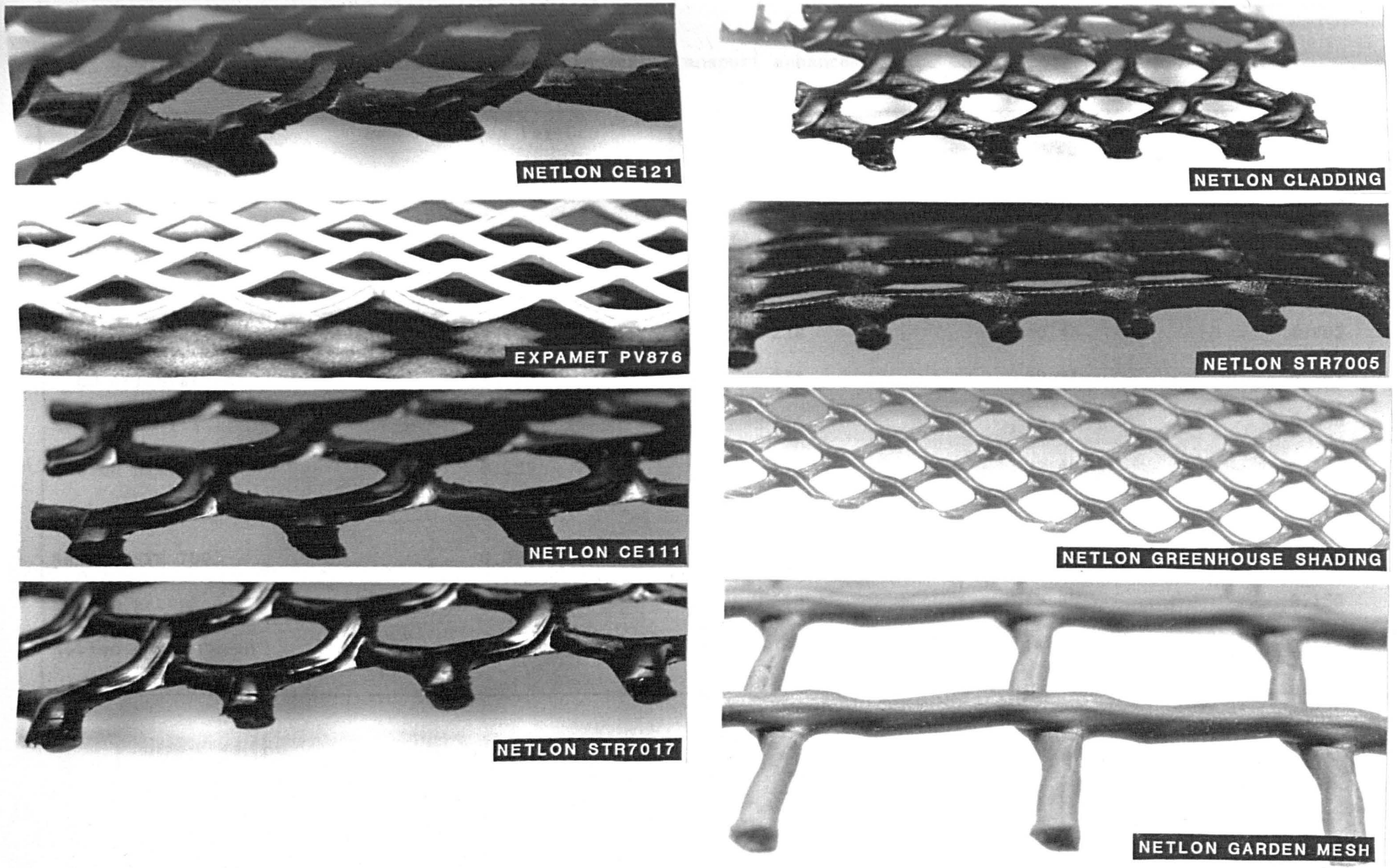

PLATE 6.2 FRONT FACE OF TURBULENCE PROMOTERS PROJECTED AT AN ANGLE TO HIGHLIGHT THE KEY AREA FOR MASS TRANSPORT ENHANCEMENT

TABLE 6.6 Promoter surface area attributed to mass transport enhancement per unit electrode area.

Promoter	Promoter Area Per Gap (cm^2)	Total Promoter Gaps Over Electrode Surface	Total Promoter Area Over Electrode Surface (cm^2)	Total Promoter Area Per Unit Electrode Area (cm^2)
Netlon CE 121	0.399	104	41.50	0.415
Expamet PV 876				
CD orientation	0.170	238	40.46	0.405
LD orientation	0.166	238	39.51	0.395
Netlon CE 111	0.230	126	28.98	0.290
Netlon STR 7017	0.239	115	27.49	0.275
Netlon cladding	0.112	195	21.84	0.218
Netlon STR 7005	0.098	190	18.62	0.186
Netlon greenhouse shading	0.025	600	15.00	0.150
Netlon garden mesh	0.42	35	14.70	0.147

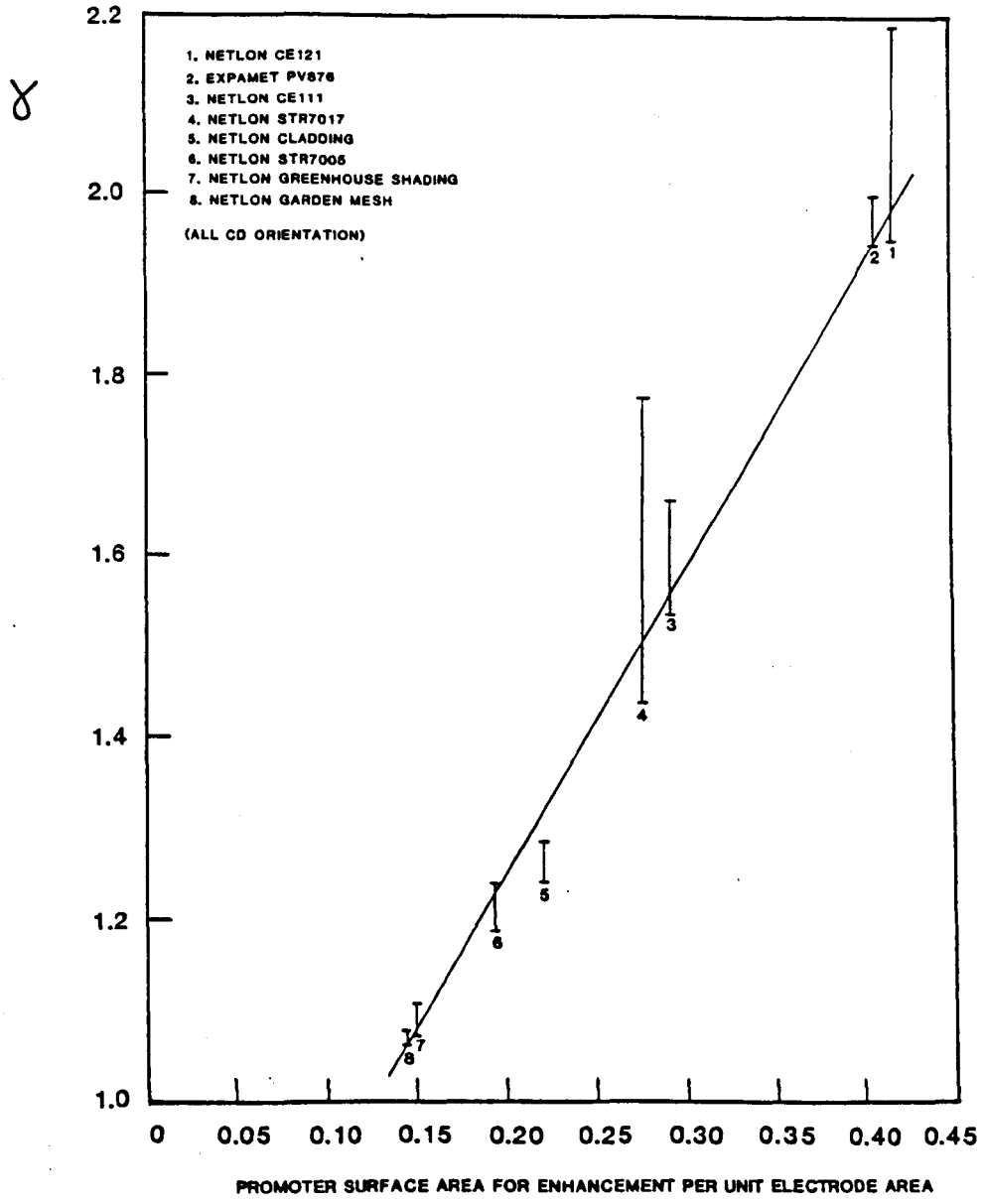

FIGURE 6.10 Correlation between γ and the identified geometrical characteristic of the turbulence promoters.

respectively. This suggests if the promotional effect is restricted to the identified promoter area, only 78% of the calculated area is effective in enhancing the rate of mass transport.

Whilst, as shown, these expanded plastic mesh turbulence promoters do provide a simple and cost effective method of enhancing mass transport they do have disadvantages. They increase the pressure drop over the reactor, thereby increasing the pumping costs. Additionally, in adverse cases, they can shield much of the electrode surface producing a non-uniform potential distribution, promote gas blinding and encouraged poor electrolyte mixing and flow segregation.

6.5 CONCLUSIONS

That comparable limiting current plateaus were obtained using cell voltage rather than cathode potential values is particularly valuable in the study of the mass transport behaviour of industrial cells. Incorporation of a reference electrode and luggin capillary is problematical in large cells. The catholyte flow in the reactor appears turbulent even in the empty channel and it seems likely that because of the relatively small size of the reactor the mass transport behaviour is dominated by an entrance effect. Consequently rates of mass transport are high over the range of catholyte flowrates. Since the objectives of this study (see Section 6.1) were fairly restricted flow visualisation studies using, for example, potassium permanganate and detailed dispersion studies using, for example, marker-pulse techniques [18] were not investigated. Nor were local mass transport coefficients measured. These are areas which certainly merit study.

For the range of turbulence promoters examined a relationship between a specified promoter surface area per unit electrode area (Figure 6.9) and the enhancement of mass transport has been identified. For materials which show

high 3D character (e.g. Expamet PV876) there may be additional geometrical effects. All of the turbulence promoters increase the average mass transport coefficient at a given volumetric flowrate when compared with the empty channel. Mass transport enhancement factors of ca. 1.05 to 2.0 were obtained. The effect of the promoters upon the pressure drop over the reactor, which may represent a severe energy penalty is, however, not known. Further studies should include measurement of this important parameter.

REFERENCES

1. Selman J.R. & Tobias W.; *Adv. in Chem. Eng.* 10, 211, (1978).

2. Landau U. in "Tutorial Lectures in Electrochemical Engineering and Technology". Eds. Alkire R.C. & Beck T. *AIChE Symp. Series No. 204* 77, 75, (1981).

3. Selman J.R. in "Tutorial Lectures in Electrochemical Engineering and Technology". Eds. Alkire R.C. & Beck T. *AIChE Symp. Series No. 204* 77, 88, (1981).

4. Berger F.P. & Ziai A.; *Chem. Eng. Research and Design* 61, 377, (1983).

5. Bazan J.C. & Arvia A.J.; *Electrochim. Acta* 10, 1025, (1965).

6. Chandrasekhar S.; *Proc. Roy. Soc.* A246, 301, (1958).

7. Ibl N.; *Electrochim. Acta* 1, 117, (1959).

8. Rousar I., Hostomsky J., Cezner V. & Stverak B.; *J. Electrochem. Soc.* 118, 881, (1971).

9. Pickett D.J. "Electrochemical Reactor Design". 2nd Edn. Elsevier, Amsterdam (1979).

10. Focke W.W. "Electrochemical Mass Transfer to Parallel Plates With and Without Turbulence Promoters". *CSIR Report CENG 421,* South Africa, (1982).

11. Heitz E. & Kreysa G. "Principles of Electrochemical Engineering". VCH Publishers, Weinheim (1986).

12. Marshall R.J. & Walsh F.C.; *Surf. Technol.* 24, 45, (1985).

13. Hammond J.K., Robinson D. & Walsh F.C. Joint Meeting of Dechema and the SCI. "Electrochemical Cell Design and Optimisation Procedures. Abstracts". Bad Soden a.Ts., Frankfurt, 24-26th. September (1990).

14. Carlsson L., Sandegren B., Simonsson D. & Rihousky M.; *J. Electrochem. Soc.* 130, 342, (1982).

15. Goodridge F., Mamoor G.M. & Plimley R.E.; *Inst. Chem. Eng. Symp. Ser.* No. 98, 61, (1986).

16. Wragg A.A. & Leontaritis A.A. Joint Meeting of Dechema and the SCI "Electrochemical Cell Design and Optimisation Procedures. Abstracts". Bad Soden a.Ts., Frankfurt, 24-26th. September (1990).

17. Quemere-Letord M.M., Legrand J. & Coeuret F.: *Inst. Chem. Eng. Symp. Ser.* No. 98, 73, (1986).

18. Jansson R.E.W. & Marshall R.J.; *Electrochim. Acta* 27, 823, (1982).

CHAPTER 7

ELECTROSYNTHESIS AT MERCURY PLATED COPPER AND LEAD CATHODES

7.1 THE ELECTROSYNTHESIS SYSTEM

The major cell processes are shown in Figure 7.1. For the cathodes at the industrially significant current densities examined (i.e. 500 A m^{-2} and above), L-cystine hydrochloride reduction is accompanied by hydrogen evolution from the acidic catholyte. The anode reaction is initially chlorine evolution but as electrolysis proceeds (and the chloride ion concentration decreases) mixed chlorine/oxygen evolution is likely [1]. A divided cell is necessary to prevent oxidation of the reactant and product and to preclude formation of explosive hydrogen/chlorine and hydrogen/oxygen gas mixtures. A cationic rather than an anionic ion-exchange membrane was selected since they show marked superiority in all respects. Cationic membranes have a lower resistance, improved chemical and physical stability, greater transport selectivity and a longer lifetime. In addition the current carrying hydroxonium ions transported through the membrane help maintain the catholyte pH. Hydrochloric acid is, however, depleted from the anolyte and must be replenished periodically.

Sulphuric acid anolyte could have been used from which the anode reaction would have been exclusively oxygen evolution. A lifetime gaurantee of 1 year is, however, available for the platinised titanium anode in aqueous 2.0 mol dm^{-3} hyrochloric acid but not in sulphuric acid [2]. Excessive oxygen evolution oxidises the titanium substrate weakening the platinum to titanium bond and thereby producing high wear rates [3,4].

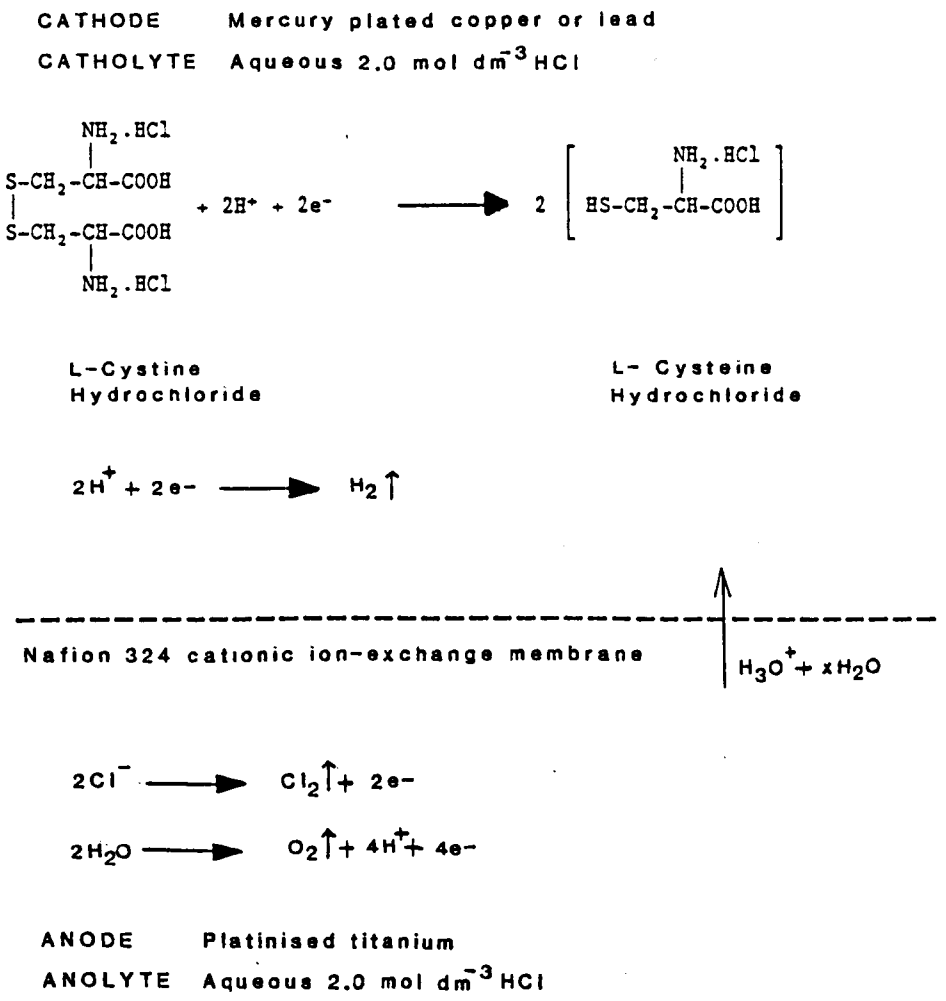

FIGURE 7.1 Major cell processes.

7.2 FIGURES OF MERIT FOR THE ELECTROCHEMICAL REACTOR

7.2.1 Introduction

One of the current trends in electrochemical engineering is the application of a set of standard performance criteria (figures of merit) to electrochemical cells [5]. This approach allows comparison of different cell designs and electrochemical reactions with respect to both technical and economic perspectives.

The figures of merit listed herein are not exhaustive (see e.g. [6]) but they are the most relevant to this study.

7.2.2 Material Yield (θ_p) and Selectivity (S)

The material yield may be defined as

$$\theta_p = \frac{\text{moles of reactant converted to desired product}}{\text{moles of reactant consumed}} \qquad (7.01)$$

The material yield has important consequences. If $\theta_p < 1$ it is usually necessary either to accept the lower price normally associated with an impure material or introduce additional unit processes to purify the product.

The overall selectivity, which is often equivalent to the material yield [6], is given by equation (7.02).

$$S = \frac{\text{moles of desired product}}{\text{moles of all products}} \qquad (7.02)$$

7.2.3 Fractional Conversion (X)

This is the fraction of reactant which is consumed by the electrochemical reaction, as shown in equation (7.03).

$$X = 1 - \frac{m_t}{m_o} \qquad (7.03)$$

where m_o and m_t are the moles of reactant initially and at time, t, respectively. Also in a fixed volume system

$$X = 1 - \frac{c_t}{c_o} \qquad (7.04)$$

where c_o and c_t are the concentrations of reactant initially and at time, t, respectively.

7.2.4 Current Efficiency (Φ)

This is the yield based upon the electrical charge passed during eletrolysis.

$$\Phi = \frac{\text{charge used in forming product}}{\text{total charge passed}}$$

From Faraday's Laws assuming a constant electrolyte volume

$$\Phi = \frac{m_p nF}{q} = \frac{nFV\Delta c}{q} \qquad (7.05)$$

where m_p is the moles of product, Δc the increase in product concentration, V the volume of electrolyte containing product and q the charge passed. Alternatively the current efficiency can be obtained from the decrease in the amount of reactant, assuming there are no side-reactions consuming reactant or the stoichiometry of all such reactions is known. A value less than unity indicates

byproducts are being formed or, although rare, the back reaction occurs to some extent. Byproducts may also arise by electrolysis of the background electrolyte (e.g. hydrogen and oxygen from water) rather than the starting material. Hence a current efficiency of less than 100% need not be associated with a material yield of less than 1.

7.2.5 Specific Energy Consumption (E_S)

The specific energy consumption is defined by equation (7.06).

$$E_S = -\frac{nFE_{CELL}}{M\,\Phi} \qquad (7.06)$$

where M (kg mol^{-1}) is the molar mass of the product and E_{CELL} is the cell voltage. It is common to express E_S in units of kWh kg^{-1}. This is achieved by division of the right hand side of equation (7.06) by 3.6×10^6 (i.e. 1 kWh kg^{-1} = 3.6×10^6 J kg^{-1}).

From equation (7.06), the energy consumption may be optimised by maximising the current efficiency and minimising the cell voltage. The various components of cell voltage are given by equation (6.26).

$$E_{CELL} = E_e^C - E_e^A - |\eta^C| - |\eta^A| - IR_{CELL} - IR_{CIRCUIT} \qquad (6.26)$$

The equation shows the cell voltage and therefore the specific energy consumption may be minimised by:

(i) Selecting a counter electrode reaction with the lowest standard electrode potential.

(ii) Finding electrocatalytic electrodes for both the cathode and

anode reactions to reduce the activation overpotentials.

(iii) If the electrode reactions are mass transport controlled maximising the mass transport coefficient to reduce the concentration overpotentials.

(iv) Reducing the cell and circuit resistance by minimising the inter-electrode gap, using highly conductive electrolyte(s) and only conductive, clean electrical cell contacts. If possible, cell separators should be avoided as they substantially increase the cell resistance.

7.2.6 Space-Time Yield (ρ_{ST})

This is one of the most valuable statements of reactor performance. It expresses the mass of product per unit time which can be obtained in a unit reactor volume.

$$\rho_{ST} = \frac{\Phi IM}{nFV_R} = \frac{\Phi iAM}{nFV_R} \qquad (7.07)$$

where M (kg mol^{-1}) is the molar mass of the product and V_R is the reactor volume. Rather than express the figure of merit in units of kg m^{-3} s^{-1}, multiplication of the right hand side of equation (7.07) by 3.6×10^3 gives units of kg m^{-3} h^{-1}. Equation (7.07) indicates that the space-time yield is directly proportional to the useful current density (i.e. $iA\Phi$) and it is favoured by a high ratio of active electrode area to reactor volume. Indeed, the low space-time yields of electrochemical reactors (e.g. 80 kg m^{-3} h^{-1} for a copper electrowinning cell [6]) compared with chemical reactors (e.g. 200 to 1,000 kg m^{-3} h^{-1}) are attributable to a much lower ratio of reactor area to reactor volume. As a

result, many studies have sought to increase this parameter in electrochemical reactors e.g. mesh electrodes, packed bed electrodes and fluidised bed electrodes.

A comparison of equations (7.06), (6.10) and (7.07) clearly shows that a balance is required between the specific energy consumption and the space-time yield, by a judicious selection of the reactor current.

7.2.7 Cumulative and Interval Values

Those figures of merit which are time dependent (e.g. X, Φ, E_s and ρ_{ST}) may be expressed as cumulative or interval values. Cumulative values are those calculated between a selected time and t = 0 whereas interval values are calculated between successive, selected times. The values quoted in this study are cumulative unless indicated otherwise.

7.3 SIMPLE MODELS FOR THE ELECTROCHEMICAL REACTOR

Traditionally, the majority of electrosynthesis cells have been designed and sized empirically. There is now a growing awareness that the performance may be modelled by standard electrochemical engineering approaches [6-10]. The approach adopted in this study is to fit the experimental data to a simple model which is approximate but adequate.

Such models have been applied satisfactorily to silver recovery from photographic fixing solutions [9,11-13] and copper electrowinning [14] in parallel plate cells operating in the batch recycle mode. Their application to more complex electroorganic reactions has been slow. The models attempt to predict the reactant concentration decay for an electrochemical reaction which is mass transport controlled, via convective-diffusion, during constant current electrolysis.

7.3.1 A Simple Batch Reactor Approximation

Consider electrolysis at a constant current, I , for a time, t, in a reactor

being supplied with electrolyte at a flow rate, Q, from an external reservoir of volume V_T (Figure 7.2). This system can be modelled by treating the reservoir as a batch reactor and assuming that:

(i) The reservoir is a perfect back-mix system and the reactant concentration can be considered uniform.

(ii) The physical properties of the electrolyte are constant in both space and time.

(iii) The working electrode has a uniform current density.

(iv) There are no side-reactions consuming reactant. The current efficiency can, consequently, be expressed in terms of the decrease in the moles of reactant.

The predicted behaviour is shown schematically in Figure 7.3. Zones I and II are predicted by the model. Zone III cannot be modelled. In zone I, the concentration decay is controlled by the magnitude of the partial current for the electrochemical reaction (i.e.$\Phi_t I$), which is much less than the limiting current (I_L). Since the current efficiency is constant, the partial current and the rate of reactant concentration decay, $dc_{i,t}/dt$, is constant. After a defined critical time, t_{CRIT}, at which the reactant concentration is c_{CRIT}, it is assumed the reaction becomes mass transport controlled by convective-diffusion. The partial current is now equal to the limiting current, which falls with the reactant concentration, and $c_{i,t}$ decreases exponentially with time as does the current efficiency. At sufficiently long times, the decrease in $c_{i,t}$ is small and eventually a steady low value of reactant concentration is reached. This final zone is complex, variable and little studied; the reaction rate is considered to be increasingly governed by electrode surface state and the electrolyte environment.

For constant current electrolysis, a mass balance in the reservoir combined

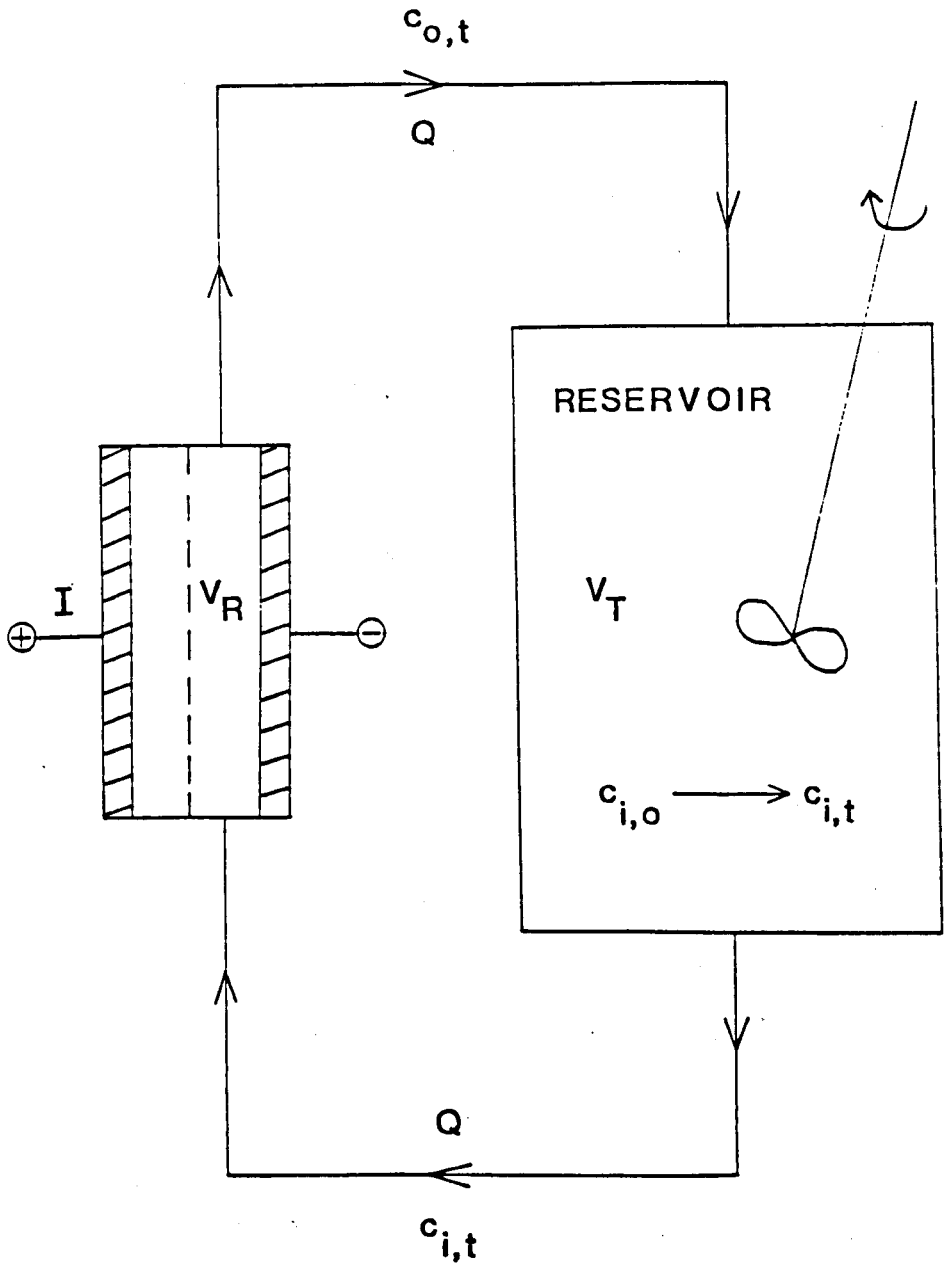

FIGURE 7.2 Batch recycle electrochemical reactor system.

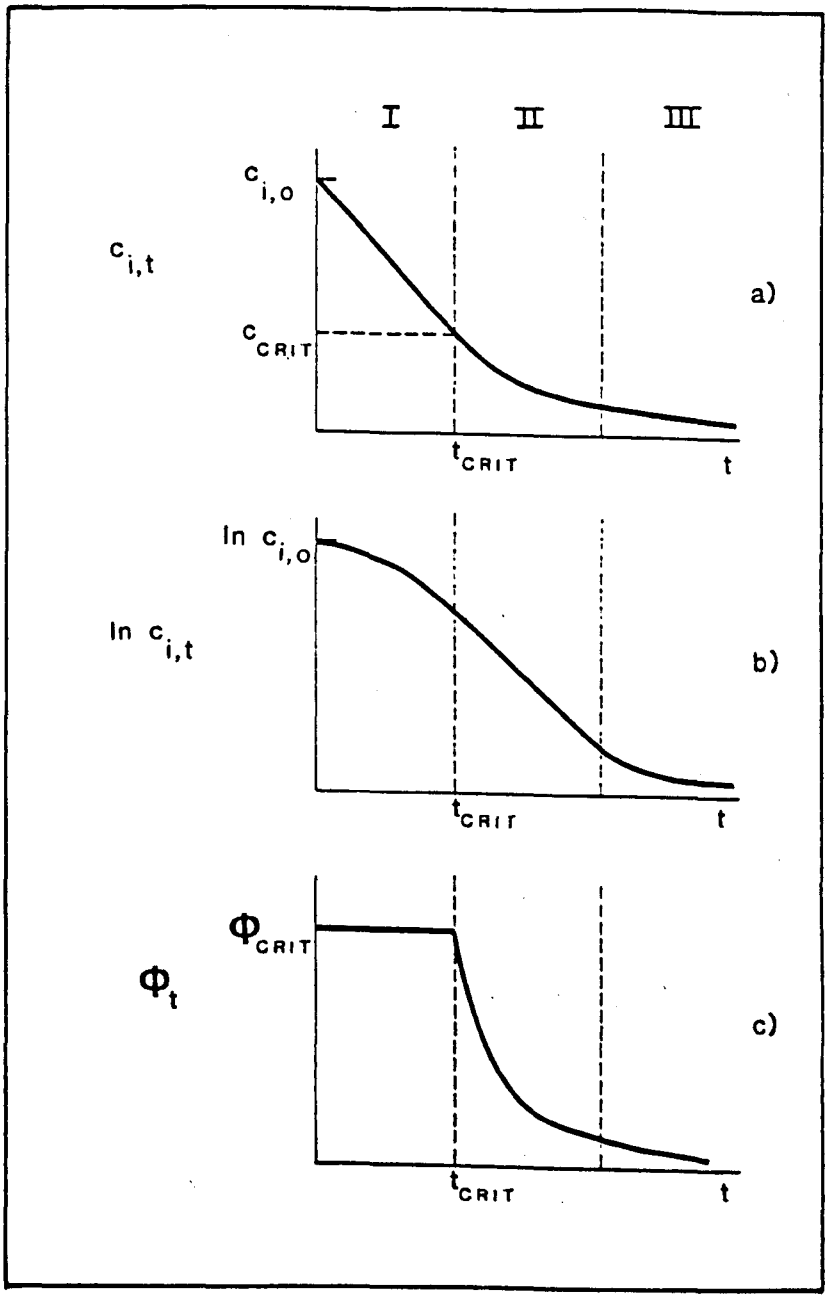

a) linear reactant concentration ordinate
b) logarithmic reactant concentration ordinate
c) cumulative current efficiency ordinate.

FIGURE 7.3 Predicted plots showing zoned beahviour for an electrochemical reaction occurring in a batch reactor.

with Faraday's Laws gives

$$c_{i,t} = c_{i,o} - \frac{\Phi_t I t}{nFV_T} \qquad (7.08)$$

In Zone I $\Phi_t I < I_{L,t}$; $t < t_{CRIT}$; $c_{i,t} > c_{CRIT}$; $\Phi_t = \Phi_{CRIT}$ = a constant

Equation (7.08) becomes

$$c_{i,t} = c_{i,o} - \frac{\Phi_{CRIT} I t}{nFV_T} \qquad (7.09)$$

In zone II $\Phi_t I = I_{L,t}$; $t > t_{CRIT}$; $c_{i,t} \leq c_{CRIT}$; $\Phi_t < \Phi_{CRIT}$

From equation (7.08):

$$\frac{dc_{i,t}}{dt} = -\frac{\Phi_t I}{nFV_T} \qquad (7.10)$$

The average mass transport coefficient is defined by equation (7.11).

$$K_L = \frac{I_{L,t}}{nFAc_{i,t}} \qquad (7.11)$$

Substituting for K_L in equation (7.10) gives

$$\frac{dc_{i,t}}{dt} = -\frac{K_L A}{V_T} \cdot c_{i,t} \qquad (7.12)$$

Integrating this equation with the boundary condition

$t = t_{CRIT}$ at $c_{i,t} = c_{CRIT}$

gives

$$c_{i,t} = c_{CRIT} \exp\left(-\frac{K_L A}{V_T}[t - t_{CRIT}]\right) \qquad (7.13)$$

or

$$\ln c_{i,t} = \ln c_{CRIT} - \frac{K_L A}{V_T}[t - t_{CRIT}] \qquad (7.14)$$

The rate of reactant concentration decay follows first order kinetics where the apparent rate constant $k = K_L A/V_T$. A plot of $\ln c_{i,t}$ against t should be linear with a slope from whick K_L can be calcualted.

Combining equations (7.08) and (7.14):

$$\Phi_t = \frac{nFK_L A}{I} \cdot \frac{(c_{i,t} - c_{CRIT})}{\ln c_{i,t}/\ln c_{CRIT}}$$

or

$$\Phi_t = \frac{nFK_L A\ (c_{i,t})_{L.M.}}{I} \qquad (7.15)$$

where $(c_{i,t})_{L.M.}$ is the logarithmic mean between $t = t_{CRIT}$ and $t = t$.

The point (t_{CRIT}, c_{CRIT}) can be obtained from the slope of the $c_{i,t}$ against t

graph in zone I and the slope of the ln $c_{i,t}$ against t graph in zone II. The slopes are equal at (t_{CRIT} , c_{CRIT}). In zone I equation (7.09) yields

$$\frac{dc_{i,t}}{dt} = -\frac{\Phi_{CRIT}I}{nFV_T} \qquad (7.16)$$

In zone II from equation (7.14):

$$\frac{dc_{i,t}}{dt} = -\frac{K_LA}{V_T}c_{CRIT} \qquad (7.17)$$

Equating (7.16) and (7.17) gives

$$c_{CRIT} = \frac{\Phi_{CRIT}I}{nFK_LA} \qquad (7.18)$$

Substituting for c_{CRIT} from equation (7.18) into equation (7.08) gives

$$t_{CRIT} = \frac{nFV_Tc_{i,o}}{\Phi_{CRIT}I} - \frac{V_T}{K_LA} \qquad (7.19)$$

Equation (7.18) shows c_{CRIT} is given by the slope of the $c_{i,t}$ against t graph in zone I divided by the slope of the ln $c_{i,t}$ against t graph in zone II. For t_{CRIT} the first term in equation (7.19) corresponds to division of $c_{i,o}$ by the slope of the $c_{i,t}$ against t graph in zone I and the second term is the reciprocal of the slope of the ln $c_{i,t}$ against t graph in zone II.

7.3.2 A Consideration of the Batch Recycle Model

It is more usual to treat the system of Figure 7.2 as a batch recycle system.

Two models are proposed which assume the reactor operates either as an 'ideal' plug flow reactor (PFR) or an 'ideal' continuous stirred tank reactor (CSTR). The models represent two extreme cases. An 'deal' PFR requires absolutely no mixing in the direction of electrolyte flow whereas an 'ideal' CSTR assumes complete mixing within the reactor such that the reactant concentration at the outlet is equal to the reactant concentration in the reactor. In addition the models assume:

(i) The reactor operates in the steady state. This assumption has been shown to be valid if $V_T >> V_R$ [15].

(ii) The reservoir is a perfect back-mix system and the reactant concentration can be considered uniform.

(iii) The physical properties of the electrolyte are constant in both space and time.

(iv) The volumetric flow rate, Q , is steady.

(v) There are no side-reactions consuming reactant. The current efficiency can, consequently, be expressed in terms of the decrease in the moles of reactant.

The predicted schematic behaviour is as shown in Figrue 7.3 for the batch reactor model. Indeed, zone I behaviour is identical for all three models with the reactant concentration decay given by equation (7.09), and it is only in zone II that the design equations differ. For the batch recycle models the zone II design equations are derived below.

In zone II, for an 'ideal' PFR a differential mass balance in an infinitely small slice, dy, of the working compartment of the reactor (see Figure 7.4) gives

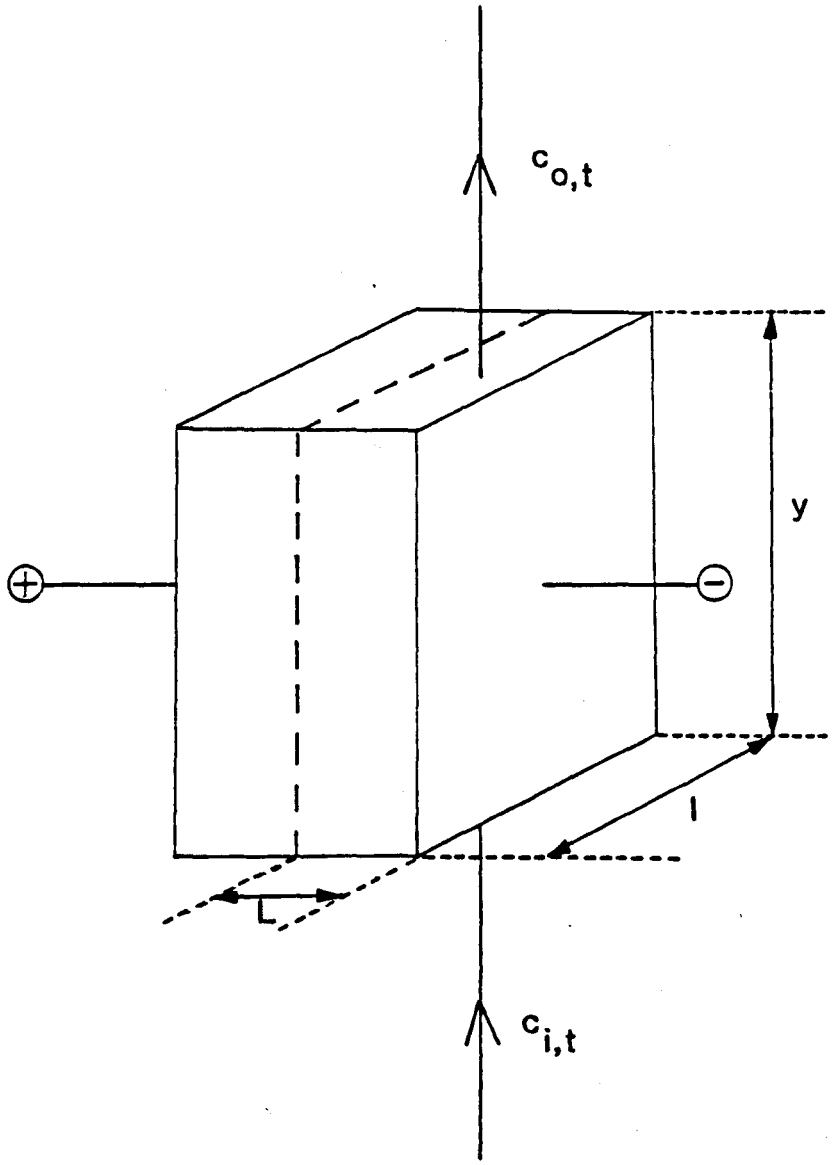

FIGURE 7.4 Reactor dimensions used in the models.

$$\frac{Q\ dc_{y,t}}{dy} + \frac{1}{nF} \cdot \frac{dI_{y,t}}{dy} = 0 \qquad (7.20)$$

(Input - Output) + Electrolysis = Accumulated

where $c_{y,t}$ is the local concentration and $I_{y,t}$ is the local mass transport controlled limiting current. By definition

$$\frac{dI_{y,t}}{dy} = nFlK_y\ c_{y,t} \qquad (7.21)$$

where K_y is the local mass transport coefficient. Substituting for $dI_{y,t}/dy$ from equation (7.21) into equation (7.20) gives

$$\frac{Q\ dc_{y,t}}{c_{y,t}} = -\ l\ K_y\ dy \qquad (7.22)$$

Integrating equation (7.22) over the reactor gives

$$c_{o,t} = c_{i,t}\ \exp\left(-\frac{K_L A}{Q}\right) \qquad (7.23)$$

where K_L is the average mass transport coefficient in the reactor. From equation (7.23) the fractional conversion per pass over the reactor is given by

$$X^{PFR}_{1,t} = 1 - \exp\left(-\frac{K_L A}{Q}\right) \qquad (7.24)$$

In zone II, for an 'ideal' CSTR an instantaneous mass balance in the working

compartment of the reactor gives

$$Q(c_{i,t} - c_{o,t}) - \frac{I_{L,t}}{nF} = 0 \qquad (7.25)$$

(Input - Output) - Electrolysis = Accumulated

where by definition

$$I_{L,t} = nFA\, K_L\, c_{o,t} \qquad (7.26)$$

Substituting for $I_{L,t}$ from equation (7.26) into equation (7.25) gives

$$c_{o,t} = \frac{c_{i,t}}{1 + K_L A/Q} \qquad (7.27)$$

From equation (7.27) the fractional conversion per pass over the reactor is given by

$$X_{i,t}^{CSTR} = 1 - \frac{1}{1 + K_L A/Q} \qquad (7.28)$$

For both the 'ideal' PFR and CSTR models, taking an instantaneous mass balance in the reservoir gives:

$$c_{o,t} = c_{i,t} + \tau_T \frac{dc_{i,t}}{dt} \qquad (7.29)$$

where $\tau_T(V_T/Q)$ is the residence time in the reservoir. Combining equation (7.29) with equation (7.24) or (7.28) gives

$$\frac{dc_{i,t}}{c_{i,t}} = -\frac{X_{1,t}}{\tau_T}\,dt \qquad (7.30)$$

where $X_{1,t}$ is defined by equation (7.24) for an 'ideal' PFR and equation (7.28) for an 'ideal' CSTR. Integrating this equation with the boundary condition

$$t = t_{CRIT} \quad \text{at} \quad c_{i,t} = c_{CRIT}$$

gives

$$c_{i,t} = c_{CRIT} \exp\left(-\frac{X_{1,t}}{\tau_T}\,[t - t_{CRIT}]\right) \qquad (7.31)$$

or

$$\ln c_{i,t} = \ln c_{CRIT} - \frac{X_{1,t}}{\tau_T}\,[t - t_{CRIT}] \qquad (7.32)$$

The rate of reactant concentration decay follows first order kinetics where the apparent rate constant $k = X_{1,t}/\tau_T$. A plot of $\ln c_{i,t}$ against t should be linear with a slope from which K_L can be calculated.

Combining equations (7.08) and (7.32):

$$\Phi_t = \frac{nFQX_{1,t}}{I} \cdot \frac{(c_{i,t} - c_{CRIT})}{\ln c_{i,t}/\ln c_{CRIT}}$$

or

$$\Phi_t = \frac{nFQX_{1,t}(c_{i,t})_{L.M.}}{I} \qquad (7.33)$$

where $(c_{i,t})_{L.M.}$ is the logarithmic mean between $t = t_{CRIT}$ and $t = t$.

As in the case of the batch reactor model the point (t_{CRIT}, c_{CRIT}) can be obtained from the slope of the $c_{i,t}$ against t graph in zone I and the ln $c_{i,t}$ against t graph in zone II. The slopes are equal at (t_{CRIT}, c_{CRIT}).

In zone II equation (7.32) yields

$$\frac{dc_{i,t}}{dt} = -\frac{X_{1,t}c_{CRIT}}{\tau_T} \qquad (7.34)$$

Equating (7.16) and (7.34) gives

$$c_{CRIT} = \frac{\Phi_{CRIT}I\tau_T}{nFV_TX_{1,t}} \qquad (7.35)$$

Substituting for c_{CRIT} from equation (7.35) into (7.08) gives

$$t_{CRIT} = \frac{nFV_Tc_{i,o}}{\Phi_{CRIT}I} - \frac{\tau_T}{X_{1,t}} \qquad (7.36)$$

Equation (7.35) shows c_{CRIT} is given by the slope of the $c_{i,t}$ against t graph in zone I divided by the slope of the ln $c_{i,t}$ against t graph in zone II. For t_{CRIT} the first term in equation (7.36) corresponds to division of $c_{i,o}$ by the slope of the $c_{i,t}$ against t graph in zone I and the second term is the reciprocal of the slope of the ln $c_{i,t}$ against t graph in zone II.

7.4 SELECTION OF AN APPROPRIATE MODEL FOR THE ELECTROSYNTHESIS

As shown in Section 7.3.2, the predicted behaviour for the three models differs only in zone II. The relevant design equations describing reactant concentration decay in this zone are shown below.

Batch Reactor

$$c_{i,t} = c_{CRIT} \exp\left(-\frac{K_L A}{V_T}[t - t_{CRIT}]\right)$$

'Ideal' PFR in batch recycle

$$c_{i,t} = c_{CRIT} \exp\left[-\frac{[1 - \exp -\frac{K_L A}{Q}]}{\tau_T} . [t - t_{CRIT}]\right]$$

'Ideal' CSTR in batch recycle

$$c_{i,t} = c_{CRIT} \exp\left[-\frac{[1 - \frac{1}{1 + K_L A/Q}]}{\tau_T} . [t - t_{CRIT}]\right]$$

If the fractional conversion per pass through the reactor is small (i.e. $K_L A/Q$ is small) all three design equations predict an identical reactant concentration decay i.e. if $x = K_L A/Q$ and $\Delta t = [t - t_{CRIT}]$:

$$\text{as } x \longrightarrow 0 \text{ then } \quad \frac{c_{i,t}}{c_{CRIT}} \longrightarrow [1 - \frac{x.\Delta t}{\tau_T}]$$

The predicted behaviour in zone II for each of the three models is shown in Table 7.1 for a typical reservoir residence time used in the electrosynthesis

TABLE 7.1 Comparison of the predicted reactant concentration decay in zone II for the models at various K_LA/Q values.

$V_T = 2 \times 10^{-3}$ m^3. $Q = 246 \times 10^{-6}$ m^3 s^{-1}. $\tau_T = 8.130$ s.

K_LA/Q	$[t - t_{CRIT}]$ (s)	$c_{i,t}/c_{CRIT}$			Deviations (%)	
		Simple Batch Reactor A	Batch Recycle Operation 'Ideal' PFR B	'Ideal' CSTR C	$\left(\frac{B-A}{A}\right)$	$\left(\frac{C-A}{A}\right)$
10^{-3}	1200	0.8628	0.8628	0.8629	0	0.01
	7200	0.4125	0.4127	0.4128	0.05	0.07
	10800	0.2649	0.2651	0.2653	0.08	0.15
	18000	0.1093	0.1094	0.1095	0.02	0.02
10^{-2}	120	0.8628	0.8634	0.8640	0.07	0.14
	600	0.4781	0.4798	0.4816	0.36	0.73
	1200	0.2286	0.2302	0.2319	0.70	1.44
	1800	0.1093	0.1105	0.1117	1.10	2.20
10^{-1}	15	0.8315	0.8390	0.8456	0.90	1.70
	60	0.4781	0.4954	0.5112	3.62	6.92
	120	0.2286	0.2455	0.2614	7.39	14.35
	180	0.1093	0.1216	0.1336	11.25	22.23
0.5	5	0.7353	0.7851	0.8147	6.77	10.80
	15	0.3975	0.4839	0.5406	21.74	36.0
	30	0.1580	0.2341	0.2923	48.2	85.0
	36	0.1093	0.1751	0.2286	60.2	109.2

experiments and selected values of K_LA/Q. Several important points are evident. At K_LA/Q values of 10^{-2} and below all three models predict an essentially equivalent $c_{i,t}/c_{CRIT}$ ratio. At K_LA/Q values of 10^{-1} and above, however, the models deviate markedly. The predicted order of reactant concentration decay is batch reactor > 'ideal' PFR > 'ideal' CSTR with the disparity between the models increasing with electrolysis time and at higher K_LA/Q values. For example, at a K_LA/Q of 10^{-1}, after 60 seconds the PFR and CSTR systems predict $c_{i,t}/c_{CRIT}$ ratios 3.62% and 6.92% higher, respectively, than the batch reactor model. After 120 seconds these deviations increase to 7.39% and 14.35% respectively. At a $c_{i,t}/c_{CRIT}$ ratio of 0.1093 for the batch reactor model, as the magnitude of K_LA/Q increases from 10^{-1} to 0.5 the deviations predicted by the PFR model increase from 11.25% to 60.2% and those predicted by the CSTR model from 22.23% to 109.2%.

In the electrosynthesis experiments, K_LA/Q values between 1×10^{-3} and 3×10^{-3} were employed in the reactor. Any of the three models outlined in Section 7.3 may, consequently, be applied (i.e. a deviation of less than 0.5% is predicted between the models at the highest K_LA/Q of 3×10^{-3} at the end of zone II which corresponds to a $c_{i,t}/c_{CRIT}$ ratio of ca. 0.1). Since it is conceptually more usual to consider a parallel plate cell operating in the batch recycle mode as an 'ideal' PFR this model will be used.

7.5 CORRECTION OF REACTANT AND PRODUCT CONCENTRATIONS MEASURED BY HPLC

L-Cystine hydrochloride and L-cysteine hydrochloride concentrations are corrected for the transport of hydroxonium ions and associated water molecules through the membrane during electrolysis, by measuring the catholyte and anolyte

volumes at the termination of a run and taking account of the volume of samples extracted. A linear rate of solvent transport is assumed. Between 2 and 3 moles of water per Faraday of charge passed was transferred in the experiments. Analysis of the anolyte indicated neither L-cystine hydrochloride nor L-cysteine hydrochloride passed through the membrane during experiments.

7.6 ABILITY OF THE MODEL TO PREDICT THE EXPERIMENTAL RESULTS

The experimental results of Figure 7.5 (mercury plated copper) and Figure 7.6 (lead) show the predicted three zones. There is a start-up period of about 30 minutes for all experiments where abnormally high current efficiencies, some in excess of 100%, are measured. In this region the cathode potential fluctuates (ca. ± 200 mV) and the cell voltage rises sharply (ca. 0.5 V) before returning towards their initial values. It is not known why this occurs but it may be due to conditioning of the electrode surface.

After this period, the partial current for L-cystine hydrochloride reduction is less than the limiting current, and since the current efficiency is constant, the reactant concentration decreases linearly with time in accordance with equation (7.09) for current control.

The model predicts an instantaneous change from current to mass transport control, at (t_{CRIT}, c_{CRIT}), but in practice there is a significant region of mixed control. In fact, it is only for the particular case where an electrode reaction initially occurs at a potential well separated from secondary electrode reactions that the transition will be sharp. Consider the change in current-potential curves during cosntant current batch electrolysis under just such a condition (Figure 7.7). Before (t_{CRIT}, c_{CRIT}), (i.e. zone I) neither charge transfer kinetics nor mixed kinetic-mass transport control of the electrode reaction has an effect on the current

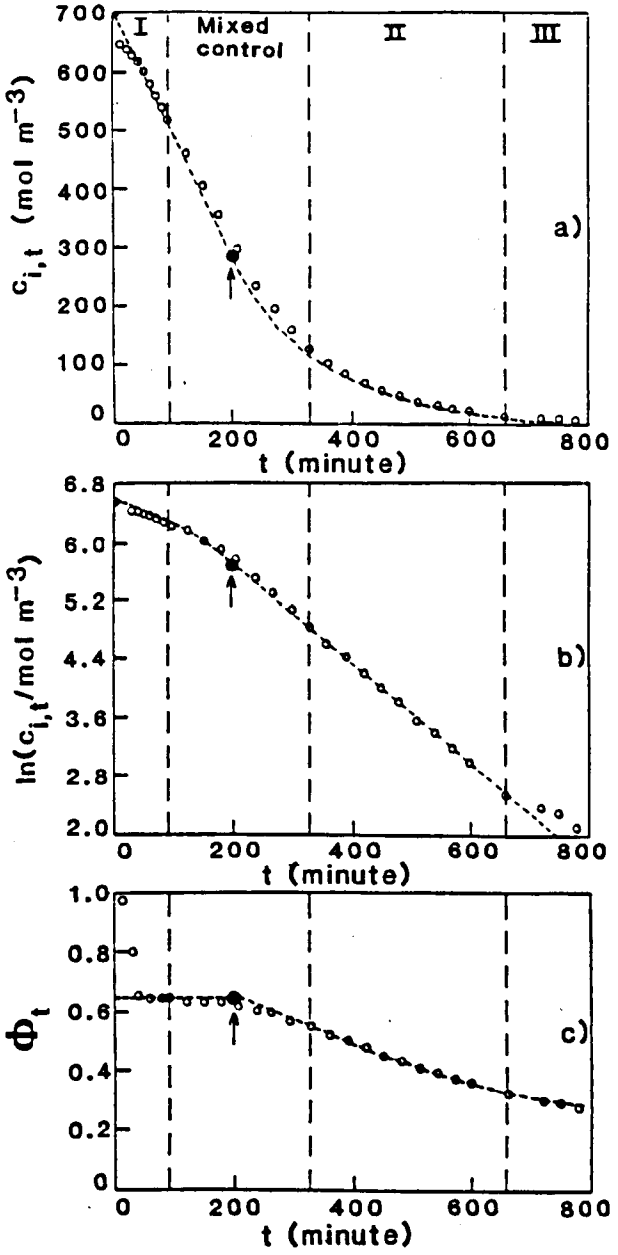

i = 2,000 A m^{-2} and $\bar{v}$ = 0.066 m s^{-1}. Expamet turbulence promoter (orientation A) in the catholyte channel. ● (t_{CRIT},c_{CRIT})
a) linear L-cystine hydrochloride concentration ordinate b) logarithmic L-cystine hydrochloride concentration ordinate and c) cumulative current efficiency ordinate.

FIGURE 7.5 Ability of the model to predict the experimental results at the mercury plated copper cathode.

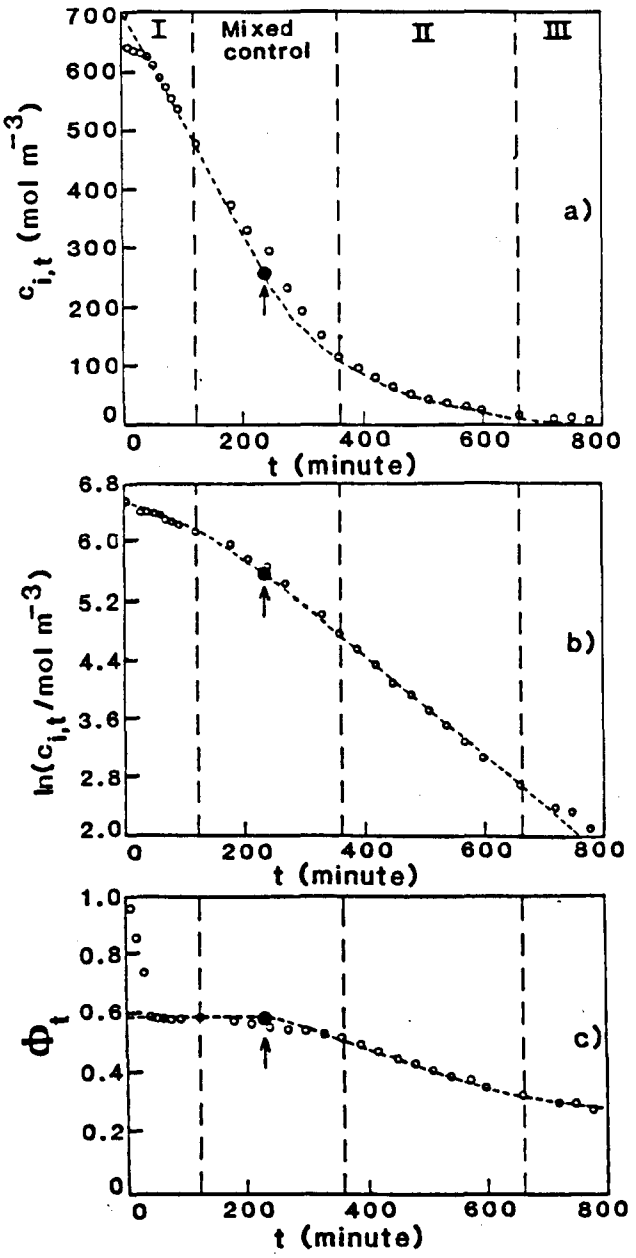

i = 2,000 A m^{-2} and $\bar{v}$ = 0.066 m s^{-1}. Expamet turbulence promoter (orientation A) in the catholyte channel. ● (t_{CRIT}, c_{CRIT})
a) linear L-cystine hydrochloride concentration ordinate b) logarithmic L-cystine hydrochloride concentration ordinate and c) cumulative current efficiency ordinate.

FIGURE 7.6 Ability of the model to predict the experimental results at the lead cathode.

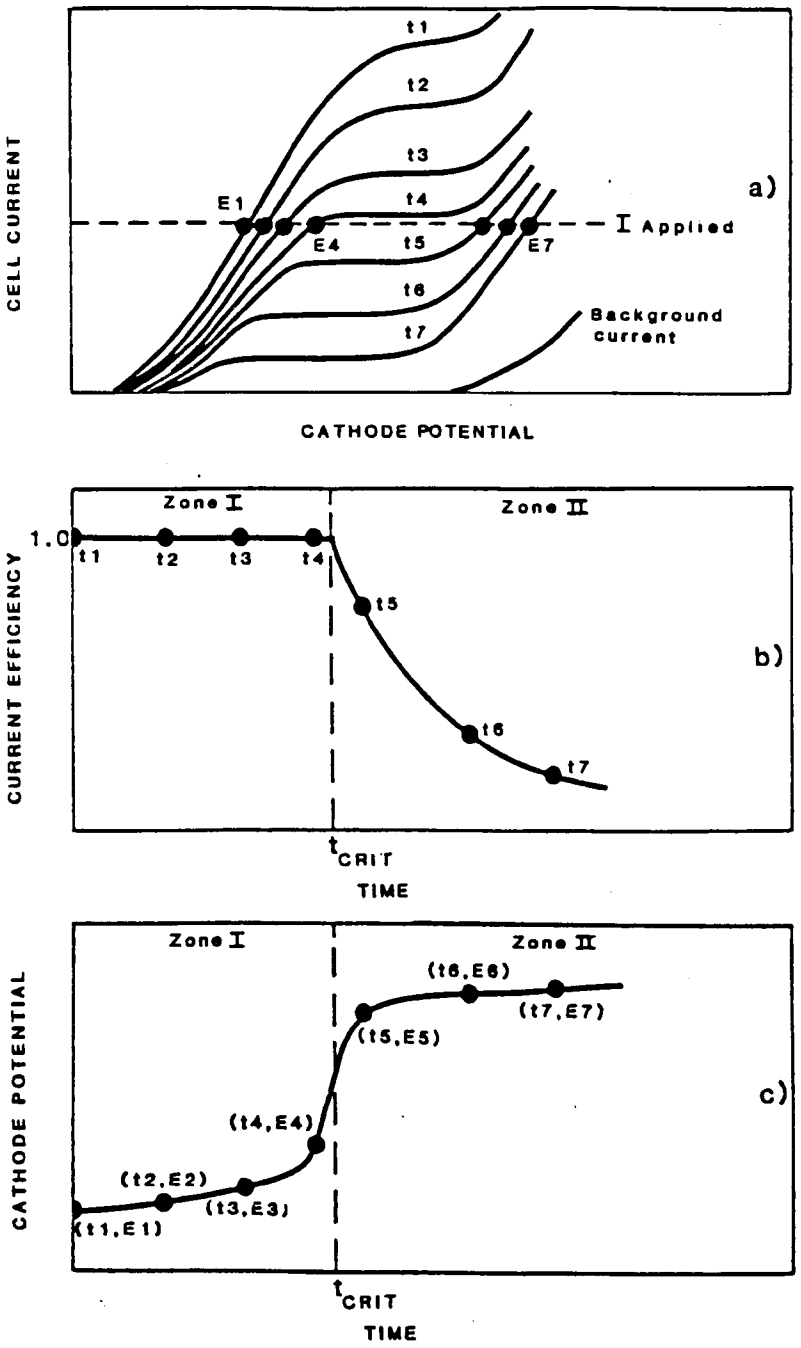

a) current–potential curves at different times b) cumulative current efficiency versus time and c) cathode potential versus time.

FIGURE 7.7 Constant current batch electrolysis of a reactant which is initially reduced at a potential well separated from secondary electrode reaction(s).

efficiency which is 100%. At (t_{CRIT}, c_{CRIT}) a sharp rise in the cathode potential should be observed, to that required for the secondary electrode reaction, with a correspondingly sharp transition from kinetic to mass transport control (i.e. zone II).

L-Cystine hydrochloride reduction, however, occurs simultaneously with hydrogen evolution to which all current losses are ascribed. In this case, the cathode potential, which is a function of both electrode reactions, is diagnostic. Figure 7.8 shows a typical change in the cathode potential around (t_{CRIT}, c_{CRIT}) during constant current batch electrolysis at the cathodes. Based upon the reasonable assumption that the hydrogen evolution reaction is activation controlled throughout the electroylsis, zone I behaviour requires essentially a small change in the cathode potential. This prevents the different electrochemcial kinetics of the two electrode reactions or mixed kinetic-mass transport control of L-cystine hydrochloride reduction from lowering the current efficiency. Tafel slopes of about 180 mV/decade for the disulphide reduction (see Chapters 3 and 4) reflect the more sluggish electrochemical kinetics compared with hydrogen evolution for which Tafel slopes of 120 mV/decade are measured at the cathodes [16]. Application of these Tafel slopes assumes, of course, the rates of the two reactions are independent in the reactor. Reference to Figure 7.8, shows the change in the cathode potential at the electrodes is, indeed, only about 25 mV in zone I. Critically, however, there is only a gradual change in the cathode potential around (t_{CRIT}, c_{CRIT}). Consequently a significant region exists, between zones I and II, where the cathode potential must correspond to a region on the current-potential curve for L-cystine hydrochloride reduction corresponding to mixed control. Figure 7.9 attempts to show this schematically (i.e. not until t = t_6 in Figure 7.9 is pure mass transport control evident). This manifests itself as the mixed region in

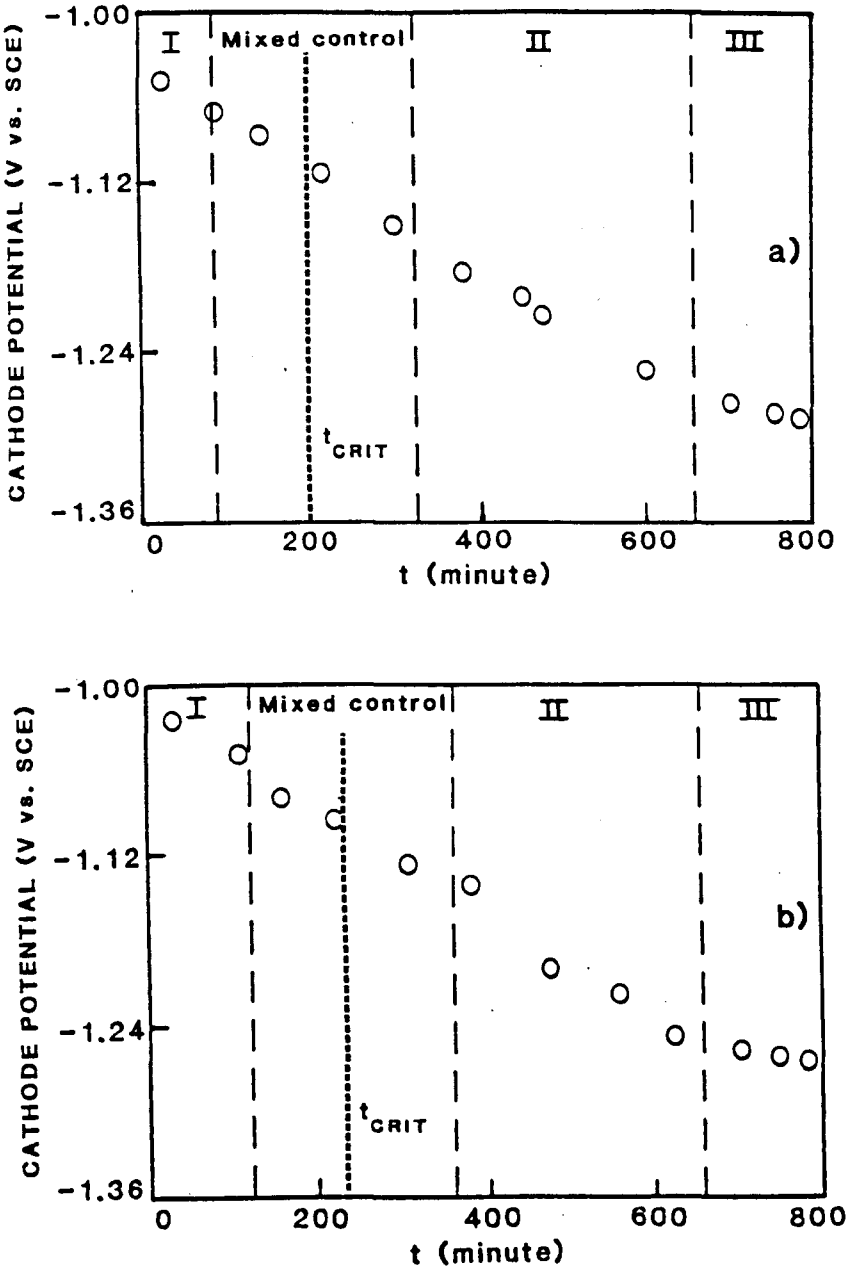

i = 2,000 A m^{-2} and $\bar{v}$ = 0.066 m s^{-1}. Expamet turbulence promoter (orientation A) in the catholyte channel.

FIGURE 7.8 Change in the cathode potential during batch electrolysis of L-cystine hydrochloride at a) mercury plated copper and b) lead cathodes.

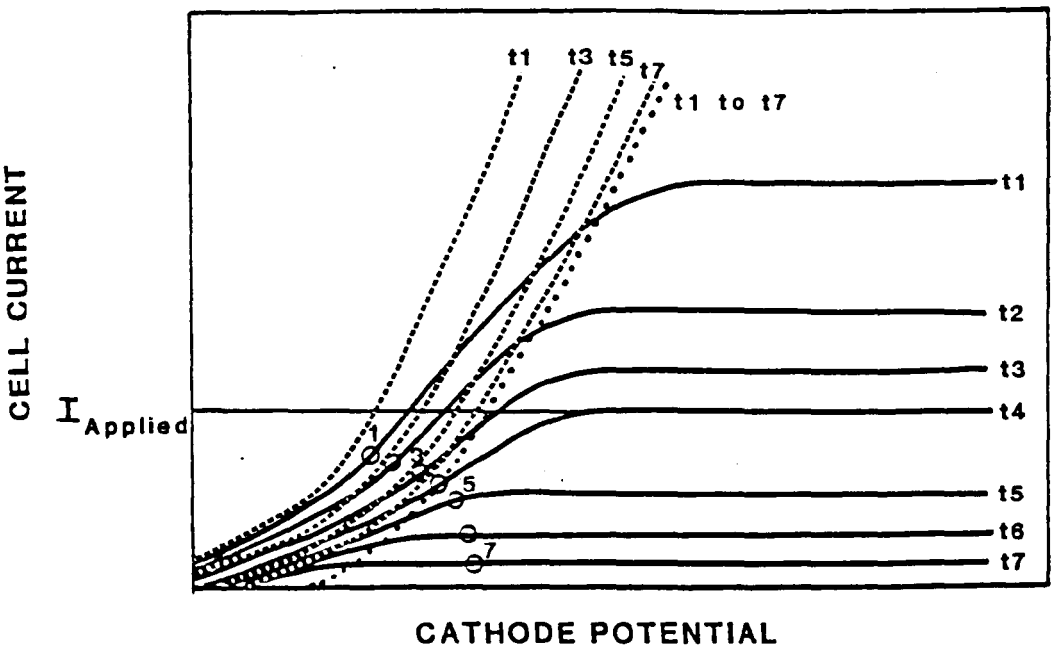

Current-potential curves for the total cell current

Current-potential curves for L-cystine hydrochloride reduction

Current-potential curve for hydrogen evolution

o Partial current for L-cystine hydrochloride reduction at times t1 to t7

FIGURE 7.9 Schematic change in the current-potential curves during constant current batch electrolysis showing the change in the partial current for L-cystine hydrochloride reduction.

Figures 7.5 and 7.6.

From equations (7.35) and (7.36) using a least squares fit to the data the critical point is estimated as (199 minutes, 297 mol m^{-3}) at mercury plated copper and (235 minutes, 269 mol m^{-3}) at lead. Zone I, however, terminates after 90 minutes at mercury plated copper and 120 minutes at lead and it is only after some 330 minutes at mercury plated copper and 360 minutes at lead that the cell is assumed to be operating at the limiting current for the reduction. After this time, the concentration decay is exponential as expected from equation (7.31) which describes mass transport control via convective-diffusion. The ln $c_{i,t}$ against t graph is linear allowing K_L to be determined (equation 7.32) and the current efficiency decays exponentially as predicted by equation (7.33).

At times longer than 720 minutes, the L-cystine hydrochloride concentration is very low and the reaction rate is variable (i.e. zone III). To identify the three zones, it is advisable to compare all the graphs shown in Figure 7.5 or 7.6.

As shown in Figure 7.5a (mercury plated copper) and Figure 7.6a (lead), equation (7.31) adequately predicts the concentration decay in zone II, with (t_{CRIT}, c_{CRIT}) obtained from equations (7.35) and (7.36). To test equation (7.31), however, K_L is deduced from the data so good agreement is inevitable. Consequently, K_L was determined independently using the diffusion limited current technique and ferricyanide reduction at a platinised titanium cathode (see Section 6.3). A comparison of the K_L values obtained from the two techniques is shown in Figure 7.10. The batch electrolysis values are between 17 and 25% lower. For example in the empty catholyte channel at a linear catholyte velocity of 0.066 m s^{-1} (i.e. a log value of -1.18) K_L from batch electrolyses is 1.20×10^{-5} m s^{-1} compared with a value of 1.40×10^{-5} m s^{-1} from limiting current measurements. To obtain a true comparison, however, it is necessary to

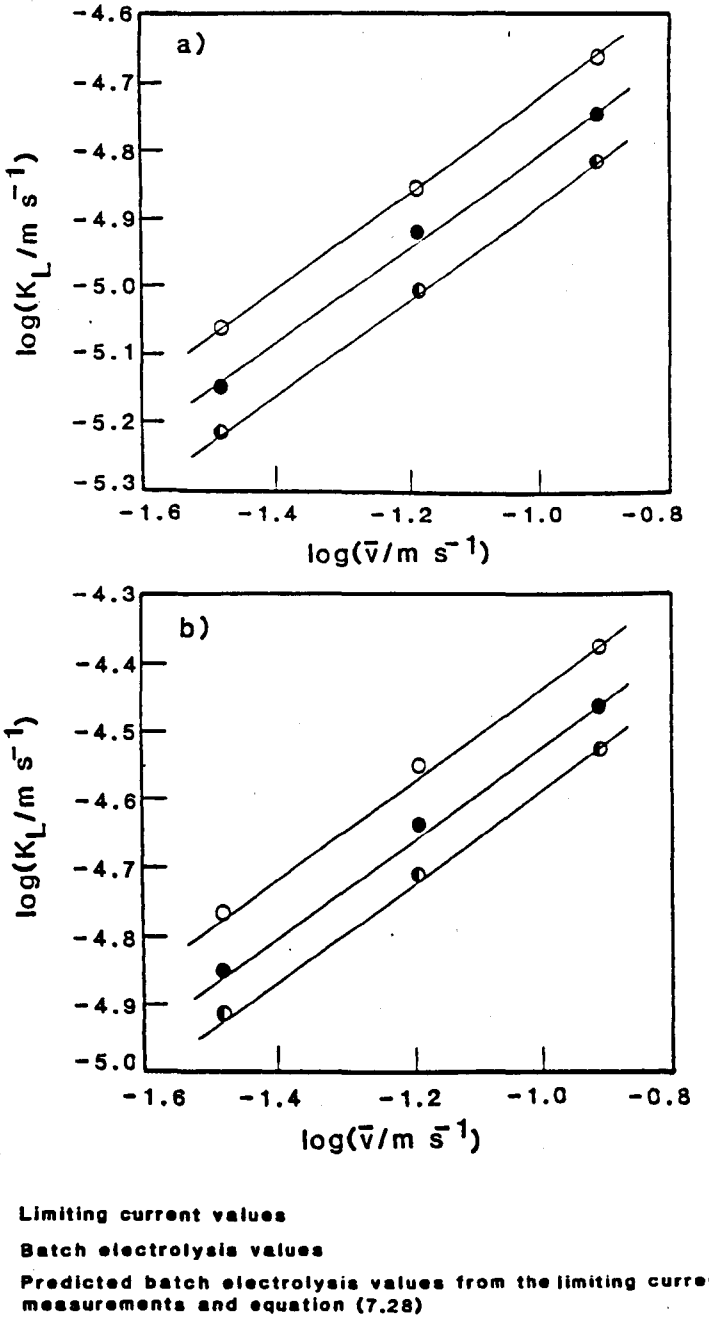

FIGURE 7.10 Comparison of the average mass transport coefficients obtained from limiting current and batch electrolysis experiments in a) the empty and b) the Expamet (orientation A) promoted catholyte channel.

correct the results to allow for the different transport properties of the electrolytes (i.e. kinematic viscosity and diffusion coefficient of the reactant) used in the two types of exoperiment. From the mass transport correlations for the cell under the conditions of Figure 7.10 (equation 6.27 and Table 6.4):

$$\frac{(Sh)_{B.E.}}{(Sh)_{L.C.}} = \frac{a\,(Re)^{0.70}_{B.E.}\,(Sc)^{1/3}_{B.E.}}{a\,(Re)^{0.70}_{L.C.}\,(Sc)^{1/3}_{L.C.}}$$

or

$$\frac{(K_L d_e/D)_{B.E.}}{(K_L d_e/D)_{L.C.}} = \frac{a\,(v\,d_e/\nu)^{0.70}_{B.E.}\,(Sc)^{1/3}_{B.E.}}{a\,(v\,d_e/\nu)^{0.70}_{L.C.}\,(Sc)^{1/3}_{L.C.}}$$

which gives

$$\frac{(K_L)_{B.E.}}{(K_L)_{L.C.}} = \frac{D_{B.E.}}{D_{L.C.}}\left(\frac{\nu_{L.C.}}{\nu_{B.E.}}\right)^{0.70}\left(\frac{Sc_{B.E.}}{Sc_{L.C.}}\right)^{1/3} \qquad (7.37)$$

where the subscripts B.E. (batch electrolysis) and L.C. (limiting current) identify the parameters for the different experiments.

For the electrolyte used in the limiting current measurements (i.e. 0.05 mol dm^{-3} potassium ferricyanide and 0.05 mol dm^{-3} potassium ferrocyanide in aqueous 1.0 mol dm^{-3} potassium hydroxide), at 25°C, the kinematic viscosity is 1.123×10^{-6} m^2 s^{-1} and the diffusion coefficient of the ferricyanide ion is 7.07×10^{-10} m^2 s^{-1}[17]. The transport properties of the electrolyte in batch electrolyses in zone II (i.e. from ca. 250 mol m^{-3} L-cystine hydrochloride and 900 mol m^{-3} L-cysteine hydrochloride to ca. 20 mol m^{-3} L-cystine hydrochloride and 1,360 mol m^{-3} L-cysteine hydrochloride, all in aqueous 2.0 mol dm^{-3} hydrochloric acid) are not available. At 25°C, however, the kinematic viscosity of 250 mol m^{-3}

L-cystine hydrochloride in aqueous 2.0 mol dm^{-3} hydrochloric acid, as measured by U-tube viscometer and density bottles, is 1.060×10^{-6} m^2 s^{-1} and from voltammetry at mercury plated copper (Chapter 3), in 20 mol m^{-3} L-cystine hydrochloride and aqueous 2.0 mol dm^{-3} hydrochloric acid, the diffusion coefficient of L-cystine hydrochloride is 4.0×10^{-10} m^2 s^{-1}. Substituting these values into equation (7.37) gives

$$\frac{(K_L)_{B.E.}}{(K_L)_{L.C.}} = \frac{4.0 \times 10^{-10}}{7.07 \times 10^{-10}} \left(\frac{1.123 \times 10^{-6}}{1.060 \times 10^{-6}}\right)^{0.70} \left(\frac{2637}{1588}\right)^{1/3}$$

or

$$\frac{(K_L)_{B.E.}}{(K_L)_{L.C.}} = 0.701 \text{ at } 25^{\circ}C \qquad (7.38)$$

This is a large correction the accuracy of which is substantially dependent upon reliable diffusion coefficients. For L-cystine hydrochloride a lower diffusion coefficient and a correspondingly larger correction might be expected at the higher amino acid concentraitons present in batch electrolysis experiments. Figure 7.10 shows the K_L values predicted for batch electrolysis experiments, by adjusting the limiting current results using equation (7.38). This suggests the batch electrolysis values rather than being 17 to 25% smaller, are, in fact, between 17 and 23% higher than the limiting current values. This discrepancy may merely encompass the accuracy of the measurements using the two techniques, although there may be some enhancement of mass transport by hydrogen evolution during L-cystine hydrochloride reduction. From Faraday's Laws and the molar volume of a gas at standard ambient temperature and pressure (i.e. 24.789×10^{-3} m^3 mol^{-1} [18]) between 6.7×10^{-5} and 15.4×10^{-5} m^3 m^{-2} s^{-1} of hydrogen is evolved at the

cathode surface in zone II. There is evidence [19] that gas evolution, even in the presence of turbulence promoters, can produce a small additional enhancement of mass transport.

7.7 ELECTROSYNTHESIS RESULTS

7.7.1 Reactor Performance In Terms of Figures of Merit

Following exhaustive electrolysis, evaporation of the catholyte yields pure L-cysteine hydrochloride. A mass balance based upon the cathode reaction (see Figure 7.1) suggested the material yield and selectivity is at least 99%. Thin layer chromatography [20] confirmed other amino acids are not produced. All current losses are conseuqently ascribed to hyrogen evolution from the background electrolyte. The optical rotation ($[\alpha]_D^{25°C}$ = + 6.5° for a concentration of 20 g dm^{-3} in 5 mol dm^{-3} hydrochloric acid) and melting point (176-178°C) of the product are in accord with the literature [21]. The optical rotation is particularly important as a criterion of purity. Material which meets this specification contains less than 1% of the reactant since the disulphide has a large negative optical rotation ($[\alpha]_D^{25°C}$ = - 232° for a concentration of 10 g dm^{-3} in 5 mol dm^{-3} hydrochloric acid [21]).

The change in the cumulative figures of merit during a batch electrolysis are, typically, as shown in Figure 7.11 (mercury plated copper) and Figure 7.12 (lead). In zone I, since the current efficiency and current density are constant the space-time yield is maintained and the fractional conversion in the reservoir rises linearly with time. The cell voltage and therefore the specific energy consumption, rise gradually. In zone II, the current efficiency and space-time yield fall, producing a more gradual rise in the fractional conversion. The cell voltage continues to increase and combines with a lower current efficiency to give a higher rate of increase in the specific energy consumption. There is, of course,

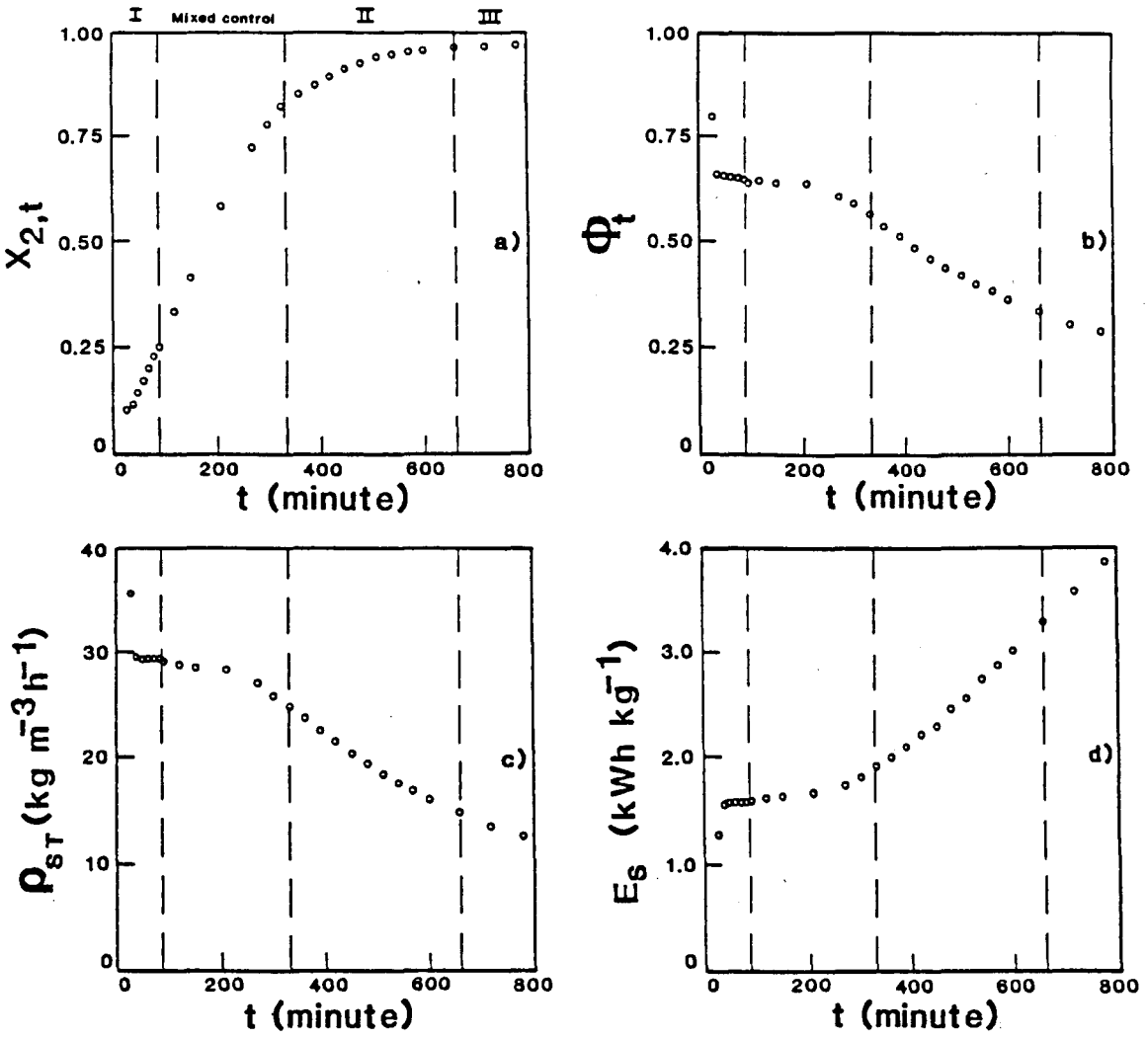

i = 2,000 A m^{-2} and $\bar{v}$ = 0.066 m s^{-1}. Expamet (orientation A) in the catholyte channel.

FIGURE 7.11 Change in the figures of merit during batch electrolysis at mercury plated copper.

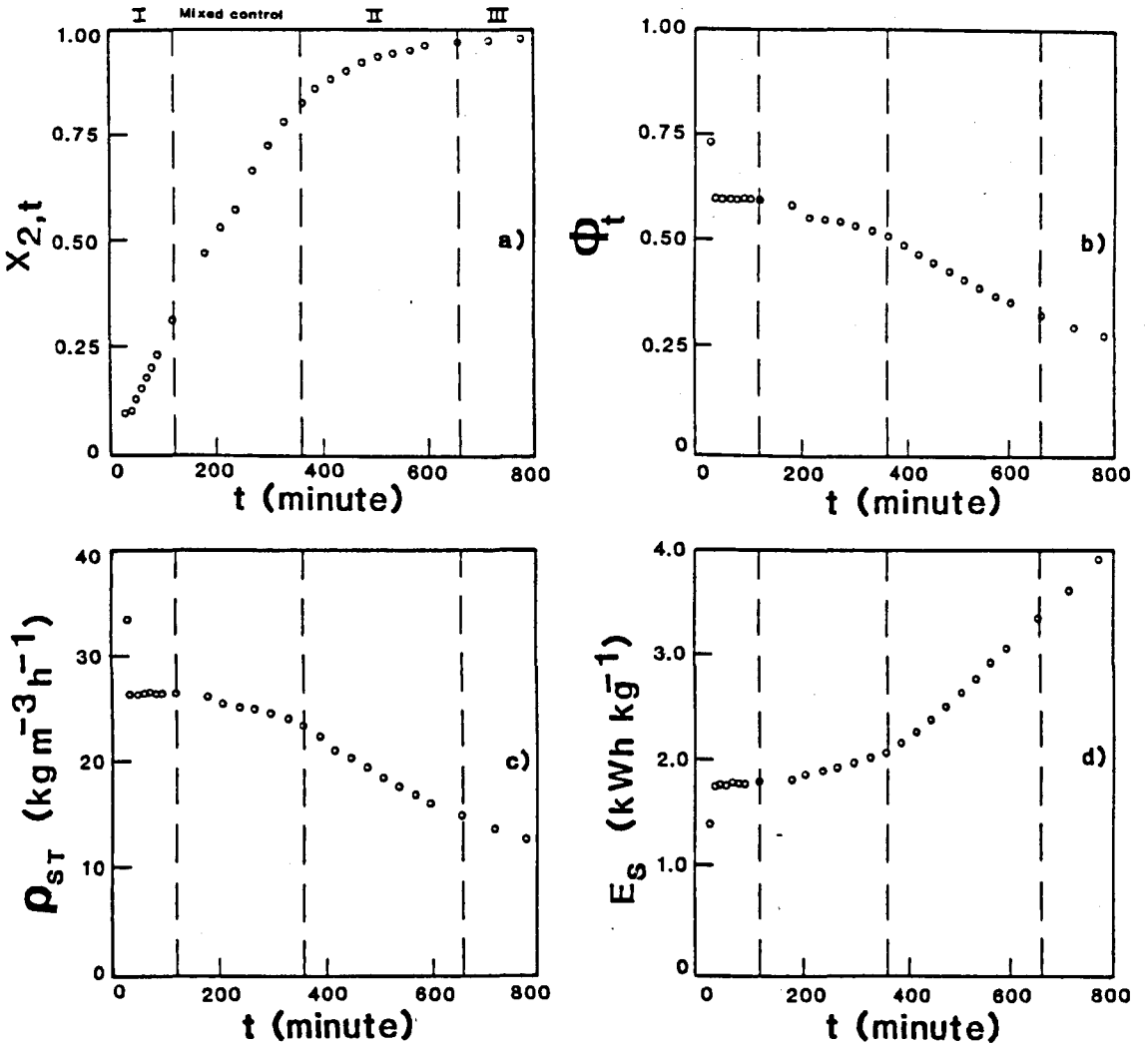

i = 2,000 A m^{-2} and $\bar{v}$ = 0.066 m s^{-1}. Expamet (orientation A) in the catholyte channel.

FIGURE 7.12 Change in the figures of merit during batch electrolysis at lead.

a gradual transition in the figures of merit between zones I and II. Clearly it is in zone II that the current efficiency, space-time yield and specific energy consumption all become much less economical.

The optimum conditions for the electrosynthesis were determined by a parameteric study of current density and catholyte flow rate. The effect of current density is best examined in zone I where mass transport has no effect on the performance. At mercury plated copper, lowering the current density from 2,000 A m^{-2} to 500 A m^{-2} (Figure 7.13) produces an increase in the batch processing time (Figure 7.13a), as evidenced by a decrease in the space-time yield from 29.5 kg m^{-3} h^{-1} to 11.0 kg m^{-3} h^{-1} in zone I (Figure 7.13b). This is offset by an increase from 66% to 98% in the current efficiency (Figure 7.13c), due to decreasing rates of hydrogen evolution, which coupled with a decrease of about 1.9 V in the cell voltage reduces the specific energy consumption from 1.55 kWh kg^{-1} to 0.55 kWh kg^{-1} (Figure 7.13d). Figure 7.17 shows the voltage balance for the cell at all current densities examined. This shows the majority of the reduced cell voltage is a result of the lower voltage drop over the membrane and circuit (0.9 V) and through the catholyte and anolyte (0.8 V), with the remaining 0.2 V attributable to a lower cathode and anode overpotential. At lead, an identical lowering of the current density (Figure 7.14) produces a similar increase in the batch processing time (Figure 7.14a), as evidenced by a decrease in the space-time yield from 26.5 kg m^{-3} h^{-1} to 10.5 kg m^{-3} h^{-1} in zone I (Figure 7.14b). Again this is offset by an increase in the current efficiency, from 59% to 94% (Figure 7.14c), and by a reduction in the specific energy consumption from 1.75 kWh kg^{-1} to 0.55 kWh kg^{-1} (Figure 7.14d). These specific energy consumption values are almost equivalent to those obtained at mercury plated copper. This reflects the essentially equivalent cell voltages (as shown in Figure

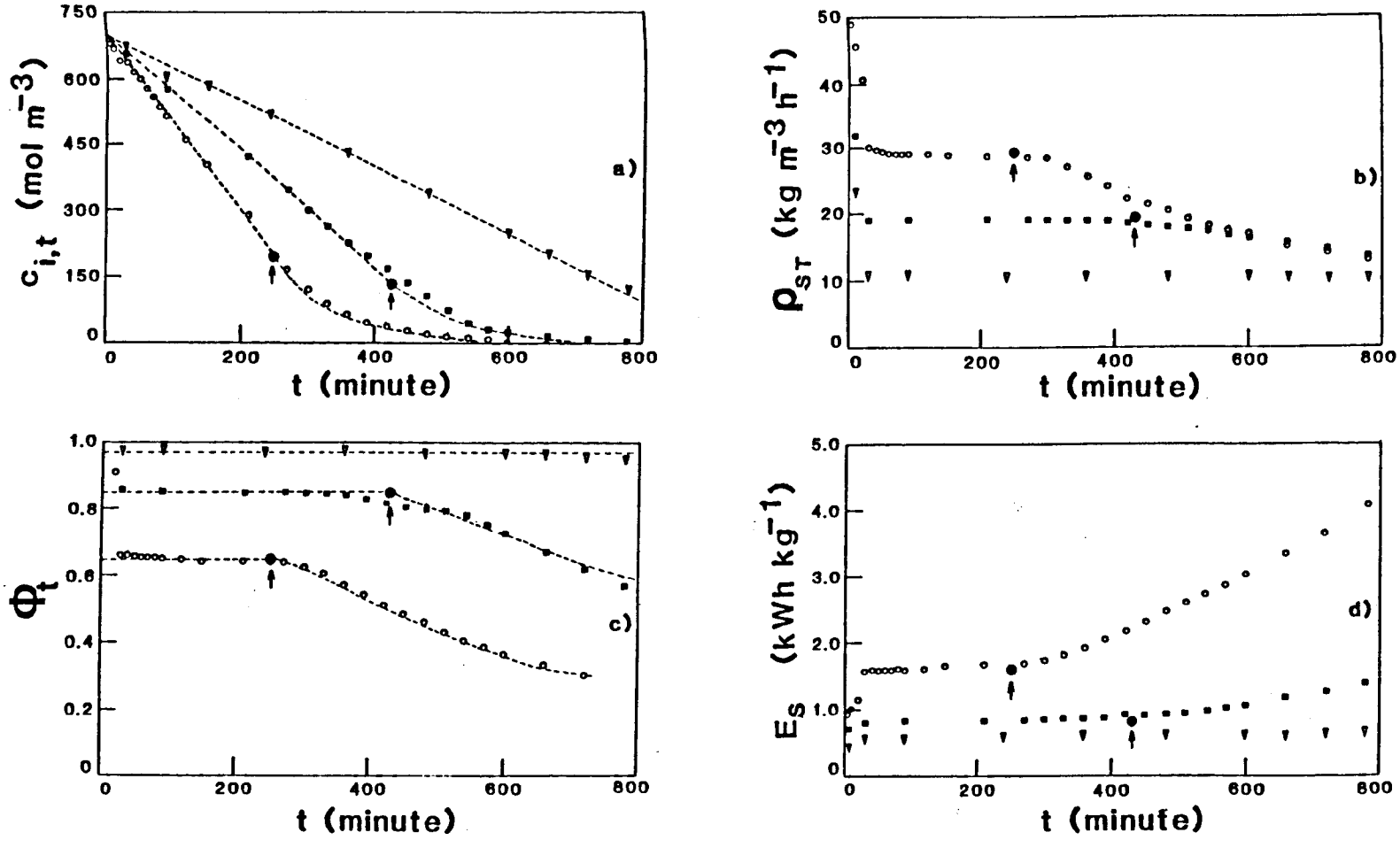

o i = 2,000 A m^{-2} ■ i = 1,000 A m^{-2} ∇ i = 500 A m^{-2} ----- PREDICTED ● (t_{CRIT}, c_{CRIT})
$\bar{v}$ = 0.123 m s^{-1}. Expamet (orientation A) in the catholyte channel.

FIGURE 7.13 .Effect of current density on L–cystine hydrochloride reduction at mercury plated copper.

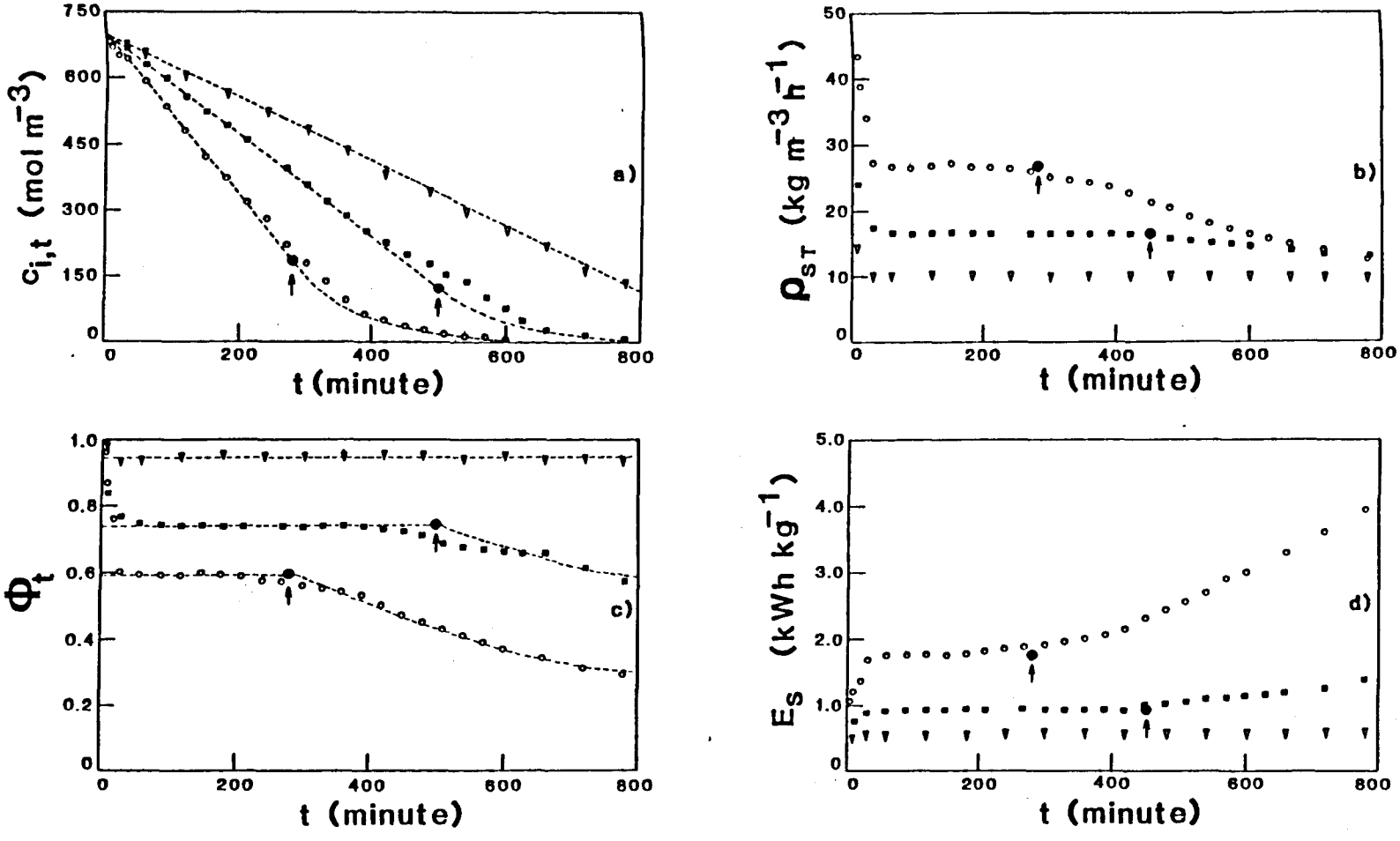

o i = 2,000 A m^{-2} ■ i = 1,000 A m^{-2} ∇ i = 500 A m^{-2} ----- PREDICTED ● (t_{CRIT},c_{CRIT})
$\bar{v}$ = 0.123 m s^{-1}. Expamet (orientation A) in the catholyte channel.

FIGURE 7.14 Effect of current density on L-cystine hydrochloride reduction at lead.

7.17) and current efficiences measured in zone I at the cathodes, for all current densities investigated. At both cathodes, 500 A m^{-2} is the optimum current density, if batch processing times are acceptable, although in zone II, particularly towards the end of an electrolysis, it may be more economical to reduce the current density to minimise current losses. A further large reduction in the current density in zone I would not be economical. For example reduction from 500 A m^{-2} to 250 A m^{-2} would produce little improvement in the current efficiency, which is already well over 90% at 500 A m^{-2}, but would half the space-time yield and, at best, reduce the cell voltage by about 0.3 V (as shown in Figure 7.17) producing a reduction of less than 0.1 kWh kg^{-1} in the specific energy consumption.

The effect of increasing the catholyte flowrate through the cell is shown in Figure 7.15 (mercury plated copper) and Figure 7.16 (lead). Raising the catholyte flowrate increases the rate of mass transport of L-cystine hydrochloride to the cathode surface, which has two effects. The point (t_{CRIT}, c_{CRIT}) moves to longer times and lower reactant concentrations, as predicted by equations (7.35) and (7.36), and the rate of reactant concentration decay in zone II is increased. For example raising the nominal, linear catholyte velocity from 0.033 m s^{-1} to 0.123 m s^{-1} moves (t_{CRIT}, c_{CRIT}) from (108 minutes, 482 mol m^{-3}) to (251 minutes, 193 mol m^{-3}) at mercury plated copper (Figure 7.15a) and from (142 minutes, 438 mol m^{-3}) to (281 minutes, 181 mol m^{-3}) at lead (Figure 7.16a). In addition, the ln $c_{i,t}$ versus t graph in zone II (Figure 7.15b and 7.16b) shows an increased slope at the higher velocity (from which K_L is calculated to increase from 1.40 x 10^{-5} m s^{-1} to 3.45 x 10^{-5} m s^{-1}), reflecting the greater rate of reactant concentration decay in zone II. The net result of both effects is a reduction in the batch processing time by minimising the duration of zone II.

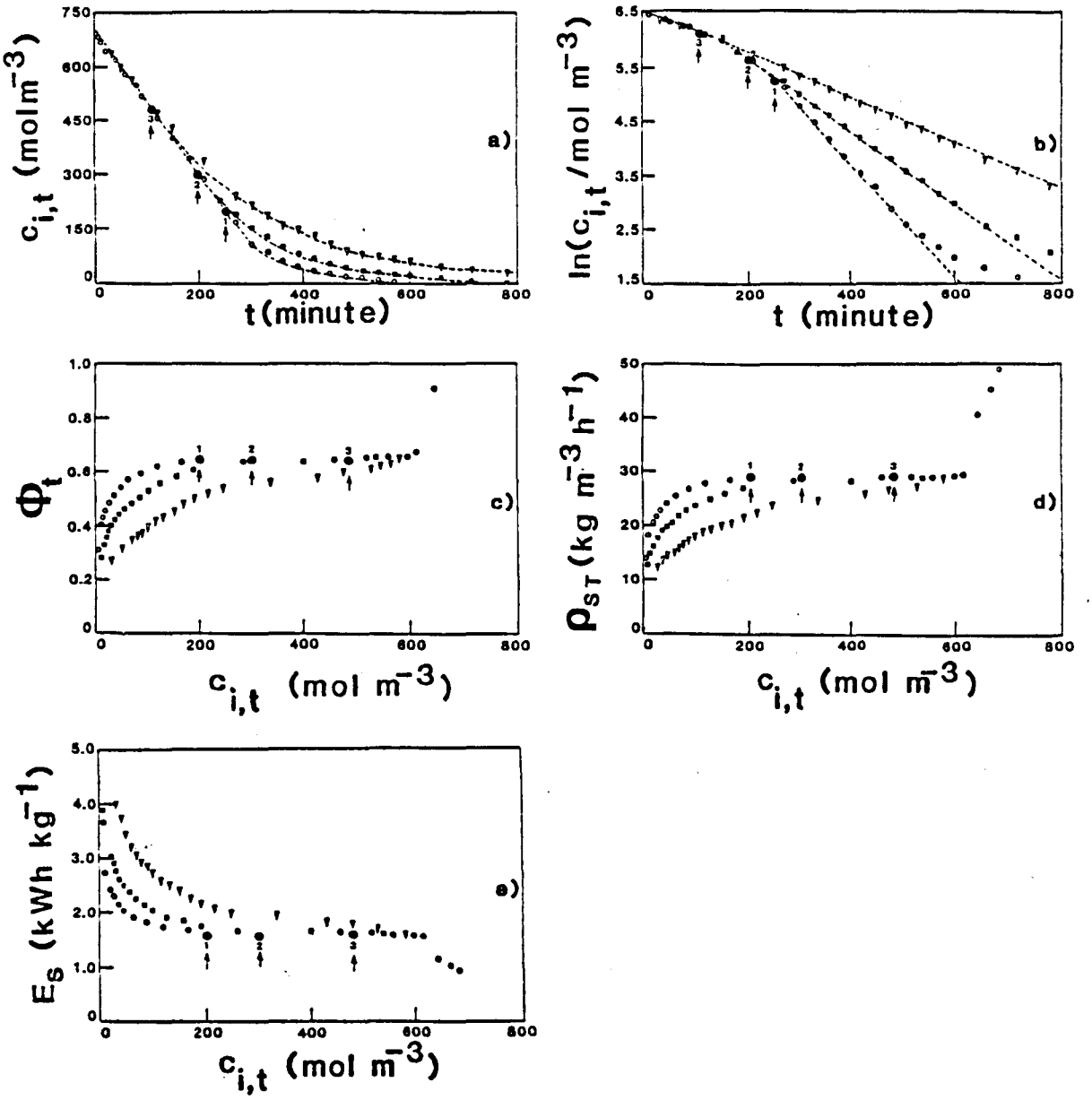

o $\bar{v}$ = 0.123 m s^{-1} ■ $\bar{v}$ = 0.066 m s^{-1} ∇ $\bar{v}$ = 0.033 m s^{-1}
● (t_{CRIT}, c_{CRIT}) for 1. $\bar{v}$ = 0.123 m s^{-1} 2. $\bar{v}$ = 0.066 m s^{-1} and
3. $\bar{v}$ = 0.033 m s^{-1}. ——— PREDICTED
i = 2,000 A m^{-2}. Expamet (orientation A) in the catholyte channel.

FIGURE 7.15 Effect of catholyte flowrate on L-cystine hydrochloride reduction at mercury plated copper.

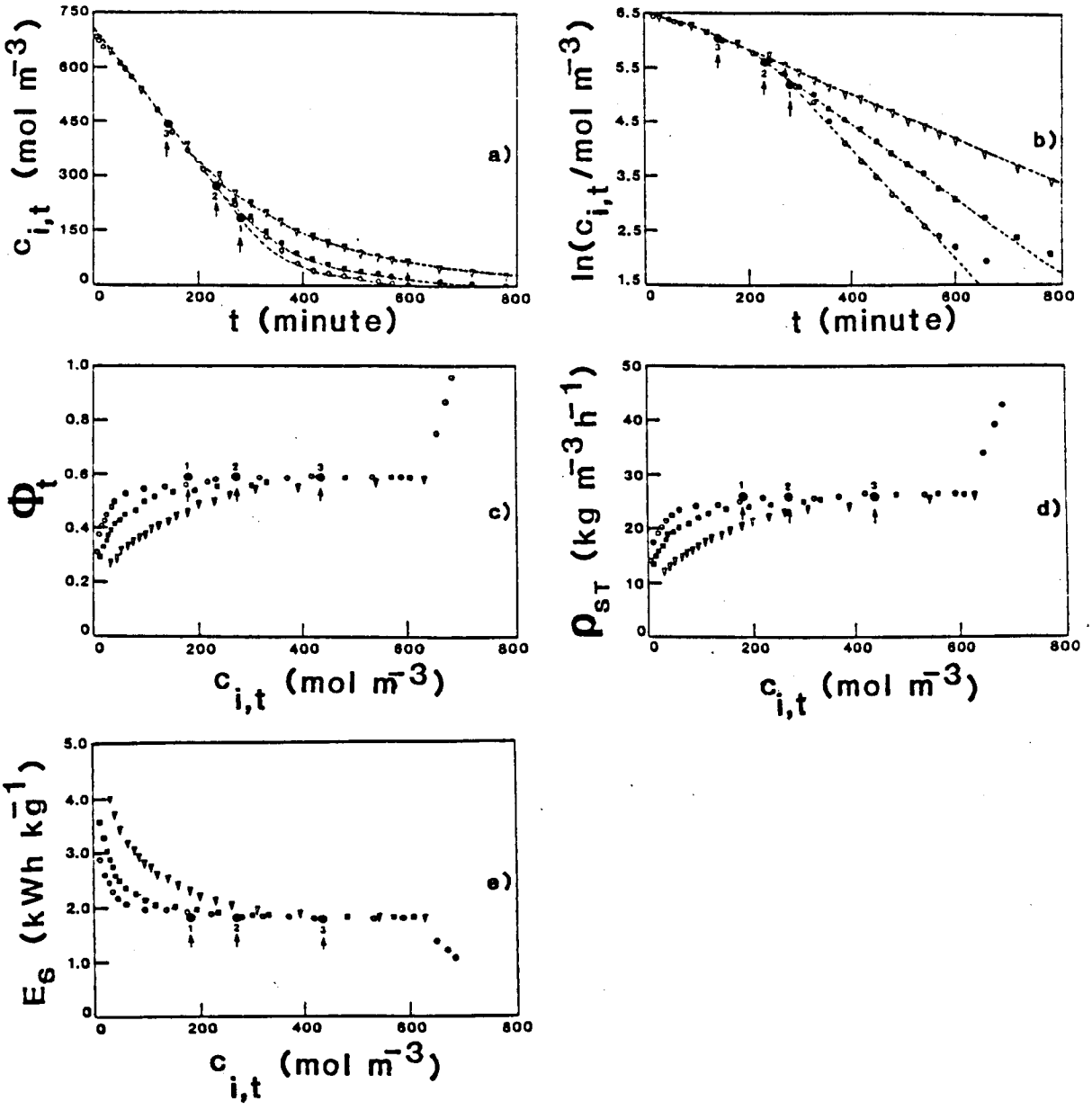

o $\bar{v}$ = 0.123 m s^{-1} ■ $\bar{v}$ = 0.066 m s^{-1} ∇ $\bar{v}$ = 0.033 m s^{-1}
● (t_{CRIT}, c_{CRIT}) for 1. $\bar{v}$ = 0.123 m s^{-1} 2. $\bar{v}$ = 0.066 m s^{-1} and
3. $\bar{v}$ = 0.033 m s^{-1}. ——— PREDICTED
i = 2,000 A m^{-2}. Expamet (orientation A) in the catholyte channel.

FIGURE 7.16 Effect of catholyte flowrate on L-cystine hydrochloride reduction at lead.

Indeed the time required for 99% reactant conversion is reduced from a value greater than 780 minutes to 600 minutes at mercury plated copper (Figure 7.15a) and to 660 minutes at lead (Figure 7.16a) as the catholyte velocity is increased from 0.066 m s^{-1} to 0.123 m s^{-1}. Economically this contraction in zone II is particularly important. This is emphasised if the figures of merit are plotted against the reactant concentration. As mass transport control of the reduction ensues there is a marked fall in the current efficiency (Figure 7.15c and 7.16c) and, consequently, in the space-time yield (Figure 7.15d and 7.16d) together with a pronounced rise in the specific energy consumption (Figure 7.15e and 7.16e). Most significantly, however, Figures 7.15 and 7.16 clearly show that it is towards the end of electrolyses, at low reactant concentrations, that the increased rate of mass transport gives figures of merit which become progressively much more economical. For example Table 7.2 shows the significant improvement in the figures of merit as the catholyte velocity is increased from 0.033 m s^{-1} to 0.123 m s^{-1} at an L-cystine hydrochloride concentration of 70 mol m^{-3}, which is equivalent to a reactant conversion of 0.90. At the higher catholyte velocity the current efficiency is 19 to 21% higher, which produces an increase in the space-time yield of between 8.7 kg m^{-3} h^{-1} and 10.1 kg m^{-3} h^{-1}, and the specific energy consumption is lowered by between 1.19 kWh kg^{-1} and 1.20 kWh kg^{-1}. Since the product specification demands greater than 99% reactant conversion, efficient mass transport of L-cystine hydrochloride is clearly of paramount importance to the process economics.

Considering the performance of this relatively small scale laboratory reactor, the space-time yields obtained are typical of parallel plate electrochemical reactors being, at best, an order of magnitude lower than comparable chemical reactors. The reactor is not, however optimised in terms of cell voltage, the components of

TABLE 7.2 Effect of catholyte velocity on the figures of merit at $X_{2,t}$ = 0.90. i = 2,000 A m^{-2}. Expamet (orientation A) in the catholyte channel.

Cathode	$\bar{v}$ (m s^{-1})	Φ_t (%)	ρ_{ST} (kg m^{-3} h^{-1})	E_s (kWh kg^{-1})
Mercury Plated Copper	0.033	34	15.2	3.22
	0.123	53	23.9	2.02
Lead	0.033	36	15.9	3.09
	0.123	57	26.0	1.90

which are given by equation (6.26).

$$E_{CELL} = -(E_e^C + |\eta^C|) - (E_e^A + |\eta^A|) - IR_{ELECTROLYTE} - IR_{MEMBRANE} - IR_{CIRCUIT} \quad (6.26)$$

or

$$E_{CELL} = E^C - E^A - IR_{ELECTROLYTE} - IR_{MEMBRANE} - IR_{CIRCUIT} \quad (7.39)$$

where E^C and E^A are the measured cathode and anode potentials at the applied current, I. Figure 7.17 shows the voltage balance for the cell at the beginning of electrolyses with a mercury plated copper and lead cathode. The cell voltage, cathode potential and anode potential were measured. The electrolyte resistance was estimated using equation (7.40) for the molar conductance of aqueous 2.0 mol dm^{-3} hydrochloric acid. The membrane and circuit resistances were obtained from equation (7.39) by difference.

$$\Lambda = \frac{1}{R_{ELECTROLYTE} \cdot A \cdot c}$$

or

$$281.4\ \Omega^{-1}\ cm^2\ mol^{-1}\ \text{at}\ 25^{\circ}C\ [22] = \frac{3.2}{R_{ELECTROLYTE} \cdot (100) \cdot (2.0 \times 10^{-3})} \quad (7.40)$$

where c is the concentration of hydrochloric acid (mol cm^{-3}), A is the cross-sectional area of the electrolyte channel (cm^2) and l is the interelectrode gap (cm). The electrolyte resistance ($5.7 \times 10^{-2}\ \Omega$ from equation 7.40) is enhanced

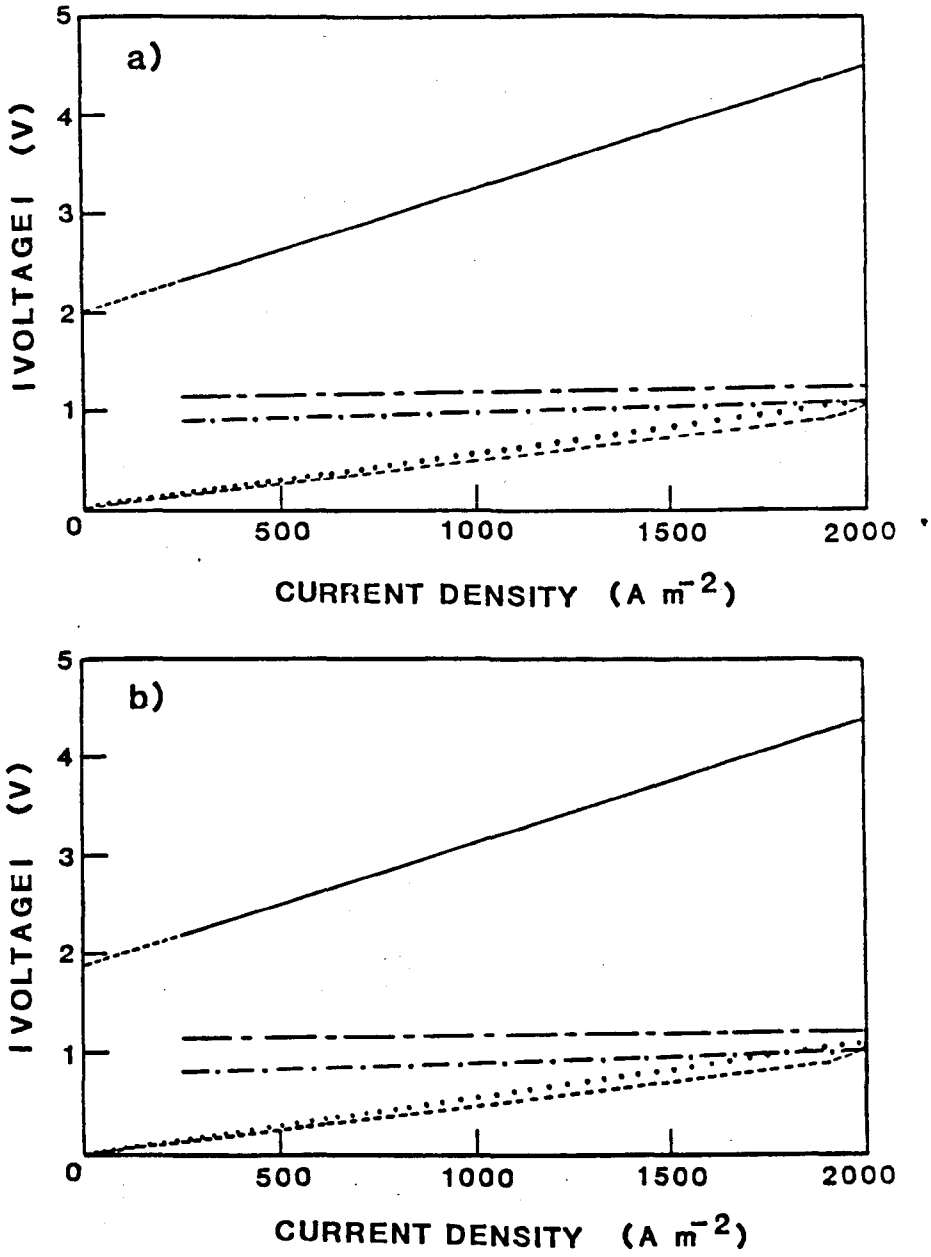

The cathode and anode potentials are corrected for the electrolyte resistance between the luggin capillary and the electrode surface.

FIGURE 7.17 Voltage balance for the cell with a) mercury plated copper and b) lead cathodes.

by the large interelectrode gap of 3.2 cm. In commercial cells the gap is often reduced to around 0.5 cm [6] which would lower the cell voltage in this reactor by 0.2 V at 500 A m^{-2}, 0.5 V at 1,000 A m^{-2} and 1.0 V at 2,000 A m^{-2}. Reducing the gap would, however, lower the upper limit of usable electrolyte flowrates, due to the greater pressure drop over the reactor which would limit the space-time yield for L-cystine hydrochloride reduction. Clearly, a balance between the interelectrode gap and the pressure drop is required.

Another related problem is the increase in the cell voltage (typically 0.5 V) during electrolysis, due to several factors. The anode potential increases as chloride ions are depleted and probably as oxygen evolution commences and competes with chlorine evolution. The cathode potential increases as L-cystine hydrochloride is depleted (see Figure 7.8), and the conductivity of the anolyte decreases as the concentration of hydrochloric acid is reduced. Although not the case in practice, assuming 100% current efficiency for chlorine evolution at the anode gives an indication of the time required for exhaustion of the anolyte i.e. 50 hours at 500 A m^{-2}, 25 hours at 1,000 A m^{-2} and 12.5 hours at 2,000 A m^{-2}. Timed additions of hydrochloric acid to the anolyte are important to minimise the increase in the anode potential and the anolyte resistance. In addition this prevents excessive oxygen evolution at the anode reducing the anode lifetime.

7.7.2 Effect of Expamet Turbulence Promoter

Electrosynthesis at the lead cathode in an empty catholyte channel was compared with the performance with the chamber completely filled by Expamet turbulence promoter (orientation A; see Section 6.4.4). The effect of the promoter for electrolysis at a current density of 2,000 A m^{-2} and a catholyte flowrate of 0.066 m s^{-1} is shown in Figure 7.18. The effect is similar to that obtained by increasing the catholyte flowrate through the cell (see Section

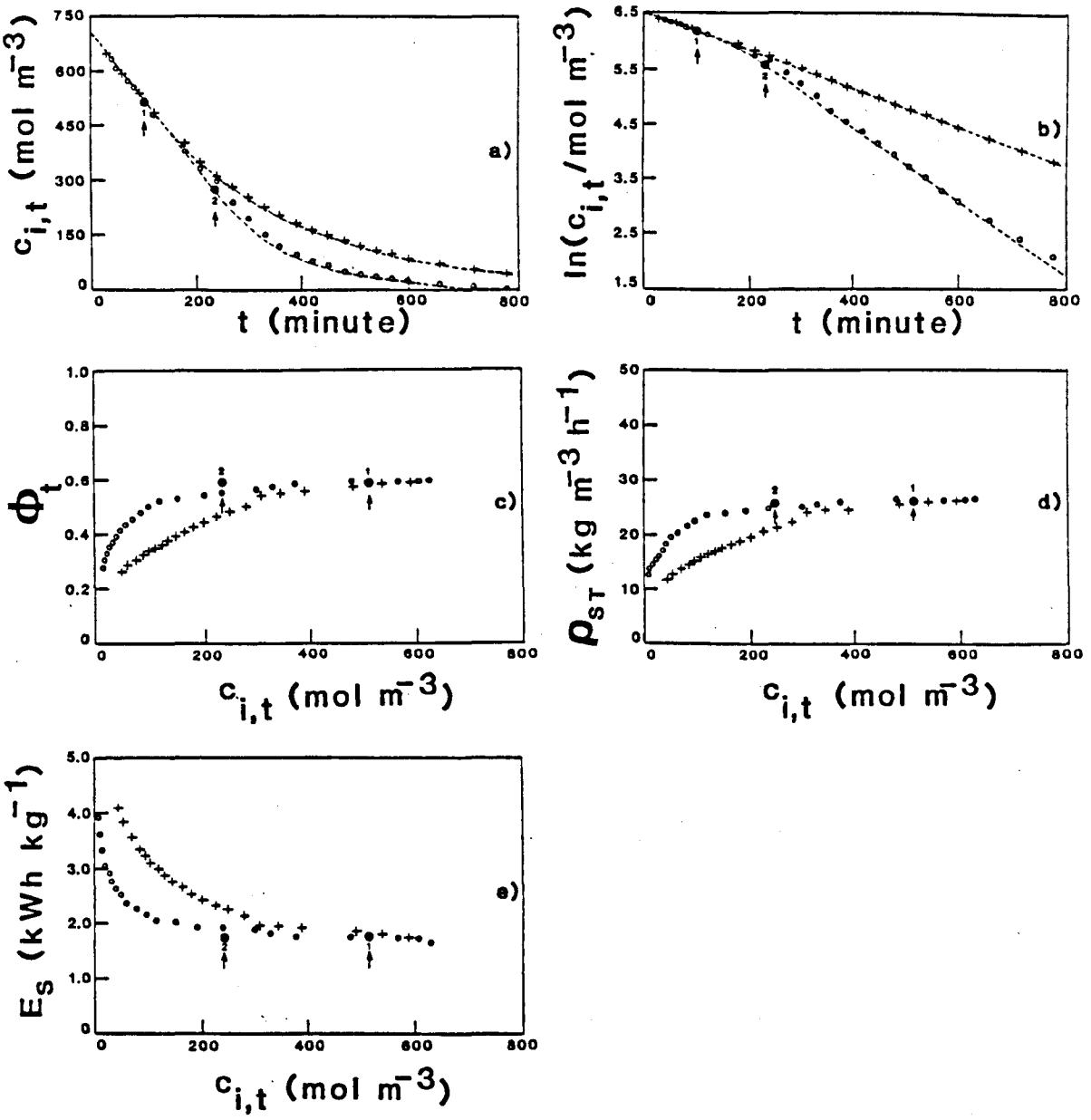

o Catholyte filled with Expamet (orientation A) + Empty catholyte channel

----- PREDICTED ● (t_{CRIT},c_{CRIT}) for 1. empty channel and 2. turbulence promoter in the catholyte channel.

i = 2,000 A m^{-2} and $\bar{v}$ = 0.066 m s^{-1}.

FIGURE 7.18 Effect of Expamet turbulence promoter on L-cystine hydrochloride reduction at lead.

7.7.1). Expamet moves (t_{CRIT}, c_{CRIT}) from (102 minutes, 269 mol m^{-3}) to (235 minutes, 269 mol m^{-3}) and increases the rate of reactant concentration decay in zone II, as shown by an increase in the magnitude of the slope of the ln $c_{i,t}$ versus t graph in zone II (Figure 7.18b). From the slopes K_L is increased from 1.20 x 10^{-5} m s^{-1} to 2.28 x 10^{-5} m s^{-1}, which is close to the doubling of the rate of mass transport predicted by the limiting current measurements for the enhancement by Expamet in this orientation (see Figure 6.7). As shown in Section 7.7.1 the net result is a contraction of zone II which produces a significant reduction in the batch processing time. The time required for 99% reactant conversion is reduced from greater than 780 minutes in the empty channel to 720 minutes with Expamet (Figure 7.18a). Consequently the current efficiency (Figure 7.18c), and therefore the space-time yield (Figure 7.18d), and the specific energy consumption (Figure 7.18e) all become progressively much more economical towards the end of the electrolysis, in the presence of Expamet. For example Table 7.3 shows the significant improvement in the figures of merit at an L-cystine hydrochloride concentration of 70 mol m^{-3} which is equivalent to a reactant conversion of 0.90. The current efficiency is 15% higher, the space-time yield raised by 7.1 kg m^{-3} h^{-1} and the specific energy consumption is lowered by 1.27 kWh kg^{-1}. Clearly, there is a significant economic benefit to be gained from the inclusion of Expamet in the catholyte channel. Turbulence promoters do, however, increase the pressure drop in reactors and thereby increase the pumping costs. They can also exhibit other disadvantages in adverse cases as detailed in Section 6.4.4.

TABLE 7.3 Effect of Expamet (orientation A) on the figures of merit at a lead cathode for $X_{2,t}$ = 0.90.

i = 2,000 A m^{-2} and $\bar{v}$ = 0.066 m s^{-1}.

Turbulence Promoter	Φ_t (%)	ρ_{ST} (kg m^{-3} h^{-1})	E_s (kWh kg^{-1})
Expamet (Orientation A)	46	20.9	2.33
Empty channel	31	13.8	3.60

7.7.3 Stability of the Cathode Materials

The surface of the mercury plated copper cathode was prepared on a daily basis since current efficiencies for L-cystine hydrochloride reduction were reduced by 30 to 40% after 24 hours. Current-potential curves in aqueous 2.0 mol dm^{-3} hydrochloric acid, with a fresh and used cathode, confirmed the overpotential for hydrogen evolution is substantially reduced on aged cathodes. This is attributed to the diffusion of copper atoms to the mercury rich surface. Indeed, batch electrolyses even on fresh cathodes are almost certainly performed on an amalgamated surface. Evidence for this was provided by electrolysis at a specifically prepared fresh, amalgamated copper cathode (see Section 5.1.3) which gave essentially identical electrosynthesis results to fresh mercury plated copper cathodes.

The performance of the lead cathode was examined over 168 hours continuous operation. Lead chloride was detected on the electrode surface by ex-situ XRD analysis [23], suggesting some corrosion occurred. A serious problem emerged after 72 hours operation. Current efficiencies fell by up to 20%. Current-potential curves in aqueous 2.0 mol dm^{-3} hydrochloric acid, with fresh and used cathodes,

confirmed promotion of hydrogen evolution on the aged cathode. This may be due to electroplating of trace metal impurities from the catholyte onto the cathode surface. BDH Analar grade hydrochloric acid may contain a variety of metals at levels of 0.01 ppm to 0.5 ppm [24]. This effect has been observed previously for lead cathodes in electroorganic syntheses [25]. There may also be an effect, however, from the lead chloride film. This is an area which merits further study.

The stability problems observed for mercury plated copper and lead cathodes are specific examples of a general problem often associated with electroorganic syntheses i.e. the inability of electrode materials to maintain electrocatalytic activity and durability during the long term performance demanded by process economics. Another problem associated with the cathodes is the presence of between 1 ppm and 2 ppm of mercury(II) or lead(II) ions (determined by ICP-MS [26]) in batches of the product obtained during these long term studies. The toxicity of mercury requires the removal of the mercury(II) ions before the product can be sold and it is likely for some applications (e.g. in certain foodstuffs and pharmaceuticals) that the lead(II) ions may also have to be removed. This presents not only an economic disadvantage but a technical challenge. As a result of these difficulties although L-cysteine hydrochloride can be synthesised efficiently at mercury plated copper and lead, for industrial manufacture an alternative cathode would be preferred.

7.8 CONCLUSIONS

The simple mathematical models adequately predict the reactant concentration decay in the reactor at mercury plated copper (Figure 7.5) and lead (Figure 7.6) cathodes, thereby allowing examination of the optimum working conditions of the

reactor. As is the case with many batch recycle operations of this type the sytem can be treated as a simple batch reactor (Table 7.1). All three diagnostic plots shown in Figure 7.3 should be used to identify the zones of behaviour.

The reactant concentration decay in zone II at the cathodes can be used to determine the average mass transport coefficient in the reactor, from the straight line plot of ln $c_{i,t}$ against t (equation 7.32). Comparison of values obtained using the models with those determined using the diffusion limited current technique show acceptable agreement (Figure 7.10).

At both cathodes L-cysteine hydrochloride can be synthesised with essentially a quantitative chemical yield to give a product with less than 1% w/w of the disulphide as required by the product specification (Table 1.3). Industrially significant current densities can be achieved with acceptable current efficiences. The optimum current density is 500 A m^{-2} if batch processing times are acceptable (Figures 7.13, 7.14 and 7.17). The mass transport in the reactor should be maximised by the use of high catholyte flowrates and the inclusion of turbulence promoters in the catholyte channel (e.g. Figures 7.15, 7.16 and 7.18). This is particularly imporant to the process economics since, under mass transport control, the figures of merit become less economical (e.g. Figures 7.11 and 7.12).

A comparison of the performance of mercury and lead, at a given current density and catholyte flowrate, shows the figures of merit are slightly less economical at lead (e.g. Table 7.2). There is, however, little to choose between the cathodes. Problems of cathode stability (Section 7.7.3) suggest for industrial manufacture an alternative electrode material would be preferred. A number of alternative materials have been examined (Chapter 8). At lead the relative role of trace metal contaminants in the catholyte and lead chloride film formation upon the cathode, in reducing the current efficiency for disulphide reduction, is an area

which merits further study. Extraction of metal contaminants and/or periodical scraping of the cathode surface might be beneficial.

During electrolysis the addition of hydrochloric acid to the anolyte is important to prevent an excessive increase in the cell voltage and an attendant reduction in the anode lifetime due to copious oxygen evolution. The cell design could easily be modified, by reducing the interelectrode gap, to achieve a balance between cell voltage and increased pumping costs.

REFERENCES

1. Conway B.E., Tilak B.V. & Novak D.M. in "Modern Aspects of Electrochemsitry No. 14". Eds. Bockris J. O'M., Conway B.E. & White R.E., Plenum Press, New York (1982). Chapter 4.
2. Millington J.P. Personal Communication.
3. Asaki T., Kamegaya Y. & Takayasu K.; *J. Electrochem. Soc.* 132, 1895, (1985).
4. Spaziante P.M. "Electrodes and Electrode Reactions". Electrochemical Process Engineering Course, University of Newcastle upon Tyne, 6-11th. July (1975).
5. Walsh F.C. 4th. International Symp. on Frontiers of Electrochemistry, Madras, India, 14-16th. November (1989).
6. Pletcher D. & Walsh F.C. "Industrial Electrochemistry". Chapman and Hall, London (1990).
7. Pickett D.J. "Electrochemical Reactor Design". 2nd Edition, Elsevier, Amsterdam (1979).
8. Coeuret F. & Storck A. "Elements de Genie Electrochimique". Tecdoc, Paris (1984).
9. Heitz E. & Kreysa G. "Princples of Electrochemical Engineering". VCH, Weinheim (1986).
10. Danly D.E. "Emerging Opportunities for Electroorganic Processes". Marcel Dekker, New York (1986).
11. Walsh F.C.; *Inst. Chem. Eng. Symp. Series No. 98*, 137, (1986).
12. Granados-Enriquez M., Valentin G. & Storck A.; *Electrochim. Acta* 28, 1407, (1983).
13. Cooley A.C.; *J. Applied Phot. Eng.* 8, 171, (1982).

14. Storck A. & Hutin D.; *Electrochim. Acta* 26, 117, (1981).

15. Walker A.T.S. & Wragg A.A.; *Electrochim. Acta* 22, 1129, (1977).

16. Appleby A.J., Kita H., Chemla M. & Bronoel G. in "Encylopedia of Electrochemistry of the Elements". Ed. Bard A.J., Marcel Dekker, New York (1982). Volume IX Part A, 413-556.

17. Arvia A.J., Marchiano S.L. & Podesta J.J.; *Electrochim. Acta* 12, 259, (1967).

18. Atkins P.W. "Physical Chemistry". 3rd Edition, Oxford University Press, Oxford (1986). Page 24.

19. Birkett M.D. & Kuhn A.; *Electrochim. Acta* 22, 1427 (1977).

20. Millington J.P. Personal Communication (The analysis was performed under contract for the Electricity Research and Development Centre).

21. Dawson R.M.C., Elliott D.C., Elliott W.H. & Jones K.M. "Data for Biochemical Research". Clarendon Press, Oxford (1986). Pages 12 and 13.

22. "Handbook of Chemistry and Physics". Eds. Weast R.C. & Astle M.J. 61st Edition, CRC Press, Florida (1980-81). Page D-171.

23. Kelly E.H.; *Electricity Research and Development Centre Research Report 0273*, April (1988).

24. BDH Chemicals Catalogue (1991).

25. Hayes M. & Kuhn A.T. in "Electrochemistry of Lead". Ed. Kuhn A.T., Academic Press, New York (1979). Chapter 8.

26. Ash P.; *Johnson Matthey Technology Centre Report M014*, May (1989).

CHAPTER 8

ELECTROSYNTHESIS AT OTHER CATHODES

8.1 THE ELECTROSYNTHESIS SYSTEM

A number of alternative cathode materials (i.e. titanium, tin, carbon, stainless steel, copper, nickel and molybdenum) were examined in the parallel plate reactor. Electrosynthesis was performed with the system described in Chapter 7 (Section 7.1) and the major cell processes are shown in Figure 7.1.

8.2 MATERIAL YIELD AND SELECTIVITY

The electroreduction of L-cystine hydrochloride to L-cysteine hydrochloride is possible at all the cathodes examined. A mass balance based upon the cathode reaction (reaction 3.04) suggests the material yield and selectivity for the product is at least 99% at all the metals. Thin layer chromatography [1] confirmed other amino acids are not produced. All current losses are, consequently, ascribed to hydrogen evolution.

$$RSSR.2HCl + 2H^+ + 2e^- \longrightarrow 2RSH.HCl \qquad (3.04)$$

For exhaustive electrolyses the optical rotation ($[\alpha]_D^{25^oC}$ = +6.5° for a concentration of 20 g dm^{-3} in 5 mol dm^{-3} hydrochloric acid) and melting point (176-178°C) of the product are in accord with the literature [2], indicating the product contains less than 1% of unconverted reactant. At nickel and molybdenum cathodes exhaustive electrolysis is not possible on the time scale of the experiments (13 hours) because of the low rates of reduction achieved in the reactor. Consequently the product is contaminated with large quantities of L-cystine hydrochloride, which produces a negative optical rotation ($[\alpha]_D^{25^oC}$ $\leq -10^o$ for a concentration of 20 g dm^{-3} in 5 mol dm^{-3} hydrochloric acid) and a suppressed and extended melting point range (155-160°C).

8.3 ABILITY OF THE MODELS TO PREDICT THE EXPERIMENTAL RESULTS

At the alternative cathodes, the simple models outlined in Section 7.3 do not predict the reactant concentration decay throughout batch electrolyses, as shown in Figure 8.1. As in the case of mercury plated copper and lead there is a start-up period where abnormally high rates of reduction are measured. This apparent conditioning of the electrode surfaces is a common phenomenon [3]. Following this a region of zone I behaviour is observed where the reduction is under charge transfer control as predicted by the models. The rate of reactant concentration decay is constant and given by equation (7.09).

$$c_{i,t} = c_{i,o} - \frac{\Phi_{CRI}\, T\, I\, t}{nFV_T} \qquad (7.09)$$

At molybdenum only zone I behaviour is observed whilst at nickel zone I followed by the start of a mixed kinetic-mass transport control region is evident (Figure 8.1f). The reactant concentration is not reduced sufficiently during electrolyses to observe other zones of behaviour, because of the low current efficiences for the disulphide reduction at these cathodes.

At the remaining cathodes there is a region of mixed kinetic-mass transport control after zone I, which persists to very low reactant concentrations irrespective of the electrolysis conditions. For example, at titanium, tin, carbon, stainless steel and copper (Figures 8.1a to 8.1e respectively) mixed control persists until the L-cystine hydrochloride concentration falls below 60 mol m^{-3}. After this mixed region there is a short period of zone II behaviour before zone III which is evident below 10 mol m^{-3} L-cystine hydrochloride.

For the alternative cathodes the onset of complete mass transport controlled reduction (zone II) may be determined from the plot of ln $c_{i,t}$ against t (e.g.

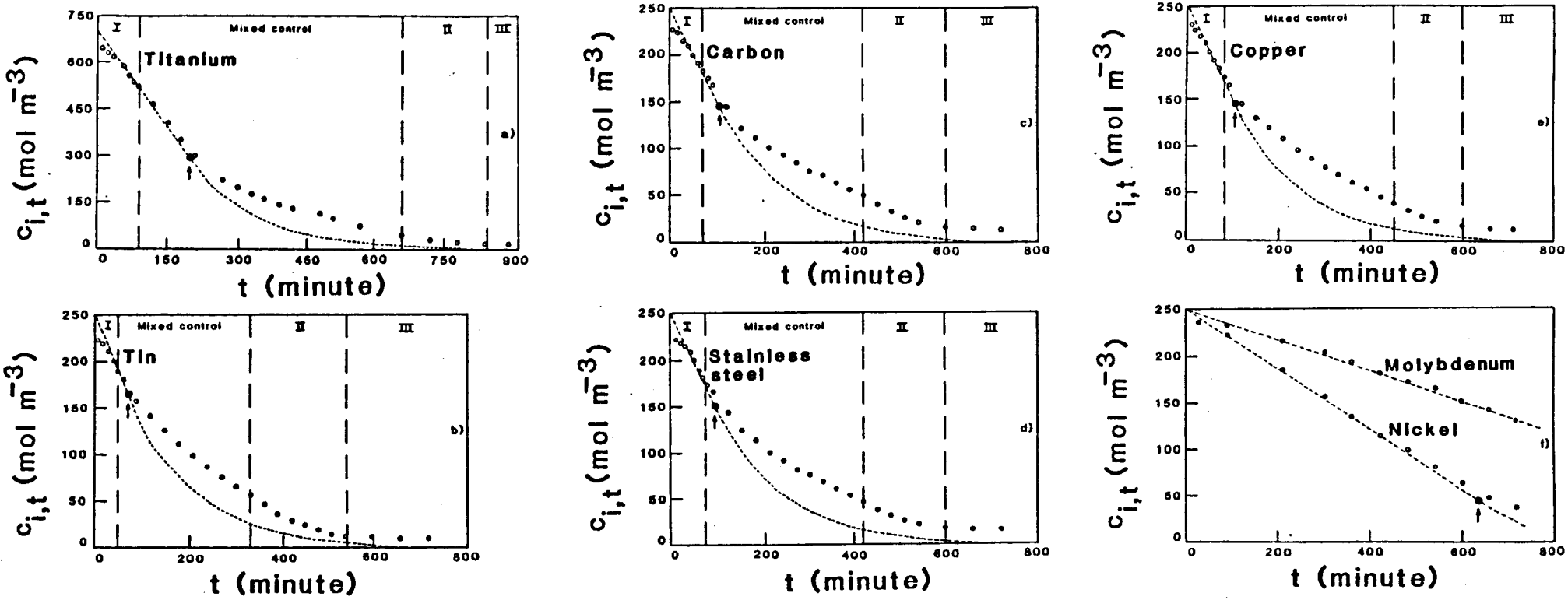

----- PREDICTED ● (t_{CRIT}, c_{CRIT})

i = 2,000 A m^{-2} and $\bar{v}$ = 0.066 m s^{-1}. Expamet (orientation A) in the catholyte channel.

FIGURE 8.1 Ability of the models to predict the experimental results.

reduction (zone II) may be determined from the plot of ln $c_{i,t}$ against t (e.g. Figure 8.2 shows a typical plot for electrolysis at a tin cathode which suggests pure mass transport control ensues at (330 minutes, 58 mol m^{-3}). Perhaps a more accurate method of determining the onset of zone II, however, since it is quantitative rather than relying upon visual inspection of the data, is to use equation (8.01) (a modification of equation 7.31) which allows the concentration decay for pure mass transport control to be calculated for any given time interval $(t_2 - t_1)$, provided K_L is known. Fortunately, K_L can be obtained from the magnitude of the slope of the ln $c_{i,t}$ against t plot in zone II.

$$c_{I,t(2)} = c_{I,t(1)} \exp\left(- \frac{X_{1,t}}{\tau_T} [t_2 - t_1] \right) \qquad (8.01)$$

Table 8.1 shows for the electrolysis at tin in Figure 8.2 the comparison between the reactant concentration values predicted by equation (8.01), for successive reactant sample times, and the experimentally measured values. This confirms the onset of pure mass transport controlled reduction of L-cystine hydrochloride at (330 minutes, 58 mol m^{-3}). Combination of the ln $c_{i,t}$ against t plot and equation (8.01) was used to determine the onset of pure mass transport control at all the alternative cathodes.

In zone II at the alternative cathodes although the reactant concentration decays exponentially, as suggested by equation (7.29) for pure mass transport control via convective-diffusion, the predicted concentration values are much lower than those obtained experimentally (Figure 8.1).

$$c_{I,t} = c_{CRIT} \exp\left(- \frac{X_{1,t}}{\tau_T} [t - t_{CRIT}] \right) \qquad (7.29)$$

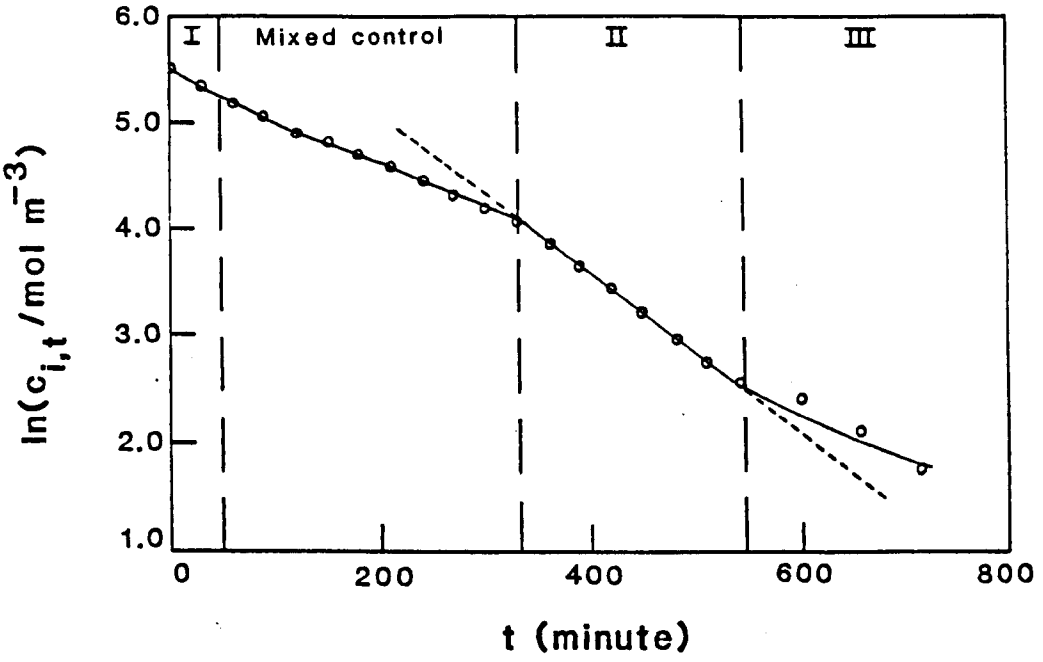

i = 2,000 A m^{-2} and $\bar{v}$ = 0.066 m s^{-1}. Expamet (orientation A) in the catholyte channel.

FIGURE 8.2 Plot of ln $c_{i,t}$ against t for electrolysis at tin.

TABLE 8.1 Comparison of experimental and predicted reactant concentration decay for complete mass transport controlled reduction of L-cystine hydrochloride at a tin cathode.

i = 2,000 A m^{-2} and $\bar{v}$ = 0.066 m s^{-1}. Expamet (orientation A) in the catholyte channel. K_L is 3.36 x 10^{-5} m s^{-1} and $X_{1,t}$ 1.365 x 10^{-3}.

Time (s)	(t_2-t_1) (s)	Experimental $c_{i,t}$ (mol m^{-3})	Predicted $c_{i,t}$ from equation (8.02) (mol m^{-3})	Zone
0	-	250	-	I
3600	1800	180	201	
5400	"	159	145	
7200	"	142	128	
9000	"	127	115	
10800	"	112	103	Mixed
12600	"	99	90	
14400	"	88	80	
16200	"	77	71	
18000	"	67	62	
19800	"	58	54	
21600	"	47	47	
23400	"	38	38	II
25200	"	31	31	
27000	"	25	25	
28800	"	20	20	
30600	"	16	16	
32400	"	13	13	
36000	3600	11	9	
39600	"	9	6	III
43200	"	6	4	

This is a result of the significant region of mixed control between zones I and II. To obtain the correct concentration values, the point (t_{CRIT}, C_{CRIT}) has to be adjusted to the time and reactant concentration corresponding to the onset of zone II (e.g. at tin in Figure 8.1b, as shown in Table 8.1 (t_{CRIT}, C_{CRIT}) is (330 minutes, 58 mol m^{-3}) compared with a value of (72 minutes, 166 mol m^{-3}) predicted by the model). In this case (t_{CRIT}, C_{CRIT}) is best determined from the plot of ln $c_{i,t}$ against t and by the application of equation (8.01) as described above. This behaviour is in contrast to that observed at mercury plated copper and at lead cathodes where there is also a mixed control region but the model does predict the reactant concentration decay in zone II (e.g. Figures 7.5 and 7.6). This is probably because mixed control lasts for a shorter time and is of a much reduced degree over this time period at mercury plated copper and lead.

As constant current electrolysis proceeds and L-cystine hydrochloride is depleted from the catholyte, the cathode potential (which is a mixed potential controlled by the amino acid reduction and hydrogen evolution) moves cathodically. This potential shift maintains the current density by increasing the relative quantity of hydrogen evolved. At mercury plated copper and lead cathodes a high hydrogen overpotential results in a much larger shift in cathode potential during electrolysis than at the other lower hydrogen overpotential cathodes (e.g. Table 8.2). The list, in Table 8.3, of exchange current densities for hydrogen evolution at the metals in aqueous 1.0 mol dm^{-3} sulphuric acid (data in hydrochloric acid is scarce) highlights the appreciably slower kinetics of gas evolution at mercury plated copper and lead. Figure 8.3 attempts to show, schematically, the effect of the variation in the hydrogen evolution kinetics on the current-potential curves for the total cell current for the two cases. At the low hydrogen overpotential metals there is a positive potential shift in the current-potential curves for the

Table 8.2 Change in the cathode potential during batch electrolysis. $i = 2{,}000$ A m^{-2} and $\bar{v} = 0.066$ m s^{-1}. Expamet turbulence promoter (orientation A) in the catholyte channel.

Cathode	$-E_{CATHODE}$ (V vs SCE) Initial	[a]Final	$X_{2,t}$ at the Final Cathode Potential	$\Delta E_{CATHODE}$ (mV)
Mercury Plated Copper	1.045	1.253	0.936	208
Lead	1.024	1.235	0.941	211
Titanium	0.962	1.060	0.963	98
Tin	0.870	0.952	0.948	82
Carbon	0.807	0.869	0.916	62
Stainless Steel	0.711	0.768	0.920	57
Copper	0.679	0.758	0.916	79

[a] This is the cathode potential corresponding to the fractional conversion in the reservoir listed in the next column.

TABLE 8.3 Exchange current densities for hydrogen evolution in aqueous 1.0 mol dm^{-3} H_2SO_4[4-7].

Metal	Log (i_o/A m^{-2})
Mercury	-8.6, -8.5, -7.9, -7.6
Lead	-8.6, -8.2, -7.3
Titanium	-4.2, -2.9
Tin	-5.3, -5.2, -4.7
Carbon	not available
Copper	-3.4, -2.7, -2.5
Iron	-2.0, -1.9, -1.8
Chromium	-3.4, -2.4
Nickel	-2.3, -1.3, -1.2
Molybdenum	-2.5, -2.2

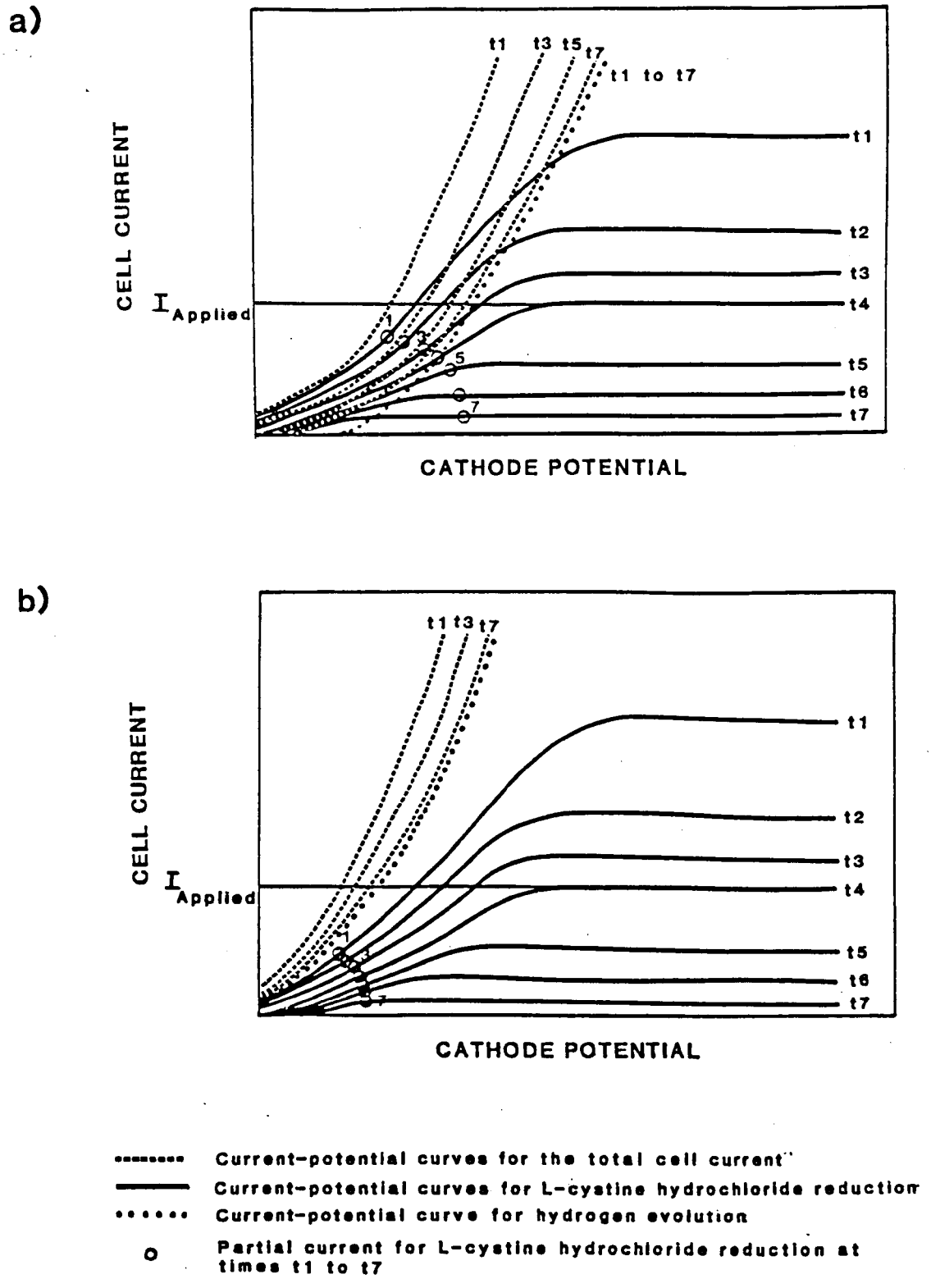

FIGURE 8.3 Schematical change in current-potential curves during constant current batch electrolysis at a) high and b) low hydrogen overpotential cathodes.

total cell current (as a result of the similar shift in the current–potential curve for hydrogen evolution) relative to the irreversible wave for L–cystine hydrochloride reduction. Consequently during electrolysis the partial currents for L–cystine hydrochloride reduction correspond to a cathode potential at which the disulphide reduction is under a greater degree of mixed control for a longer time at the low hydrogen overpotential metals. This is indicated schematically by the comparison between Figure 8.2b and 8.2a. At the low hydrogen overpotential metals pure mass transport control is not evident until $t = t_7$ (Figure 8.2b) but at the high hydrogen overpotential metals at $t = t_5$ (Figure 8.2a) the reduction is almost under complete mass transport control.

Some experimental evidence for this explanation is provided by plotting the interval partial currents for L–cystine hydrochloride reduction against the cathode potential during batch electrolysis at the metals. Figure 8.4 shows typical plots for lead and carbon (representative of the alternative cathodes). There is some scatter in the data since interval current efficiencies have been used to calculate the partial currents but the general shape of the graphs is as predicted schematically in Figure 8.3. Of course what is not known is the exact shape of the current–potential for reduction of the amino acid at the different metals. In Figure 8.3 an identical wave shape for the current–potential curves at all cathode materials has been assumed.

Although the simple models do not predict the reactant concentration decay in zone II at the cathodes, the average mass transport coefficient in the cell can still be determined from the magnitude of the slope of the $\ln c_{i,t}$ against t graph in zone II. Table 8.4 shows that a reasonable agreement is obtained between the K_L values obtained at all cathodes. Consequently, any variation in electrode surface roughness and the different quantitites of hydrogen evolved at the

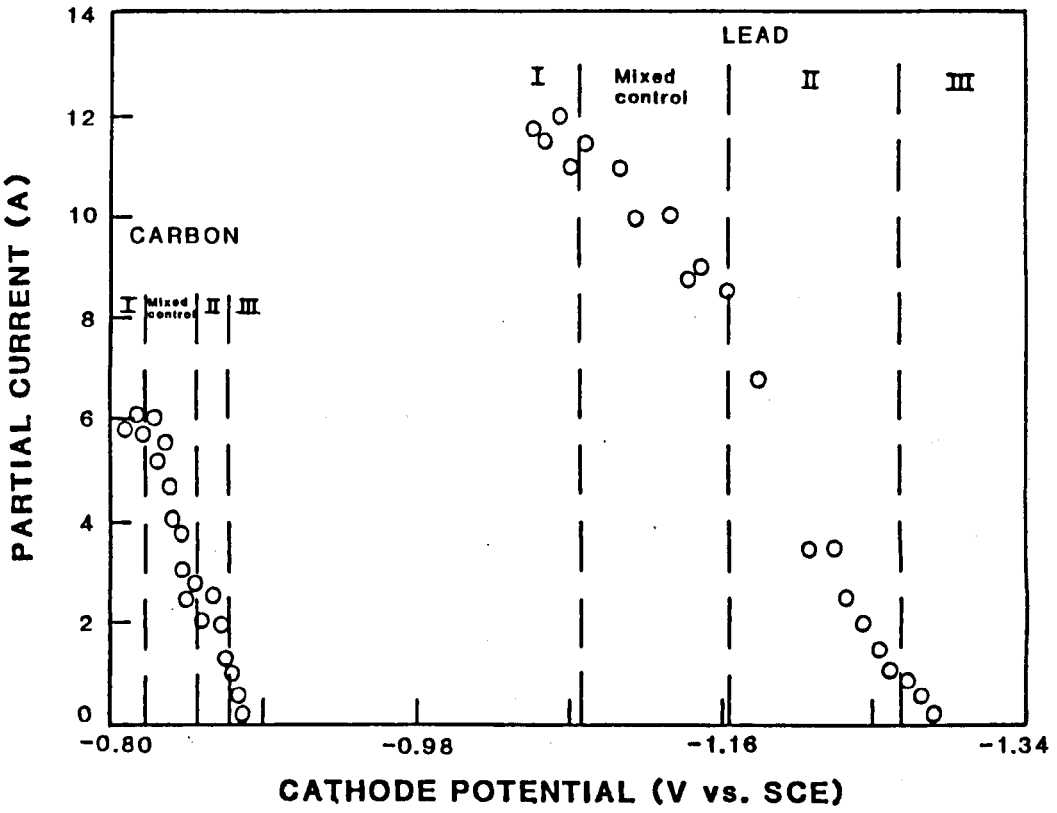

i = 2,000 A m^{-2} and $\bar{v}$ = 0.066 m s^{-1}. Expamet (orientation A) in the catholyte channel.

FIGURE 8.4 Variation of partial current for L-cystine hydrochloride reduction with cathode potential during batch electrolysis at lead and carbon cathodes.

electrodes, which are known to effect rates of mass transport [8], has little effect. This is perhaps not unexpected since the catholyte contains Expamet (orientation A) turbulence promoter which approximately doubles the average mass transport coefficient in the reactor and, as shown in Chapter 6, the flow in the reactor is turbulent even in the empty catholyte channel. Consequently the rate of mass transport is high over the complete range of electrolyte flow rates used.

TABLE 8.4 Comparison of the average mass transport coefficients obtained from batch electrolyses at the cathodes.

i = 2,000 A m^{-2}. Expamet (orientation A) in the catholyte channel.

Cathode	Average Mass Transport Coefficient $K_L \times 10^{-5}$ (m s^{-1}) for various Nominal, Average Linear Catholyte Velocities $\bar{v}$ (m s^{-1})		
	0.123 m s^{-1}	0.066 m s^{-1}	0.033 m s^{-1}
Mercury Plated Copper	3.48	2.27	1.40
Lead	3.41	2.28	1.40
Titanium	3.38	2.36	1.42
Tin	3.36	2.38	1.41
Carbon	3.33	2.30	not available[a]
Stainless steel	3.35	2.26	not available[a]
Copper	3.35	2.29	not available[a]

[a]The reactant concentration is not reduced sufficiently during electrolysis to observe zone II behaviour.

8.4 EFFECT OF THE MAJOR PROCESS VARIABLES ON THE ELECTROSYNTHESIS

The optimum conditions for the electrosynthesis at each metal, in terms of selected figures of merit, was determined by a parametric study of the effects of current density and catholyte flowrate. In all electrolyses Expamet (orientation A) turbulence promoter filled the catholyte channel to reduce electrolysis times.

8.4.1 Effect of Current Density

As noted previously in Chapter 7 the effect of current density is best examined in zone I where mass transport has no effect on the performance. At a fractional conversion in the reservoir of 0.20 zone I behaviour is evident at all metals. For all cathodes, apart from titanium which is anomalous, at this fractional conversion there is a similar response to a lowering of the current density from 2,000 A m^{-2} to 500 A m^{-2}. The batch processing time increases as shown by a decrease in the space-time yield (Figure 8.5a). This is offset by an increase in the current efficiency (Figure 8.6a), due to decreasing rates of hydrogen evolution, which coupled with a reduction in the cell voltage (Figure 8.7a) reduces the specific energy consumption (Figure 8.8a). None of the alternative cathodes which show this behaviour, however, give figures of merit which are equivalent to those for mercury plated copper or lead over the range of commercially useful current densities examined.

With the exception of titanium, the metals show the same order in terms of performance based upon the figures of merit, at all current densities. The order of decreasing performance is mercury plated copper, lead, tin, carbon, stainless steel, copper, nickel and molybdenum. Consideration of the exchange current densities for hydrogen evolution at the metals (Table 8.3) suggets it is the hydrogen overpotential which principally grades the performance of the cathodes,

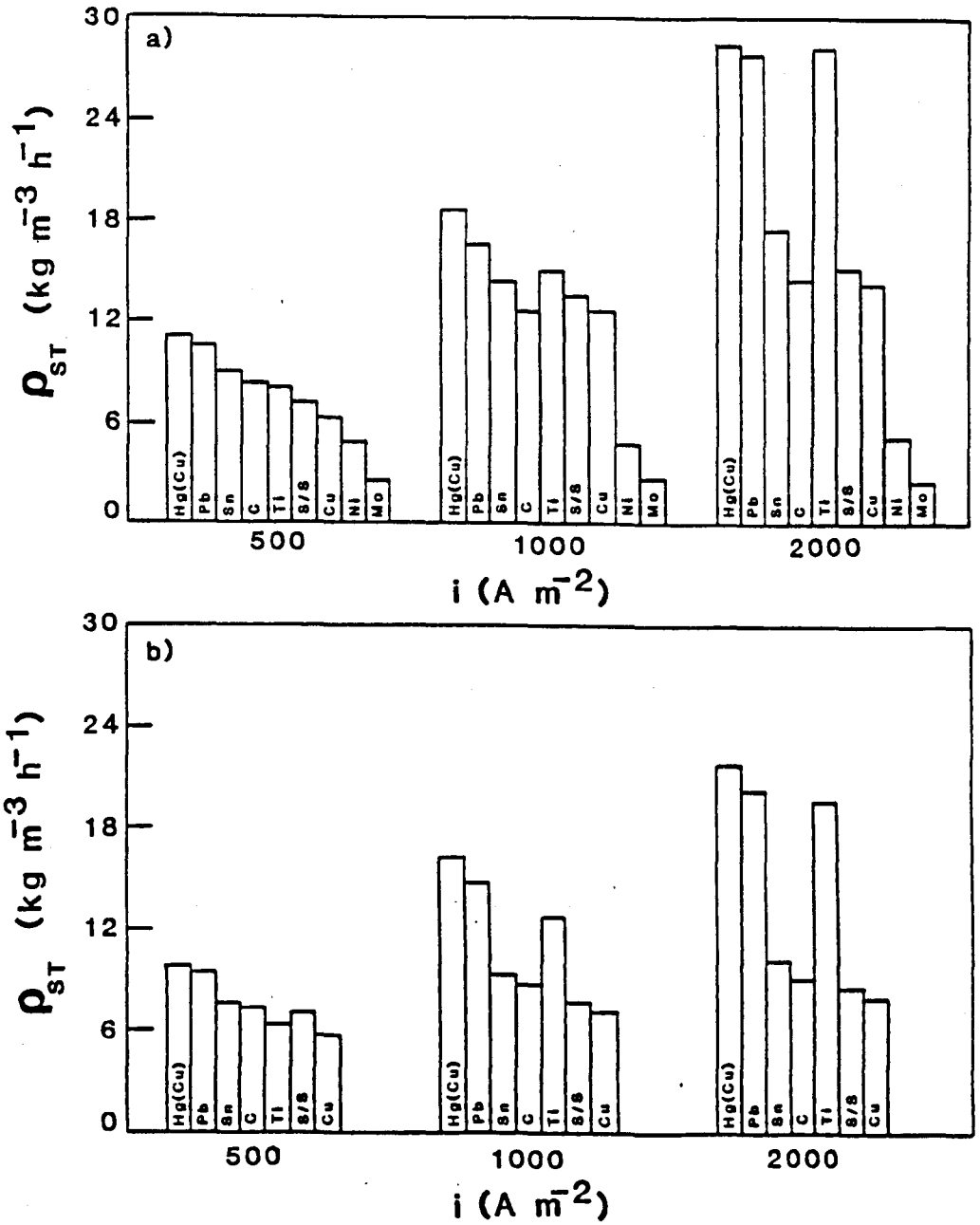

$\bar{v}$ = 0.123 m s^{-1}. Expamet (orientation A) in the catholyte channel.

FIGURE 8.5 Effect of current density on the space-time yield at the cathodes for a) $X_{2,t}$ = 0.20 and b) $X_{2,t}$ = 0.90.

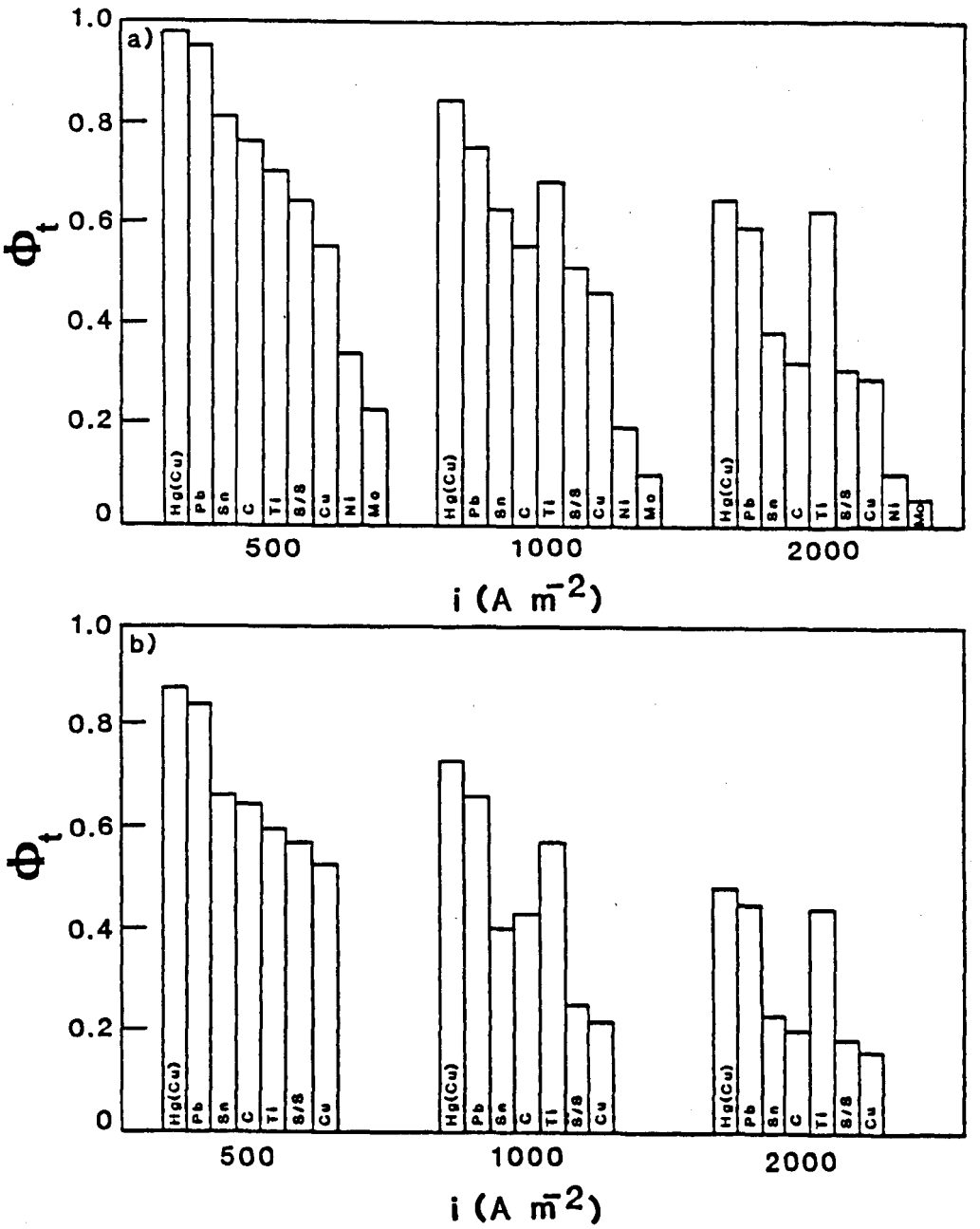

$\bar{v}$ ≐ 0.123 m s^{-1}. Expamet (orientation A) in the catholyte channel.

FIGURE 8.6 Effect of current density on the current efficiency at the cathodes for a) $X_{2,t}$ = 0.20 and b) $X_{2,t}$ = 0.90.

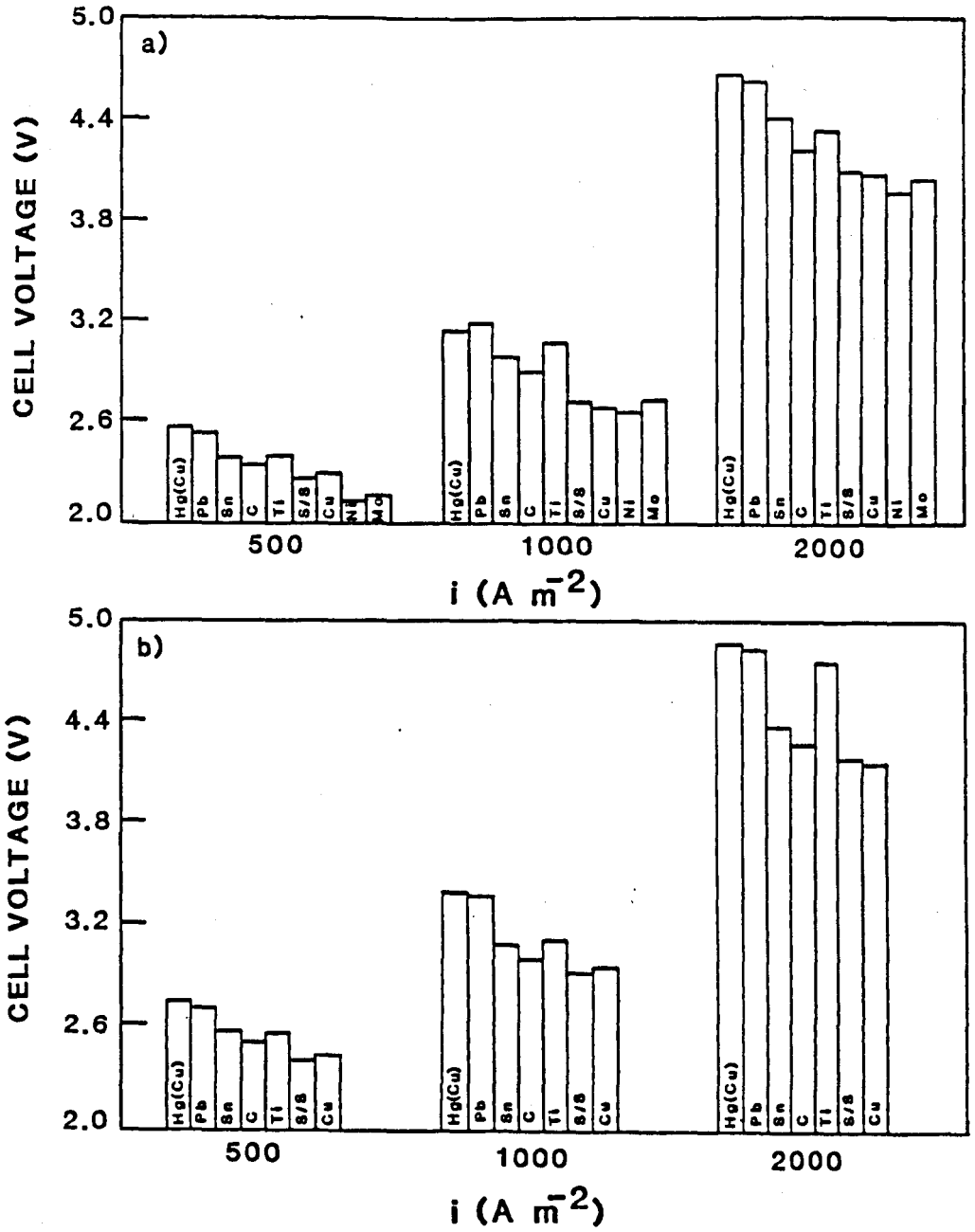

$\bar{v}$ = 0.123 m s^{-1}. Expamet (orientation A) in the catholyte channel.

FIGURE 8.7 Effect of current density on the cell voltage at the cathodes for a) $X_{2,t}$ = 0.20 and b) $X_{2,t}$ = 0.90.

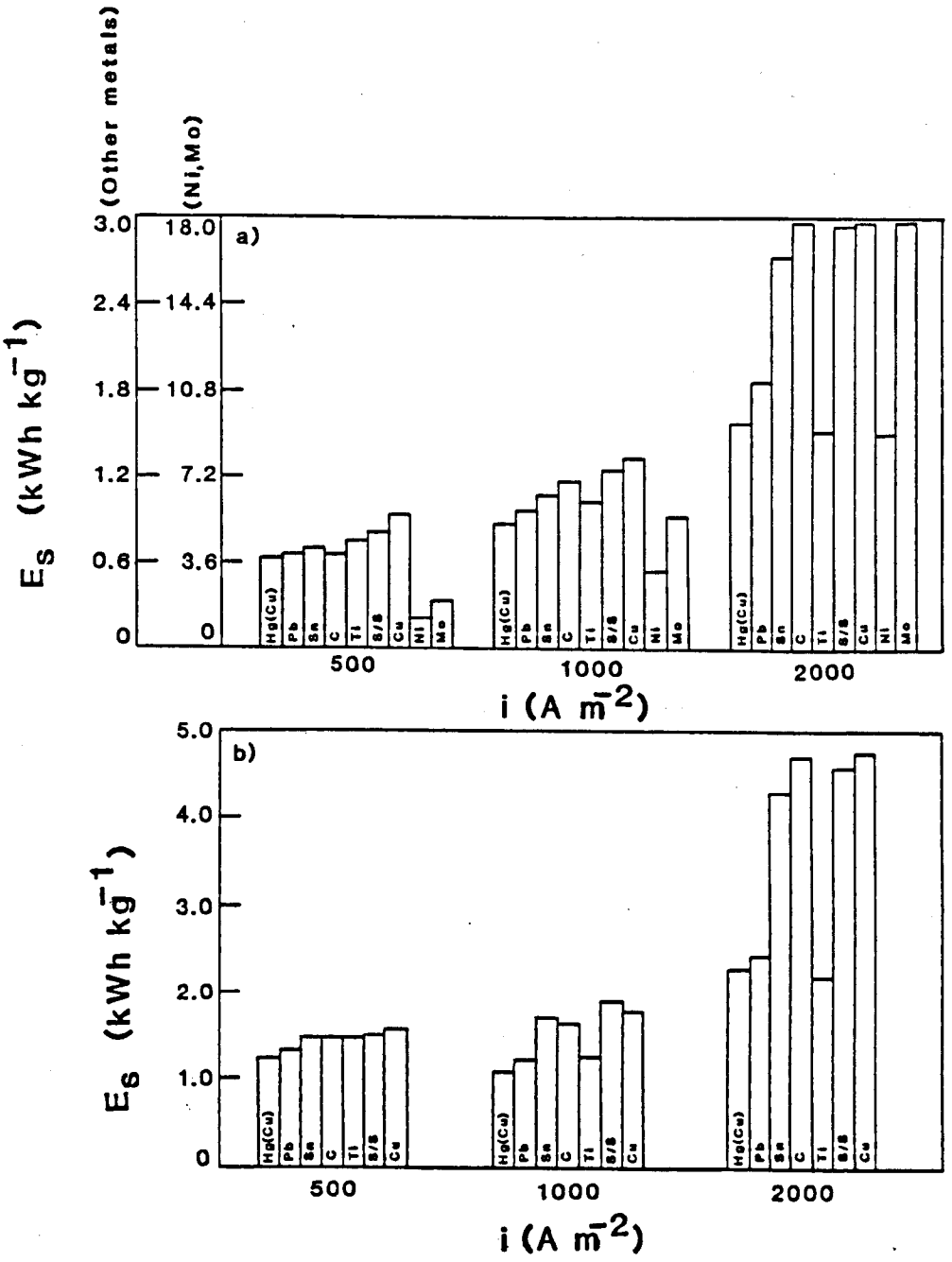

$\bar{v}$ = 0.123 m s^{-1}. Expamet (orientation A) in the catholyte channel.

FIGURE 8.8 Effect of current density on the specific energy consumption at the cathodes for a) $X_{2,t}$ = 0.20 and b) $X_{2,t}$ = 0.90.

through the effect upon the current efficiency for L-cystine hydrochloride reduction. None of the cathodes show any great electrocatalytic effect for reduction of the amino acid relative to that for hydrogen evolution, despite indirect evidence of disulphide adsorption at all cathodes from the lowering of the current efficiency for L-cystine hydrochloride reduction in zone I with increasing applied current density.

As discussed in Section 7.4 lowering of the current efficiency in zone I at mercury plated copper and lead cathodes probably arises as a result of the higher Tafel slope of ca. 180 mV/decade for reduction of the disulphide compared with ca. 120 mV/decade for hydrogen evolution. Since the most often quoted Tafel slope for hydrogen evolution at all the metals examined is ca. 120 mV/decade [4-7] (although there is a variation of ± 10 mV/decade at most metals and more than ± 30 mV/decade in some cases, reflecting the effect of variation in the electrode surface state and solution purity) the similar reduction in the current efficiency at all metals, with increasing current density, suggests the Tafel slope for L-cystine hydrochloride reduction may be similarily high at these cathodes. Such a high Tafel slope cannot be accounted for using classical electrochemical theory for the kinetics of electron transfer. The best explanation of the high Tafel slope for L-cystine hydrochloride reduction is modification of the kinetics of electron transfer by adsorption of the reactant at the electrode surface (see Section 3.5.1). This may also partially account for the start-up behaviour observed with all cathodes in constant current electrolyses.

Contrasting this behaviour, at titanium there is little change in the current efficiency for L-cystine hydrochloride reduction between 500 A m^{-2} and 2,000 A m^{-2} (Figure 8.6a). The net result is figures of merit, which although much inferior at 500 A m^{-2}, (the metal is fifth in the above perfromance list) are just as economical as those at either mercury plated copper or lead at 2,000 A m^{-2}

(Figures 8.6a to 8.8a). For example using titanium, at a fractional conversion in the reservoir of 0.20, at 2,000 A m^{-2} the current efficiency is 62% which gives a space-time yield of 28.2 kg m^{-3} h^{-1} of product and the cell voltage is 4.34 V, which combined with the current efficiency, gives a specific energy consumption of 1.53 kWh kg^{-1}. By comparison at mercury plated copper (which is slightly more efficient than lead) the current efficiency is 64% which gives a space-time yield of 28.5 kg m^{-3} h^{-1} of product. The cell voltage is 4.67 V which produces a slightly higher specific energy consumption of 1.57 kWh kg^{-1}. In industrial electrosyntheses, high current densities are often required to achieve the necessary space-time yields. Certainly, the results for titanium identified the metal as a possible alternative to mercury plated copper and lead for the industrial process, particularly bearing in mind the stability and product contamination problems associated with the heavy metal cathodes (Section 7.7.3). Long term stability tests were therefore performed on titanium the results of which are given in Section 8.5.

At titanium the near independence of the current efficiency for L-cystine hydrochloride reduction in zone I upon the applied current density must be due to an essentially equivalent Tafel slope for the two competing reactions. Measurement of the Tafel slope for hydrogen evolution from aqueous 2.0 mol dm^{-3} hydrochloric acid in the reactor, at a fresh titanium cathode, gave a value of 147 mV/decade at 25°C. This is not inconsistent with the available literature. Of the metals investigated titanium gives the widest reported range of Tafel slopes for hydrogen evolution (e.g. 119 mV/decade, 135 mV/decade, 150 mV/decade and 172 mV/decade have all been reported in aqueous 1 mol dm^{-3} sulphuric acid at 25°C and 120 mV/decade, 150 mV/decade, 153 mV/decade and 180 mV/decade in aqueous 1 mol dm^{-3} hydrochloric acid at 25°C [9]). Variation in electrode surface condition is

undoubtedly the cause of the wide variation. Kinetic studies are complicated by an oxide film on the metal, which forms spontaneously in air, and by the formation of titanium hydride [9-12] on the electrode surface under conditions of copious hydrogen evolution. Thus if hydrogen evolution and disulphide reduction occur independently in the reactor it appears that the Tafel slope for disulphide reduction at a 'fresh' titanium surface is also ca. 147 mV/decade.

8.4.2 Effect of Catholyte Flowrate

At all cathodes during a batch electrolysis the figures of merit become much less economical as electrolysis proceeds. This is illustrated in Figures 8.5 to 8.8 by comparing the values for typical electrolyses at a reactant conversion of 20% with those for 90% converison. In all cases at the higher reactant conversion the current efficiency (Figure 8.6) and space-time yield (Figure 8.5) are substantially lower and the cell voltage (Figure 8.7) and specific energy consumption (Figure 8.8) significantly higher. This arises principally as a result of the effect of mass transport on the electrosynthesis. At the beginning of electrolyses, in zone I, the current efficiency is constant and since the applied current density is constant the space-time yield is maintained. The fractional conversion in the reservoir rises linearly with time. The cell voltage and therefore the specific energy consumption rise gradually. As soon as the rate of mass transport of the reactant starts to influence the reduction rate (i.e. in the mixed kinetic-mass transport controlled region and zone II) the current efficiency and space-time yield fall producing a more gradual rise in the fractional conversion. The cell voltage continues to increase and combines with the lower current efficiency to give a higher rate of increase in the specific energy consumption. These trends are exemplified in Figure 8.9 for a typical electrosynthesis at titanium.

Compared with mercury plated copper and lead there is a significant region of

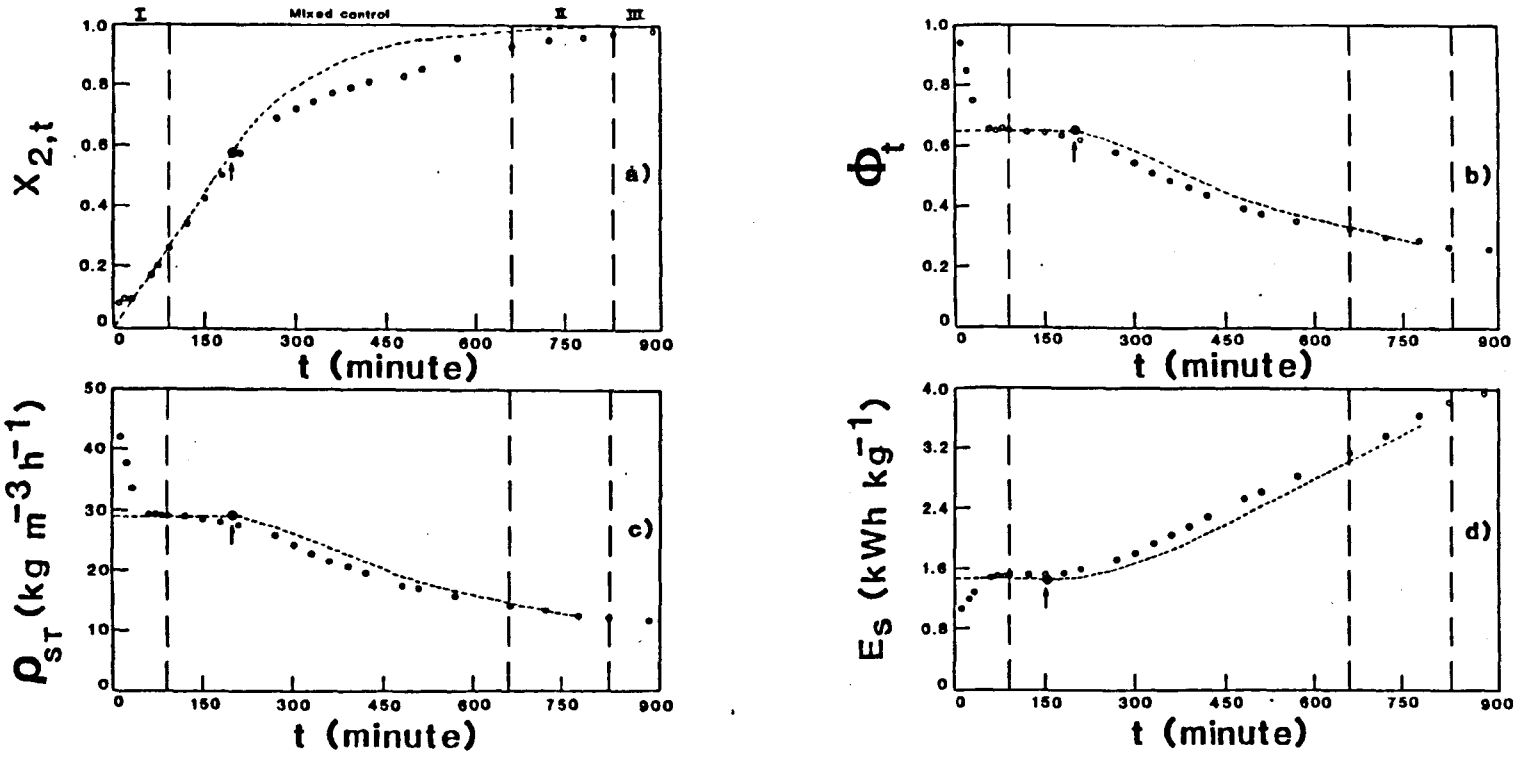

------ Figures of merit predicted by the model. ● (t_{CRIT}, C_{CRIT})

i = 2,000 A m^{-2} and $\bar{v}$ = 0.066 m s^{-1}. Expamet (orientation A) in the catholyte channel.

FIGURE 8.9 Change in the figures of merit during batch electrolysis at titanium.

mixed kinetic-mass transport controlled reduction at the alternative cathodes (Figure 8.1). This produces a greater degradation in the figures of merit than would be observed for a sharper transition from kinetic to mass transport controlled reduction, evident at the heavy metal cathodes. This is also exemplified in Figure 8.9 by the comparison between the experimental and predicted figures of merit. It might therefore be expected that it is even more important to maximise the rate of mass transport at the alternative cathodes.

The effect of increasing the rate of mass transport of the disulphide to the cathode surface,by increasing the catholyte flowrate through the cell, was investigated. The result of an increase in the nominal, linear catholyte velocity from 0.033 m s^{-1} to 0.123 m s^{-1} on the figures of merit at the cathodes for a reactant conversion of 70% is shown in Figure 8.9. Higher reactant conversions were not achieved on the timescale of electrolyses with the least efficient cathodes at the lowest catholyte flowrate . As expected, at all cathodes there is a significant improvement in the figures of merit at the higher catholyte velocity (Figure 8.10). For example at carbon over the range of catholyte velocities the current efficiency is raised from 12% to 27% which produces an increase in the space-time yield from 5.2 kg m^{-3} h^{-1} to 12.0 kg m^{-3} h^{-1} and the specific energy consumption is lowered from 8.00 kWh kg^{-1} to 3.61 kWh kg^{-1}. The results in Figure 8.10 coupled with the demand for greater than 99% reactant conversion shows the great requirement for the rate of mass transport to be maximised in the reactor with the alternative cathodes.

8.5 STABILITY OF THE TITANIUM CATHODE

The performance of the titanium cathode was examined over 168 hours continuous operation at a current density of 500 A m^{-2}. After approximately 48

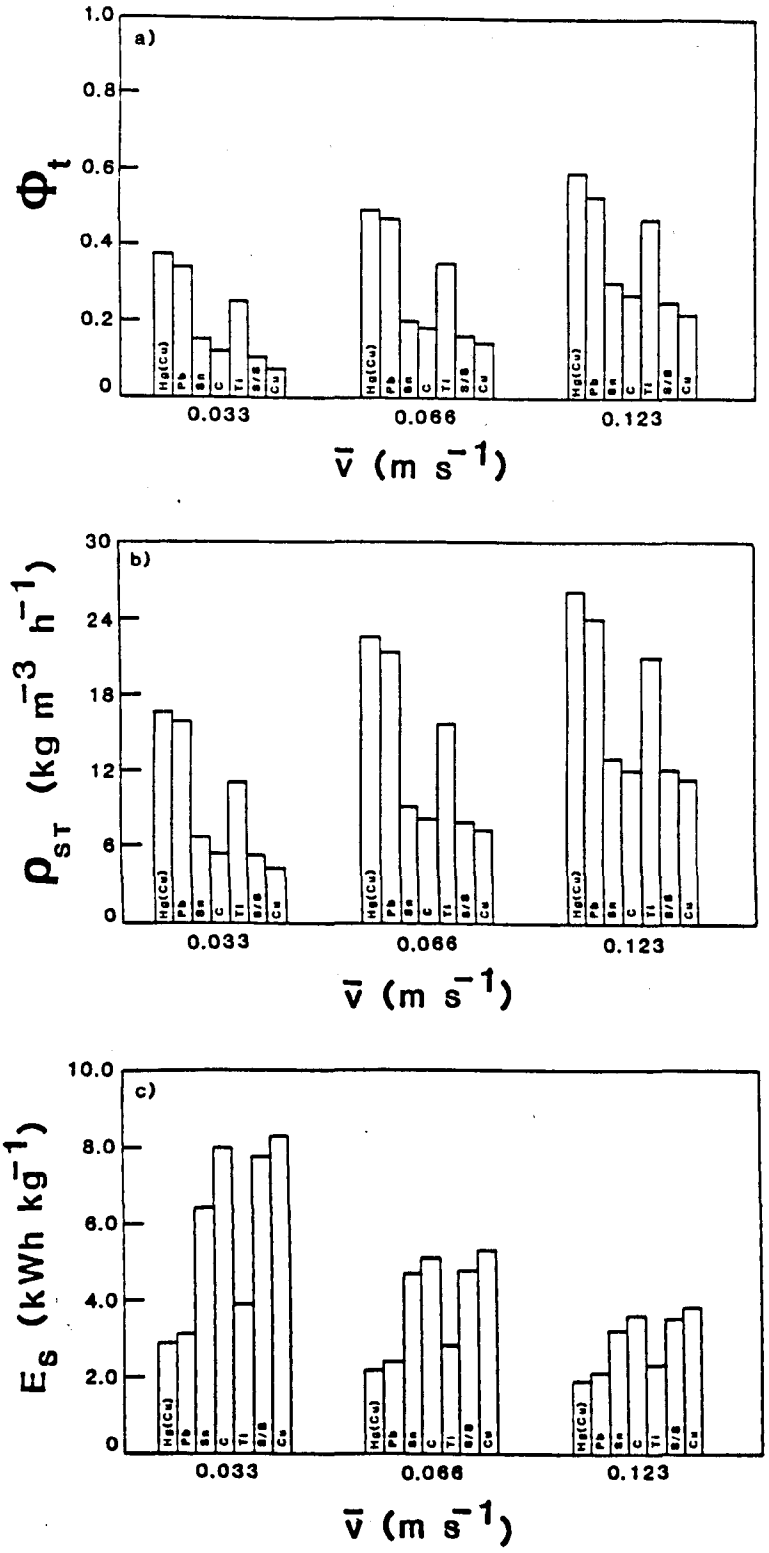

All values are for $X_{2,t}$ = 0.70 and i = 2,000 A m^{-2}. Expamet (orientation A) in the catholyte channel.

FIGURE 8.10 Effect of catholyte flowrate on L-cystine hydrochloride reduction at the cathodes.

hours current efficiencies fell by about 50%. This was due to formation of titanium hydride on the cathode surface. Visual examination showed a greyish-black surface coating on the cathode which was identified as titanium hydride (i.e. TiH_x with x = 1 to 2) by ex-situ XRD analysis [12]. Current-potential curves in aqueous 2.0 mol dm^{-3} hydrochloric acid, at fresh and aged cathodes, confirmed promotion of hydrogen evolution at the hydrided cathode in agreement with the literature [9,13] and the observed drop in current efficiency for disulphide reduction in the reactor. There is an additional problem that titanium hydride is also known to embrittle titanium [11]. Titanium ions were not detected in the product (< 1 ppm), however, which met the product specifciation even after the reactor had been in operation for 168 hours. Nonetheless this further example of an electrode failing to maintain performance over an acceptable time period in an electroorganic synthesis prevents the use of the metal for the industrial manufacture of thiol.

8.6 CONCLUSIONS

The simple mathematical models outlined in Section 7.3 do not adequately predict the reactant concentration decay in the system at the alternative cathodes. This is because there is a large region of mixed control between zones I and II. Despite this analysis of the reactant concentration decay in zone II still yields the average mass transport coefficient in the reactor. The coefficients obtained at the range of metals are in reasonable agreement.

At all cathodes L-cysteine hydrochloride can be synthesised in quantitative yield. Of the alternative cathodes, however, only titanium gives figures of merit which are comparable to those at mercury plated copper and lead. This is achieved only at the industrially significant current density of 2,000 A m^{-2}. The

metal cannot be used in the industrial process, however, because of the formation of titanium hydride after 48 hours operation which halves the current efficiency and may eventually cause cathode embrittlement.

At a current density of 500 A m^{-2}, which is the optimum current density for all cathodes apart from titanium, if batch processing times are acceptable, the order of cathode performance based upon the figures of merit is controlled by the hydrogen overpotential of the metals. High hydrogen overpotential metals are clearly favoured. As a result of the extensive region of mixed control between zones I and II at the alternative cathodes, it is even more important to maximise the rate of mass transport to these cathodes compared with mercury plated copper and lead. High catholyte flowrates and turbulence promoters should be used in the reactor.

REFERENCES

1. Millington J. P. Personal Communication (The analysis was performed under contract for the Electricity Research and Development Centre).
2. Dawson R.M.C., Elliott D.C., Elliott W.H. & Jones K.M. "Data for Biochemical Research". Clarendon Press, Oxford (1986). Pages 12 and 13.
3. Storck A. Electrosynthesis Conference 9-11th July, Novohotel, Southampton (1990).
4. Appleby A.J., Kita H., Chemla M. & Bronoel G. in "Encyclopedia of Electrochemistry of the Elements". Ed. Bard A.J., Marcel Dekker, New York (1982). Volume IX Part A, 413-556.
5. Pourbaix M. "Atlas of Electrochemical Equilibria in Aqueous Solutions". National Association of Corrosion Engineers (1974). Pages 115-117.
6. Trasatti S.; *J. Electroanal. Chem.* 39, 163, (1972).
7. Kuhn A.T., Mortimer C.J., Bond G.C. & Lindley J.; *J. Electroanal. Chem.* 34, 1, (1974).
8. Selman J.R. & Tobias W.; *Adv. in Chem. Eng.* 10, 211, (1978).
9. Kelly E.J. in "Modern Aspects of Electrochemistry No. 14". Eds. Bockris J.O'M., Conway B.E. & White R.E., Plenum Press, New York (1982). Chapter 5.
10. Morozumi T. & Mizuno T.; *Nippon Kinzoku Gakkai Kaiho* 16, 119, (1977). (Chem. Abs. 88, 160508s, 1979).
11. Millenbach P. & Givon M.; *J. Less Common Metals* 87, 179, (1982).
12. Kelly E.H.; *Electricity Research and Development Centre Report 4273*, May (1988).

13. Pourbaix A. & Marek M.; *Cent. Belge Etude Corros. Rapp. Tech.* 118 (RT. 197), RT. 197–RT.197/5 (1971).

(Chem. Abs. 76, 120646f, 1972).

CHAPTER 9

GENERAL OBSERVATIONS AND SUGGESTIONS FOR FURTHER WORK

At the end of each chapter, conclusions have been drawn from the results presented in that chapter. Therefore no attempt is made here to give detailed conclusions about all aspects of the work. Rather some general observations and some suggestions for following up these observations are presented.

As discussed in Chapter 1 the electrosynthesis of L-cysteine hydrochloride is possible at any one of a wide range of electrode materials (e.g. mercury, lead, transition metal macrocycles, titanium tin, zinc, carbon, stainless steel, silver, copper, nickel and molybdenum). There is little evidence in the current work or the literature of by-product formation at any of these materials (see Sections 1.4.2(b), 1.4.4, 7.7.1 and 8.1). This suggests that the key to an efficient electrosynthesis is an electrode material which exhibits a much lower overpotential for L-cystine hydrochloride reduction than hydrogen evolution. Whilst the extensive literature on the kinetics of hydrogen evolution [1-4] provides a selection guide based upon the hydrogen overpotential of materials, there is little to aid the selection of materials with the possibility of a low overpotential for L-cystine hydrochloride reduction.

It does appear, however, that adsorption of the disulphide at the electrode surface plays an important role in the control of the L-cystine hydrochloride overpotential. At mercury, direct evidence of this is provided by the effect of the disulphide coverage on k_f^o for the reduction reaction. Up to disulphide coverages of 0.68, k_f^o is about 2×10^{-7} m s^{-1}, but is reduced to 6.6×10^{-10} m s^{-1} at the maximum surface coverage (Section 3.8.5). Comparison of the voltammetric response at mercury (Figure 3.3) and lead (Figures 4.2) with that at cobalt tetrasulfophthalocyanine adsorbed onto ordinary pyrolytic graphite (Co-TSP/OPG) (Figure 1.8) and heat-treated cobalt tetramethoxyphenylporphyrin adsorbed onto graphite (Co-TMPP/graphite) (Figure 1.10) also highlights the importance of

adsorption phenomena. Although, as far as can be ascertained, the mechanism of reduction, shown below,

$$RSSR.2HCl + H^+ + e^- \longrightarrow RSH.HCl + RS^{\bullet}.HCl$$

$$RS^{\bullet}.HCl + H^+ + e^- \rightleftharpoons RSH.HCl$$

is equivalent at the four electrodes, reduction commences at potentials about 0.5 V less negative at the cobalt macrocycles. Combined with the comparison of Tafel slopes at the electrodes (i.e. about 240 mV/decade at Co-TSP/OPG, 120 mV/decade at Co-TMPP/graphite and close to 180 mV/decade at mercury and lead) this represents a significant electrocatalytic effect. It appears that the strength and/or orientation of adsorption of L-cystine hydrochloride at the cobalt macrocycles is more favourable than at either mercury or lead. Macrocyclic materials were not, however, examined in this study, for although electrocatalytic for L-cystine hydrochloride reduction they also exhibit a significant enhancement in the rate of hydrogen evolution over rates at mercury and lead. In electrolyses of disulphide solutions at the Co-TMPP/graphite electrode at a current density of 200 A m^{-2} the current efficiency in the initial stages of reduction was only 60% [5]. This contrasts with a current efficiency of greater than 96% at 500 A m^{-2}, at mercury and lead cathodes (Section 7.7.1). Also there is the problem that hydrogen evolution removed Co-TSP from the OPG surface [6].

From this study it appears that the disulphide (and thiol) adsorb at many metal surfaces. This is exemplified by voltammetric studies (Section 1.4.3) and, in electrosynthesis experiments, by the projected high Tafel slopes for L-cystine hydrochloride reduction (Section 8.4) and the significant start-up period observed

(Sections 7.6 and 8.3). Consequently, development of a set of cathode selection criteria, based upon the overpotential for L-cystine hydrochloride, would be provided by a fundamental study of the chemistry of metal-disulphide and metal-thiol interactions. There are a number of in-situ spectroelectrochemical techniques [see e.g. 7] capable of providing real time information on the nature of the electrode interface together with the electrocatalytic activity for electrochemical reactions. In-situ Infra-Red and Raman spectroscopy, which are capable of providing much detailed and complementary information on the bonding and relative orientation of chemisorbed species, are particularly promising for the L-cystine/L-cysteine system.

The many variants of in-situ Infra-Red spectroscopy which have been applied to electrochemical systems have been reviewed by Weeks [8]. The common problems are solvent IR absorption, particularly in aqueous media, and achieving the required sensitivity to detect surface species. It might be possible to examine the L-cystine/L-cysteine system using 'bulk' electrode materials in a suitable thin film cell using Electrochemically Modulated Infra-Red Spectroscopy (EMIRS), Subtractively Normalised Infrared Fourier Transform Infra-Red Spectroscopy (SNIFTIRS) and Infra-Red Reflection Absorption Spectroscopy (IRRAS). Alternatively thin metal films, deposited by evaporation or sputtering, upon quartz or some other Infra-Red transparent substrate could be employed as working electrodes and analysed using Multiple Internal Reflection Fourier Transform Infra-Red Spectroscopy (MIRFTIRS).

Surface studies are improbable using Raman spectroscopy due to the inherently low sensitivity of the technique. Surface Enhanced Raman Scattering (SERS) must be employed [9]. Indeed, Watanabe and Maeda [10] have shown that it is possible to obtain information for the L-cystine/L-cysteine system using in-situ

SERS at a silver electrode (Section 1.4.2(c)). The technique involves roughening the electrode surface by potential cycling, or pulsing, between potential regions where the metal electrode is oxidised and reduced. Unfortunately the SERS effect has only been reported [9] to be useful at silver, gold and copper electrodes under certain conditions. Leung et al [11] have, however, reported a successful extension of the range of electrode materials which can be examined. They deposited a thin film (< a few monolayers) of various metals on a gold surface. Although there must be considerable concern regarding the properties of such films compared with those of a bulk metal, the approach is one which could yield valuable data for the L-cystine/L-cysteine system.

Surface plasmon resonance (SPR) [12] is another technique which might be particularly applicable to the amino acid system since it has been used widely in the study of biological compounds. SPR is a phenomenon which occurs between incoming U.V.-visible photons and the electrons in the surface of a thin metal film usually mounted on a glass support. At a specific angle of incident light, energy is transferred to the electrons in the metal surface causing the reflected light to disappear. This angle, called the resonance angle, changes as the mass concentration in the vicinity of the metal surface changes. Significantly, the resonance angle may be used not only to determine if adsorption occurs but can be related to the quantity of material adsorbed. It should therefore be possible, by using the multiple internal reflection mode of operation, to determine adsorption isotherms and perhaps also the kinetics of adsorption if not too fast, for the amino acids at a series of metals, in real time, as a function of electrode potential.

There is some measure of agreement between the results of the voltammetric studies (Chapters 3 and 4) and the electrosynthesis studies (Chapters 7 and 8). The voltammetry at mercury and lead shows that the reduction of L-cystine

hydrochloride is electrochemically irreversible (Figures 3.3 and 4.2 respectively). At lower overpotentials the reduction rate is under pure kinetic control; at intermediate overpotentials mixed kinetic–mass transport control ensues and at higher overpotentials pure mass transport control prevails. Application of simple mathematical models for constant current electrolysis in the reactor (Sections 7.6 and 8.3), indicates that the reduction rate is governed by kinetic control, at all cathodes in the early stages of the electrosynthesis, since the overpotential is low. As the reactant is depleted, however, the overpotential becomes intermediate and mixed kinetic–mass transport control is evident. Eventually pure mass transport control ensues at higher overpotentials.

The voltammetry predicts that mercury and lead are the most efficient cathodes at low current densities (Section 4.1). At 500 A m^{-2}, the lowest current density used in the reactor, this behaviour is observed (Figure 8.6). For kinetically controlled reduction of L–cystine hydrochloride, the current efficiency is close to 100% at mercury and lead but is restricted to between 81% (i.e. at tin) and 23% (i.e. at molybdenum) at the other cathodes. In voltammograms at these other metals, it is not possible to separate L–cystine hydrochloride reduction from hydrogen evolution (Section 4.1).

The performance of titanium does, however, illustrate the danger of using voltammetry to grade cathodes for electrosynthesis performance. L–Cystine hydrochloride reduction cannot be separated from hydrogen evolution in voltammograms at the metal (Section 4.1). Consequently at a current density of 500 A m^{-2} in the reactor the current efficiency is only 70% in the kinetic region (Figure 8.6a). As the current density is increased to the industrially advantageous 2,000 A m^{-2}, however, the current efficiency drops to only 62% in the kinetic region. This behaviour contrasts with the much sharper drops observed at all

other metals (Figure 8.6a). Consequently, at a current density of 2,000 A m^{-2}, the figures of merit at titanium are comparable to those at mercury plated copper and lead (Figures 8.5a to 8.8a). The effect has been attributed to similar Tafel slopes for reduction of the disulphide and hydrogen evolution at titanium (Section 8.4.1). This contrasts with a lower Tafel slope for hydrogen evolution compared with the slope for disulphide reduction at the remaining cathodes. Voltammetry should be coupled with constant potential coulometry and product analysis whenever possible. This allows calculation of partial currents for a given reaction at selected electrode potentials.

The real drawback of voltammetric studies in terms of translation into electrochemical performance, as stressed in the introduction (Section 1.5) - the inability of electrode materials to maintain peformance in durability tests, is amply demonstrated in this study. Mercury plated copper (24 hours), lead (72 hours and titanium (48 hours) all showed significant reductions in current efficiency over the short time scales (in electrosynthesis terms) shown above. The hydrogen overpotential of the metals was substantially reduced by, respectively, the diffusion of copper to the mercury surface, the contamination of lead by trace metal impurities in the catholyte, and perhaps also by the effect of a lead chloride film formed as a result of cathode corrosion, and by the hydriding of titanium (Sections 7.7.3 and 8.5).

In light of the observed durability problems, there is a requirement for a continuing study of new cathode materials. Materials selected should ideally satisfy a number of criteria. They should have a high hydrogen overpotential and have the possibility of adsorbing the disulphide molecule neither very strongly nor very weakly. Materials must be good electronic conductors and exhibit adequate stability in the hydrochloric acid catholyte. These last two criteria suggest nitrides

and carbides [13] are classes of materials which might be useful cathodes. Since titanium is a good catalyst for the organic reduction at high current densities one might consider using titanium carbide or titanium nitride where hydriding should be less of a problem due to the change in the crystal structure and bonding of titanium. Titanium metal has a hexagonal close packed structure whereas titanium carbide and titanium nitride both have sodium chloride structures with fairly strong metal/non-metal bonding proposed [13]. Hydriding involves the formation of TiH_x (x = 1 to 2) which has a fluorite structure [14]. If, as suggested, adsorption of L-cystine hdyrochloride is a prerequisite for a good electrocatalyst, the fact that titanium nitride and carbide are electron deficient may possibly change the adsorption strength of the disulphide compared with that at titanium to produce increased rates of amino acid reduction. The effect upon the hydrogen overpotential, compared with titanium metal, may be just as significant.

Another approach might be the use of titanium 'bronzes' (i.e. $Na_x TiO_2$ with x = 0.20 to 0.25) [15] which also exhibit high electrical conductivity and chemical inertness. Significantly they also have a different crystal structure to titanium metal and have the titanium bonded. They may just allow rates of hydrogen evolution no faster, and disulphide reduction rates no lower, than on pure titanium metal, without the problem of hydriding. Of course, successful results from this applied study of new materials could be incorporated into the fundamental studies proposed earlier.

The effect of the major process variables (i.e. current density and catholyte flowrate) upon the electrosynthesis is clear. At titanium, 2,000 A m^{-2} is the optimum current density whilst at the remaining cathodes, 500 A m^{-2} is optimum if batch processing times are acceptable (Figures 8.5 to 8.8). At all cathodes, and particularly the alternatives to mercury plated copper and lead, which show a large

region of mixed kinetic–mass transport controlled behaviour (e.g. Figure 8.9), the rate of mass transport should be maximised in the reactor. All the figures of merit examined (Figure 8.10) become much more attractive at higher rates of mass transport. High catholyte flowrates should be used and efficient turbulence promoters should be employed in the catholyte channel.

This suggests that a more comprehensive engineering study of alternative methods of mass transport enhancement could be beneficial for the process. The use of porous 3'D' electrodes [16] should be evaluated. They offer the possibility of mass transport enhancement without the problem of electrode blinding observed with inert turbulence promoters, although potential and current distribution can be problematical [16]. As a more novel approach, the effect of ultrasound on the electrosynthesis could be evaluated. The technique has been applied to metal plating processes and, at best, a doubling of the rate of mass transport of metal ions reported [17,18], from perturbation of the boundary layer. Practically, however, health and safety is a concern, reliable acoustic sources are not always available and there is the danger of mechanical damage to the electrode surface from the cavitation produced by the ultrasound [19].

REFERENCES

1. Appleby A.J., Kita H., Chemla M. & Bronoel G. in "Encyclopedia of Electrochemistry of the Elements". Ed. Bard A.J., Marcel Dekker, New York (1982). Volume IX Part A, 413-556.
2. Pourbaix M. "Atlas of Electrochemical Equilibria in Aqueous Solutions". National Association of Corrosion Engineers (1974). Pages 115-117.
3. Trasatti S.; *J. Electroanal. Chem.* 39, 163, (1972).
4. Kuhn A.T., Mortimer C.J., Bond G.C. & Lindley J.; *J. Electroanal. Chem.* 34, 1, (1974).
5. Wang Z., Li C., Deng Z. & Zha Q.; *Huaxue Xuebao* 44, 863, (1986). Chem. Abs. 105, 199030z, (1986).
6. Zagal J. & Herrera P.; *Electrochim. Acta* 30, 449, (1985).
7. Southampton Electrochemistry Group. "Instrumental Methods in Electrochemistry". Ellis Horwood Ltd., Chichester, (1985). Chapter 10.
8. Weeks S.A. PhD Thesis, St. Catherine's College, Oxford (1988).
9. Chang R.K. & Laube B.L.; *Rev. Solid State Mat. Sci.* 12, 1, (1984).
10. Watanabe T. & Maeda H.; *J. Phys. Chem.* 93, 3258, (1989).
11. Leung L.-W. H. & Weaver M.J.; *J. Am. Chem. Soc.* 109, 5113, (1987).
12. Otto A.; *Surf. Sci.* 101, 99, (1980).
13. Wells A.F. "Structural Inorganic Chemistry". 4th Edition, Clarendon Press, Oxford (1975). Pages 1051-1059.
14. Wells A.F. "Structural Inorganic Chemistry". 4th Edition, Clarendon Press, Oxford (1975). Page 297.
15. Greenwood N.N. & Earnshaw A. "Chemistry of the Elements". Pergamon Press, Oxford (1984). Page 1123.

16. Pletcher D. & Walsh F.C. "Industrial Electrochemistry". Chapman and Hall, London (1990). Chapter 2.

17. Walker R. & Clements J.E.; *Metal Finishing* April (1970). Page 100.

18. Kochergin S.G. & Vyaseleva G.Y.; *Consultants Bureau Report*, New York (1966).

19. Walsh F.C. PhD Thesis, Loughborough University (1981).